Bcl-2 proteins and membranes: insights on their interaction

Dissertation

der Mathematisch-Naturwissenschaftlichen Fakultät

der Eberhard Karls Universität Tübingen

zur Erlangung des Grades eines

Doktors der Naturwissenschaften

(Dr. rer. nat.)

vorlegt von

Joseph D. Unsay

aus Manila, Philippines

Tübingen

2016

Gedruckt mit Genehmigung der Mathematisch-Naturwissenschaftlichen Fakultät der Eberhard Karls Universität Tübingen.

Tag der mündlichen Qualifikation:	21.10.2016
Dekan:	Prof. Dr. Wolfgang Rosenstiel
1. Berichterstatter:	Prof. Dr. Ana J. García-Sáez
2. Berichterstatter:	Prof. Dr. Dirk-Peter Herten

Kapag nasabi na ang lahat ng masasabi,
ang pinakamahalaga ay hindi masasabi.
Magagawa lamang

ZHUANG ZHOU

When everything has been said,
the most important thing cannot be said.
It can only be done.

ZHUANG ZHOU

Summary

The Bcl-2 family of proteins regulates mitochondrial outer membrane permeabilization (MOMP) – considered as the point-of-no-return in apoptosis. As the gatekeeper for survival or death of cells, this network is tightly regulated by interactions of its members with opposing functions. The embedded together model remains as one of the most accepted models to describe the interactions between family members. This model highlights the role of the mitochondrial membrane to augment these interactions. And while this model has been repeatedly exemplified *in vitro*, the effect of membranes on Bcl-2 protein interactions has not yet been fully explored in living cells.

On the other hand, the Bcl-2 proteins could also affect the physical properties of the membrane. Bax and Bak are the main effectors of apoptosis, believed to form pores on the mitochondrial outer membrane. However, no one has seen an apoptotic pore. Aside from its permeabilizing activity, the effect of Bcl-2 proteins on the physical properties of the membrane is not yet well-elucidated. As such, the main question of this thesis is: how do Bcl-2 proteins affect the membrane (and vice versa)?

This work has shown the effect of pro-apoptotic member Bax and its activator, cleaved Bid (cBid), on membranes using atomic force microscopy (AFM). Cleaved Bid was shown to lower the breakthrough force of membranes, but not permeabilize it. This suggests that cBid may have a role in paving the way for Bax insertion and oligomerization. On the other hand, Bax's ability to change membrane properties depends on its oligomerization state – monomeric Bax does not change the membrane's properties, but oligomerized Bax lowers the membrane's breakthrough force. I also show through AFM imaging that Bax forms rings, arcs and lines in model membranes. In instances where pores are visible on the membrane, structures at the edge of the pore, which may correspond to Bax, does not necessarily need to line the edge completely. This further supports previous findings that Bax forms toroidal pores and that these pores can have a varied range of sizes.

Furthermore, this work has also shown the potential of scanning Fluorescence Correlation Spectroscopy (FCS) as a tool to measure interactions of Bcl-2 proteins in the mitochondria of living cells. I first validated scanning FCS' applicability using green fluorescent protein (GFP) targeted to mitochondria. I also evaluated possible models that characterize the diffusion of molecules in the mitochonodria. Using two color FCS, I report for the first time, to the best of my knowledge, a calculated dissociation constant between truncated Bid and anti-apoptotic member, Bcl-xL, in the mitochondria.

Based on these results, I highlight the important interplay between the membrane and the Bcl-2 proteins – in deciding a cell's fate, both membrane and Bcl-2 proteins work with and change each other.

Zusammenfassung

Die Bcl-2 Proteinfamilie reguliert die Permeabilisierung der äußeren mitochondrialen Membrane (MOMP), die als irreversivler Punkt der Apoptose gilt. Als ein Schalter zwisschen Leben und Tod der Zellen, ist dieses Netzwerk durch das Zusammenspiel seiner Mitglieder mit gegensätzlichen Funktionen stark reguliert. Das ,,embedded together" Modell ist eines der meist akzeptiertesten Modelle, dass das Zusammenspiel der Proteinfamilienmitglieder beschreibt. Dieses Modell hebt die Wichtigkeit der mitochondrialen Membran, zur Verstärkung des Zusammenspiels, hervor. Während dieses Modell in vitro wiederholt veranschaulicht wurde, ist der Effekt der Membran auf das Zusammenspiel der Bcl-2 Proteine in lebenden Zellen noch nicht vollständig untersucht.

Andererseits können die Bcl-2 Proteine auch die Eigenschaften von Membranen beeinflussen. Die Haupteffektoren der Apoptose sind Bax und Bak, von welchen angenommen wird, dass sie Poren in der äußeren mitochondrialen Membran bilden. Jedoch, hat wurde eine apoptotische Pore noch nicht gesehen. Abgesehen von der permeabilisierenden Aktivität ist der Effekt der Bcl-2 Proteine auf die physikalischen Eigenschaften der Membran noch nicht gut aufgeklärt. Deshalb ist die wichtigste Frage in dieser Doktorarbeit: Wie beeinflussen die Bcl-2 Proteine die Membran, und umgekehrt.

In dieser Arbeit wurde der Effekt von pro-apoptotischem Bax und seinem Aktivator, cBid (cleaved Bid), auf die Membran mithilfe von Rasterkraftmikroskopie (AFM), gezeigt. cBid zeigte eine Minderung der Durchbruchskraft der Membranen, permeabilisierte sie jedoch nicht. Dies lässt darauf schliessen, dass cBid eine Rolle in der Insertion von Bax und dessen Oligomerisierung spielen könnte. Andererseits hängt die Fähigkeit von Bax, die Membraneigenschaften zu verändern, von dessen Oligomerisierungzustand ab – monomeres Bax verändert die Membraneigenschaften nicht, oligomerisiertes Bax jedoch reduziert die Durchbruchskraft der Membran. Weiter zeige ich mithilfe von AFM Abbildungen, dass Bax Ringe, Kreisbögen und Linien in Modellmembranen formt. Die Strukturen am Rand von sichtbaren Poren in der Membran, die Bax entsprechen könnten, müssen den Rand nicht komplett umschließen. Dies unterstützt vorherige Untersuchungsergebnisse, dass Bax torodiale Poren formt, welche in ihrer Größe variieren können.

Darüber hinaus zeigt diese Arbeit das Potential von scanning Fluoreszenzkorrelationsspektroskopie (FCS), als ein Tool zur Messung von Interaktionen von Bcl-2 Proteinen in Mitochondrien von lebenden Zellen. Zuerst bestätigte ich die Verwendbarkeit von scanning FCS, mithilfe des grün-fluoreszierenden Proteins (GFP), das gezielt an Mitochondrien bindet. Ich bewertete zusätzlich mögliche Modelle, zur Charakterisierung der Diffusion von Molekülen in Mitochondrien. Mittels ,,two color" FCS berichte ich zum ersten Mal, nach meinem besten Wissen, eine kalkulierte Dissoziationskonstante zwischen ,,truncated" Bid und anti-apoptotischem Bcl-xL in Mitochondrien.

Basierend auf diesen Ergebnissen, hebe ich das wichtige Zusammenspiel der Membran und den Bcl-2 Proteinen hervor – beide die Membran und die Bcl-2 Proteine arbeiten mit- und ändern einander bei der Entscheidung über das Schicksal einer Zelle.

Acknowledgements

I would like to express my deepest gratitude to my supervisor, Prof. Dr. Ana J. Garcia-Saez. Her guidance allowed me to grow not only as a scientist but also as a person. She gave me the freedom to pursue my research goals in my own way, while keeping me on track these last five years. Her ideas, comments and suggestions – which are always in abundance, proved to be invaluable. She also fostered an environment of collaboration within and outside of the group, which also helped me get to know my contemporaries in the field, some of which, I'm happy to call my friends.

My laboratory colleagues have always been a source of support, knowledge, and encouragement during my PhD. As such, I would also like to give them thanks for this dissertation. Dr. Katia Cosentino and Dr. Yamunadevi Subburaj have been my constant workmates and collaborators with supported bilayers and atomic force microscopy. Both have been a blessing to work with. Eduard Hermann was my partner-in-crime in the lab until he left for the dark side (*cough* industry *cough*), providing a listening ear for all my crazy ideas during our dinners at the Cafe Botanik. Dr. Stephanie Bleicken was the guru of everything related to Bax structure and Bcl-2 proteins interaction next to Ana; she provided invaluable insights on the science as well as life in the sciences through discussions. Dr. Begoña Ugarte Uribe, Dr. Corinna Wagner, Raquel Salvador Gallego, Aida Peña Blanco, and Fabronia Murad provided all the assistance necessary to move forward with any part of project that involves biochemistry techniques. I thank Dr. Monika Zelman who first taught me FCS and cell culture. Fabronia Murad helped me by cloning a lot of my constructs for the FCS project, as well as supporting me through cell culture work. I would also like to thank my students: Tobias Schmidt was my extremely talented practical student who did well in the 7 weeks he was working on the p53 project, Katharina Sporbeck, who contributed in part by performing some of the permeabilization and lipid packing assays, and Bobby Vazquez who did some AFM work. To Dr. Uris Ros, who together with Katia, Aida and Bego, motivated me and encouraged me whenever I'm not feeling good about my science. To Kushal Das for our technical talks and cultural exchange; he was the first person I had to teach FCS in great detail so he also helped me understand FCS. To Vanessa Hertlein for our chats about football and german culture. To Dr. John Danial and Dr. Simon Poly, who despite being new to the lab, contributed to the warm, light and caring atmosphere. Carolin Stegmüller, Britta Liebler, and Sabine Schäfer for the technical support that ultimately helped us do well with our work. Specifically, I thank their work in purifying my proteins Bax and cBid, producing plasmids, and helping in the cell culture. And to those who I have met through their short/long stays in our lab (a shout out to Manuel Haschka, who introduced us to the CRISPR/Cas9 system), the institute administration and technicians, you were all part of this amazing, roller coaster journey!

Part of this work would have not been possible without the expertise and guidance of Dr. Jonas Ries. He gave valuable insights and direction for the FCS project, and his help in all matters related to optical microscopy allowed us to do our work with ease. Furthermore, he has also served as a second mentor, after Ana, not only in matters pertaining to the projects but also to the broader context of science and life.

I would also like to thank my thesis advisory committee at the German Cancer Research Center (Deutsches Krebsforschungzentrum, DKFZ): Prof. Dr. Jörg Langowski and Prof. Dr. Dirk-Peter Herten. Their comments challenged me to think more critically, to maintain clarity in the way I present my work and to always look at the bigger picture.

I also thank people I collaborated with that helped me hone my skills in AFM and FCS both in Heidelberg and Tübingen: (1) Nadinath and Bernd Bukau, (2) Ikhwan Sudji, (3) Helena Andreas and Walter Nickel, (4) Anna Pryszlak and Felix Hoppe-Seyler, (4) Marilia Campos and Gabriel Schaaf,(5) Michael Lorenz and Wolfram Antonin, (6) Christine Kiefer and Erik Schaeffer, and (7) Virtudes Mira-Rodado, Kenneth Berendzen and Klaus Harter.

I would also like to extend my warmest thanks to Dr. Lindsay Murrells of the Helmholtz International Graduate School at the DKFZ and Dr. Barbara Janssens of the DKFZ Career Services (and their staff, Evelyn, Heike, and Magdalena). They were instrumental in organizing events and conducting consultations that support not only me, but all the PhD Students at the DKFZ.

My PhD life wouldn't be as exciting and as bearable as it would have been without the undying support of my friends. My sanity was also kept intact thanks to the respite from lab work offered by The Wildtypes (my band), Studentenchor Heidelberg (my choir) and other friends in Heidelberg, Mannheim, and Tübingen. Special thanks go to Carole Loable, Gelo De La Cruz, David Peralta, Janet Lei, Kookie Cortina, Oui Buenafe, Jennifer Constantino, Jerome Unidad, Pao Bugarin, Ian Ken Dimzon, Philipp Timmer (and Markus!), Shaun Presow (and Uwe!), Robert Schramm, Dennis Fritzinger, Simon Faller, Foivos Tsokanos, Milene Costa da Silva, and Klaus Yserentant for providing me a home away from home in the last 5 years (especially after I moved to Tübingen). You have all seen me at my best, been with me at my worst and continue to be the greatest friends any person could have.

My sincerest gratitude also goes to my master's thesis mentor, Dr. Fabian Dayrit, who continues to support my scientific career and helped me in whatever way he can. *Salamat po!!*

This line is dedicated to all the people who inspired me (and eventually broke my heart) while in Europe. You know who you are.

During my PhD, I was also met with a medical condition that kept me away from the lab for one and a half months, and a further 8 months of recovery (with reduced working time). I would like to thank my friends who helped me during my recovery: Janet Lei, Kookie Cortina, David Peralta, Dan De Guia, Simon Faller, Max Ihmels, Max Knickmeyer, Philipp Werther, and Fengying Liu.

Lastly, this part would not be complete without giving thanks to my first inspirations in science, my parents, Jun and Lou Unsay. *Nagpapasalamat ako sa walang humpay niyong pagsupporta sa bawat interes, bawat adhikain at bawat pangarap. Nagpapasalamat ako sa araw-araw na sakripisyo, sa araw-araw na pagmamalasakit, at sa araw-araw na pagmamahal. Kayo ang rason kung bakit mahal ko lang ogham, kung bakit mahal ko ang matuto, magturo at magbahagi. Sa inyo ko una namalas ang kahulugan ng salita ni Zhuang Zhou, "Ang pinakamahalaga ay di masasabi. Magagawa lamang". Para sa inyo ang karangalang ito. Isinasama ko sa aking pasasalamat ang aking kuya Joshua (kasama na si Glady at baby Freyja) at bunsong kapatid na si Judith, na katulad ni Mama at Papa, ay patuloy na nagpapaalala sakin kung ano ang mga mahalagang bagay sa buhay.*

Who can say if I've been changed for the better, but, because I knew you, I have been changed for good

Elphaba and Glinda, Wicked

Contents

List of Figures

List of Tables

[title=List of Abbreviations]

Part I

Introduction

Chapter 1

Bcl-2 Proteins and the Mitochondria

Bcl-2 proteins are key determinants of cell fate in response to stress. They regulate the intrinsic pathway of apoptosis by controlling mitochondrial outer membrane permeabilization (MOMP). During apoptosis, release of apoptotic factors from the mitochondria, such as cytochrome c and Smac/DIABLO, trigger downstream processes that activate the caspase cascade and lead to cell death. MOMP is considered as the 'point of no return' in this pathway, and an understanding many of the key processes involved and the structures of the main players remain elusive. In this chapter, I introduce the Bcl-2 family and mitochondria, paying close attention to the dynamic interactions of the proteins with each other and the lipid membrane, as well as the resulting alterations undergone by mitochondria during apoptosis.

1.1 Apoptosis

Programmed cell death plays an important role in the life of multicellular organisms. From development to immunity, different modes of programmed cell death keep the organism in balance maintain homeostasis. Coined by Kerr, Wyllie, and Currie in 1972, apoptosis is one distinct form of programmed cell death. Its dysregulation leads to many diseases (Thompson, 1995) including: auto-immune lymphoproliferative syndrome, where autoreactive T-cells are not removed via apoptosis (Straus et al., 1999); cancer, due to a loss in sensitivity to apoptotic stimuli in tumor cells (Fernald and Kurokawa, 2013, Fuentes-González et al., 2013, Lowe and Lin, 2000, Wyllie et al., 1999); and several neurodegenerative disorders, characterized by premature loss of neurons related to excessive apoptosis (Desjardins and Ledoux, 1998, Mattson, 2000). Bacteria and viruses also have mechanisms that hijack apoptosis to their advantage and evade inflammatory immune response (Ashida et al., 2011, McCurrach et al., 1997).

Hallmarks of apoptosis include DNA fragmentation, plasma membrane blebbing and lipid rearrangement, and the formation of apoptotic bodies (Edinger and Thompson, 2004, Taylor et al., 2008). Such apoptotic bodies are phagocytosed by neighboring cells or macrophages, and thus apoptosis is traditionally considered a "clean" process. In contrast, necrosis releases the cell contents into the extra cellular environment, which may damage neighboring cells and trigger inflammatory response.

The main executioners of apoptosis are caspases (cysteine aspartic acid-specific proteases) (Taylor et al., 2008). Caspases are subdivided into initiator caspases (Caspase-8 and -9) or executioner caspases (Caspase-3, -6 and -7). Caspases are made up of a propeptide domain, followed by a large subunit and a small subunit. There are two possible pro-peptide domains: a caspase-recruitment domain or the death effector domain. These

domains facilitate interactions with proteins containing the same motif. Caspases are activated by a proteolytic process between the large and small subunits leading to rearrangement and consequent activation via heterotetramerization.

There are two main pathways of apoptosis. The extrinsic or death receptor pathway uses external signals to trigger apoptosis. Death receptors in the plasma membrane oligomerize into death-inducing signaling complexes (DISC) upon binding of ligands such as FasL or TNFα. DISC activates caspase-8, which in turn activates the executioner caspases.

The intrinsic or mitochondrial pathway responds to internal damage or stress induced by physico-chemical agents. In this pathway, a family of proteins called the Bcl-2 family, regulates the release of apoptotic factors (such as cytochrome *c*) from the mitochondria. The permeabilization of the mitochondrial outer membrane (MOM) is carried out by Bax and Bak. The release of these factors prompts the formation of the apoptosome (composed of cytochrome *c*, APAF1 and caspase-9) and this complex activates downstream executioner caspases.

The two pathways are not completely independent. In some cell types called type II cells, Caspase-8 activation in the extrinsic pathway also leads to activation of a Bcl-2 family member, Bid (Hao and Mak, 2010, Jost et al., 2009, Ozoren and El-Deiry, 2002). The truncated form of Bid, tBid (resulting from caspase cleavage), activates Bax and Bak, which then amplifies apoptosis by releasing the apoptotic factors.

1.2 Bcl-2 Proteins

First characterized in follicular lymphoma as a translocation t(14:18), the Bcl-2 proto-oncogene produces Bcl-2 protein that promotes cell survival rather than proliferation (Tsujimoto et al., 1984). Homologous proteins discovered later comprise the Bcl-2 family of proteins. This family of proteins, which currently contains more than 20 members, was found to regulate apoptosis and they have opposing roles in determining cell death or survival (Cory et al., 2003).

1.2.1 Members of the Bcl-2 family

The proteins of this family are divided into three groups based on their function and presence of Bcl-2 homology domains (BH domains) (Figure 1.1) (Adams and Cory, 1998, Cory et al., 2003, Gross et al., 1999):

- The anti-apoptotic or pro-survival proteins like Bcl-2, Bcl-xL, Mcl-1, and A1, inhibit apoptosis and thus promote survival.
- The pro-apoptotic effectors, which includes the executioners the Bax and Bak, are believed to form pores on the MOM that release apoptotic factors that activate downstream processes.
- The pro-apoptotic BH3-only proteins, as their name indicates, only contain the BH3 domain. They act as sensors of cellular stress. These include the sensitizers (e.g. Bad, Hrk, Bik) that inhibit the anti-apoptotic members and the direct activators (e.g. Bid, Bim) that also directly activate pro-apoptotic effectors.

In healthy cells, the BH3-only proteins remain in the cytosol or associated to the MOM. In the presence of apoptotic stimuli, the BH3-only proteins are activated and can either: (1) bind and activate the executioners Bax/Bak or (2) interact and inhibit anti-apoptotic members, which then free direct activators and/or Bax and Bak to perform their pro-apoptotic function. Upon activation, Bax inserts into the MOM and together

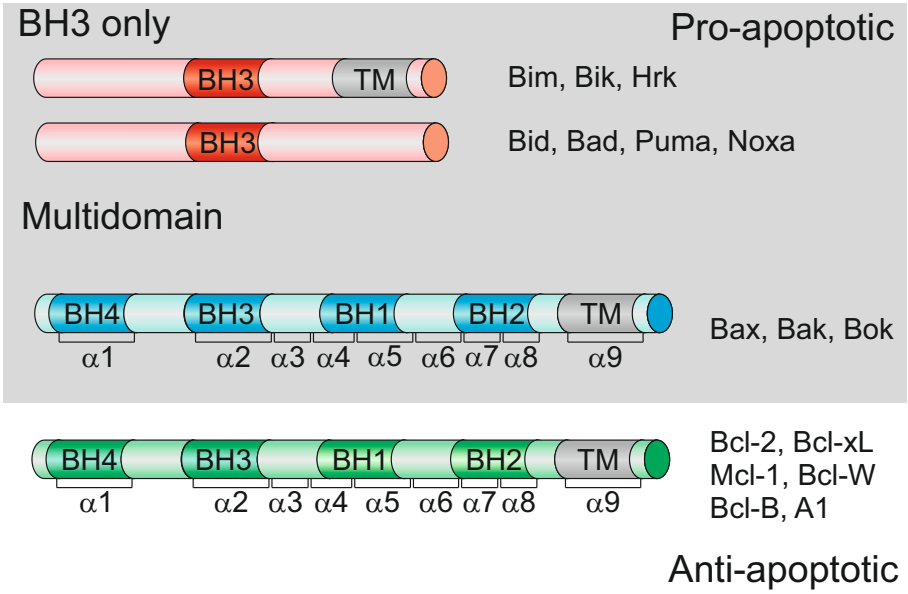

Figure 1.1: Bcl-2 family of proteins Bcl-2 family of proteins regulate MOMP. Together with their opposing functions, BH distinguish the different family members. Anti- apoptotic members are composed of multiple BH domains and inhibit apoptosis. Pro-apoptotic members are divided into those that contain multiple BH domains, and the BH3-only proteins. Pro-apoptotic members that contain multiple BH domains are also believed to form apoptotic pores in the mitochondrial outer membrane and are thus termed as effectors of MOMP. BH3-only proteins promote apoptosis by either activating the effectors (therefore called activators) or inhibiting the anti-apoptotic members (also called sensitizers).

with active Bak (which is constitutively associated to the MOM) oligomerizes and induces MOMP. MOMP releases intermembrane space proteins like cytochrome c, and triggers the downstream caspase cascade of apoptotic signaling. Anti-apoptotic members also interact and inhibit with Bax/Bak or BH3-only activators.

1.2.2 Models of Bcl-2 family interaction

The interaction between the members of the Bcl-2 family is very intricate. Several models have been proposed to explain the events responsible for MOMP (Figure 2) (Chipuk and Green, 2008, Czabotar et al., 2014).

In the direct activation model (Figure 1.2A), the effector proteins Bax and Bak are activated by 'direct activator' BH3-only proteins in order to promote MOM (Kuwana et al., 2002, Wei et al., 2000). In the indirect or "displacement" model (Figure 1.2B), the BH3-only proteins sequester the anti-apoptotic Bcl-2 proteins and block their function. This releases Bax and Bak to induce apoptosis (Willis et al., 2005, 2007). In this model, Bax and Bak are constitutively active and apoptosis is mainly regulated by inhibition and protein expression.

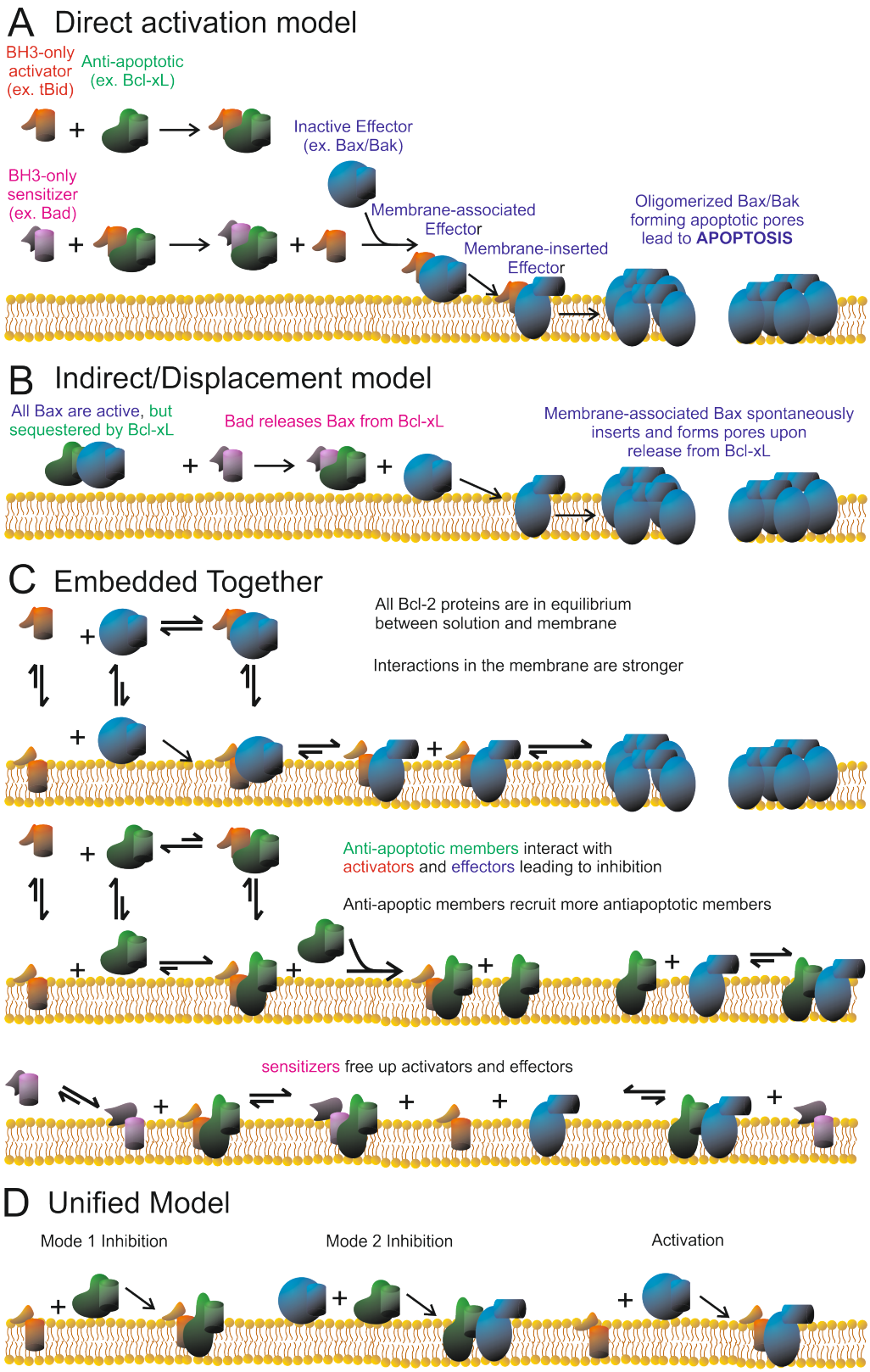
A Direct activation model
BH3-only activator (ex. tBid)
Anti-apoptotic (ex. Bcl-xL)
Inactive Effector (ex. Bax/Bak)
BH3-only sensitizer (ex. Bad)
Membrane-associated Effector
Membrane-inserted Effector
Oligomerized Bax/Bak forming apoptotic pores lead to APOPTOSIS
B Indirect/Displacement model
All Bax are active, but sequestered by Bcl-xL
Bad releases Bax from Bcl-xL
Membrane-associated Bax spontaneously inserts and forms pores upon release from Bcl-xL
C Embedded Together
All Bcl-2 proteins are in equilibrium between solution and membrane
Interactions in the membrane are stronger
Anti-apoptotic members interact with activators and effectors leading to inhibition
Anti-apoptic members recruit more antiapoptotic members
sensitizers free up activators and effectors
D Unified Model
Mode 1 Inhibition
Mode 2 Inhibition
Activation

Figure 1.2 (previous page): Models of Bcl-2 family activity. (A) In the direct activation model, the effector proteins Bax and Bak are activated by BH3-only protein activators (ex. tBid and Bim). Association of the anti-apoptotic members to activators prevent this activation thereby inhibiting apoptosis. (B) The indirect/displacement model argues Bax and Bak are constitutetively active. Anti-apoptotic members interact with Bax and Bak to prevent MOMP and are only released when BH3-only protein sensitizers (like Bad and PUMA) are activated. (C) Embedded together model combines both direct activation and indirect model: effectors need to be activated by BH3-only activators, anti-apoptotic members sequester the activators and effectors, BH3- only sensitizers release the effectors and activators from the anti-apoptotic members. Furthermore, the embedded together model presents the effect of the membrane on Bcl-2 protein interactions. (D) The unified model, extends the embedded together model by distinguishing the interaction of anti-apoptotic members with activators (Mode 1) and effectors (Mode 2). Both of these interactions inhibit apoptosis. Reproduced from (Das et al., 2015) with permission from Elsevier.

The embedded together model combines the previous two models and takes into account the role of the membrane (Figure 1.2C) (Leber et al., 2007): BH3-only proteins sequester the anti-apoptotic Bcl-2 proteins, blocking their interaction with Bax/Bak (the indirect model), and/or activate Bax and Bak (the direct model). This model introduces the important role of the membrane-induced conformational changes of Bcl-2 proteins that affect binding affinities between Bcl-2 family members: Bcl-2 proteins exist in an equilibrium between solution and membrane, and membrane interactions are stronger than solution interactions (Lovell et al., 2008). In this model anti-apoptotic members are thought to be functionally similar to Bax and Bak except in their oligomerization properties. As such, these members interfere strongly with Bax and Bak during all the steps: association to membrane, insertion, and oligomerization.

Finally the unified model, extends the embedded together model by distinguishing the interaction of anti-apoptotic members with activators (Mode 1) and effectors (Mode 2) (Figure 1.2D). Both of these interactions inhibit apoptosis. (Llambi et al., 2011). The sequestration of the activator BH3-only proteins is less efficient and is easily overcome by the sensitizer BH3-only proteins. The unified model also introduces the role of mitochondrial dynamics in MOMP (Llambi et al., 2011).

1.2.3 Bid

Bid connects the two pathways of apoptosis in the cell (Leber et al., 2010, Shamas-Din et al., 2013b). Caspase-8 cleaves Bid into a p7 fragment and an active p15 fragment (also called truncated Bid (tBid)). In solution, the cleaved products form a stable complex (also referred collectively as cleaved Bid (cBid)) that dissociates reversibly in the presence of membranes (Bleicken et al., 2012). tBid in turn activates effectors Bax and Bak to promote MOMP (Kuwana et al., 2002, Terrones et al., 2004, Wei et al., 2000). The interaction of Bid and Bax requires the membrane, and the series of events leading to Bax insertion has previously been characterized (Lovell et al., 2008). tBid rapidly binds to the MOM, and it interacts with Bax. Bax then inserts into the membrane, oligomerizes, finally leading to permeabilization. The study also suggested that tBid and Bax interacts in a 'kiss-and-run' fashion, and that tBid may not be required for oligomerization

Translocation of Bax and Bcl-xL into the membrane also requires tBid (Bleicken et al., 2013b, García-Sáez et al., 2009, **?**, Shamas-Din et al., 2013a). While the direct evidence of a recruitment mechanism is absent, these studies show that the interactions of Bax and Bcl-xL with membrane-bound tBid may be an important precursor to the insertion of these two proteins. In contrast, these interactions are absent or very weak in solution (García-Sáez et al., 2009, Shamas-Din et al., 2013a). It has been proposed that tBid undergoes several conformational changes upon insertion to the membrane, exposing its BH3 domain

that can in turn interact with other Bcl-2 proteins (Shamas-Din et al., 2013a).

Cardiolipin (CL), a specific lipid in the mitchondria, facilitates the interaction of tBid with the membrane (Lutter et al., 2000, Raemy and Martinou, 2014, Shamas-Din et al., 2015). This interaction of tBid with cardiolipin does not require the BH3-domain, is very specific and cannot be blocked by the anti-apoptotic protein, Bcl-xL (Kim et al., 2004). Once inserted, tBid was shown to induce non-lamellar phases in the presence of calcium as well as membrane permeabilization in vesicles containing lipids with negative intrinsic curvature (Epand et al., 2002a).

1.2.4 Bax

Bax is a 21 kDa protein, whose cytosolic structure was determined in 2000 by nuclear magnetic resonance (NMR) (Suzuki et al., 2000). The protein has nine alpha helices connected by short loops. Three of these helices (α5, α6 and α9) interact with the MOM during apoptosis (Bleicken et al., 2010, García-Sáez et al., 2004). Both α5 and α6 were believed to form hairpin similar to pore-forming toxins from bacteria (García-Sáez et al., 2005, 2006, Schlesinger et al., 1997). In the cytosol, hydrophobic helix α9 is located at the hydrophobic group of Bax, making it easier to analyze compared to other multi-domain Bcl-2 proteins. Upon activation, Bax translocates to the mitochondria and the three helices insert to the membrane and form oligomers in what was described as the umbrella model (Annis et al., 2005). The assembly mechanism and consequently, the structure of Bax in the membrane has been under debate since, and there are opposing views of asymmetric assembly (Gavathiotis et al., 2010) or assembly via symmetric dimers (Bleicken et al., 2010, Kim et al., 2009). Recent studies point to the presence of a dimerization domain made up of helices α2-5 (Bleicken et al., 2014, Czabotar et al., 2013) challenging the umbrella model, due to a partially open conformation between the helices α5 and α6 in the hairpin(Bleicken et al., 2014). In this new model, Bax dimers forms a clamp with a subunit extending on each leaflet of the bilayer (Figure 1.3).

Further characterization of larger assemblies of Bax were carried out using Atomic Force Microscopy (AFM) (Epand et al., 2002b) . Epand and colleagues saw a 100-300-nm pore on the supported bilayer. However in these studies, Bax was activated with detergents and high amounts of Ca^{2+} prior to contact with the membrane, which may have affected its over-all 3D structure. Further increase in Ca^{2+} concentration was needed to be able to form these pores. With the membrane composition used, a high amount of calcium would also lead to formation of non-lamellar phases. Recently, a single molecule study of Bax in supported bilayers showed further evidence of Bax dimerization and assembly of oligomers of multiple species via dimer association (Subburaj et al., 2015). This paper also shares further insights into the assembly mechanism of Bax: Bax inserts as a monomer before oligomerization: Bax oligomers have no definite stoichiometry; and insertion and oligomerization is a very fast process. In another study, the size of Bax and Bak pores were shown to be dependent on concentration (Bleicken et al., 2013a). Taken together, these two papers further strengthen the argument for Bax forming toroidal pores that do not have a definite size.

To further characterize Bax's pore-forming properties, groups have made an effort to understand the effect of Bax on the membrane (Bleicken et al., 2013b, García-Sáez et al., 2007a, Kuwana et al., 2002). Bleicken et al. (2013b) suggested that Bax oligomers stabilize the permeabilized state of the membrane by lowering the line tension at the edge of the pore. A related study on Bax-α5 was carried out via AFM and Force Spectroscopy and reached similar conclusions (García-Sáez et al., 2007a).

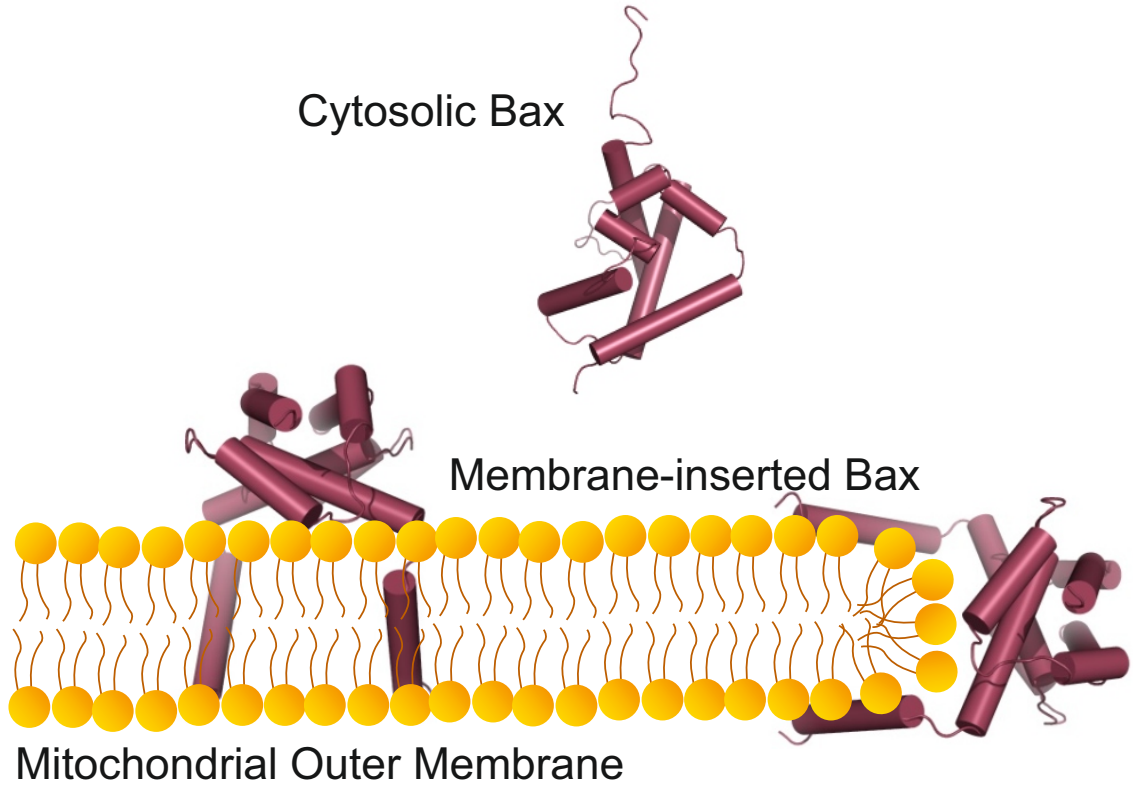

Figure 1.3: Structure of Bax The structure of Bax in solution has been solved by Suzuki et al. in 2000 using NMR. Recently, Bleicken and colleagues proposed a membrane-embedded structure of Bax dimers using double electron-electron resonance.

1.3 Mitochondria in Sickness and Health

Mitochondria play an essential role in the life and death of the cell. Their primary function involves the production of energy, which includes proteins of the tricarboxylic acid (TCA) cycle, the respiratory chain complexes and the adenosine triphosphate (ATP) synthase. Aside from this, they are also active regulators of apoptosis.

1.3.1 Mitochondrial Architecture

Mitochondria are cytosolic organelles with a unique structure composed of a double membrane called the MOM and mitochondrial inner membrane (MIM). The MIM folds into invaginations called cristae while the MOM is smooth. The lipid composition of the MOM and MIM are quite different, most notably in CL content (Horvath and Daum, 2013). In eukaryotic cells, CL is a lipid found almost exclusively in mitochondria and chloroplast. MOM is also constitutively permeable to small molecules (3-5 kDa) due to the presence of channels, while transfer of metabolites in through the MIM is highly regulated. Protein biogenesis in the MOM and MIM are regulated by translocases in the outer (translocase of the outer membrane (TOM)) and inner (translocase of the inner membrane (TIM)) membrane, respectively (Chacinska et al., 2009, Schmidt et al., 2010). Contact points between the MOM and MIM also help to shuttle metabolites including proteins and lipids between the two membranes and have been dubbed mitochondrial contact sites (Harner et al., 2011, Reichert and Neupert, 2002). Furthermore, the mitochondria also interacts with other organelles, particularly the endoplasmic reticulum (ER) to facilitate lipid trafficking (Tatsuta et al., 2014) and are termed mitochondria associated membranes or ER-mitochondria contact sites.

Healthy mitochondria have dynamic morphologies. Depending on the cell type, they can be tubular or vesicular with sizes ranging between 1 and 10 μm and diameters of around 0.5-1 μm (Picard et al., 2013). Morphology is governed by different sets of proteins that regulate fusion and fission (Ugarte-Uribe and García-Sáez, 2014). These include the mitofusins (Mitofusin 1 (Mfn1) and Mitofusin 2 (Mfn2)), and Optic atrophy protein 1 (OPA1) that regulate fusion in the MOM and MIM, respectively (Chen and Chan, 2010, Delettre et al., 2000, Legros et al., 2002), and Dynamin related protein 1 (Drp1) that regulates fission (Smirnova et al., 2001). Unlike dynamin, Drp1 requires membrane adaptors (like Mff, Mid49 and Mid51) because it doesn't possess a lipid-binding domain (Koirala et al., 2013, Palmer et al., 2011). OPA1 is also responsible for stabilizing the cristae junctions (Scorrano et al., 2002).

1.3.2 Lipids of the Mitochondria

Mitochondria contains mostly phosphatidylcholine (PC) (44%) and phosphatidylethanolamine (PE) (35%) (Daum and Vance, 1997, Horvath and Daum, 2013). Other minor components include phosphatidylinositol (PI) (5%), sphingomyelin (SM) (1%), phosphatidylserine (PS) (1%) and CL (14%). CL is only found in mitochondria (and chloroplast in plants), and it supports many membrane-dependent processes (Arnold and Kadenbach, 1997, Hoch, 1998, Yamauchi et al., 1981). Impairment of CL synthesis in humans leads to diseases such heart failure (Sparagna et al., 2007), diabetes (Han et al., 2007) and Barth syndrome (Schlame et al., 2002). The amount of CL in MOM and MIM also differ, with MOM having 5-10% and MIM having 20% (Horvath and Daum, 2013).

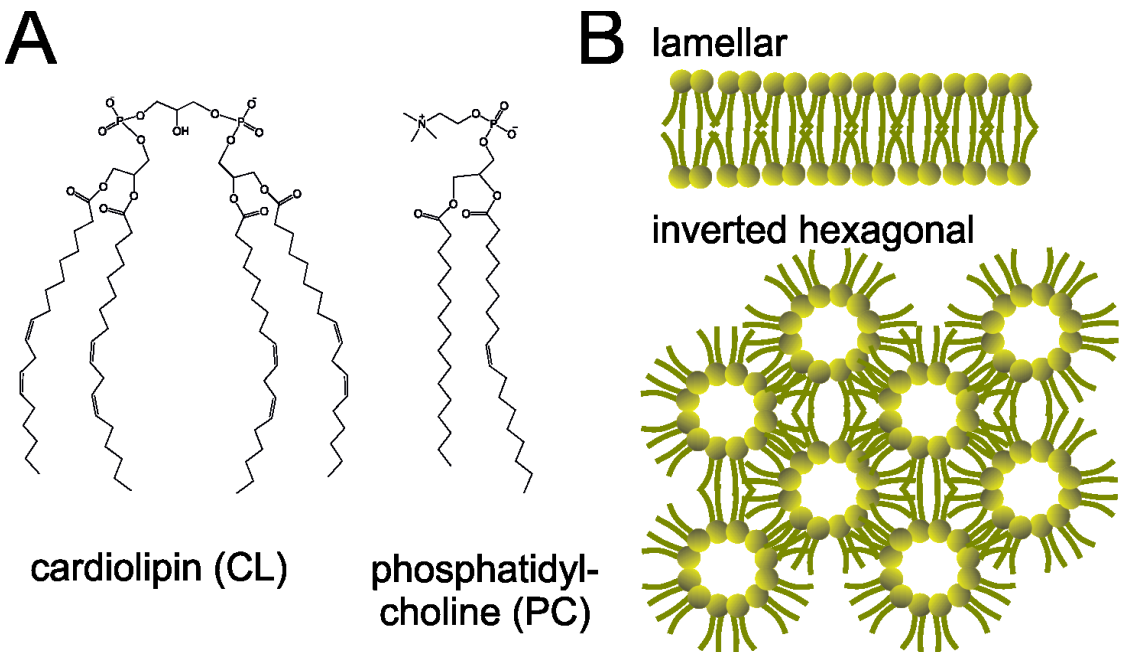

Figure 1.4: Structure Cardiolipin(A) Structures of predominant species of cardiolipin (CL) from bovine heart and phosphatidylcholine (PC) from egg. PC is the major lipid species in the mitochondria, and the importance of CL in structure of mitochondria and stability and function of many mitochondrial proteins has been previously shown. (B) Shows the two phases of cardiolipin: lamellar and inverted hexagonal phase.

CL is a peculiar lipid with four acyl chains (Figure 1.4) unlike most phospholipids like PC. At physiological pH, it has two negative charges due to its phosphate groups. This leads to the propensity of CL to form non-lamellar/inverted hexagonal structures in the presence of divalent cations or in conditions of low pH (De Kruijff et al., 1982, Rand and

Sengupta, 1972, Vail and Stollery, 1979). In vitro studies have characterized CL-containing membranes and they also show propensity to form non-lamellar structures (Khalifat et al., 2011, Macdonald and Seelig, 1987, Tomsie et al., 2005). Lipid packing studies also point to a condensing effect of CL resulting in lower area per molecule of lipids (Domènech et al., 2006, Nichols-Smith et al., 2004). Most of these studies used monolayers (Domènech et al., 2007a, 2006), bilayers (Domènech et al., 2007b, Unsay et al., 2013) or liposomes (Beales et al., 2011, Fuertes et al., 2010, Powell and Marsh, 1985) as model membranes, using varying molar concentrations of CL in combination with PC and/or PE. More complex lipid mixtures mimicking the MOM have been also used (Bleicken et al., 2013a, Lovell et al., 2008).

1.3.3 Mitochondrial Alterations in Apoptosis

While MOMP is the point of no return and the most characterized change in the mitochondria during apoptosis, there are other related processes that can be observed. These include changes in the lipid composition, loss of function due to the loss of mitochondrial potential, mitochondrial fragmentation and cristae remodeling (Cosentino and García-Sáez, 2014).

CL and PE have been suggested to localize at mitochondrial contact sites, due in part to the high curvature expected for the membrane at these sites (Aguilar et al., 1999, Ardail et al., 1990, Reichert and Neupert, 2002). In early stages of apoptosis, CL redistributes between the MOM and MIM. The mechanism of this transfer is still unclear, but studies suggest that tBid, thanks to its ability induce non-lamellar phases and its propensity to localize at the mitochondrial contact sites, could act as a probable pathway for this redistribution of lipids (Kim et al., 2004, Reichert and Neupert, 2002). Furthermore, Chipuk et al, have demonstrated the importance of ER-mitochondria contact sites during MOMP 2012. They proposed that the ER provides SM to the mitochondria that is eventually transformed to hexadecenal and sphingosine-1-phosphate. These two metabolites have been implicated in Bak and Bax activation. Loss of mitochondrial function is concomitant with MOMP (Ricci et al., 2003, 2004, Wang, 2001). Caspase activation interrupts the respiratory electron transfer chain and eventual loss of inner membrane potential (Ly et al., 2003, Ricci et al., 2003, 2004). Consequently, mitochondrial depolarization leads to interruption of mitochondrial fusion (Cereghetti et al., 2008). In addition, tBid inhibits the ability of mitochondria to buffer calcium and affects calcium homeostasis (Wang, 2001). Ca^{2+} accumulated in mitochondria interacts with CL, making lipids prone to peroxidation and leads to an increase in the production of reactive oxygen species (Grijalba et al., 1999). CL-Ca^{2+} interaction is also believed to be involved in Ca^{2+}-induced MOMP. Ca^{2+} is also involved in the opening of mitochondrial permeability transition pores in the mitochondrial matrix causing loss of membrane potential, matrix swelling and membrane rupture (Basso et al., 2005, Feldmann et al., 2000). This process is mediated by Bcl-2 proteins (Scorrano et al., 2003).

Massive mitochondrial fragmentation has always been associated to apoptosis (Martinou and Youle, 2011, Suen et al., 2008). Bax co-localizes with Drp1 and Mfn2 foci at the mitochondria constriction sites (Karbowski et al., 2002, Montessuit et al., 2010). ER tubules wrap around mitochondria creating these constriction sites (Friedman et al., 2011). Drp1 is believed to act upstream of Bax insertion and oligomerization (Yuan et al., 2007). In vitro studies show that Drp1 action requires CL in the membrane to form non-lamellar structures (Ugarte-Uribe et al., 2014), triggering tBid-induced Bax oligomerization (Montessuit et al., 2010). Furthermore, inhibition of Drp1 hinders Bax insertion (**?**). However, it has also been shown that Bax translocation can help bring Drp1 to the mitochondria (Karbowski et al., 2002). Mfn2 on the other hand, co-localizes with the Bax/Bak and Drp1 foci when Bak is present and slows apoptosis. In the absence of Mfn2,

apoptosis proceeds faster (Karbowski et al., 2006). In addition, Mfn2 is associated more closely with the ER-mitochondria contact sites and the exchange of lipids of between the ER and mitochondria during apoptosis (Wasilewski and Scorrano, 2009). These data reveal a strong connection between mitochondrial dynamics and MOMP, but the molecular mechanisms involved remain obscure.

In addition to MIM fusion, OPA1 also forms complexes responsible for the cristae junctions. Within these cristae, cytochrome c is confined to the side of the intermembrane space (Scorrano et al., 2002). Disassembly of OPA1 complexes during apoptosis causes cytochrome c release. It is thought that tBid widens the junctions and therefore disrupts the complexes Frezza et al. (2006).

Defining a sequence of events is controversial as I have discussed so far. A general working hypothesis was presented by Cosentino and Garcia-Saez (Cosentino and García-Sáez, 2014) and they explain that changes in lipid composition recruits membrane remodeling proteins (Mfn2, Drp1) and MOMP proteins (tBid, Bax, and Bak) to specific sites. Coincident or following these events, cristae remodeling occurs, further inducing the release of apoptotic factors. Simultaneous to these changes in the mitochondria, its energy-producing and homeostasis functions cease to work.

Chapter 2

Objectives

The Bcl-2 family of proteins regulates MOMP leading to apoptosis. As a gateway for survival or death of cells, this network is tightly regulated. One regulatory element of this network is the mitochondrial membrane: the strength of the interaction between members is stronger in membranes compared to solution. This conclusion was derived from in vitro measurements in model membranes. While highlighted in the embedded together model, the effect of membranes on Bcl-2 protein interactions has not yet been fully explored especially in vivo. On the other hand, the Bcl-2 proteins could also affect the membrane. While the most known function of Bcl-2 proteins is to permeabilize the membrane, no one has seen an apoptotic pore. Furthermore, the role of other members of the family in facilitating or producing a membrane environment that makes this pore has never been characterized. As such, the main question this thesis seeks to answer is how do Bcl-2 proteins affect the membrane (and vice versa)?

The aim of this thesis was to:

Uncover Bcl-2 protein and membrane interactions

Specifically, the goals of this thesis were:

First, was to characterize the supported lipid bilayer on which we embed the Bcl-2 proteins. In this part, I used a combination of techniques including confocal microscopy, fluorescence correlation spectroscopy (FCS) and atomic force microscopy (AFM).

Second, was to study the effect of Bax and cBid on membrane physical properties using AFM force spectroscopy.

Third, was to survey the structures formed by Bax in supported bilayers using AFM imaging.

Finally, I wanted to examine interactions of Bcl-2 protein in live cells, however a robust method has not yet been developed. In this part, I extended the scanning FCS technique to become applicable to mitochondria of live cells.

Part II

Experimental Approach

Chapter 3

Atomic Force Microscopy

Atomic force microscopy (AFM) is a type of Scanning Probe Microscopy (SPM) that uses the interaction of a sharp tip with the surface of a sample to create high-resolution images. Aside from its imaging capability, the cantilever can act as a spring to probe forces and interaction between the sample and the tip. This makes AFM a high-resolution surface imaging instrument with the ability to probe mechanical properties of the sample.

3.1 Basics of Atomic Force Microscopy

In the 1980s, Binnig and Rohrer invented the Scanning Tunneling Microscope (STM), the first of this family of scanning probe microscopy (Binnig et al., 1982, Binnig and Rohrer, 1983). The aim was to study the electrical properties of thin insulating layers. In their experiments, they used a conducting surface and conducting probe and looked at the tunneling of electrons through the insulating layer. Later on, they adapted this configuration for non-conducting samples by using the STM probe to characterize the movement of another probe directly touching the non-conducting sample and called this scanning force microscope (Binnig et al., 1986).

SPMs are not strictly microscopes, as it doesn't 'look' at the sample, but rather 'feel' it. The sharp probe interacts with the sample using attractive or repulsive forces depending on the distance between them. Figure 3.1 shows a schematic of a modern atomic force microscope. The sample movement is controlled by a piezo-electric scanner. This scanner expands or contracts based on electric current, and the movement can be precisely controlled by feedback loops. The sample is then moved while interacting with the tip situated on a cantilever. As the sample moves, the cantilever will be deflected towards or away from the sample. The movement of the cantilever is monitored resulting in a quantifiable signal. In the following sections, I will discuss the different aspects of this apparatus.

3.1.1 Piezoelectric scanners

Precise movement allows the atomic force microscope to construct high resolution images and make sensitive force measurement. The atomic force microscope achieves this using piezoelectric crystals that are able to accurately change shape depending on the applied voltage at high speeds (normally achieved with fast feedback loops).

First introduced as a tripod configuration that can moved in the three orthogonal directions (x, y, z), tube scanners and flexure stages have now superseded this configuration (Figure 3.2).

Tube scanners consist of a thin-walled, radially-polarized piezoelectric ceramic (Figure 3.2A). Electrodes are attached to the internal and external faces of the tube. The external

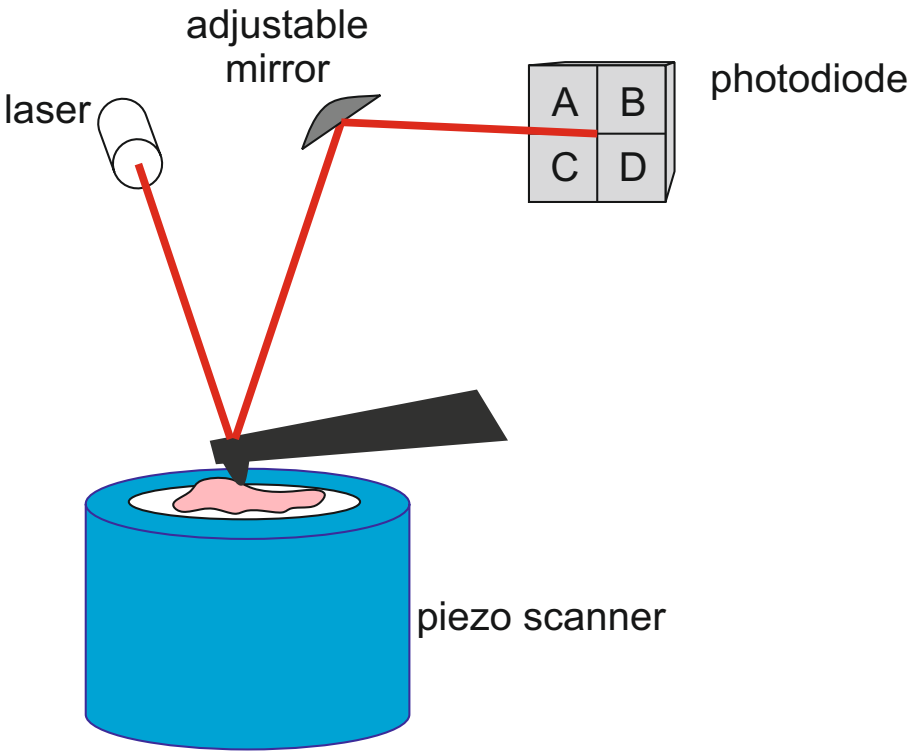

Figure 3.1: Schematics of an Atomic Force Microscope. Sample interacts with a sharp probe mounted on a spring-like cantilever. These interactions deflect the cantilever. The deflection is monitored by shining a laser at the back of the cantilever, and the reflected laser spot is directed to the center of a photodiode. Deflection of the cantilever moves the spot to different regions of the photodiode. The sample (or in some setups, the cantilever) is mounted on a piezoelectric scanner that can quickly and accurately move in the μm or nm regime.

face is divided into four parallel to the axis of the tube. When voltage is applied between the inner and all the outer electrodes, the tube expands and contracts uniformly along the axis (z-direction). When only the outer electrodes are excited, the tube bends in the x or y direction. To make the bending more pronounced, two opposing electrodes may be used in conjunction. Taylor 1993 gives a detailed mathematical study of the dynamics of tube scanners.

There are three main challenges with using tube scanners (Morris et al., 2010). The first one is called 'eyeballing' as the tube moves in a spherical motion across larger distances vs. a flat scanner. The second challenge is that of speed as piezoelectric scanner tubes cannot move so fast. The third is more of a practical aspect. Samples are usually mounted on top of the piezoelectric tube, care has to be taken to not expose the piezoelectric component to buffers and solutions.

Flexure stages are used in more modern high-performance microscopes (Figure 3.2B). The piezoelectric elements are placed within a nested cradle-like mechanism made out of a single piece of thin alloy sheet. The piezoelectric elements push against separate arms causing flexure at the fulcrum region at the base of each arm. The two directions are isolated using flexure hinges and prevents axis crosstalk. This design traces the selected area with greater precision and removes the 'eyeballing' effect inherent to tube scanners. The design also allows the incorporation of motion sensors that feeds into a feedback mechanism to ensure accuracy.

In most modern instruments, the flexure stage is used to hold the tip, and by doing so, also protects the piezoelectric elements from the sample. In this configuration, the sample is set on an immobile stage and the tip moves across the sample. Furthermore, their flat

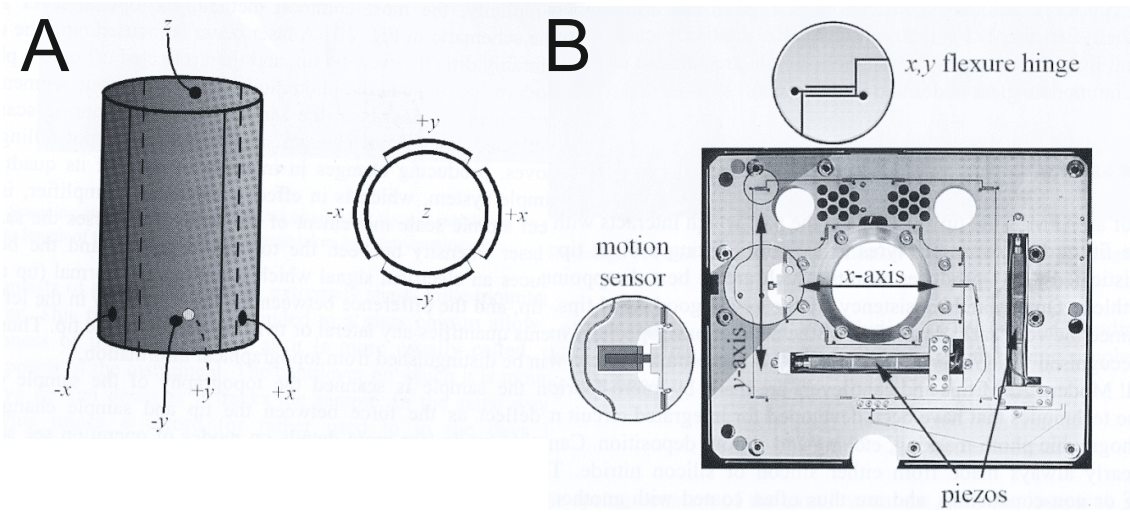

Figure 3.2: Piezoelectric Scanners in Modern AFM (A) Tube scanners are controlled by five electrodes: four on the outer (+x,-x, +y, -y) and one inner (z). The tube bends in the x-y plane in response to electrical signal from the four outer electrodes. To move the sample in the z-direction all electrodes must be active. (B) Flexure stages encloses the piezo element in metallic casing with flexure hinges to isolate each axes. Piezo movement is further refined by motion sensors that operate feedback loops.

shape makes them easy to integrate on light microscopes, making possible the use of these complementary techniques to extract more information.

3.1.2 Cantilever

The tip and the cantilever that holds it are at the heart of all AFM experiments. AFM tips and cantilevers are manufactured similar to techniques used in integrated circuits, such as lithographic photo-masking, etching and vapor deposition. The material used is most often silicon or silicon nitride. They can have multiple geometries and sizes and various properties: conducting, magnetic, and chemically/biologically functionalized (Morris et al., 2010).

There are two basic shapes for cantilevers: rectangular and triangular/V-shaped (Figure 3.3A). The original reason for using the V-shaped cantilever is to minimize torsional strains or cantilever twisting due to friction (Sader, 2003). In 2003, Sader and Sader confirmed that rectangular levers are actually torsionally stiffer than V-shaped levers.

One important aspect of the cantilever is its ability to bend in response to force (F) interactions. The behavior is characterized by a simple spring following Hooke's law:

$$F = -ks \tag{3.1}$$

Where k is the spring constant and s is the displacement. In general, the spring constant increases with thickness and decreases with length. It is then tempting to use longer cantilevers for soft biological samples. However the main drawback is its lower sensitivity and susceptibility to noise and vibrations, which will be discussed in further sections. Recently, there are efforts to make shorter cantilevers that have lower spring constants to make the sensitivity higher.

The spring constant also determines the suitability of cantilevers for each AFM application. Stiffer cantilevers are better used for experiments in air, while softer cantilevers are better suited for liquid (Butt et al., 1993).

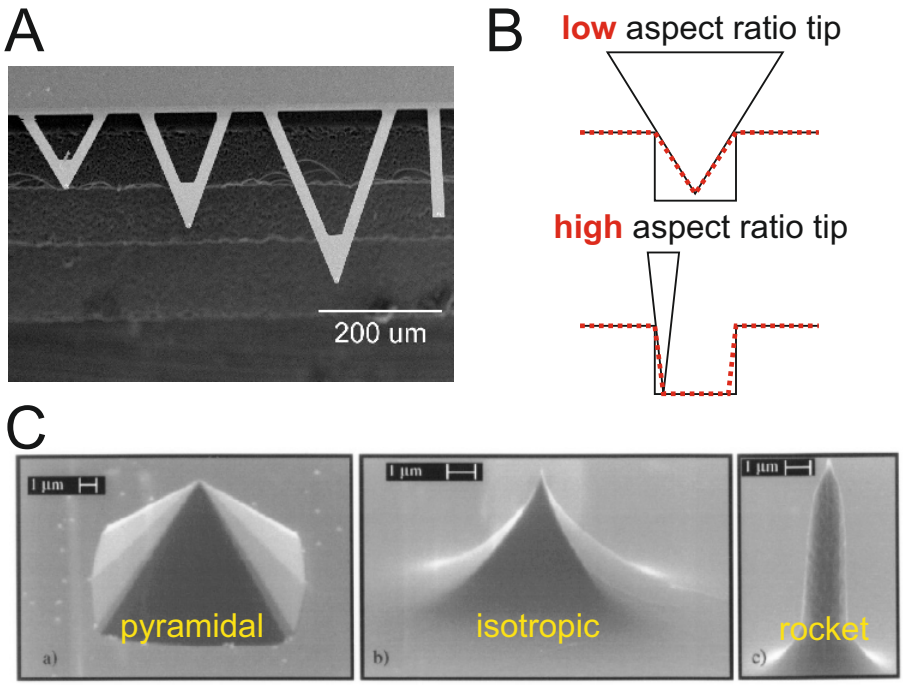

Figure 3.3: Cantilever and Tip Properties. (A) shows the triangular or V-shaped and rectangular (rightmost) cantilever geometries. (B) differentiates between high and low aspect ratio tips. For the same feature (black solid line), the resulting image (red dashed lines) differs. The lower aspect ratio tips produce images of lower resolution. (C) Common tip geometries (left to right): pyramidal, isotropic and rocket/sharpened.

3.1.3 Tip

The tip is the point of contact of the microscope with the sample, and the tip geometry and properties directly affect the results of AFM experiments (Torre et al., 2011b). Tips can be classified by aspect ratio (Figure 3.3B). High aspect ratio tips are good for rough samples, while for smoother samples, the low aspect ratio tips are sufficient. Some low aspect ratio tips are chemically sharpened towards the apex so that it produces a high aspect ratio at this region. In this case, the manufacturing process remains as cost effective as low aspect ratio tips, but have the ability to measure rougher samples.

The overall shape of the tip may also affect image resolution (Boisen et al., 1996, Torre et al., 2011b). The opening angle of pyramidal tips compared to isotropic or rocket tips are bigger. Figure 3.3C shows some examples of the pyramidal, isotropic and rocket tips. The tip shape also influences force or indentation measurements.

Lastly, the tip sharpness at the apex of the tip determines overall resolution of the AFM image (Torre et al., 2011b). This is measured by the curvature radius at the apex of the tip. Commercially available tips have a nominal tip radius of around 30 nm. Sharpened tips can have a tip radius as low as 5 nm. The main drawback of sharp tips is their fragility. As such, sharp tips are not advisable to image large areas or rough samples.

Cantilever and tips are sometimes coated with substances to exhibit desired properties. For example, to increase reflectivity of the cantilever that affects the detection of cantilever movement, a gold coating may be used. The extra coating may affect the tip sharpness and result to tips with bigger tip radius. The metal coating may also be useful for doing conductivity and magnetic measurements of samples, including tip-enhanced Raman spectroscopy (Meng et al., 2015). Lastly, tips may be functionalized using molecules, such as biotin, to allow measurement of specific interactions (Barattin and Voyer, 2011, Blanchette et al., 2008).

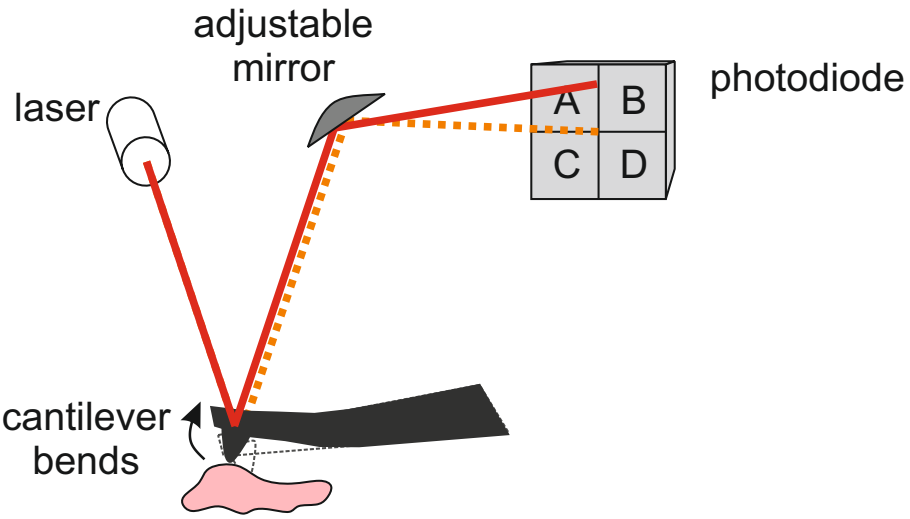

Figure 3.4: Light lever mechanism. The laser spot is aligned at the center of the photodiode detector (dashed line) before the start of an AFM experiment. Deflection of the cantilever due to the sample's topology results in the displacement of the laser spot (solid line). The photodiode detector is divided into quadrants and the relative intensities at each quadrant quantifies the degree of deflection of the cantilever.

3.1.4 Detection Methods

As the tip moves through the sample (or vice versa), the cantilever bends according to the topography and other interactions with the surface. The movement of the cantilever needs to be accurately monitored to provide the best results for AFM. The earliest method to detect cantilever movement was the use of an STM probe. Modern instruments use the light-lever mechanism developed by Meyer and Amer 1988. A laser is reflected at the back of the cantilever and directed towards the center of a photodiode. Movement is recorded as a displacement of the laser spot within the photodiode. To monitor this, the photodiode is divided into quadrants (labeled A, B, C, and D in Figure 3.4). The total light recorded by the photodiode is given as the sum:

$$\text{Sum} = A + B + C + D \tag{3.2}$$

Vertical deflection of the cantilever is monitored by the change in signal in the upper quadrants vs. the lower quadrants:

$$\text{Vertical deflection} = \frac{(A + B) - (C + D)}{\text{Sum}} \tag{3.3}$$

Lateral deflection monitors the twisting of the cantilever as it interacts with the sample.

$$\text{Lateral deflection} = \frac{(A + C) - (B + D)}{\text{Sum}} \tag{3.4}$$

The sensitivity of this method depends on the amount of light hitting the photodiode, the distance of the lever to the photodiode, and the length and stiffness of the cantilever. An increase in the amount of light reflected increases the photodiode?s ability to distinguish signal from noise. The distance of the cantilever determines the relationship between the amount of bending of the cantilever and the displacement of the laser spot in the photodiode. For longer distances, slight bending will result in a big displacement of the laser spot. In most modern instruments, this can be assumed to be constant.

The laser spot can also introduce noise. A very small laser spot will be very sensitive to vibrations. However, a laser spot larger than the back of the cantilever will diffract

light and produce patterns in the final image (Morris et al., 2010). This will be discussed in further chapters.

3.1.5 Electronics and Feedback Loops

The performance of AFM is determined by the quality of monitoring and maintenance of cantilever movement. As such, modern electronics require extremely good feedback loops to monitor proper positioning of the cantilever in the sample, and movement induced by its interactions with the sample. Electronics also control the piezoelectric element, which in most cases also holds the cantilever (Morris et al., 2010).

Feedback loops maintain a set point for the cantilever in a sample. The set point is any constant property, such as the force against the sample, the height of the cantilever over the sample, or the amplitude of the oscillating cantilever. The set point is similar to a thermostat setting in an oven. For simple systems like the heating plate or incubators, an on-off feedback system is sufficient. These systems raise the value of a property over the set point and then turn off allowing stochastic processes to decrease the value to the set point. However, because the system is off, the value will continue decreasing until a threshold at which point, the system becomes active again. The re-activated system will overshoot again and turn off, repeating the cycle and resulting in an oscillating signal, where the set point is not maintained. Such a system is unacceptable for the sensitive measurements in AFM. Furthermore, this is usually a very slow feedback mechanism

To achieve speed and accuracy, atomic force microscopes use additional control terms/feedback mechanism known as the proportional, integral and derivative gains. This mechanism is also known as a PID controller.

In proportional gain, the control mechanism amplifies the error between the signal and the set point in order to establish the size of the required correction signal. In practice, the proportional gain corresponds to a tolerance around the set point. A lower gain means higher tolerance, which is useful when a signal deviates greatly from the set point. The system attempts to correct the signal gradually until the set point is reached. A higher gain means lower tolerance, and this means that a small deviation of the signal from the set point results in a large and abrupt response. If the tip encounters a small feature, the proportional gain is the main controller of the response to this small deviation. If the proportional gain is too low, then the control is sluggish and the microscope will simply treat this small feature as noise. If the proportional gain is too high then the system will begin to oscillate, tricking the microscope to think all small deviations are actual features causing the system to behave erratically.

Integral gain helps to remove the offset of the signal from the set point by adding an extra term that integrates the deviation over a short time period. Integral gain helps maintain an accurate set point. Though it is not as fast as the proportional gain, integral gain stabilizes the control. A high integral gain leads to a disproportionally strong response and eventually oscillations, as the deviation is integrated over a smaller period of time. If this time period is faster than the response speed of the piezoelectric material, then the feedback loop will try to perpetually attempt to correct this mismatch between the set point and the movement of the piezoelectric material. If the integral gain is too low then the overall response to deviations will be slower as a longer integration time is needed.

As a final correction, a derivative term proportional to the rate of the change of the signal is applied to reduce the tendency for the control loop to undergo erratic behavior. This is the most useful control to handle large deviations. In most cases, this is set to zero. However derivative gains become important in particularly sensitive measurements, such as in non-contact mode. In most cases, the user will have some control over these feedback control systems.

3.1.6 Vibration Isolation and Environmental Factors

High resolution measuring devices require stable environments to operate at its optimum. The AFM is especially susceptible to vibration because it observes the miniscule movement of a cantilever. Sources are either thermal or mechanical.

Most AFM are often designed to reduce thermal noise, but it is important to keep the room within 1°C, to prevent thermal drift. Some people advocate leaving the sample 1-2 hours before measurement to make sure that the sample is thermally equilibrated with the microscope.

Mechanical vibration is the major enemy of AFM. As such, an atomic force microscope should be placed in a room with the least vibration sources or to mount the microscope in some form of mechanically-isolated platform. These range from optical tables with air-bearings to heavy stone plinths hanging from bungee cords. Active vibration isolation platforms are also common. These are platforms that senses the background noise and generate a signal out-of-phase of the noise to cancel it out.

3.2 AFM Imaging

AFM imaging is achieved by scanning the tip on the surface of the sample. The tip follows the topography of the sample in the different imaging modes.

Imaging can be performed in different modes: (1) contact, (2) intermittent contact or tapping, or (3) non-contact (Torre et al., 2011a).

3.2.1 Tip-sample Interactions

The tip and the sample interaction is the main property sensed by the AFM. Depending on the tip-sample separation, these could be intermolecular attractive forces or repulsive forces.

Van der Waals forces

Van der Waals forces arise from the asymmetrical distribution of electrons in molecules. While a neutral molecule will have, on average, a symmetrical distribution of electrons, asymmetry may arise at specific moments resulting in the presence of short-lived dipoles. This asymmetry is enough to induce weak attractive or repulsive forces against another molecule. Normally these are masked by other stronger forces, but it is important to note that these van der Waals forces are present in all molecules.

To model the interaction between the tip and the sample, one can examine at the potential variations due to the interaction of the apex of the tip and a discrete particle in the sample. This is mathematically described by the Lennard-Jones potential:

$$E(r) = 4\varepsilon \left[\left(\frac{\sigma}{r}\right)^{12} - \left(\frac{\sigma}{r}\right)^{6} \right] \tag{3.5}$$

Where ε and σ are constants that depend on the material. Incidentally, σ is approximately equal to the diameter of the atoms involved and sometimes called the 'hard sphere diameter'. Figure 3.5 illustrates this potential. The $(1/r)^{12}$ term accounts for the steep increase in $E(r)$ at small separations. When $r < \sigma$, the atoms strongly repel each other because of Pauli Exclusion Principle. The $(1/r)^6$ term is responsible for the slower change in the attractive behavior at relatively large separations, where the van der Waals forces dominate.

In the case of the AFM tip and sample, there is not enough attractive force to exhibit a significant effect on the cantilever deflection even at a separation of a few hundred nm.

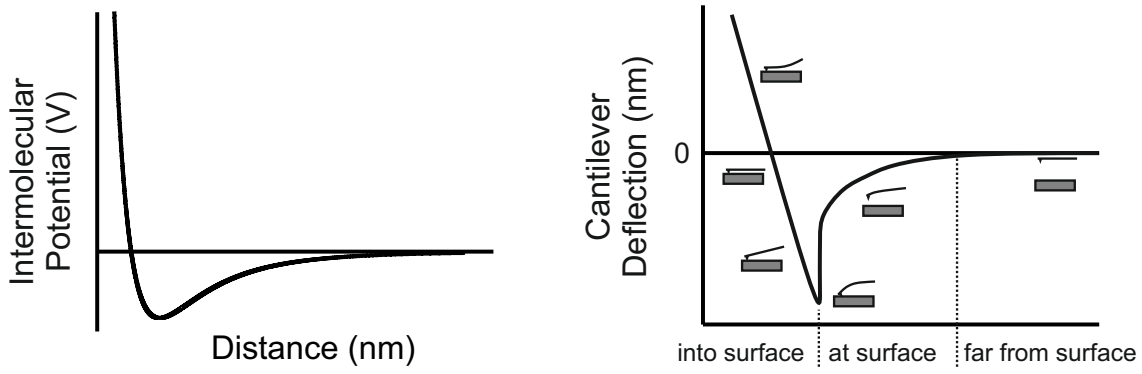

Figure 3.5: Tip-Sample Interaction. The interaction between the tip and the sample can be modelled using the Lennard-Jones potential (left). The force between the two particles at large distances is neglible. As the two particles approach each other, attractive forces start to manifest as a decrease in potential until the two particles are in contact. When the two particles are further pushed towards each other, the overlapping electron clouds produce repulsive forces and the potential increases. In practice, the tip-sample interaction can be monitored by the cantilever deflection (right). Far away from the sample, the cantilever is not deflected. As it approaches the sample, attractive forces causes it to bend towards the sample. Further approaching the sample results in deflection in opposite direction. In this regime, the tip is exerting force on the sample following Hooke's law.

As the tip approaches, attractive van der Waals forces begin to manifest resulting in the bending of the cantilever. At a certain distance, the cantilever suddenly lands on the surface of the sample in an abrupt change in deflection. This phenomenon is called the jump-to-contact phenomena. As the tip pushes onto the sample, the cantilever straightens out. Further movement towards the sample results in a deflection in the opposite direction.

Capillary and Adhesive Forces

The jump-to-contact phenomenon is a result of moisture condensation that occurs when a point contact with a small radius is resting on a surface. Essentially, this spot becomes an enticing nucleation site for water vapor condensation. In addition, a thin layer of water will naturally condense on the surface of the sample depending on the relative humidity. With this in mind, the pulling of the tip at a very close distance to the surface is a result of the capillary force exerted by the water layer. This is a problem because the capillary force is not compensated by the instrument. In some cases, the capillary force could be big enough to damage very soft samples. One way to circumvent this is the use an enclosure feeding dry air to the AFM.

AFM in air has been used in purified biological samples. However, to keep samples in a near-native state, AFM under liquid is preferred. AFM in liquid removes the problem of the jump-to-contact phenomena, and therefore reduces friction. However, it also poses a different set of challenges.

3.2.2 Imaging Modes

There are many imaging modes in AFM (Figure 3.6), each with its own advantage and disadvantage. The following paragraphs discuss some of these modes

Contact Mode

In contact mode imaging, the tip is in direct contact with the sample by ensuring that the cantilever is bent in the repulsive direction (in most instruments, this results in

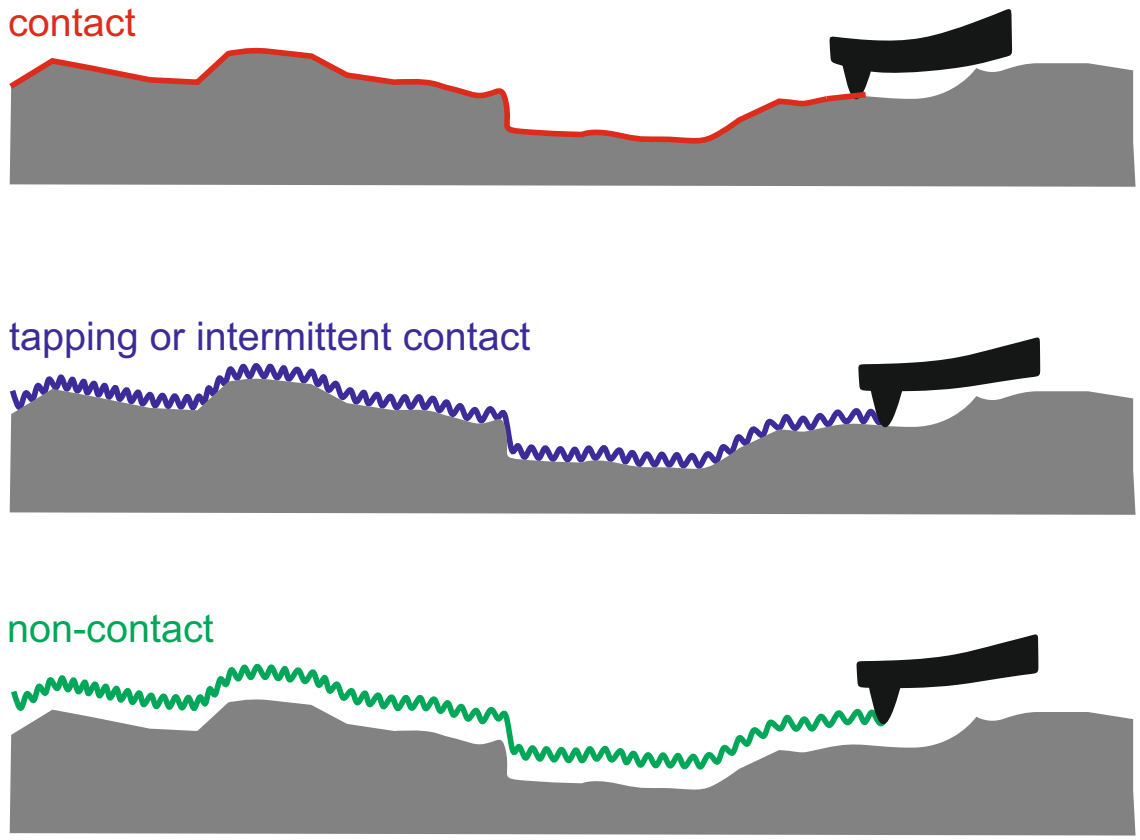

Figure 3.6: AFM Imaging Modes Contact mode (top) follows the contour of the sample. Tapping mode (middle) oscillates cantilever near resonant frequency and also follows the contour of the bilayer. Non-contact (bottom) oscillates cantilever far away from sample surface.

a positive vertical deflection). The tip is then scanned across the surface of the sample. There are two sub-modes in contact imaging: (1) constant height or (2) constant force.

In constant height imaging, the distance between the sample and cantilever (measured by the z-piezo displacement) is fixed, and the cantilever bends as it encounters features in the sample. The image is constructed based on the amount of deflection of the cantilever as it bends. This method provides fast scan rates with very smooth samples (few high features), including atomically flat samples such as mica.

In constant force imaging, the vertical deflection is fixed to maintain a constant force on the sample. To achieve this, the AFM uses feedback loops to move the cantilever nearer to or farther from the sample as it encounters features and structures. The image is then constructed based on the approaching or retracting movement of the cantilever rather than its deflection. Because of its reliance on feedback loops, this requires a slower speed compared to constant height imaging. However, it is applicable for samples with great height differences and bigger features.

The choice of cantilever stiffness is also not a major problem, as most cantilevers are able to image in contact. The main consideration is whether the expected hardness of the material can withstand the contact force and friction as the tip scans across it. In these cases, it is then better to image with constant force rather than constant height so that the force can be adjusted as needed. In membranes, this becomes increasingly important because of their fragile nature (Butt et al., 1993). In practice, the force is set as low as possible so that the tip is 'just in contact'.

Tapping Mode

In tapping mode, the cantilever oscillates near the resonance frequency at a given amplitude. In this mode, the cantilever touches the sample intermittently preventing friction. This is one of the main advantages of tapping mode for soft samples. The amplitude of oscillation is inversely proportional to the force generated by this mode. A higher amplitude means the cantilever must be further away from the sample, and will exert a smaller force. A lower amplitude will exert a higher force. The image is generated in a manner similar to constant force imaging in contact mode. In this case, instead of maintaining a constant deflection, a constant force is achieved by a constant amplitude. As the tip encounters features, the z-piezo moves the cantilever farther or closer to the sample as needed.

Imaging in air requires a stiffer cantilever to allow the tip to break free from capillary forces. In liquid, cantilevers need not be as stiff as that in air. This is the ideal imaging mode for soft samples like membranes (Basak and Raman, 2007, Hansma et al., 1994).

Non-contact Mode

In non-contact mode, the tip is oscillated at the resonance frequency, allowing it to come very close to, but not directly in contact with the surface (Garcia and San Paulo, 2000). In this regime, the imaging sensitivity depends on the van der Waals attractive forces between the tip and the sample. These forces are detected by a shift in resonance frequency as the tip approaches the sample because of a damping effect. The amplitude of oscillation then decreases. By maintaining a specific amplitude of oscillation, one can make sure that the tip is not in contact with the sample.

In air, this is challenging due to the capillary forces, which may trap the tip and prevent oscillations. Non-contact imaging is also not ideal in liquid, because the liquid itself interacts with the tip through similar van der Waals forces.

Recently, non-contact mode AFM has acquired atomic resolution by looking at repulsive forces between highly conjugated systems and a CO-functionalized tip (Zhang et al.,

2013). This was only achievable in high vacuum environments (to remove humidity and ultimately, capillary forces).

Cantilever Tuning

Cantilever tuning is an important step in tapping and non-contact modes. In this step, the resonance frequency is identified and the drive frequency is set near the resonance frequency. In most modern AFMs, a frequency sweep can be performed, where the cantilever is driven to oscillate at a given range of frequencies. At specific frequencies, the cantilever will show peaks depending on its fundamental and higher order resonance frequencies. Figure 3.7A shows a sample frequency sweep in air where the amplitude (in terms of V) is measured as a function of frequency. The sharpness of the peak is defined by the Q-factor. A high Q-factor means that the oscillation can be induced at a narrow frequency band.

In liquid, this becomes a challenge, as the viscosity of the liquid dampens the oscillations. This results in a lower fundamental resonance frequency, and even peak broadening (Figure 3.7A).

Once the resonance frequency has been identified, the cantilever actual oscillation frequency for imaging can be set near this frequency – also known as the drive frequency. It is set near the resonance frequency because as the cantilever approaches the surface, the resonance frequency will drop and influence the measurement.

For tapping mode, the drive frequency is set lower than the resonance frequency (Figure 3.7B). As the cantilever approaches the sample, the resonance frequency will decrease. By setting the drive frequency lower, we compensate for this decrease. The frequency shift also leads to an increase in amplitude corresponding to a lower force exerted by the tip on the sample.

In non-contact mode, the drive frequency is set higher than the resonance frequency. As the cantilever approaches the sample, the resonance frequency again decreases. By setting the drive frequency higher, the cantilever then oscillates at a lower amplitude compared to its amplitude in free oscillation. Maintaining a small oscillation amplitude ensures that the sample is not in contact with the tip (Figure 3.7C).

3.2.3 Imaging Types

This section discusses the different ways the data can be displayed: (1) topography, (2) error signal, (3) friction or lateral force, and (4) phase (Figure 3.8).

In topography imaging, the atomic force microscope uses the deflection (or the cantilever z-piezo movement) to map out the height of the sample. This is the most common type of image for AFM and the information gathered is fairly straightforward. This suffers from the sensitivity of the cantilever to detect features, which is also dependent on scan speed, environmental factors, and the size of the features themselves. In practice, a peak-to-peak noise of around 0.2-0.5 nm is acceptable. This reflects a limit of height difference detection of between 0.6 to 1.2 nm.

In rough samples like cells or bacteria, imaging at constant force requires very slow speeds, making it somewhat impractical. However constant height imaging is also not ideal for soft biological samples. The compromise between the two is imaging the 'error signal' (Figure 3.8A). In this mode, the sample is scanned similar to constant height imaging, but with low levels of feedback to maintain a set point. The image is recorded based on the difference between the actual deflection and the original set point of the cantilever. In this mode, the reduced feedback mechanism corrects for the small deviations from the set point (such as undulations of the sample), but not the bigger deviations from large features.

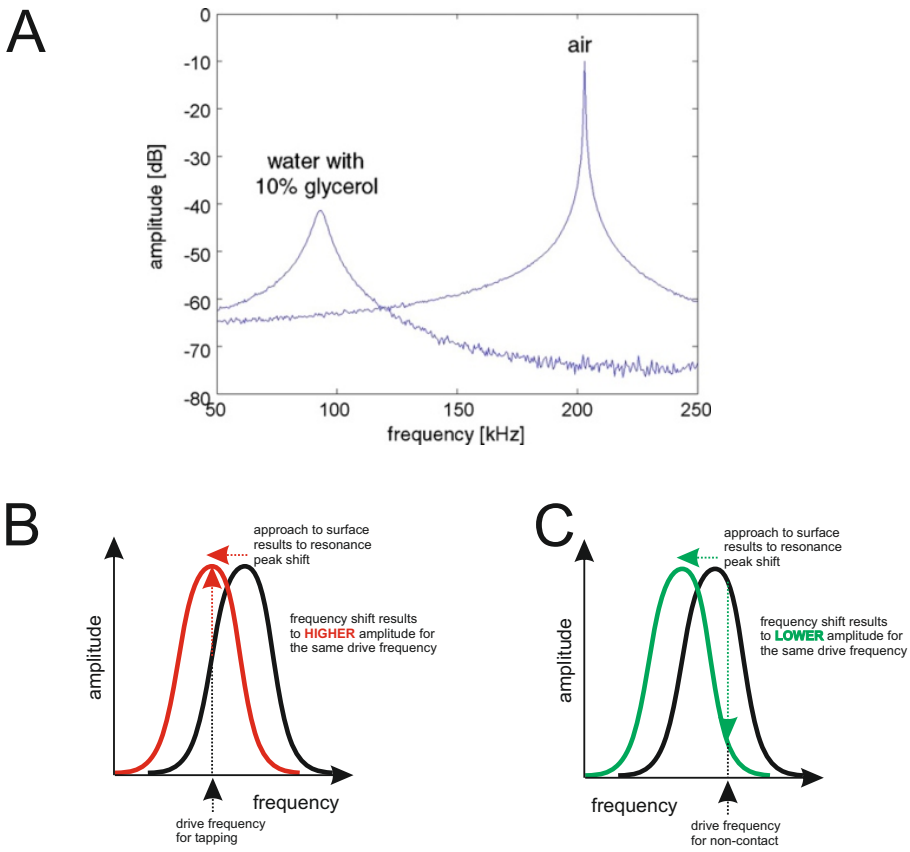

Figure 3.7: Cantilever Tuning. (A) A sample frequency sweep of a cantilever in air vs. liquid, where the resonance frequency is shown as peaks in the amplitude vs. frequency curve. In air, the peak is sharp (high Q-factor) and well defined. A second smaller peak is observed at higher frequencies indicating the second harmonic resonance. In liquid, the peak is shifted to a lower frequency due to damping of the medium. The peak is also broader. Higher order resonance peaks are also observed as they are all shifted. In tapping and non-contact mode, the drive frequency is set around and not directly on the fundamental resonance frequency, because the resonance frequency shifts as it approaches the sample. (B) In tapping mode, the drive frequency is set lower. This results in a higher amplitude (and consequently, low force during imaging) when the peak shifts upon approach. (C) In non-contact mode, the drive frequency is set higher, resulting in a decrease in the amplitude due to the resonance peak shift as the tip approaches the sample. By maintaining a constant amplitude, the system will adjust the cantilever distance to keep the tip out of contact.

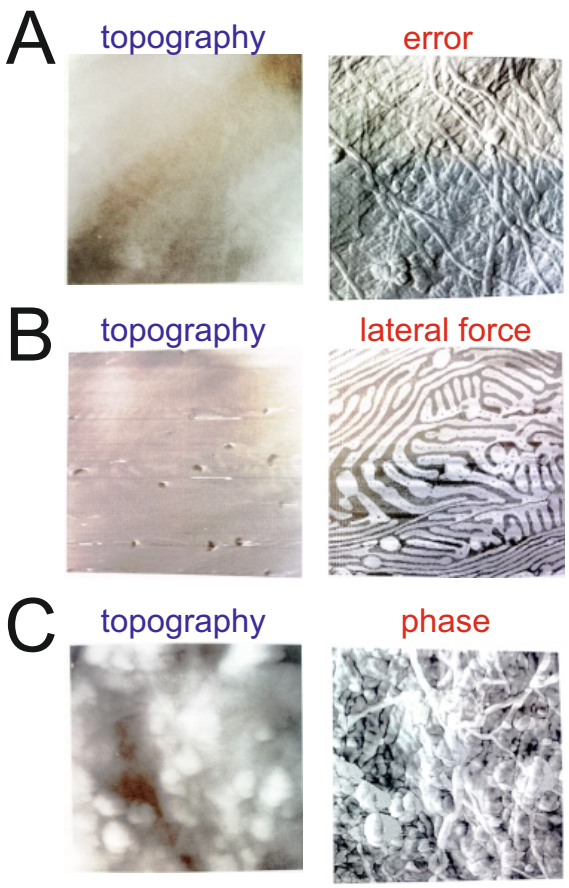

Figure 3.8: AFM Image Types. Some imaging types offer various advantages over topography image. (A) Error signal shows finer structures over coarse structure, (B) Lateral force or friction uses cantilever twisting induced by changes in rigidity of heterogeneous samples. (C) Phase imaging uses the phase shift during tapping mode induced by energy dissipation as the tip comes into contact with the sample.

Other information may be used when the height difference is extremely low and cannot be distinguished using simple topography. Aside from vertical deflection, AFM also measures the lateral deflection, a measure of friction. In some samples where there is difference in material properties that lead to cantilever twisting, the friction-based image, may be a good alternative (Figure 3.8B).

In tapping mode, the cantilever oscillates at a specific frequency. When it hits a sample, the phase of the cantilever is not the same as that of the electrical driving mechanism. This is due to energy transfer and dissipation during the brief contact period, resulting in a phase shift/difference (Figure 3.8C). The amount of phase shift depends on the viscoelastic properties of the sample (Magonov et al., 1997). Interpreting the contrast is not a trivial matter, and a positive or negative shift cannot be directly translated to even a relative material stiffness (Bar et al., 1998, Basak and Raman, 2007).

3.2.4 Artifacts in Imaging

As with any technique, AFM comes with its own drawbacks and challenges. This section discusses common sources of artifacts in AFM imaging and how to avoid or correct for them. There are three major sources of artifacts. The first sources of artifact are those induced by the environment, such as vibrations and thermal drift. The second are tip-related artifacts and they may be due to the aspect ratio, tip radius, or damaged and dirty tips. The third source is electronics-related artifacts. These usually manifest in the non-linear behavior of the piezoelectric element and limitations of the feedback loop.

Thermal Drift

As mentioned in the section on vibrations and environmental factors, thermal instability is a problem in AFM imaging (Morris et al., 2010). Thermal drift causes variations in cantilever bending and this results in deviations from the alignment of the laser onto the photodiode. This becomes a problem when a constant deflection or amplitude are used to image a sample, as it changes the amount of force exerted on the sample. In these cases, varying the set point to compensate for drift is required during a running experiment. Otherwise, a re-alignment of the laser spot to the photodiode should be done before starting a new image.

A second effect of thermal drift is the positioning of the sample, as small thermal fluctuations may cause the sample to shift.

Tip Effects

As the main part in contact with the sample, the tip can impart artifacts on AFM images through tip broadening, damaged tip deformations, and flattening of pits and holes (Canale et al., 2011).

Tip broadening is due to using a low aspect ratio tip on high or deep but small (in terms of width) features (Figure 3.9A-B). This is also known as tip convolution, because the feature appears bigger than it is. The geometry of the tip can also affect the amount of convolution. Blunt tips will also result in convolution.

Damaged tips are often characterized by repeating patterns. Damaged tips usually appear as having multiple peaks, resulting in “double” or “multiple” images. (Figure 3.9C).

Lastly a cantilever-related artifact can cause diffraction patterns or reflection patterns on the images. This usually happens when the laser is larger than the back of the cantilever and produces diffraction. In relatively flat samples, this may appear as repeating lines or a specific pattern across the image, which may or may not be removed by simple imaging correction.

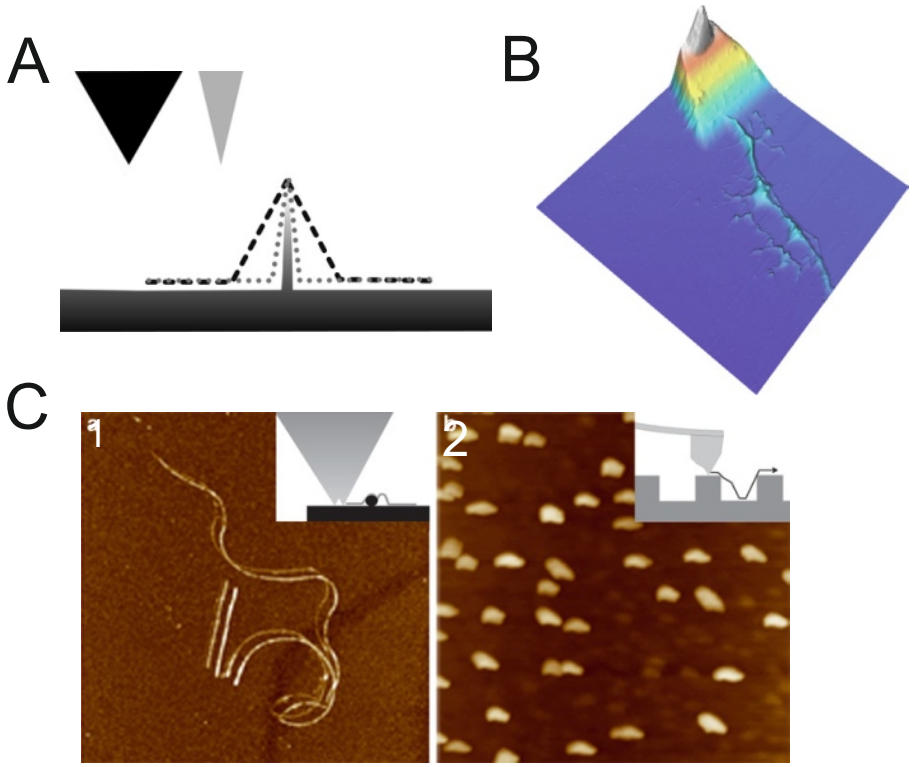

Figure 3.9: AFM Imaging Artifacts. (A) Tip convolution is shown for different aspect ratio tips. (B) a sample showing tip convolution as it touches larger features. (C) Double tips and damaged tips show double (1) or irregular features (2).

3.3 Force Spectroscopy

Acting as a spring, the AFM cantilever also serves as force probe for the sample in an application called force spectroscopy (FS). In this mode, the cantilever approaches the sample until contact is made. Once in contact the cantilever continues to push on the sample until a certain force set by the user (Figure 3.10) After reaching the set force, the cantilever retracts. A force vs. distance curve is generated for both the approach and retraction (Figure 3.11) and these curves are used to analyze mechanical properties such as stiffness or adhesion of the material (Ikai, 2008). It can also be used to probe protein structure by mechanical unfolding (Rief, 1997).

3.3.1 Cantilever calibration: raw data for force-distance curves

To accurately quantify forces, the AFM cantilever should be properly characterized or calibrated. Hooke's law shows that the force is proportional to the negative of the displacement of the spring. The proportionality constant is given by the spring constant. In every force spectroscopy measurement, it is important to calibrate the cantilever to determine these two properties (Figure 3.10B).

Measuring cantilever displacement

Most AFM instruments use the light lever mechanism to monitor the movement of the cantilever. The vertical deflection of the cantilever is based the change in position of a centered laser spot changes position in the photodiode detector.

Cantilever deflection is quantified by pushing the tip with accurate piezoelectric elements on a hard sample. The vertical deflection signal in volts (which is related to the

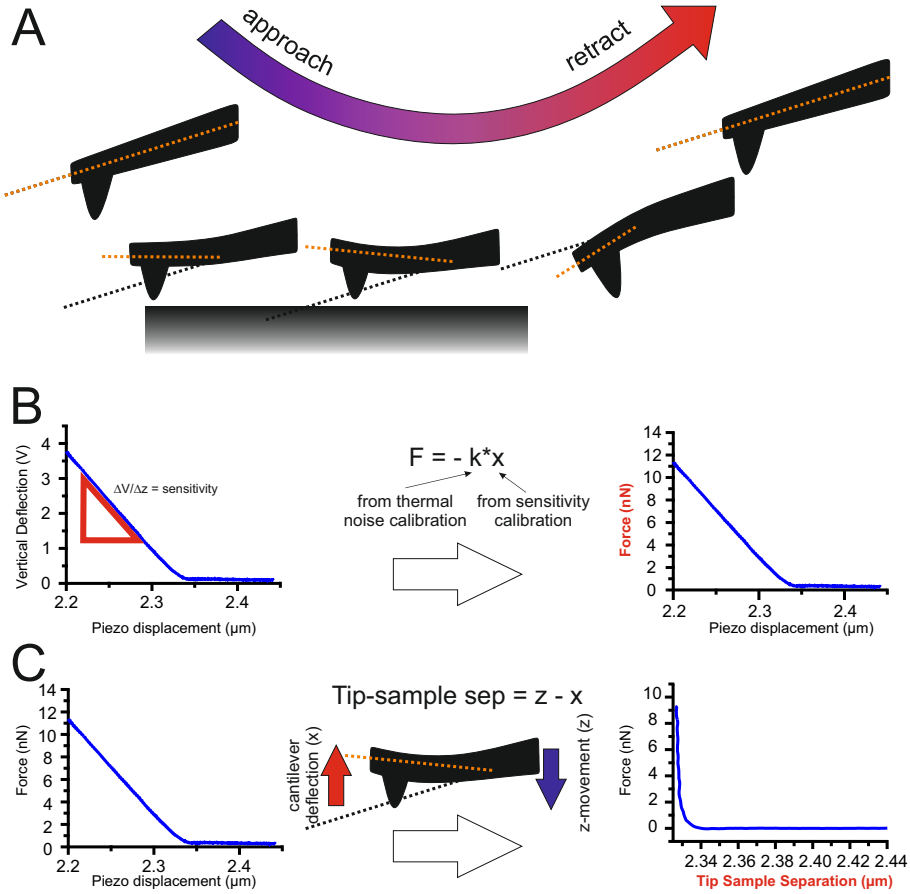

Figure 3.10: Cantilever Calibration (A) Depiction of the cantilever deflection during approach and retraction steps of a force spectroscopy measurements. In the approach step, the cantilever bends as it exerts force on the sample. In the retract step, the cantilever bends in the opposite direction because of adhesion forces between the sample and the tip. (B) Sample approach curve showing deflection (in V) vs. piezo scanner movement. Using the calibration value of sensitivity and spring constant, deflection can be converted to force as a function of piezo scanner displacement. (C) In indentation and pulling experiments, piezo scanner displacement does not allow the calculation of the amount of indentation caused by the tip on the sample or distance between sample and tip, respectively. By accounting for cantilever bending (through the sensitivity calibration), the piezo scanner movement can be transformed to the real tip-sample separation.Image reproduced with permission from (Unsay et al., 2015)

bending) can be correlated to the displacement of the piezoelectric element. This converts the electric signal to a displacement value. This correction factor is often called the inverse optical lever sensitivity or simply 'sensitivity'. Sensitivity is also used to correct for cantilever bending so that instead of the piezo movement, the system tracks the real tip-sample separation and indentation. This procedure involves subtracting the sensitivity value from the piezo scanner movement (Figure 3.10C).

Determining the spring constant

There are different ways to calibrate the spring constant of a cantilever (Burnham et al., 2002), including the Sader method (Sader et al., 1995) and the thermal noise method (Butt and Jaschke, 1995, Sader, 1998, Sader et al., 2005). The latter is more commonly used today due to its simplicity and availability of software to automatically analyze thermal noise profile.

In the thermal noise method, a cantilever is allowed to oscillate freely. A power spectral density of the deflection is plotted with respect to frequency (Fourier transform of the deflection over time). Peaks in the power spectral density of the free oscillation show the resonance frequencies of the cantilever. Fitting the peak fundamental with a Lorentzian will yield the spring constant. The theory behind the parameters of this fitting is non-trivial, but the procedure has been elegantly explained by Cook and colleagues 2006.

3.3.2 The force-distance curve

In a typical force spectroscopy experiment, the cantilever is allowed to approach the sample at a fixed speed using the z-piezo. As the tip approaches the sample, a jump-to-contact phenomenon may occur. Further movement of the z-piezo bends the cantilever resulting in an applied force on the sample. The z-piezo continues to move until a given force value. This part is mostly known as the approach or extend curve (Figure 3.11).

After reaching the set force value, the z-piezo moves in the opposite direction, thereby reducing the force of the cantilever on the sample. After a certain distance the tip will lose contact with the sample and the force will become zero. In some cases, the cantilever will bend on the opposite direction if adhesion forces are present. The resulting force-distance curve is known as the retract curve (Figure 3.11).

These force-distance curves can give quantitative results on the forces that govern material interactions. As such, it has been heavily applied in biology to measure the binding/unbinding of molecules (Benoit and Selhuber-Unkel, 2011), indentation and other material properties of biological samples such as cells (Azeloglu and Costa, 2011), and structural features via unwinding and pulling experiments (Ikai, 2008).

3.4 AFM in Model Membranes

While liposomes have been widely used as model membranes, supported lipid bilayers (SLB) are a more appropriate system for AFM (Muller, 2008, Raviakine and Brisson, 2000). Liposomes are relatively fragile, and may rupture due to the force of an AFM tip. They are also easily pushed around by the AFM, resulting in vesicle fusion and the eventual formation of flat bilayers on the surface of the sample chamber (Raviakine and Brisson, 2000) (Figure 3.12). Aside from imaging, force spectroscopy has also been applied SLBs by measuring the force needed to pierce the bilayer (Figure 3.13) (Canale et al., 2010). Force spectroscopy is mainly used study lipid structure and packing.

SLBs are biological model membranes lying on top of a solid support usually mica, borosilicate glass, fused silica, or oxidized silicon (Castellana and Cremer, 2006). They are prepared using various techniques including vesicle deposition, Langmuir-Blodgett

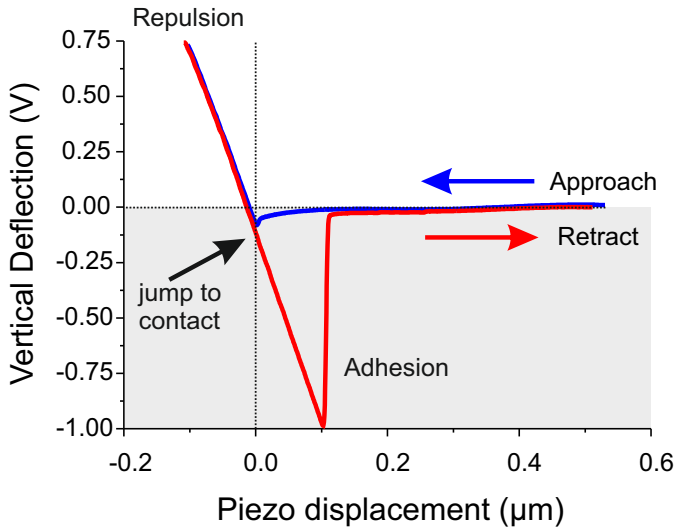

Figure 3.11: Sample Force Curve. Shown are the approach (blue) and retract (red) curves of a cantilever on a glass sample. Far away from the sample, the cantilever does not experience any adhesive or repulsive forces, as shown by zero deflection. As the tip approaches the cantilever feels some adhesion to the surface (slight bending on the adhesion regime). At a distance of zero, the deflection suddenly jumps downward, showing the jump-to-contact phenomenon. As the cantilever approaches closer, the cantilever bends in the opposite direction and is now in the repulsion regime). After it reaches the set point, the cantilever retracts. The large adhesion peak during retraction is due to capillary forces and even dirt on the surface of the glass. As the cantilever moves farther away, this adhesion force is overcome and the deflection returns to zero.

method and spin-coating (Frederix et al., 2009, Mennicke and Salditt, 2002). AFM imaging has been used to follow the formation of these supported bilayers (Raviakine and Brisson, 2000), and probe different structures formed by membranes of different compositions (Chiantia et al., 2006, Domènech et al., 2007b, 2006, García-Sáez et al., 2007b, Unsay et al., 2013). Figure 3.14 shows an example of a phase-separating bilayer composed of dioleoylphosphatidylcholine (DOPC), sphingomyelin (SM) and cholesterol at 2:2:1 ratio.

The use of force spectroscopy on supported bilayers results in a peak in the approach curve. This peak indicates the force needed to pierce the bilayer, and is called breakthrough force. The bilayer thickness can also be measured using the force curve (Redondo-Morata et al., 2012) . The typical breakthrough force of bilayers range between 1-50 nN (Redondo-Morata et al., 2012). These properties depend on lipid packing (liquid or gel phase) and structure (acyl chain length and degree of unsaturation) and can be altered by membrane-active agents (Alessandrini et al., 2012). Theoretical models of the rupture event has been explained by Butt and Frank 2002. Other experimental parameters such as cantilever softness, tip radius and approach speed also affect the breakthrough force (Alessandrini et al., 2012, Garcia-Manyes et al., 2005, García-Sáez et al., 2007b). Force spectroscopy has been used to analyze properties of different lipid phases (Chiantia et al., 2007, 2006) (Figure 3.14), composition-dependent changes (Canale et al., 2010, Unsay et al., 2013), as well as effects of other biomolecules, like peptides, on the stability of the membrane (García-Sáez et al., 2007a).

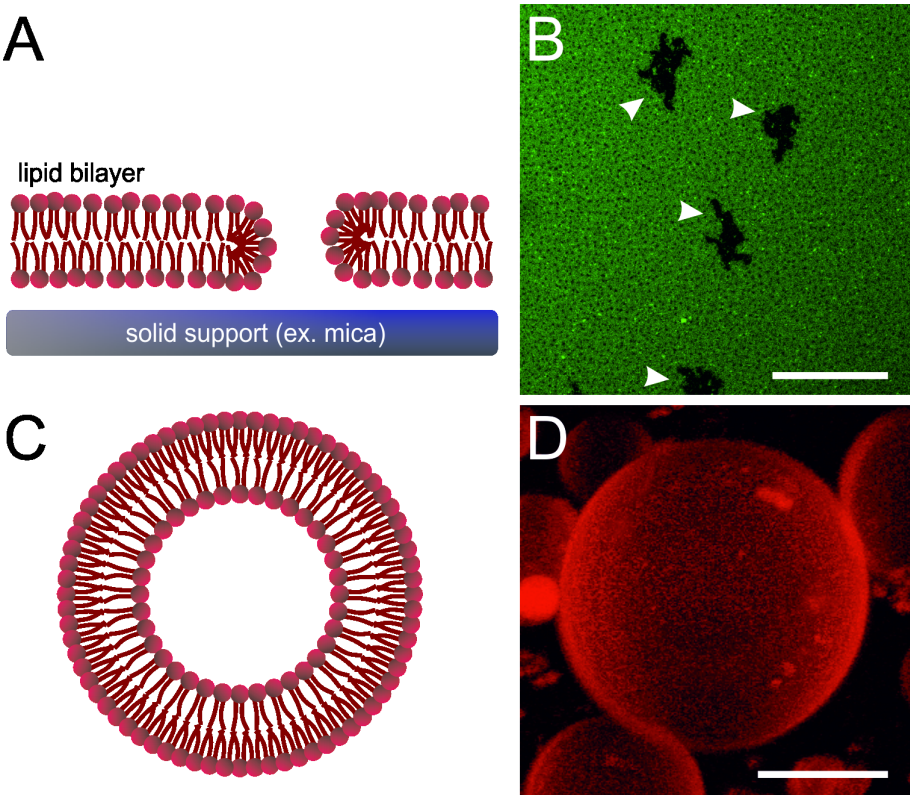

Figure 3.12: Model Membranes.(A) Model of a supported lipid bilayer formed on a solid support with its hydrophilic head groups orienting toward the aqueous environment. A small hydration layer separates the lipid bilayer from the support. Bilayers also do not cover the whole area of the support producing holes or membrane defects. (B) Supported lipid bilayer composed of dioleoylphosphatidylcholine/sphingomyelin/ cholesterol (2:2:1) containing 0.05% lipidic dye DiO (λ_{ex}= 488 nm) viewed using a laser confocal microscope. Membrane defects are irregular dark areas indicated by the white arrow. The lipidic dye partitions to the continuous liquid disordered phase (green), but not to the less fluid liquid ordered phase (small, black circular regions). Scale bar, 50 μm. (C) Model of a liposome showing hydrophilic head groups orienting to the inner aqueous compartment and outer environment. (D) 3D projection of a GUV composed of PC/CL 8:2 with 0.05% lipidic dye DiD (λ_{ex}= 633 nm). Scale bar, 10 μm. Reproduced from (Das et al., 2015) with permission from Elsevier.

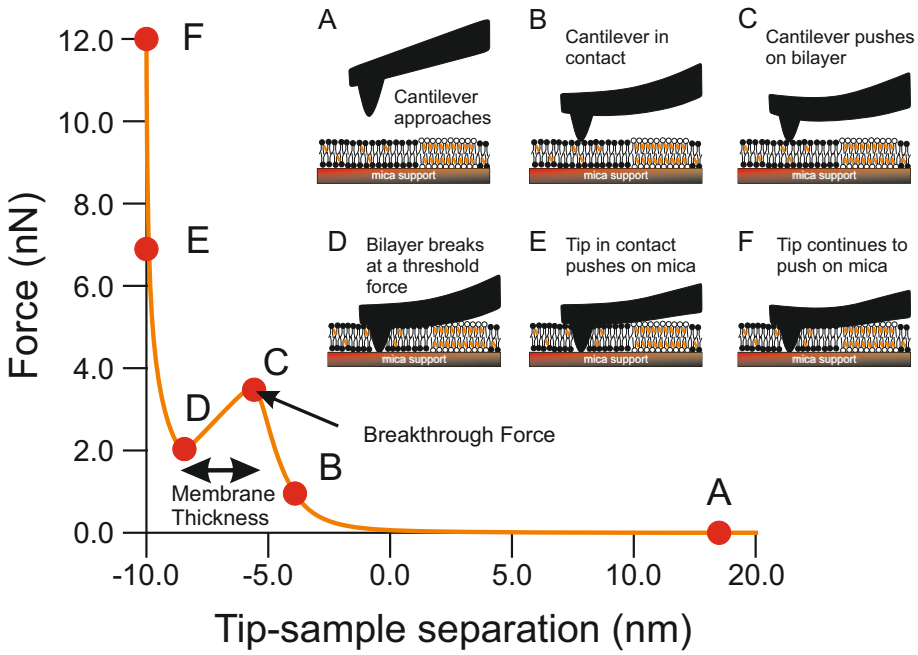

Figure 3.13: Force Spectroscopy of Supported Lipid Bilayers. Sample force curve and piercing experiment: (A) Cantilever approaches bilayer until it comes in contact. (B) Upon contact, cantilever exerts a force on the bilayer. (C) Further movement of the cantilever exerts force on the bilayer until a breakthrough force is reached. (D) During breakthrough, the cantilever partially relaxes as it comes in contact with the solid support. (E) The cantilever continues to press on the solid support. (F) It stops pushing at a set point specified by the use. The breakthrough force is the peak on the force curve and the membrane thickness is the difference in the distance traveled by the tip during the breakthrough event. Image reproduced with permission from (Unsay et al., 2015)

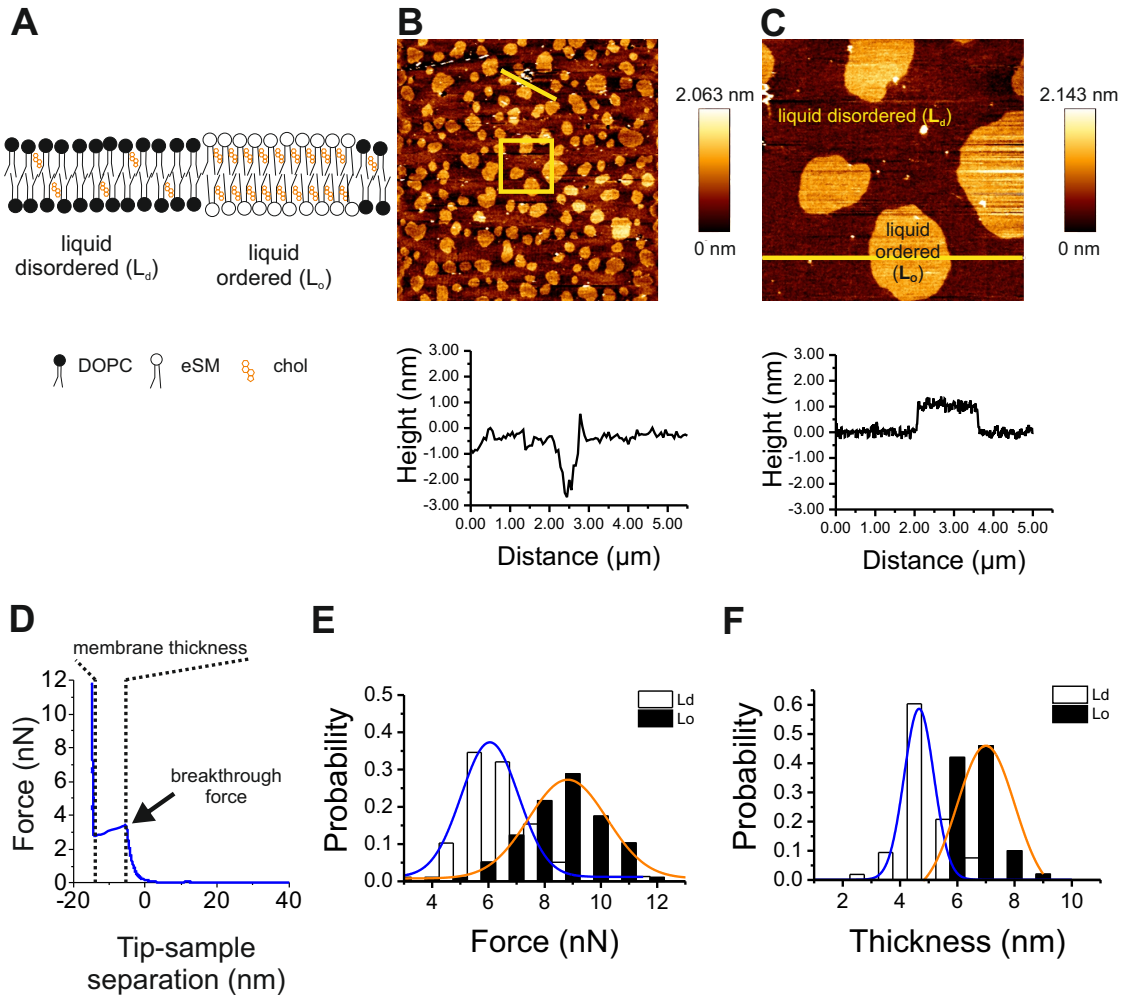

Figure 3.14: AFM of Phase-separating SLBs. (A) Scheme of SLBs composed of DOPC:SM:Chol (2:2:1) separating into liquid disordered (L_d) and liquid ordered (L_o) phases. (B) A 50 μm x 50 μm AFM image of the SLBs. The line profile below corresponds to the yellow line in the image. Membrane defects (blue arrow) show the thickness of the bilayer to be approx. 4 nm. (C) corresponds to the yellow square in B (10 μm x 10 μm). L_o and L_d phases are labeled. The line profile below corresponds to the yellow line in the image. The L_o phase appears 1-2 nm higher than the L_d phase. (D) A sample force curve showing how the breakthrough force and membrane thickness are derived. (E) Breakthrough force and (F) membrane thickness distribution for Ld and Lo phases with Gaussian fitting for quantification. Breakthrough force of L_o is lower than L_d, due to rigid packing of saturated lipids (SM) and cholesterol. Thickness measured by force spectroscopy also reproduces the L_o/L_d height difference observed in AFM imaging. Image reproduced with permission from (Unsay et al., 2015)

Chapter 4

Fluorescence Correlation Spectroscopy

Fluorescence Correlation Spectroscopy (FCS) uses fluorescence fluctuations mainly arising from the diffusion of individual molecules through a sub-micrometer detection volume, usually the focal volume of a confocal microscope. Autocorrelation analysis of the fluctuations depends on local concentration and translational (and/or rotational) diffusion coefficients. From these parameters, other properties such as chemical rate constants, association and dissociation constants, and structural dynamics can be calculated. Furthermore, recent advances in microscopy technology have allowed the use of new acquisition modes such as two focus and/or two color that further improve characterization.

4.1 Basics of FCS

4.1.1 Fluorescence

Fluorescence is the property of some molecules to absorb and emit light of different wavelengths. This process is often depicted schematically in Jablonski diagrams (Figure 4.1) (Lakowicz, 2006). After absorption of a photon of appropriate wavelength electrons pass from the singlet ground state to an excited quantum state, where the fluorophore undergoes fast vibrational relaxation. The relaxation of the electron back to the ground state is either coupled to the emission of a fluorescent photon or mediated by other non-radiative processes. For example, a dissipation of the energy through heat by internal conversion may occur. Another process called intersystem crossing can be achieved by the electron from singlet excited state to a quantum-mechanically forbidden triplet state. From this state, the molecule can emit a phosphorescent photon. In solution, phosphorescence is a process that is almost completely quenched.

An alternative non-radiative decay is the transfer of energy through collisions or by non-radiative dipole-dipole interactions (Förster Resonance Energy Transfer (FRET)). All these processes are characterized as quenching and depend on the concentration of quencher molecules. The fraction of excited molecules that get de-excited through fluorescence is the quantum yield and is the ratio between the amount of the particles undergoing radiative decay and normalized to all de-excitation processes.

Excitation to higher vibrational excited states and decay to higher vibrational ground states result in a longer wavelength of emitted photons compared to absorbed photons. This effect is called Stokes-shift and is the basis for experimentally separating excitation light from emission using dichroic mirrors and filters.

Fluorophores may eventually be destroyed by repeated excitation and emission in a process called photobleaching. As with any fluorescence based technique, this is a serious

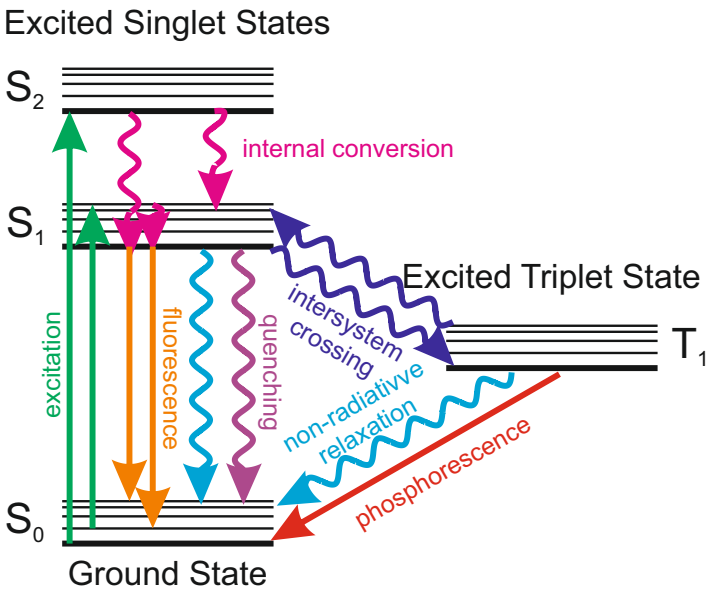

Figure 4.1: Jablonski Diagram. The fluorophore is excited into the first or higher excited singlet states ($\sim 10^{-15}$ s), undergoes vibrational and rotational relaxation ($\sim 10^{-14} - 10^{-11}$ s) and returns to the ground state S_0 with (straight lines) or without (squiggly lines) emission of a photon ($\sim 10^{-9}$ s). Alternatively, it can undergo a forbidden transition to the triplet state T_1 from which it can either relax radiatively via phosphorescence ($> 10^{-4}$ s) or non-radiatively.

limitation and challenge in FCS.

4.1.2 Microscope Set-up

Despite the many molecules contributing to the fluorescence signal, FCS is considered a technique with single molecule sensitivity since it relies on the fluctuations in small molecular ensembles ($N < 100$). There are several pre-requisites to detect signal of individual fluorescent molecules:

- Bright and photostable fluorescent dyes
- Background reduction to increase signal-to-noise ratio
- Sensitive detection: objectives with high collection efficiency and photon counting detectors.
- Working at low concentrations or very small volume to be able to record fluctuations

The last point is important as it dictates the optical geometries that can be used for FCS. Many optical setups are now available to work with FCS, the easiest of which is to use a confocal microscope (Rigler et al., 1993).

The basic setup of a confocal microscope is given in Figure 4.2A. The excitation laser is focused through a high numerical aperture objective to a diffraction-limited spot. Due to the Stokes shift, the fluorescent light is separated using a dichroic mirror. A pinhole in the image plane, adjusted to image the focal spot, removes out-of-focus fluorescence.

The pinhole is then projected onto the aperture of a photon-counting device such as an Avalanche Photodiode (APD), which produces a digital signal for every incident photon. These signals are often stored as photon arrival times in a computer or special electronic components (hardware correlator) for further processing.

This set-up produces a sub-femtoliter detection volume (observation volume), comparable to the size of a small bacterium. Fluorescence is detected as bursts of photons, which

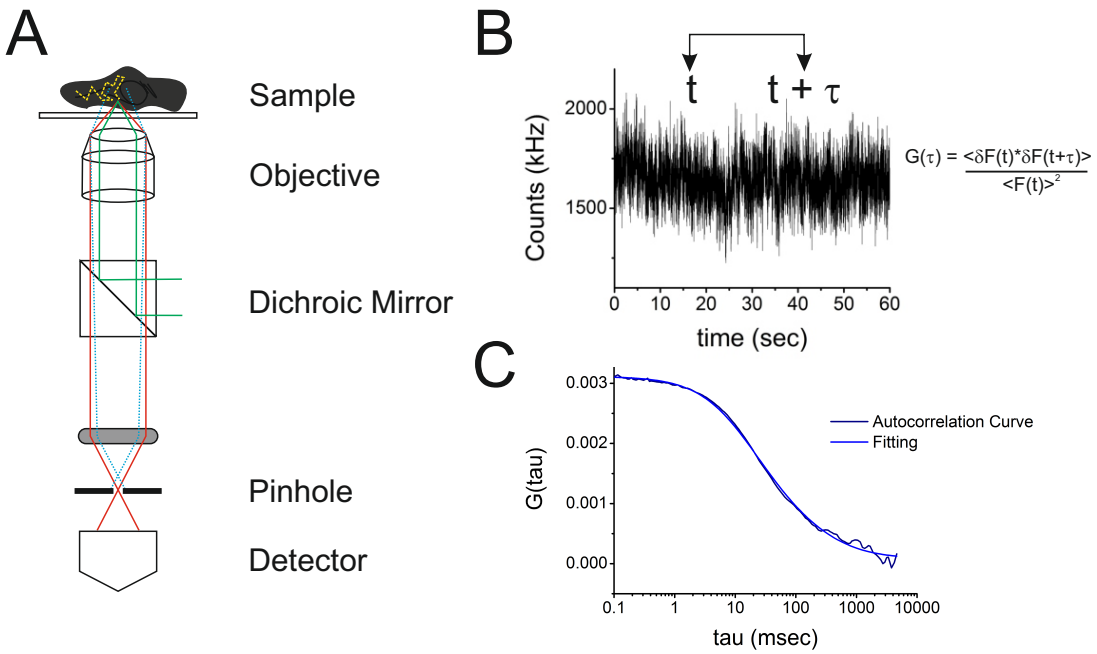

Figure 4.2: Principles of FCS. (A) Schematic showing of a confocal microscope setup. Fluorescence molecules diffuse through the confocal volume. The photons from the excitation and subsequent emission of these molecules are recorded by a very sensitive photon counting detector (ex. avalanche photodiodes, APD). (B) Photon counts are plotted vs. time, producing a fluctuation trace. (C) The fluctuation trace is temporally auto correlated to measure self-similarity of the signal over time and then fitted with a model function to acquire properties like diffusion time and concentration.

provide a slew of information. From the relative number of bursts, the concentration can be estimated. From the average duration, the residence time of the molecule and thus its mobility can be calculated. Using two spectral channels allows coinciding events to be analyzed and information on interactions to be extracted.

4.1.3 FCS as a Single Molecule Method

Rather than isolating bursts from a single molecule, FCS extracts physical properties from temporal (and in some cases also spatial) correlation analysis (Magde et al., 1972). FCS is usually measured at low excitation powers, resulting in a signal of 1-10 kHz per particle (or Counts per molecule (CPM)). This means that a particle emits only a few photons during its transit through the detection volume (Ries et al., 2012). This is fewer than the amount needed for single molecule analysis. The passage of a few hundred particles pass through the detection volume translates into a local concentration in the nM range.

Temporal autocorrelation analysis measures self-similarity of the signal with itself over time. The following expression describes the autocorrelation function:

$$G(\tau) = \frac{\langle \delta F(t) \cdot \delta F(t+\tau) \rangle}{\langle F(t) \rangle^2} \tag{4.1}$$

Where $G(\tau)$ is the autocorrelation function, $F(t)$ is the fluorescence intensity as a function of time t, and τ is the correlation time or time lag. $\langle F(t) \rangle = \frac{1}{T} \int_0^T F(t)dt$, denotes the time average of the signal, $\delta F(t) = F(t) - \langle F(t) \rangle$ are the fluctuations around the mean value. The curve multiplies the signal at t with that at a shifted time lag $t+\tau$ and averages this product for all intensity pairs over the trace (Figure 4.2B). This produces a temporal

decay, reflecting the probability that the signal still belongs to the same molecular event. If time lags are small, then the numerator results a finite positive number (individual fluctuations may be both either positive or negative, which is eventually averaged along the whole trace). If time lags are large, the two intensities will distribute above or below the mean, but will eventually average to zero. Therefore resulting in a decay curve(Figure 4.2C). The decay time, τ_D (also called the diffusion time) is related to the amount of time the fluorescent molecules stay in the detection volume.

The magnitude of the fluorescence signal is directly reflected in the intercept of the autocorrelation curve with the y axis, $G(0)$. The amplitude is inversely proportional to the average number of molecules and therefore to the concentration of the fluorophore. As such one can use the following equations to derive the relationship assuming that the particle events of N follow a Poissonian distribution:

$$G(\tau) = \frac{\langle \delta F(t)^2 \rangle}{\langle F(t) \rangle^2} = \frac{\langle \delta N(t)^2 \rangle}{\langle N(t) \rangle^2} = \frac{var(N)}{N^2} = \frac{N}{N^2} = \frac{1}{N} \tag{4.2}$$

A quick inspection of the curves can provide a qualitative estimate of τ_D and N. A precise quantitative analysis requires fitting of diffusion models, which are correlation functions describing the sources of the intensity of the fluctuations (Magde et al., 1972, Haustein and Schwille, 2007, Petrov and Schwille, 2008).

The particular expression of the correlation function depends on both the shape of the detection volume and the molecular sources of fluorescence intensity fluctuations. The following section breaks down the correlation function. The expression for freely diffusing particles in solution through a confocal detection volume, approximated by a three dimensional (3D) Gaussian profile, is:

$$G(\tau) = \frac{1}{N} \left(1 + \frac{\tau}{\tau_D} \right)^{-1} \left(1 + \frac{\tau}{\tau_D S^2} \right)^{-1/2} \tag{4.3}$$

With $N = V_{eff} C$, as the average number of particles in the effective volume V_{eff}, τ_D is the diffusion time, and S is the aspect ratio of the detection volume. All of these parameters will be discussed in a later section.

4.2 The Correlation Function

Fluorescence signals can be thought of as contributions of the local concentration over time and space in the detection volume $C(r,t)$, the photophysical properties of the fluorophore γ, and the optical setup defined as the molecule detection function $W(r)$:

$$F(t) = \int \gamma W(r) C(r,t) d^3 r \tag{4.4}$$

The average fluorescence intensity is given by

$$\langle F(t) \rangle = \int \gamma W(r) \langle C(r,t) \rangle d^3 r \tag{4.5}$$

Therefore the fluctuations are given by

$$\delta F(t) = F(t) - \langle F(t) \rangle = \int W(r) \delta(\gamma C(r,t)) d^3 r \tag{4.6}$$

The non-normalized correlation function is then given by:

$$g(\tau) = \langle \delta F(t) \cdot \delta F(t+\tau) \rangle = \iint W(r)W(r') \langle \delta(\gamma C(r,t)) \cdot \delta(\gamma C(r', t+\tau)) \rangle d^3r d^3r' \quad (4.7)$$

If γ is constant, the previous equation can be simplified using the concentration correlation function:

$$\phi(r, r', \tau) = \langle \delta(\gamma C(r,t)) \cdot \delta(\gamma C(r', t+\tau)) \rangle \quad (4.8)$$

leading to the following non-normalized correlation function:

$$g(\tau) = \langle \delta F(t) \cdot \delta F(t+\tau) \rangle = \iint W(r)W(r') \phi(r, r', \tau) d^3r d^3r' \quad (4.9)$$

Here, the correlation function is time-independent and we can consider an ideal solution of point-like particles in an open volume, where the fluctuations are governed by Poisson statistics (Lifshitz and Pitaevskii, 1980).

The normalized correlation function is therefore given as:

$$G(\tau) = \frac{\langle \delta F(t) \cdot \delta F(t+\tau) \rangle = \iint W(r)W(r') \phi(r, r', \tau) d^3r d^3r'}{(\int \gamma W(r) \langle C(r,t) \rangle d^3r)^2} \quad (4.10)$$

4.2.1 Concentration Correlation Function

Concentration correlation functions, $\phi(r, r', \tau)$, can be calculated by solving the differential equations describing concentration fluctuations, $\delta C(r,t)$. For pure diffusion, this is simply Fick's law of diffusion:

$$\begin{aligned} \partial_t C(r,t) &= D \nabla^2 C(r,t) \\ \partial_t \delta C(r,t) &= D \nabla^2 \delta C(r,t) \end{aligned} \quad (4.11)$$

This requires a definition of boundary and initial conditions. In the simple case, a boundary condition could include zero concentration fluctuations at infinity could be assumed, and an initial condition of molecules being released at the origin of the coordinate system could be considered. These conditions give rise to a solution described by a Gaussian function:

$$C(r,t) = \frac{N_0}{(4\pi D t)^{\frac{3}{2}}} \exp\left[-\frac{r^2}{4Dt} \right] \quad (4.12)$$

The solution for the concentration correlation function which is based on $\delta C(r,t)$ can be similarly derived for a freely diffusing particle in 3 dimensions.

$$\phi(r, r', \tau) = \frac{\langle C \rangle}{(4\pi D t)^{\frac{3}{2}}} \exp\left[-\frac{(r-r')^2}{4Dt} \right] \quad (4.13)$$

For diffusion in d dimensions, the general expression is:

$$\phi(r, r', \tau) = \frac{\langle C \rangle}{(4\pi D t)^{\frac{d}{2}}} \exp\left[-\frac{(r-r')^2}{4Dt} \right] \quad (4.14)$$

4.2.2 Gaussian Detection Profile

In confocal FCS, the molecule detection function can be approximated by a Gaussian detection profile (Rigler et al., 1993):

$$W(x,y,z) = \frac{2^{\frac{3}{2}}}{\pi^{\frac{3}{2}}\omega_0^2\omega_z} \exp\left[-\frac{2(x^2+y^2)}{\omega_0^2} - \frac{2z^2}{\omega_z^2}\right] \tag{4.15}$$

where ω_0 is the radius of the focal beam waist and ω_z describes the axial extension of the 3D Gaussian profile.

4.2.3 Diffusion of Point-like Particles

After inserting the concentration correlation function for 3D diffusion (Eq. 4.13) and the Gaussian detection function (Eq. 4.15) to the autocorrelation function (Eq. 4.10), we get:

$$\begin{aligned} G(\tau) &= \frac{1}{N}\left(1+\frac{4D\tau}{\omega_0^2}\right)^{-1}\left(1+\frac{4D\tau}{\omega_z^2}\right)^{-1/2} \\ &= \frac{1}{N}\left(1+\frac{\tau}{\tau_D}\right)^{-1}\left(1+\frac{\tau}{\tau_D S^2}\right)^{-1/2} \end{aligned} \tag{4.16}$$

In the second equation, the physical parameters C, D, ω_0 and ω_z were re-defined as $N = V_{eff}C$, where $V_{eff} = \pi^{3/2}\omega_0^2\omega_z$. $S = \frac{\omega_z}{\omega_0}$ is also called the structure parameter, and the diffusion time, $\tau_D = \frac{\omega_0^2}{4D}$.

The diffusional part of the correlation function factorizes into components along the three dimensions:

$$\begin{aligned} G_D(\tau) &= \frac{1}{N}\left(1+\frac{4D\tau}{\omega_0^2}\right)^{-1/2}\left(1+\frac{4D\tau}{\omega_0^2}\right)^{-1/2}\left(1+\frac{4D\tau}{\omega_z^2}\right)^{-1/2} \\ &= G_{D,x}(\tau) * G_{D,y}(\tau) * G_{D,z}(\tau) \end{aligned} \tag{4.17}$$

The autocorrelation function may also be extended to include multicomponents and photophysical processes such as triplet conversion. Furthermore, complicated geometries in cells may restrict or promote diffusion and as such, an anomalous diffusion or assisted transport/flow model may be used (Ries et al., 2012). A few of these different diffusion models are given in Table 4.1.

4.3 Practical Aspects

This section covers the practical aspects of FCS: what a typical experiment entails, the technical capabilities and limitations, and the issue of calibration.

4.3.1 Typical FCS Experiment

FCS determines mobility-related parameters. Figure 4.3 shows examples of different correlation functions. From the shape of the correlation curve, different molecular motions can already be inferred. For example, assisted transport leads to a steeper decay of the correlation curve than random Brownian diffusion, whereas anomalous diffusion would

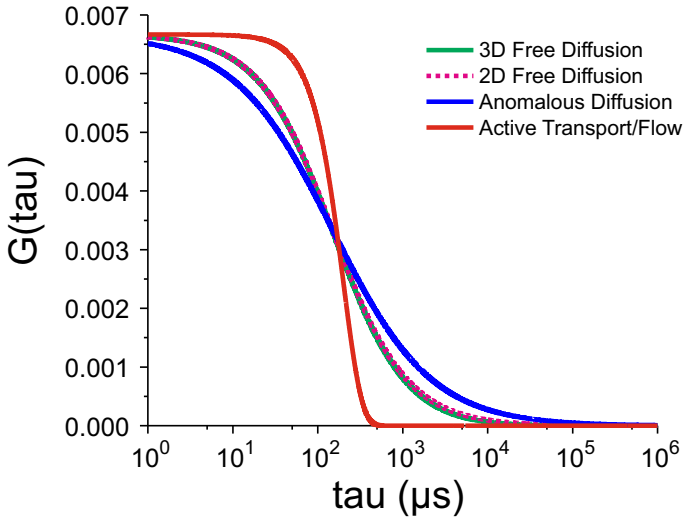

Figure 4.3: FCS Curves of Different Diffusion Models. Simulated auto-correlation curves based on different diffusion models. The shape of the curve may provide insight on the kind of diffusion a fluorescent species undergoes. However, this is not very trivial as some models will produce similar-looking curves (eg. 3D free diffusion vs. 2D free diffusion).

yield a flatter curve. However, this approach is limited as different models may result to very similar looking curves.

Once a model has been selected and the curves have been fitted, the diffusion time, τ_D, is used to calculate the diffusion coefficient once the shape and size of the detection volume are properly characterized.

$$D = \frac{\omega_0^2}{4\tau_D} \tag{4.18}$$

The Stokes-Einstein-equation defines the diffusion coefficient as dependent on two important parameters: the hydrodynamic radius of the molecule, R_H, and the microviscosity of the surrounding medium, η:

$$D = \frac{k_B T}{6\pi\eta R_H} \tag{4.19}$$

R_H is a measure of size, and is related to the molecular weight (MW) of the fluorescent species by the specific gravity, $\bar{\nu}$.

$$\frac{4}{3}\pi R_H^3 = MW\bar{\nu} \tag{4.20}$$

Changes in molecular size are especially interesting specifically in binding between fluorescent molecules and larger molecules or structures (such as protein complexes, DNA strands, or membrane vesicles). FCS is able to characterize these binding events of small molecules to larger complexes through the use of multi-component diffusion models . The limit at which FCS can distinguish multi-components not only depends in molecular size, but also microviscosity of the surrounding medium. In solution, the association of molecules of similar size can be identified as a change in diffusion time. Meseth et al (1999) showed that the larger molecule must have a diffusion time 1.6 times larger than the smaller molecule. However in membranes, this is not applicable (see below).

While temperature may appear to weakly influence the diffusion coefficient (Equation 4.19), the microviscosity (η) is dramatically changed by temperature (T). This is especially important in membranes where phase transitions can lead to complicated non-linear behavior of microvisity.

Table 4.1: Common Diffusion Models for FCS

Model	Equation
3D free diffusion	$G_{3D}(\tau) = \frac{1}{N}\left(1+\frac{\tau}{\tau_D}\right)^{-1}\left(1+\frac{\tau}{\tau_D S^2}\right)^{-1/2}$
3D free diffusion with triplet state	$G_{3D+T}(\tau) = G_{3D}(\tau) * \left[1+\frac{T}{1-T}exp-\frac{\tau}{\tau_T}\right]$
3D free diffusion with two components	$G_{3D+2C}(\tau) = \frac{1}{N_{total}}\frac{q_f^2 Y_f G_{3Df}(\tau) + q_s^2 Y_s G_{3Ds}(\tau)}{(q_f Y_f + q_s Y s)^2}$
2D free diffusion	$G_{2D}(\tau) = \frac{1}{N}\left(1+\frac{\tau}{\tau_D}\right)^{-1}$
2D free diffusion with elliptical gaussian detection	$G_{2DGauss}(\tau) = \frac{1}{N}\left(1+\frac{\tau}{\tau_D}\right)^{-1/2}\left(1+\frac{\tau}{\tau_D S^2}\right)^{-1/2}$

$G(\tau)$ is the correlation function, N is the average number of particles in the detection volume, τ is the lag time, τ_D is the diffusion time, S is the structure parameter related to the shape of the confocal volume $S = \frac{\omega_z}{\omega_0}$, where ω_0 is the waist radius of the detection volume and ω_z is the axial extension of the detection volume. In addition, q is the molecular brightness of the f (fast) and s (slow) diffusing components, Y refers to their molar fraction, T is the fraction of the fluorophores in the triplet state and τ_T corresponds to the triplet time. The terms introduced for the two components and triplet are also valid for 2D diffusion.

4.3.2 Statistical Accuracy

FCS measurements suffer from two sources of statistical noise: photon noise and particle noise (Ries et al., 2012).

Photon noise is due to issues with molecular brightness. A fluorophore with low CPM will result in an intensity trace with higher noise, especially at small lag times. This noise is reduced quadratically with brightness. As such, one main strategy is to use higher excitation laser power or fluorophores with high quantum yield. Photon noise is usually the main source of noise in solution FCS.

Particle noise arises from random movement of fluorescent particles through the detection volume. FCS relies on the average of a sufficient number of events. As such, a greater number of events ensures accurate correlation curves. Increasing molecular brightness will not improve the accuracy of the correlation curve as the concentration will remain fixed. The accuracy can only be improved by increasing the measuring time. A measurement time of 10^4 - 10^5 times longer than the relevant diffusion time is recommended (Tcherniak et al., 2009). Particle noise is usually the limiting factor for slow diffusing particles, such as those found in membranes (Koppel, 1974, Saffarian and Elson, 2003).

Lastly, the background intensity from sources other than the fluorophore of interest also affects statistical accuracy, especially when measuring concentrations (Kohl and Schwille, 2005, Schwille et al., 1999). Strong background fluorescence could lead to an overestimation of the actual particle number and underestimation of molecular brightness values, and will therefore affect the correlation amplitude. The main sources of background include dark counts of the detector, insufficient blocking of the excitation beam, stray light or scattered light from the buffer. With biological samples, autofluorescence presents an additional source of background. It comes from residual fluorescence of other

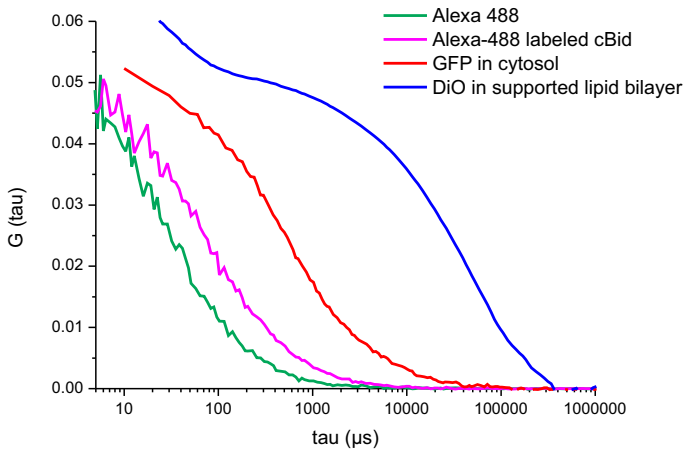

Figure 4.4: Diffusion at different time scales. FCS can measure diffusion of fast and slow molecules. The autocorrelation curves of different species are shown: Alexa 488 in water (green, D = 435 $\mu m^2/s$), cBid, a 22 kDa protein, labeled with Alexa 488 in buffer (purple, D = 90 $\mu m^2/s$), green fluorescent protein (27 kDa) in the cytosol of living cells (red, D = 30 $\mu m^2/s$, and 3,3'-dioctadecyloxacarbocyanine, DiO ($\lambda_{ex} = 488nm$), a lipidic dye in supported lipid bilayers composed of Egg PC (purple, D = 5 $\mu m^2/s$).

abundant moelcules inside the buffer or the cytoplasm of the cell (NADPH, flavonoids, etc.). Immobile or slow sources of autofluorescence will contribute to uncorrelated fluorescence which should be mathematically corrected or photobleached before acquiring relevant data. Uncorrelated background does not affect the diffusion time, as they are constant at all measured lag times. On the other hand, correlated background affect both concentration and diffusion and should be taken as a second component and should be included in the fitting and analysis.

4.3.3 Dynamic Range and Accessible Concentration

FCS can reach multiple orders of magnitude in the temporal range. It is limited by the speed of the photon counting detectors on the fast time lag regime, and the stability of the system towards longer time lag regime. Figure 4.4 shows sample autocorrelation curves of molecules with different diffusion types. The diffusion of molecules inside a cell shows a significant decrease compared to a similar sized molecule in water due to the crowded nature of the cytosol. Diffusion in membranes are also slower compared to diffusion in solution, and this poses some challenges for FCS measurements in membranes.

FCS can also probe a significant range of concentration (Figure 4.5). The lower limit is in the picomolar range when there is less than one particle in the detection volume ($N \sim 0.1$). In this range, the measurement needs to be longer to compensate for the low number of independent molecular transits. In addition, background from the solution, ambient light, or detector dark counts are significant, as such, FCS suffers from low signal-to-noise ratio. The upper limit of concentration is in the lower micromolar range ($N < 1000$). High concentrations will make the fluctuations weaker as the transit of one molecule in and out of the confocal volume will have little effect on the total photon count. In cells, this limit is also imposed by the detector or the instabilities in the sample, such as membrane and organelle movement, which can drastically distort correlation curves.

If diffusion is too slow or concentrations are too high, complementary techniques such as Fluorescence Recovery After Photobleaching (FRAP) (Reits and Neefjes, 2001), single particle tracking (Saxton and Jacobson, 1997) or image correlation spectroscopy (Digman et al., 2005, Ruan et al., 2004) might be possible alternatives to FCS.

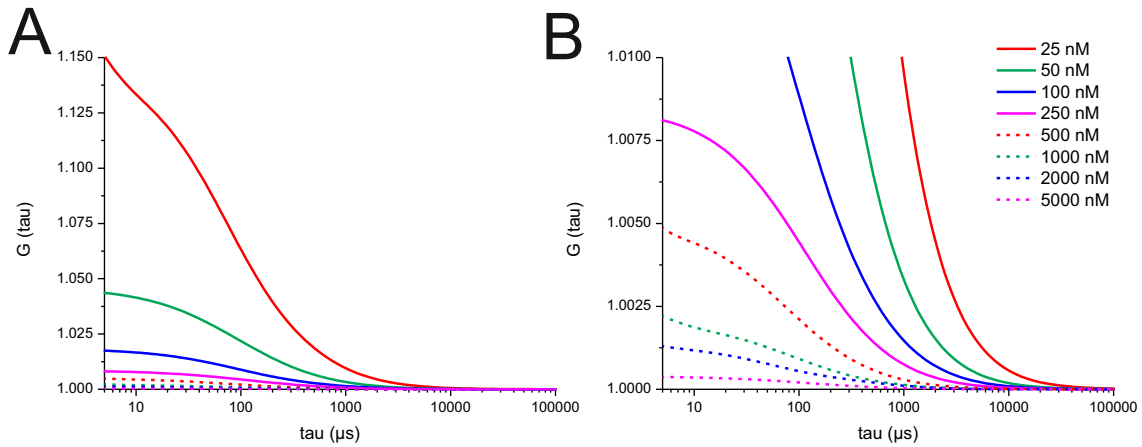

Figure 4.5: Dynamic Range of FCS. FCS can be used in a wide range of concentrations. (A) Diffusion of Alexa 633 in water at different concentrations: 25 nM (red, solid), 50 nM (green, solid), 100 nM (blue, solid), 250 nM (purple, solid), 500 nM (red, dashed), 1000 nM (green, dashed), 2000 nM (blue, dashed) and 5000 nM (purple, dashed). (B) is the same data in (A) with the y-axis zoomed in between 1.00 and 1.01 to show the curves of the more concentrated samples (>500 nM) better.

4.3.4 Calibration

As mentioned in previous sections, the concentration and diffusion coefficients are computed from the fitted parameters of N and τ_D. However, to arrive at these quantities, one must have an accurate idea of the size and shape of the detection volume. The shape is most often assumed to be a 3D Gaussian. The size is determined by calibration using fluorescent species with known diffusion coefficient in solution D_{cal}.

The calibration experiment entails acquiring an FCS curve for this calibration dye. The resulting autocorrelation curve is fitted with the 3D free diffusion model in which we can get the parameters for N_{cal}, τ_{Dcal} and S. Using equation 4.18, we can calculate for the ω_0. These size parameters can then be used to determine the concentration and diffusion coefficient of the unknown samples. Recently, accurate diffusion coefficients have been measured for numerous dyes and some common values are given in Table 4.2.

Table 4.2: Diffusion Coefficient of Common Fluorescent Dyes

Dye ($\lambda_{ex}/\lambda_{em}$)	Diffusion Coefficient ($\mu m^2/s$)	Reference
Alexa 488 (495/519)	435	(Petrášek and Schwille, 2008)
Rhodamine B (570/590)	450	(Culbertson et al., 2002)
Alexa 633 (633/647)	340	(Kapusta, 2010)

It is important that the size of the detection volume be constant between the calibration and the actual sample. Unfortunately, there are several artifacts that lead to distortion of the detection volume.

4.4 Artifacts

Commercial FCS set-up, while widely available, poses challenge in data interpretation as there are some artifacts that often occur in daily practice. Subtle changes in the slope or curvature of a correlation curve can lead to differences in fitting output, and these are not self-evident even to a trained eye. Furthermore, choosing appropriate model functions and correction requires a thorough knowledge of the measured system, and this makes data analysis iterative and at times cumbersome.

This section discusses some of these artifacts including optical aberrations that change the size and shape of the detection volume. Other effects from photobleaching, bright events and instabilities that distort the correlation curve will be discussed

4.4.1 Optical Artifacts

If the detection volume is distorted whether in the calibration or actual sample, the model function becomes invalid. A distortion in the detection volume usually corresponds to enlargement as the laser is focused to a nearly diffraction-limited spot. Enderlein et al, explored some of these optical artifacts (Enderlein et al., 2005, 2004).

One such distortion is affected by the coverslip thickness. Commercial coverslips can vary by 20 μm in one batch. Water immersion objectives with a correction collar are readily available to correct for the coverslip thickness.

Differences in refractive index between calibration and sample also lead to distortions. Calibration is usually done in water with a refraction index of 1.33. Biological tissues on the other hand can have a refractive index of up to 1.38. Even a change to 1.36 can lead to differences in concentration and reduction in the apparent diffusion coefficient (Ries et al., 2012). Such distortions are more dominant the farther one is from the surface of the glass. It was shown in glycerol solutions that within 10 μm depth, a refractive index up to 1.4 is tolerable. This indicates that such deviations are less severe when measuring in a monolayer of culture cells which rarely exceed 10 μm in height.

4.4.2 Photobleaching

Photobleaching cannot be entirely avoided because a fluorescent dye can undergo about 10^6 excitation-emission cycles before it is irreversibly bleached. The reason for bleaching is chemical oxidation reactions, which destroy the conjugated electron system in fluorophores. Molecules in the excited states are more susceptible to these oxidation reactions. Photobleaching changes the distribution of fluorophores in the detection volume. However after sometime, the rate of bleaching is the same as the diffusion that the bleached particles are replenished and the fluctuation normalizes. In this part, the amount of molecules is underestimated. A simple approach to prevent this is to adjust the laser excitation to a range where diffusion times are not changing systematically with laser excitation power. Simply looking at a constant trace is not enough because at higher concentrations, replenishing the bleached particles is so fast that the effect of bleaching is overlooked.

At higher excitation powers, high concentrations or a limited reservoir of fluorophores, bleaching becomes more visible in the intensity traces, which will have severe consequences on the FCS measurement. Rescaling the trace can be done to correct for the depletion (Ries et al., 2009a).

4.4.3 Bright Events and Instabilities

Bright aggregates (and in some cases, vesicles) pose a special problem of correlation curve distortion. They manifest as spikes in the fluctuation trace and this can dominate the entire correlation curve. One can take several short measurements instead of one long measurements to manually discard distorted curves. However this approach is not ideal as manually picking the right curve is time-consuming and introduces subjective bias. Furthermore reducing the measurement time reduces the statistical accuracy of the measurement (See Section 4.3.2), therefore a measurement of 1 x 100 s is different than a measurement of 10 x 10 s. The latter cannot be correlated at lag times longer than 10 s.

4.4.4 Challenges in Membranes

Confocal FCS in solution is considered a well-established technique. The application of FCS on membranes is still evolving due to slow diffusion and 2D geometry.

The viscosity of membranes is higher, decreasing the diffusion by several orders of magnitude compared to solution. This requires longer measuring times, exposing the measurement to artifacts of photobleaching and system instabilities. Transport between solution and membrane is also problematic in cells (Unsay and García-Sáez, 2013)).

To address these problems scanning FCS has been developed (Digman et al., 2005). Other advanced modalities and microscope set-up have been employed such as z-scan FCS (Humpolíčková et al., 2006, Przybylo et al., 2006), Total Internal Reflectance Fluorescence Microscopy (TIRF)-FCS (Lieto et al., 2003, Ohsugi et al., 2006, Ries et al., 2008a, Thompson and Axelrod, 1983, Thompson et al., 1981), Single Plane Illumination Microscopy (SPIM)-FCS (Krieger et al., 2015, Sankaran et al., 2009, Wohland et al., 2010), Imaging FCS(Digman et al., 2005, Ruan et al., 2004), supercritical angle FCS (Ries et al., 2008b) and Stimulated Emmission Depletion (STED)-FCS (Eggeling et al., 2009, Kastrup et al., 2005).

4.5 Advanced FCS

The limitations of solution FCS resulted in the evolution of the technique to other modalities. This section talks about three of them.

4.5.1 Two Color FCS

Binding events are extremely important in biological samples. Changes in diffusion times due to a change in molecular weight is not very evident when the association is between similar sized particles. Diffusion times of the ligand and the receptor have been shown to require a difference of at least a factor of 1.6 (Meseth et al., 1999). The cubic root dependence of the hydrodynamic radius on the molecular weight indicates that the molecular weight of the binding partners must differ by a factor of 8. Because of this, dual color FCS was developed (Figure 4.6).

Spectral cross-correlation measures dynamic co-localization of molecules with differently colored fluorescent dyes. In practice, this means recording fluctuations in two channels, and correlating the signal of one channel to the other with a technique called Fluorescence Cross Correlation Spectroscopy (FCCS):

$$G(\tau) = \frac{\langle \delta F_r(t) * \delta F_g(t+\tau) \rangle}{\langle F_r(t) \rangle \langle F_g(t) \rangle} \tag{4.21}$$

Here, $F_g(t)$ and $F_r(t)$ are the intensity traces of the 'green' channel and 'red' channel, respectively. Only if two species are interacting and diffusing together will there be a positive contribution to the cross-correlation amplitude. In case of a complete overlap of the detection volumes between the two spectral channels, the concentrations of bound (C_{rg}) and unbound (C_r and C_g) can be determined from the amplitudes of the auto- and cross-correlation curves:

$$\%CC_r = \frac{G_{rg}(0)}{G_r(0)} = \frac{C_{rg}}{C_{rg}+C_g}, \%CC_g = \frac{G_{rg}(0)}{G_g(0)} = \frac{C_{rg}}{C_{rg}+C_r} \tag{4.22}$$

In this case, it is important to fully label all the species, as the degree of labelling restricts the amount of cross-correlation that one can measure.

One main factor to consider is the overlap of the detection volumes in the two spectral channels. The detection volumes may have different sizes and they may also be displaced

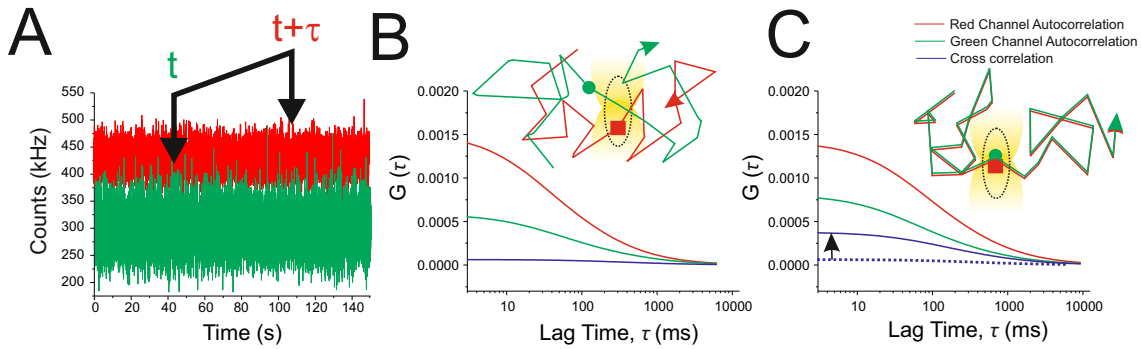

Figure 4.6: Two-color FCS. (A) Fluorescence signal from two spectral channels are collected and cross-correlated to obtain a cross correlation curve. (B) If the two species are diffusing separately through the focal volume, the cross correlation amplitude is zero. (C) If the two species are diffusing together in a complex through the focal volume, the cross correlation amplitude increases. The degree of cross correlation determines the amount of complexes.

(by a vector $d = d_x + d_y + d_z$). To correct for this, an extra parameter may be included in the fitting of the cross-correlation curve:

$$G_{rg}(\tau) = G_D(\tau) * exp\left[\frac{d_x + d_y}{4D\tau + \omega_{0,eff}^2}\right] * exp\left[\frac{d_z}{4D\tau + \omega_{z,eff}^2}\right] \tag{4.23}$$

Where $\omega_{0,eff}^2 = \frac{\omega_{0,g}^2 + \omega_{0,r}^2}{2}$ and $\omega_{z,eff}^2 = \frac{\omega_{z,g}^2 + \omega_{z,r}^2}{2}$.

This can be experimentally circumvented by calibrating the cross-correlation with a species that is perfectly labeled in both colors. This shows the maximum cross-correlation amplitude achievable by the system.

A second problem of two-color FCS is spectral cross-talk, which leads to false positive cross-correlation. This is especially challenging in cells. In most cell experiments, Green Fluorescing Protein (GFP) is used in conjunction with its red fluorescing variant Red Fluorescing Protein (RFP) or mCherry. To avoid cross-talk alternating or pulsed interleaved excitation (PIE) can be used, but this is more challenging to implement experimentally (Muller et al., 2005, Thews et al., 2005).

4.5.2 Two Focus FCS

The size of the detection volume is an important part of the calculation for concentration and diffusion coefficients from single-point FCS. Usually, this is determined by calibration. The calibration may always bear uncertainties because of the fitting errors. In addition, the fitting makes D and ω_0 coupled variables because of their relation $\tau_D = \frac{\omega_0^2}{4D}$.

Equation 4.23 gives us an idea of using two laterally displaced foci (of distance, d) for single-color measurements (Dertinger et al., 2008) (Figure 4.7). Removing displacements parallel to the optical axis, this simplifies the cross-correlation function to:

$$G_{12}(\tau) = G_1(\tau) * exp\left[-\frac{d^2}{4D\tau + \omega_0^2}\right] \tag{4.24}$$

Where the distance d is the only extra parameter. If we accurately know the distance by independent methods, D and ω_0 are now decoupled and can be determined as free fitting parameters (ie. measurements are calibration free).

In practice, d has to be small and is of the order of magnitude of the beam diameter. The two foci should be well-separated to prevent cross-talk from one detection area to

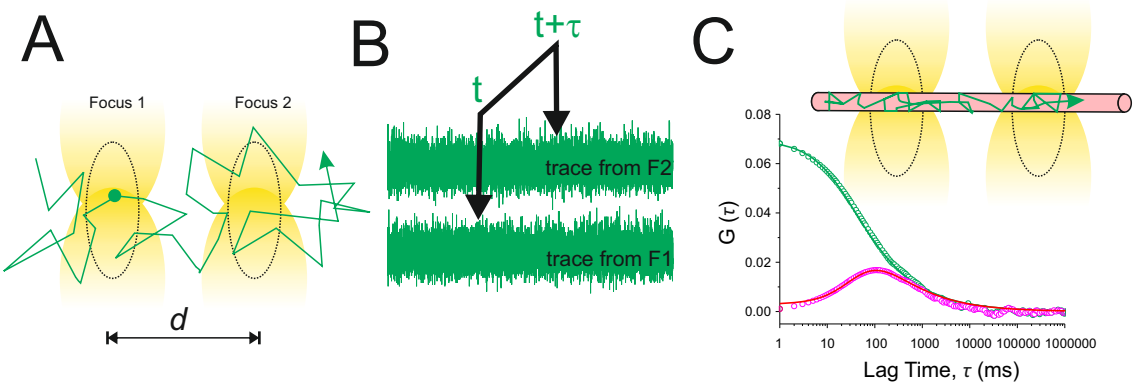

Figure 4.7: Two-focus FCS. (A) Two confocal detection volumes (Focus 1, $F1$ and Focus 2, $F2$) are generated at a fixed distance, d. (B) fluorescence signal from the two foci are cross correlated. The cross correlation curve gives a characteristic peak around the time it takes for the molecule to diffuse from one focus to another. (C) A simulation of two-focus FCS curves are shown for a particle diffusing through a narrow tube ($D_{simulation} = 1\ \mu m^2/s$). The two foci are displaced 500 nm apart and have a waist radius of 250 nm. The green symbols represent the autocorrelation curve while the magenta symbols represent the cross-correlation curve. The green lines and the magenta lines represent the fitting for the auto- and cross-correlation curves, respectively, using a 1D free diffusion model.

another. When the excitation is alternated between the two foci, the photon arrival times can then be sorted based on which focus is excited.

There are several ways to generate a two-focus instrument. The simplest is to use two laser beams at slightly different incidence angles. However, the distance generated might be unstable. Using Nomarski-prisms, a fixed angle between two parallel beams with orthogonal polarizations can be produced (Dertinger et al., 2008).

Another application of two focus FCS is the accurate quantification of flow, when the cross-correlation with focus 1 with 2 (forward) is different for focus 2 with focus 1 (backward). The accuracy of these measurements are better than fitting a single point FCS.

By combining dual focus with dual color FCS, several more parameters may be measured. In this case, one gets four autocorrelation curves for each spectral channel in two spatial regions, 2 spatial cross-correlation, 2 spectral cross-correlation, and 2 spatial-spectral cross-correlation channels. The information that can be derived are not limited to concentrations and diffusion coefficients, but also spatial overlap of the two spectral detection volumes. This setup allows for quantitative binding studies without the need of a perfect cross-correlation sample to calibrate the chromatic aberrations.

4.5.3 Scanning FCS

Scanning Fluorescence Correlation Spectroscopy (SFCS) employs a scanning unit of a commercial laser-scanning microscope to move the detection volume. Scanning results in reduced residence times of fluorophores and reduces photobleaching (Ries et al., 2009a, Ries and Schwille, 2006, Unsay and García-Sáez, 2013), which enables longer measuring times. SFCS is mainly limited by the speed of the scanning unit. The scanning paths may be as simple as a line or circle, or even across a whole area (through raster scanning).

SFCS is notably applied to membranes. Line-scan and circular scanning FCS, are employed on a flat membrane (such as supported bilayers). In this application, the scanning path is parallel to the orientation of the membrane. Because of this geometry, the scanning path produces many laterally displaced detection volumes along the membrane,

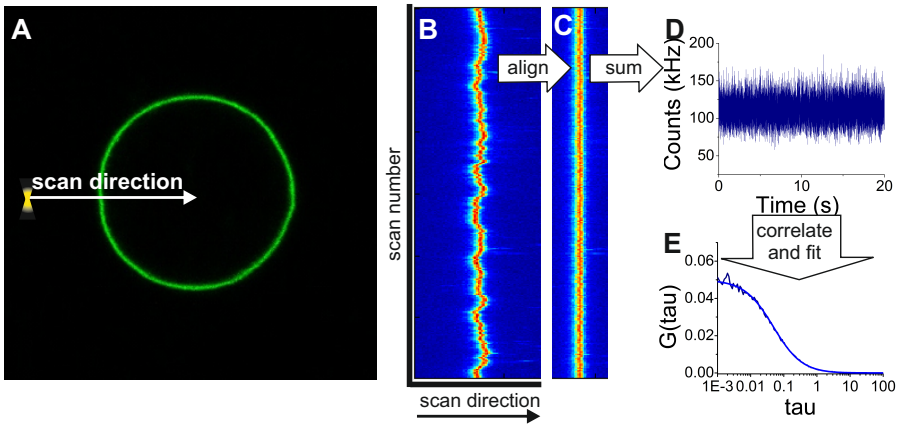

Figure 4.8: Principles of Scanning FCS. (A) The detection volume of a confocal microscope is scanned repeatedly perpendicular to the membrane plane of the GUV at the equator. At this region, the membrane is virtually flat. (B) Each scan is then used to make a pseudo image where the intensity in each scan position is plotted for all the scans (scan position vs. scan number). Because the fluorescent molecules are solely in the membrane, only a small region per scan will show high intensity. This region is the point where the confocal volume passes through the membrane. (C) Membrane movements are corrected by aligning the maxima for each scan. Each scan is fitted with a Gaussian and the integrated area serves as the intensity of the membrane for one time point. (D) Fluorescence fluctuation trace is constructed by using one scan as one time point. (E) As with standard FCS, the fluctuation trace is autocorrelated and the resulting autocorrelation curve is fitted with model functions.

from which the time-delay factors and displacement factors can be accurately calculated. This eliminates the need for calibration. It is often applied in temperature-dependence experiments of membranes that are otherwise inaccessible to static confocal FCS (Ries et al., 2009a).

Scanning perpendicular to free standing membranes, such as Giant Unilamellar Vesicles (GUV), has also been employed to elucidate the contributions of the surface to the lateral diffusion of the molecules (Ries and Schwille, 2006). In this case, the membrane is only detected at one point in the scan path, and the intensity of the membrane for each scan serves as one point in the fluctuation trace. Figure 4.8 shows the membrane position is different from scan to scan due to membrane undulations, which is otherwise undetectable in static FCS or SFCS parallel to the membrane. Two color, two focus SFCS is easily applied to GUVs with commercial laser scanning microscopes by scanning two parallel lines perpendicular to the GUV with two excitation lasers. PIE-FCS can also be applied in cases where spectral cross talk needs to be avoided.

4.6 Applications

4.6.1 Model Membranes

The application of FCS to membranes presents a set of challenges that have been recently circumvented by current microscope modalities. Traditionally, FRAP is used to examine diffusion in membranes. However, the derivation of diffusion coefficients from FRAP measurements is not straightforward. It is here that FCS becomes more applicable. FCS is now considered a very powerful tool to answer questions of membrane organization and functions.

Kahya et al, studied the changes in diffusion between liquid ordered and liquid disordered phases in GUVs of different compositions, and note the diffusion coefficient's dependence on cholesterol content (Kahya, 2003, Kahya and Schwille, 2006).

Furthermore, Chiantia et al, combined line-scanning FCS with AFM, to examine at

differences in the diffusion of fluorescent dyes between liquid ordered and liquid disordered phases and correlate it with the physical properties of the membrane through force spectroscopy (Chiantia et al., 2006, 2007). They also showed that the binding of proteins to membrane and diffusion can be easily seen by confocal microscopy and FCS, but not necessarily AFM. While the AFM is good for high-resolution imaging capability, its slow imaging time underestimates the amount of protein in the membrane, due to the fast diffusion.

Finally, Garcia-Saez et al, showed the importance of the membrane in promoting Bcl-2 protein interactions, further supporting the embedded together model (García-Sáez et al., 2009). They calculated the strength of interaction of tBid and Bcl-xL in solution and in membrane using two color FCCS. The interaction is reversible and can be inhibited competitively.

4.6.2 Cells

Cells present one of the most complicated biological systems to analyze. FCS in cells allows for the quantification of multiple of parameters inside a living system. However, the challenges of heterogeneity, molecular crowding, and phototoxicity should always be considered.

In one particular example, Weidemann et al, examined at the molecular diffusion of Histone H2B in HeLa cells (Weidemann et al., 2003). By sampling different regions of the cell, they found location-dependent diffusion: free diffusion in the periphery of the cytoplasm, anomalous diffusion in the perinuclear region, and strongly anomalous and hindered diffusion in the nucleolus and chromatin regions. Photobleaching was examined and revealed that many H2B molecules were bound to DNA, rendering them immobile (Figure 4.9).

FCS of the plasma membrane has also been shown by many groups. In one particular example, Ries et al, showed that scanning two focus and two color FCCS can be used to characterize binding of fibroblast growth factor receptor to its ligand (Ries et al., 2009b). Meanwhile Eggeling et al showed the nanoscale dynamics of membrane lipids using STED-FCS (Eggeling et al., 2009).

FCS has also been used to measure dynamics (Gennerich and Schild, 2000, Krieger et al., 2015, Wohland et al., 2010) and interactions (Maeder et al., 2007, Slaughter et al., 2007) of proteins in the cytosol. Though FCS has been used to examine organelles (Kim et al., 2007, Kohl and Schwille, 2005), there has been very little work on mitochondria. Using mitoEYFP, Koopman et al. (2007) characterized the motility of mitochondria and diffusion of particles in the matrix (via mitoEYFP) before and after inhibition of NADH:ubiquinone oxidoreductase by rotenone. All of these studies were performed with single focus point FCS and therefore suffer from artifacts due to the refractive index mismatch between buffer and cells.

Furthermore, FCS is often used in complement to other fluorescent techniques to get a more complete picture of the biological problem. Table 4.3 shows where certain fluorescent techniques are applicable and might be better than FCS. For example, FCS is very good for very fast dynamics, and suffers increased acquisition time with slower molecules. In this case, single particle tracking or FRAP may be better alternatives. Sample heterogeneity is also an issue, especially if diffusion can be hindered by underlying structures. This is not the case for single particle tracking where an individual particle's trajectory can be characterized and multiple populations can be easily inferred given enough sample statistics.

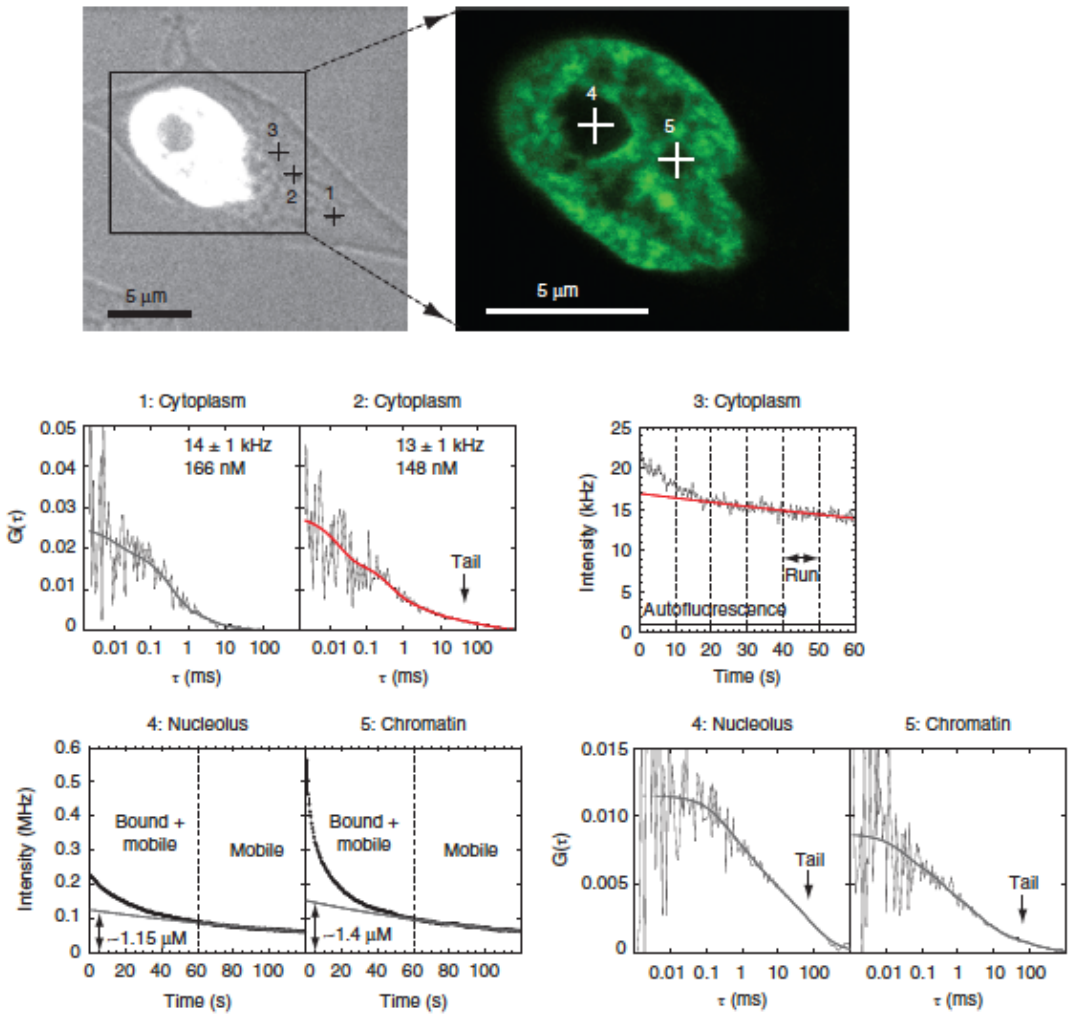

Figure 4.9: FCS in different parts of the cell. HeLa cell stably expressing an EYFP tagged histone H2B. FCS or intensity traces are shown for five positions: (1) free diffusion in the periphery of the cytoplasm, (2) anomalous diffusion within perinuclear membrane systems, (3) intensity trace indicating transient binding close to the nuclear envelope, (4) strongly anomalous diffusion in the dense nucleolus, and (5) slightly hindered diffusion in chromatin regions. DNA-bound nucleosomal fluorescent histones were quantified by continuous photobleaching before measuring FCS

Table 4.3: Applicability of Different Fluorescence Techniques

Parameter	Single Particle Tracking	FCS	FRAP
Diffusion	Very slow ($< 10^{-3}$-$1\mu m^2 s^{-1}$)	Fast ($< 10^{-1}$-$10^3 \mu m^2 s^{-1}$)	Very slow ($< 10^{-1} \mu m^2 s^{-1}$)
Concentration	Extremely low ($< 1\mu m^3$)	Physiological (10-$10^4 \mu m^3$)	High
Required Photons per molecule	> 100	> 1	No limit
Measurement time	Minutes to hours	Seconds to Minutes	Seconds to Minutes
Heteregeneity	Single molecule level	Average	Diffcult

Chapter 5

Materials and Methods

5.1 Materials

5.1.1 Chemicals, Proteins and Kits

The following lipids were used in this study: L-α-phosphatidylcholine from egg (EPC), L-α-phosphatidylethanolamine (PE), L-α-phosphatidylinositol from bovine liver (PI), phosphatidylserine from brain (PS) and cardiolipin (CL) from bovine heart (Avanti Polar Lipids, Inc., Alabaster, AL).

The following fluorescent dyes were used in this study: 1,1'-dioctadecyl-3,3,3',3'-tetramethylndodicarbocyanine-4-chlorobenzenesulfonate salt (DiD-C18 or DiD), Alexa Fluor® 488 (Alexa 488) and Alexa Fluor® 633 (Alexa 633) were purchased from Molecular Probes, Eugene, OR. Rhodamine B and calcein were purchased from Sigma-Aldrich.

The following antibodies were used in this study: polyclonal goat anti-Bid (Santa Cruz Biotech, sc-6538, 1:1000 dilution), monoclonal mouse anti-GFP (eBioscience, 14667482, 1:1000), polyclonal rabbit anti-BclxL (BD, 610212, 1:1000), Horseradish peroxidase (HRP)-conjugated goat anti-mouse (Jackson ImmunoResearch, 115-035-003, 1:10,000), HRP-conjugated goat anti-rabbit (Jackson ImmunoResearch 111-035-003, 1:10,000), and HRP-conjugated donkey anti-goat (Santa Cruz Biotech, sc2020, 1:10,000).

Table 5.1 shows the kits used to prepare DNA.

Table 5.1: Kits

Name	Manufacturer	Catalogue #
E.z.n.a. Plasmid Mini Kit	VWR (Omega)	D6945-02
QIAquick Gel Extraction Kit	Qiagen	28704
Gene Jet PCR Purification Kit	Thermo Fisher Scientific	K0702
Q5 High Fidelity DNA Polymerase PCR Kit	New England Biolabs (NEB)	E0555L

Enzymes used for cloning were restriction enzymes KpnI-HF, HindIII and BbsI (New England Biolabs), polymerase Q5 High Fidelity DNA Polymerase (New England Biolabs), Shrimp Alkaline Phosphatase (New England Biolabs), T4 Polynucleotide Kinase (New England Biolabs), T4 DNA ligase (New England Biolabs), and Gateway® enzymes LR Clonase® II. DNAse I used for protein purification was purchased from Roche. Purified Caspase 8 used in Bid cleavage was a gift from Prof. Dr. Jean-Claude Martinou (University of Geneva, Switzerland).

Agarose gel standards (1kb DNA ladder), Color Prestained Protein Standard, Broad range (11-245 kDa), and Unstained Protein Ladder, Broad range (10-250 kDa) were purchased from New England Biolabs. Western Lightning® Plus ECL, Enhanced Chemilu-

minescence Substrate (NEL103001EA) was purchased from Perkin Elmer.

5.1.2 Laboratory Instruments and Equipment

Table 5.2 lists laboratory instruments used in this study. Table 5.3 lists important laboratory materials/glasswares/consumables.

Table 5.2: Laboratory Instruments

Equipment	Manufacturer	Model
Atomic Force Microscope	JPK	JPK Nanowizard II mounted on Zeiss Axiovert 200
Bacterial Incubator	Infors-HT	Multitron Standard
Balance, Analytical (0.0001 g)	Kern and Sohn GmbH	ALJ160-4M
Balance, Classical (0.01g)	Kern and Sohn GmbH	440-33N
Bath Sonicator	Bandelin Sonorex Digitec	DT-31
Cell Culture Hood	Thermo Fisher Scientific	MSC-Advantage®
Cell Disruptor	Avestin	EmulsiFlex-C5
Cell Sorter	BD Biosciences	BD FACS Aria
Centrifuge (For small tubes)	Thermo Fisher Scientific	Heraeus Pico17
Centrifuge (For small tubes, refrigerated)	Eppendorf	5417R
Centrifuge (Swing bucket)	Thermo Fisher Scientific	Sorvall ST8
Centrifuge (Swing bucket, refrigerated)	Thermo Fisher Scientific	Megafuge 16R
Centrifugre (Fixed Angle, refrigerated)	Thermo Fisher Scientific	Sorvall RC 6 Plus
Chemiluminiscence Imager	Vilber Lourmat	Fusion FX
CO2 incubator	Thermo Fisher Scientific	BB15
Electrophoresis Power Supply (Agarose Gel)	Bio-Rad	PowerPac HC
Electrophoresis Power Supply (SDS-PAGE)	Bio-Rad	PowerPac Basic
Electrophoresis System (SDS-PAGE)	Bio-Rad	System Mini-PROTEAN Tetra Cell (1658001)
Electroporation Apparatus	Bio-Rad	MicroPulser
Fast-protein liquid chromatograph	GE Healthcare Lifesciences	KTA Micro System

Continued on next page

Table 5.2 – continued from previous page

Equipment	Manufacturer	Model
Fluorescence Microscope, Confocal	Carl Zeiss, Inc	LSM 710 with Confocor 3 module
Fluorescence Microscope, Widefield	Carl Zeiss, Inc	Axio Vert A.1
Fluorimeter	Jasco Analytical Instruments	FP8300
Hardware Correlator	Flex02-01D	`http://correlator.com`
Heating Block/Mixer for small tubes	Eppendorf	Thermomixer Comfort
Heating Plate	VWR	12621-090
Heating Plate with Mixer	NeoLab	D6010
Liposome Extruder	Avestin	LiposoFast-Basic
microDrop plate	Thermo Fisher Scientific	N12391
pH Meter	Sartorius	PB11
Plate Reader	Tecan	Infinity 5000 M
Plate Reader	Thermo Fisher Scientific	MultiSkan Go
Punch and Die Set	Precision Brand Products, Inc	40105
Scanner for SDS-PAGE	EPSON	Perfection 4990 Photo
Semidry electrophoresis transfer cell	Bio-Rad	Trans-Blot Turbo Blotting
Thermal cycler PCR	Bio-Rad	MyCycler
UV transilluminator	Intas	UV Systeme
Vacuum Pump	VacuuBrand	MZ 2C NT +AK+EK
Vortexer	Ika	Vortex Genius 3
Water purifier	Millipore	Milli-Q Reference A+ System

Table 5.3: Other laboratory equipment and consumables

Name	Manufacturer	Catalogue #
Adhesive Tape	3M	Scotch® Magic™ Tape 810 (1-inch)
Anion Exchange Column	GE Healthcare Life-sciences	HiTrap Q HP (17-1153-01)
Chromatography Paper	Whatman	Whatman Protran Ba 83 Nitrocellulose 0.2 μm 20 cm x 3 m roll
X-ray Film	Laborversand	FUJI Medical X-Ray Film SuperRX (RF11)
Glass coverslip	Duran Group	24x60 mm, 1mm thickness (2355036)
Laboratory Equipment Grease	Borer Chemie AG	Glisseal N
LabTek Chambers	Nunc	8-well microscopy Chamber (155411)
Mica blocks	NSC Mica Exports Ltd.	
Optical Adhesive	Norland Products, Inc.	NOA 88
PD-10 Columns	GE Healthcare Life-sciences	17-0851-01
Polycarbonate membranes	Avestin	200nm pore size, 19mm Diam. 50/box (LFM-200)
Polyvinylidene fluoride (PVDF) blotting membrane	Merck Millipore	Immobilon (R) P-^{SQ} PVDF Membrane
Silicon Nitride AFM Cantilever	Bruker AFM Probes	DNP-10

5.1.3 Buffers and Solutions

Water used for all solutions was purified (18.18 $M\Omega - cm$, de-ionized) using Milli-Q Reference A+ System from Millipore. Table 5.4 lists all reagents and buffers used in the thesis per given experiment.

Table 5.4: Buffer and Solution Recipes

Experiment	**Buffer or Solution**	**Components or Catalogue Number**
Bacterial Cell Culture	Lysogeny broth (LB) media	For 1L of LB media, 5g NaCl, 5g Yeast Extract, 10 g Tryptone Peptone For Agar plates add g agar to 1L LB media
	Phosphate Buffer for Terrific Broth (TB) Media	For 1L, 24.14 g KH_2PO_4, 164.32 g $K_2HPO_4 \cdot H_2O$
	TB Media	For 1L of TB media, 24 g Yeast Extract, 12 g Tryptone Peptone, 5 mL Glycerol (86%) + 100 mL Phosphate buffer
	Antibiotics	Stock Solutions: Ampicillin (100 mg/mLH_2O), Chloramphenicol (30 mg/mL 50% Isopropanol) and Kanamycin (50 mg/mL H_2O) Final Concentration: Ampicillin (100 μg/mL), Chloramphenicol (30 μg/mL), and Kanamycin (50 μg/mL)
	Isopropyl β-D-1-thiogalacto-pyranoside (IPTG)	Stock solution 1 M

Continued on next page

Table 5.4 – continued from previous page

Experiment	Buffer or Solution	Components or Catalogue Number
Mammalian Cell Culture	Dulbecco's Modified Eagle Medium (DMEM)	Gibco Life Technologies (D6046)
	Dulbecco's Phosphate Buffered Saline (PBS)	Gibco Life Technologies (D8537)
	Trypsin-EDTA solution (10x)	Sigma Aldrich (59418C)
	PenStrep	Sigma Aldrich (P4333)
	Fetal Calf Serum	Sigma Aldrich
	Opti®-MEM	Gibco Life Technologies (31985-047)
	Lipofectamine ®2000	Invitrogen (11668019)
	Geniticin ® G418 Sulfate	Invitrogen (10131019)
	Air Buffer	150 mM NaCl, 20 mM HEPES, 15 mM D-Glucose, 20 mM Trehalose, 5.4 mM KCl, 0.85 mM $MgSO_4$, 0.6 mM $CaCl_2$, 150 μg/mL Bovine Serum Albumin, pH 7.4
	RIPA buffer	150 mM NaCl, 50 mM Tris pH 8.0, 1% Triton X-100, 0.5% sodium deoxycholate, 0.1% SDS
	Earle's Balanced Salt Solution (EBSS)	400 mg/L KCl, 2200 mg/L $NaHCO_3$, 6800 mg/L NaCl, 140 mg/mL $NaH_2PO_4 \cdot H_2O$, 1000 mg/mL D-Glucose
Electrophoresis (SDS-PAGE)	30% acrylamide/bis-acrylamide, 29:1 (3.3% crosslinker) solution	Bio-Rad (161-0156)
	Lower Tris (4x)	1.5M Tris, pH 8.8, 0.4% SDS
	Upper Tris (4x)	0.42M Tris, pH 6.8, 0.4% SDS
	Ammonium persulfate (APS)	10% (w/v) in water
	TEMED	Sigma (T9281)
	6x SDS-PAGE Sample Buffer	4% SDS, 10% β-mercaptoethanol 20% glycerol, 0.004% bromophenol blue, 0.125 M Tris, pH 6.8
	Running Buffer	125mM Tris, pH 8.9, 0.5%SDS
	Low Toxicity Staining Solution	0.1% Coomassie blue, 10% acetic acid, 40% ethanol
	Destaining Solution	10% acetic acid, 40% ethanol

Continued on next page

Table 5.4 – continued from previous page

Experiment	Buffer or Solution	Components or Catalogue Number
Electrophoresis (Western Blot)	Tris-buffered saline with Tween buffer (TBST)	40 mM Tris, 5 mM sodium acetate, 1mM EDTA, 20 mM TrisHCl, 135 mM NaCl, pH 7.6, 0.05% Tween 20
	Membrane-blocking buffer	5 g milk powder in 100 mL TBST
	Anode I Buffer	0.3 M Tris pH 10.4, 10% methanol
	Anode II Buffer	25 mM Tris, 10% methanol
	Cathode Buffer	25 mM Tris, 40 mM glycin, 10% methanol
Electrophoresis (Agarose gel)	Tris-acetate-EDTA (TAE) buffer	40 mM Tris, 20 nM acetate, 1 mM EDTA, pH 8.0
	1%Agarose solution	0.5 g agarose in 50 mL TAE
	GelRed ™	Biotium
	DNA gel loading buffer	New England Biolabs (B7021S)
Bax Purification	Chitin Buffer	500 nM NaCl, 20 mM Tris, pH 8.1 For cell lysis and affinity chromatography with Chitin Beads
	Protease Inhibitors	Complete Mini Protease EDTA-Inhibitor Mix (Roche, 11836170001)
	Chitin Beads	New England Biolabs (S6651S)
	Mono A	20 mM Tris, pH 8.0 for loading Bax into Ion-exchange column
	Mono B	20 mM Tris, 1 M NaCl, pH 8.0 for eluting Bax from ion-exchange column
	Smart A	20 nM Tris, 150 mM NaCl, pH 7.5
cBid Purification	Nickel A	300 mM NaCl, 20 mM Tris, 20 mM NaH_2PO_4, pH 7.5
	Nickel B	300 mM NaCl, 20 mM Tris, 20 mM NaH_2PO_4, 250 mM Imidazole, pH 7.0
	Nickel-NTA Agarose	Qiagen(30210)
	Cleaving Buffer	50 mM HEPES pH 7.5, 100 mM NaCL, 10 mM DTT, 1 mM EDTA and 10% (w/v) sucrose

Continued on next page

Table 5.4 – continued from previous page

Experiment	Buffer or Solution	Components or Catalogue Number
Protein Concentration Assay	Assay Reagent Concentrate (4x)	Bio-Rad (500-0006)
	BSA Standards	Concentration (mg/mL in water) 1.5, 1.25, 1, 0.8, 0.6, 0.4, 0.2
Calcein Assay and Lipid Packing Assay	Chloroform	
	Outside Buffer (OB)	40 mM NaCl, 20 mM HEPES pH 7.0, 1 mM EDTA
	Calcein Solution	80 mM in OB
	Triton Solution	5% v/v in OB
	BSA blocking Solution	10 mg/mL BSA in OB
	MC540	Sigma Aldrich (323756)
Supported Lipid Bilayers (SLB)	PBS for SLBs	2.7 mM KCl, 1.5 mM KH_2PO_4, 8mM Na_2HPO_4, and 137 mM NaCl, pH 7.2
	SLB Buffer	150 mM NaCl, 10 mM HEPES, pH 7.4
	Calcium Solution	1 M $CaCl_2$

5.1.4 Plasmids and Oligonucleotides

Plasmids for Recombinant Protein Purification

- **pTYB1-BaxWT**: pTYB1 contains an intein domain and a chitin-binding domain C-terminal of the human wild type Bax
- **pET23-Bid**: Mouse Bid was cloned into pET23. There is a 6xHistidine tag at the N-terminal of Bid.

Plasmids for Gateway® cloning

- **Destination Vectors** based on pDEST26 (Gateway® destination vector with *ccd*B gene and chloramphenicol resistance in between the LR recombination sites). Gift from Dr. Stefan Pusch (University of Heidelberg).
  - **EGFP-N**: LR recombination site downstream of the EGFP, produces a fusion protein with N-terminal EGFP tag.
  - **EGFP-C**: LR recombination site upstream of the EGFP, produces a fusion protein with C-terminal EGFP tag.
  - **TagRFP-N**: Similar to EGFP-N, but has TagRFP instead of EGFP
  - **TagRFP-C**: Similar to EGFP-C, but has TagRFP instead of EGFP

- **Entry Clones** were purchased from the German Cancer Research Center (Deutsches Krebsforschungzentrum, DKFZ) genomics facility. They are based on pENTR221 (Gateway® entry vector) with the specific human gene cloned in between the LR recombination sites.
  - **SDHA**: Succinyl dehydrogenase subunit A
  - **SDHC**: Succinyl dehydrogenase subunit C
  - **SDHD**: Succinyl dehydrogenase subunit D
  - **TOMM20**: Translocase of the outer mitochondrial membrane (20 kDa)
  - **TOMM22**: Translocase of the outer mitochondrial membrane (22 kDa)
  - **TOMM40**: Translocase of the outer mitochondrial membrane (40 kDa)
  - **TOMM70A**: Translocase of the outer mitochondrial membrane (70 kDa)
  - **TIMM23**: Translocase of the inner mitochondrial membrane (23 kDa)
  - **VDAC1** Voltage dependent anion channel 1

Plasmids for Mammalian Cell Expression

- **Empty Vectors**
  - **pEGFP-N1**: multiple cloning site upstream of EGFP, producing a fusion protein with a C-terminal GFP tag. Gift from Dr. J. Andres Melendez (State University of New York, Albany, NY)
  - **pcDNA3.1(-)-mCherry**: cloning site upstream of mCherry producing a fusion protein with C-terminal mCherry tag. Gift from Paul Vogel and Dr. Thorsten Stafforst (University of Tübingen)
  - **pmCherry-N2**: multiple cloning site upstream of mCherry producing a fusion protein with C-terminal mCherry tag. Created by Dr. Uris Ros by exchanging the EGFP of pEGFP-N2 with mCherry.
  - **pSpCas9(BB)-2A-Puro (pX459)**: Vector with human codon-optimized SpCas9 chimeric to a clonable site for guide sequences. Purchased from AddGene. Selection via puromycin resistance gene
- **Mitochondrial compartment markers**
  - **EGFP-TMB-x-BclxL**: EGFP fused to the transmembrane C-terminal domain of human BclxL. Gift from Prof. Dr. Christoph Borner (University of Freiburg)
  - **mito-GFP**: GFP with an N-terminal signaling sequence of the subunit VIII of cytochrome c oxidase. Targets mitochondrial inner membrane. Gift from Dr. Nathan Brady (DKFZ, Heidelberg)
  - **pEGFP-N1-SOD2**: Human superoxide dismutase 2 with C-terminal EGFP tag. Gift from Prof. Dr. J. Andres Melendez (State University of New York, Albany, NY)
  - **mito-GFP-mCherry**: mitochondrial targeting GFP-mCherry fusion. Cloned mito-GFP sequence into pmCherry-N2
- **Bcl-2 proteins**
  - **BclxL-GFP**: human BclxL fused to GFP. Gift from PD. Dr. Frank Essmann (University of Tübingen)

  - **pmCherry-BclxL**: human BclxL cloned to pmCherry-C. Gift from Dr. Nathan Brady (DKFZ, Heidelberg)
  - **pEGFP-tBid**: human truncated Bid cloud to pEGFP-C. Gift from Dr. Nathan Brady (DKFZ, Heidelberg)

- **Translocase**: Constructs were cloned by Fabronia Murad using the Gateway® LR Recombination reaction. EGFP-N or TagRFP-N were used as destination vectors.
  - TOMM20-GFP
  - TOMM20-TagRFP
  - TOMM40-GFP
  - TOMM40-TagRFP
  - TOMM70A-GFP
  - TOMM70A-TagRFP
  - TIMM23-GFP
  - TIMM23-TagRFP

- **Succinyl Dehydrogenase**: Constructs were cloned by Fabronia Murad using the Gateway® LR Recombination reaction. EGFP-C or TagRFP-C were used as destination vectors.
  - SDHA-GFP
  - SDHA-TagRFP
  - SDHC-GFP
  - SDHC-TagRFP
  - SDHD-GFP
  - SDHD-TagRFP

- **pX459-BclxL-gs**: pX459 vector cloned with BclxL guide sequences at the BbsI cutting site.

Primers for cloning

Table 5.5 shows the primers used to add linkers at the end of mito-GFP via site-directed mutagenesis. Table 5.6 shows the primers used for cloning mitoGFP to pmCherry-N2.

Table 5.5: Primers for Addition of Linkers to mito-GFP via site-directed mutagenesis

Name	Sequence (5' - 3')
Short Linker-noRS-Fwd	GGTGCCGCGCAAAGCGGCCGCGACTCTA
Short Linker-noRS-Rev	AGGCTGCCGCGCTTGTACAGCTCGTCCATGC
Long Linker-noRS-Fwd	CCTGGTGCCGCGCGGCAGCGCGAGCAAAGC GGCCGCGACTCTA
Long Linker-noRS-Rev	CCGCCGCCGCCGCTCGCGCTGCCGCGCTTG TACAGCTCGTCCATGC

Table 5.6: Primers for Cloning mito-GFP-Linker constructs to pmCherry-N2

Name	Sequence (5' - 3')
mitoGFP-XhoI-Fwd	TGCTGAGGTACCATGTCCGTCCTGACGCCGCT
mitoGFP-noL-SmaI-Rev	TAAGATCCCGGGTACTTGTACAGCTCGTCCAT
mitoGFP-SL-SmaI-Rev	TAAGATCCCGGGTAGCGCGGCACCAGGCTG
mitoGFP-LL-SmaI-Rev	TAAGATCCCGGGTAGCTCGCGCTGCCGCGC

noL - No Linker, SL - Short Linker, LL - Long Linker
underlined sequences are the restriction sites for the indicated enzymes in the name of the primers

Guide Sequences for CRISPR/Cas9

Table 5.7 shows the guide sequences targeting mouse BclxL used in generating the Bid BclxL double knockout mouse embryonic fibroblasts (DKO MEF).

Table 5.7: Guide Sequences for CRISPR/Cas9

Name	Sequence (5' - 3')
BclxL 1	Forward: CACCGAAAGTCGACCACCAGCTCC
	Reverse: AAACGGAGCTGGTGGTCGACTTTC
BclxL 2	Forward: CACCGTCACGGCCGGGCTATCCGCC
	Reverse: AAACGGCGGATAGCCCGGCCGTGAC
BclxL 3	Forward: CACCGTCTCAGAGCAACCGGGAGC
	Reverse: AAACGCTCCCGGTTGCTCTGAGAC
BclxL 4	Forward: CACCGCGGATAGCCCGGCCGTGAA
	Reverse: AAACTTCACGGCCGGGCTATCCGC

underlined sequence shows the overhangs that recognize BbsI digested plasmids.

5.1.5 Biological Material

Bacterial Cells

- DH5α *E. coli* strains were used to propagate all plasmids except pDEST26-based *ccd*B gene-containing plasmids.
- BL21-RIPL *E. coli* strain was used to express full length human Bax and mouse Bid for further purification.
- One Shot®*ccd*B Survival$^{\text{TM}}$2 $T1^{R}$ Competent Cells from Invitrogen were used to propagate pDEST26-based *ccd*B gene-containing plasmids (EGFP-C, EGFP-N, TagRFP-C and TagRFP-N)

Mammalian Cells

- Human cervical epithelial adenocarcinoma cells (HeLa) cells
- SV40 Immortalized BclxL knockout mouse embroyinc fibroblasts (BclxL KO MEFs) were a gift from Dr. Andreas Villunger (Innsbrück Medical University)
- Bid knockout mouse embroyinc fibroblasts (Bid KO MEFs) were a gift from Dr. Klaus Schulze-Osthoff (Universität Tübingen)
- Bid BclxL double knockout mouse embryonic fibroblasts (Bid BclxL DKO MEFs) were generated by Fabronia Murad using the CRISPR/Cas9 system from Bid KO MEFs

5.1.6 Software

Proprietary software from the manufacturer were used for laboratory instruments. Table 5.8 lists software used for data analysis.

Corel Draw X6 and Adobe Photoshop was used for figure layout and editing. ChemSketch was used for making chemical structures,

MS Word, Excel, Powerpoint, and OneNote (MS Office 2013 for Windows and 2011 for Mac), Adobe Acrobat Reader, and EndNote X6 were used in numerous tasks for this study.

The thesis was prepared and typeset in LaTeX (TeXShop for Mac and TeXworks for Windows)

Table 5.8: Software for Data Analysis

Experiment	**Software**	**Notes and Manufacturer**
Fluorescence Microscopy	ZEN software	Carl Zeiss, Inc.
	ImageJ	`http://fiji.sc/Fiji`
Atomic Force Microscopy	JPK Data Processing Software	JPK
	Customized software written by Eduard Hermann (AFM Force Analyzer)	MatLab (Mathworks Inc.)
Fluorescence Correlation Spectroscopy	ZEN software for online analysis	Carl Zeiss, Inc.
	Fluctuation Analyzer 4G for solution FCS in cells	Malte Wachsmut `http://www.embl.de/~wachsmut/downloads.html`
	Customized software written by Jonas Ries (FCSFit, SFCS) and scripts written by Joseph Unsay	MatLab (Mathworks Inc.)
Particle-based Simulations	Smoldyn 2.39	Steve Andrews `http://www.smoldyn.org/`
DNA Sequences	A plasmid Editor (ApE)	M. Wayne Davis `http://biologylabs.utah.edu/jorgensen/wayned/ape/`
Graphing and Statistical Analysis	Origin Pro	OriginLab
	GraphPad Prism 6	GraphPad Software
Online tools	NCBI-Blast	National Center for Biotechnology Information `http://blast.ncbi.nlm.nih.gov/Blast.cgi`
	MyGATC	`https://www.gatc-biotech.com/de/index.html`

Continued on next page

Table 5.8 – continued from previous page

Experiment	Software	Notes and Manufacturer
	NEB Double Digest Finder	New England Biolabs `https://www.neb.com/tools-and-resources/interactive-tools/double-digest-finder`
	NEB Tm Calculator	New England Biolabs `http://tmcalculator.neb.com/`
	NEBaseChanger	New England Biolabs `http://nebasechanger.neb.com/`
	Promega BioMath Calculators	`http://www.promega.com/a/apps/biomath/`
	E-CRISPR	Michael Boutros `http://www.e-crisp.org/E-CRISP/index.html`
	CRISPR Design	Feng Zhang `http://crispr.mit.edu/`

5.2 General Biochemistry Methods

5.2.1 Plasmid Propagation

Plasmids were electrotransformed to 50-μL aliquots DH5α cells or One Shot®*ccd*B Survival^{TM}2 $T1^R$ Competent Cells. The cells were allowed to grow in 2 mL of LB Media for 1 hour. The cells were then plated in LB Agar plates containing appropriate antibiotics and incubated overnight at 37°C.

Single colonies were picked and grown on 25 mL of LB media with appropriate antibiotics at 37°C for 12 hours. From the culture, 2 mL was used to prepare glycerol stocks by adding 2 mL of glycerol and flash freezing in liquid nitrogen. Stocks were stored at -80°C. The remaining culture was used to purify plasmids using E.Z.N.A® HP Plasmid Mini Kit (Omega). The plasmids were stored at -20°C.

5.2.2 Mammalian Cell Culture

Maintenance

HeLa cells were cultured in DMEM with 10% fetal calf serum, 1% penicillin and streptomycin (full media) at 37°C and in the presence of 5% CO_2. All cells were regularly passaged at subconfluence. Cell lines were screened to be mycoplasma free and were passaged to a maximum of 50 passages.

Transient Transfection

About 10,000 to 12,000 HeLa cells per well were seeded in 8-well Nunc^{TM}Lab-Tek^{TM} chambered coverglass, 24 hours before transfection. Transfection solution was prepared

directly before transfection by mixing Lipofectamine®2000 (Life Technologies, Inc) (about 0.25 to 0.5 μL per well) with appropriate amount of plasmids (between 10-50 ng per well) and dissolved in Opti-MEM®(Life Technologies, Inc). Transfection solution was then added to cells in full media and incubated 24 hours more at 37°C and in the presence of 5% CO_2. Directly before microscopy, media was replaced with Air Buffer.

Preparation of Cells for Western Blotting

Cells (250,000 cells) for western blot analysis were seeded on 6-well plates and grown until confluent. Cells were trypsinized and washed twice with cold PBS. Cell pellet was then incubated in 50-100 μL RIPA buffer for 30 mins and centrifuged for 30 mins at 14000 rpm at 4°C. The supernatant was collected and stored at -20°C until needed.

Total protein concentration of the cell lysates were measured using the Bradford Assay. A 1:5 dilution of the cell lysates were used for the Bradford Assay to fall within the calibration range of the assay.

Cell lysates were then subjected to SDS-PAGE to separate the proteins (see section 5.2.4). Around 10-20 ng of total protein was loaded per well.

Generation of Stable mito-GFP Expressing Cell Lines

HeLa cells (approx. 500,000 cells) were plated on a 10-cm dish on full media. After 24 hours, the cells were transfected with 2500 ng mito-GFP and 3 μL Lipofectamine®2000 (Life Technologies, Inc) dissolved in Opti-MEM®(Life Technologies, Inc). After 24 hours of the transfection, the media was exchanged for full media + 500 $\mu g/mL$ Geniticin®. Antibiotic selection was carried out for 14 days. The cells were transferred and split to bigger dishes as needed. After antibiotic selection and the cells were sorted for GFP-containing cells using a BD FACS Aria at the Universitätsklinikum Tübingen FACS Core Facility. Single colonies were isolated from the sorted cells.

Generation of Bcl-xL/Bid double knock out MEFs

Guide sequences for the target proteins were constructed according to Ran et al. (2013) using the online E-CRISP tool (http://www.e-crisp.org/E-CRISP/index.html) (Heigwer et al., 2014). The guide sequences were annealed and then ligated to BbsI-digested pX459 plasmids. To generate the Bid BclxL DKO MEFs, Bid KO MEFs were transfected with the pX459 containing guide sequences to Bcl-xL (px459-BclxL-sg). After 24 hours of transfection, the media was exchanged for full media + 400 mg/mL Geniticin, and antibiotic selection was carried out for at least 14 days. Single colonies were generated after antibiotic selection and these were subjected to Western Blot to confirm the knockout of Bcl-xL.

5.2.3 Cloning

Cloning Mitochondria-targetting GFP-mCherry fusion consruct

Mitochondrial targeting-GFP-mCherry (mito-GFP-mCherry) fusion construct was made by inserting the mito-GFP sequence from the mito-GFP plasmid into a pmCherry-N2 plasmid. The pmCherry-N2 plasmid was constructed by exchanging the EGFP of a pEGFP-N2 plasmid with mCherry. Linker sequences were also added in between mito-GFP and mCherry to facilitate folding of individual fluorescent proteins (Albertazzi et al., 2008).

Using site-directed mutagenesis, a linker sequence was inserted after mito-GFP (See Table 5.5). The mito-GFP-linker sequence was PCR amplified to contain flanking XhoI (5') and SmaI (3') restriction sites (See Table 5.6). PCR was done using the Q5 High

Fidelity PCR Kit on a BioRad MyCycler Personal Thermal Cycler. The mCherry plasmid and PCR insert were digested using XhoI and SmaI. The mCherry plasmid was further treated with Shrimp Alkaline Phosphatase (rSAP) to prevent re-ligation of the plasmid. Ligation of plasmid and insert was done using T4 DNA ligase at 16°C overnight. The ligation reaction was electrotransformed into DH5α cells and plasmids were harvested from a single clone.

Gateway® Cloning

Using Gateway®compatible plasmids, fluorescent protein fusion constructs with desired human proteins were constructed. Destination vectors contain the LR homologous recombination sites before or after the fluorescent proteins. Destination vectors may only be propagated in One Shot®*ccd*B Survival^{TM}2 $T1^R$ Competent Cells because they contain the *ccd*B gene, which is toxic to usual strains like DH5α. Entry clones contain the gene of interest between LR homologous recombination sites.

The reaction mixture was composed of 150 ng of destination vector and 50-150 ng of entry clone dissolved in TE Buffer (10 mM Tris, 1 mM EDTA, pH 8) to a final solution volume of 8 μL. Gateway® LR Clonase® II enzyme mix (2 μL) was added to the reaction mixture. The mixture was vortexed and the reaction was allowed to proceed at 25°C for 1 hour. Proteinase K solution (1 μL) was added to the mixture and incubated for 10 min at 37°C.

The whole reaction mixture is then transformed to electro-competent DH5α cells using the Micropulser (Bio-Rad) and processed as in section 5.2.1. A successful reaction would yield about >5000 colonies if the whole reaction is transformed and plated. Unsuccessful reaction would mean the *ccd*B gene is still intact and would thus kill the DH5α cells

5.2.4 Electrophoresis

Agarose Gel

Agarose gel electrophoresis was used to separate and visualize DNA. To prepare agarose gels, 1% (w/v) agarose in 50 mL TAE buffer was boiled using a microwave oven. The solution was cooled to around 70°C and 5 μL of GelRed^{TM}(1:10,000) was added and mixed. The solution was poured into casting molds while clearing out any bubbles. The gel was then placed in Sub-Cell®GT Agarose Gel Electrophoresis system (Bio-Rad) and submerged under TAE buffer. Samples prepared with DNA gel loading buffer (6x, Thermo Fisher Scientific) were then loaded in to the wells. The gel was run at 120V for 30 min. DNA bands were visualized using a gel documentation system (UV-Systeme, Intas,)

SDS-PAGE

SDS-PAGE was used to ascertain the quality of purified proteins as well as an initial separation step before immunoblotting.

To prepare one 1.5 mm-gel composed of 12% resolving gel and 5.4% stacking gel, the components were mixed according to Table 5.9. The resolving gels were prepared first by pouring the solution onto casting slides until 2 cm from the top, followed by an isopropanol overlay. These were allowed to set for at least 45 min. The isopropanol was removed and the top of the gels were washed with water and dried. The stacking gel solution was then layered on top, bubbles were removed and a 10- or 15-well comb was placed. The gels were allowed to set for at least 30 min.

Protein samples were mixed with 6x SDS sample buffer for a final 2X buffer concentration. Samples were boiled for 5 mins at 95°C shaking in a thermomixer, then cooled

Table 5.9: SDS-PAGE Gel Recipes

Component	Volume
12% Resolving Gel	
H_2O	4.2 mL
30% acrylamide/bis-acrylamide, 29:1 (3.3% crosslinker) solution	4.8 mL
Lower Tris buffer (4x)	3 mL
10% APS	80 μL
TEMED	10 μL
5.4% Stacking Gel	
H_2O	2.72 mL
30% acrylamide/bis-acrylamide, 29:1 (3.3% crosslinker) solution	0.96 mL
Upper Tris buffer (4x)	1.6 mL
10% APS	40 μL
TEMED	3 μL

on ice for another 5 min. The samples were run using a Mini-PROTEAN®Tetra Vertical Electrophoresis Cell (Bio-Rad) at 80V for about 15 min, then 120V for about 75-90 min.

The gels were then either used for immunoblotting or visualized directly. To stain, the gel was immersed on a low toxicity staining solution for at least 1 hr with shaking and destained until the blue background faded (destaining solution was changed three to four times). Gels were documented using a computer scanner.

Western Blotting

Proteins from SDS-PAGE were transferred to polyvinylidene fluoride (PVDF) membranes (GE Healthcare) by semi-dry blotting on a Trans-Blot Turbo Blotting System (Bio-Rad). Freshly run gels were incubated in Cathode buffer for 10 mins to remove SDS. PVDF membrane was activated using methanol (2 min incubation) and then washed and left on Anode II buffer. 2 sheets of chromatography papers (Whatman) were immersed in Anode I buffer, 1 sheet was immersed in Anode II buffer and 3 sheets were immersed in Cathode buffer. The gels, membrane and papers were assembled on the transfer cassette as follows (from bottom to top): 2 sheets in Anode I buffer, 1 sheet in Anode II buffer, PVDF membrane, Gel, 3 sheets in Cathode buffer (Figure 5.1). The transfer was done at 25V, 1 A, for 30 mins ("Standard SD" program of the Trans-Blot Turbo Blotting System).

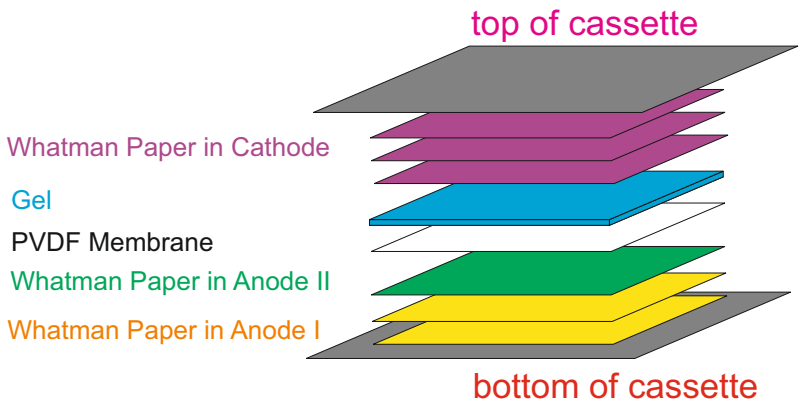

Figure 5.1: Set-up for Trans-Blot Turbo Blotting System

After transfer, the membrane was labeled and washed with water and placed in membrane-blocking buffer, shaking at room temperature for 30 mins. The membrane was incubated with primary antibody (5 mL, 1:1000 dilution in membrane-blocking buffer) with shaking at 4°C overnight. The following day, the membrane is washed with TBST three to four times for 10 minutes each, with shaking at room temperature. The membrane is then incubated with the secondary antibody (10 mL, 1:10,000 dilution in membrane-blocking buffer). The membrane was washed five times with TBST for 10 minutes each, with shaking at room temperature.

The membrane is then placed on a developing cassette with plastic foil and about 1 mL of the chemiluminiscence substrate (Western Ligtning®Plus, Perkin Elmer) was added. The blots were imaged using the Fusion FX (Vilber Gourmet).

5.2.5 Protein Purification

Full length human Bax and mouse Bid were expressed in BL21-RIPL *E. coli* and purified according to (Bleicken et al., 2010) and (Desagher et al., 1999), respectively. Cells were homogenized using the cell disruptor, Emulsiflex-C5 (Avestin). Protease inhibitors and DNAse were added to the homogenate and then centrifuged at 17,000 rpm at 4 °C to remove cell debris and inclusion bodies.

Bax was purified using affinity chromatography via the intein/chitin-binding-domain tag. Cell lysates were passed through a column made of chitin resin. The chitin resin was then incubated with 0.1 mM DTT in Chitin Buffer overnight at 4 °C to facilitate self-cleavage of the intein and release of Bax from the chitin beads. Bax was then eluted with Chitin buffer and further purified using anion exchange chromatography via the ÄKTA FPLC System (GE Healthcare). Bax was then dialysed against Smart A buffer to remove salt.

Bid was purified using affinity chromatography via the 6xHis tag. Cell lysates were mixed with Ni-NTA Agarose for 2 h at 4°C. The resin was washed with Nickel A buffer to remove unbound particles. Nickel B buffer (with Imidazole) was used to elute Bid from the resin. Bid was then dialyzed overnight against Smart A buffer to remove the imidazole. Full length mouse Bid was cleaved *in vitro* using caspase 8 in cleaving buffer for n min.

Protein quality was checked using SDS-PAGE and activity was assessed using calcein release assays. Purification was done by Carolin Stegmüller and Dr. Stephanie Bleicken.

5.3 Model Membranes

5.3.1 Calcein Release Assay

Dried lipid mixtures were suspended in 80 mM calcein solution to a concentration of 4 mg/mL. The lipid suspension was transferred to a cryogenic tube and subjected to at least 10 freeze-thaw cycles using liquid nitrogen. Lipid suspension was then extruded 31 times through 200-nm polycarbonate filter to obtain large unilamellar vesicles (LUV). They can be stored at 4°C for 1-2 days. Block the black 96-well plates with 100 μL BSA (10 mg/mL) for at least 1 hour and wash with ddH_2O. To separate LUVs from free calcein, run the liposome solution through a desalting column (PD 10, GE Healthcare), collecting 100-μL fractions in the process. Take the first orange fraction (Frac N) and 5 more before it (Frac N-1, Frac N-2, Frac N-3, Frac N-4, and Frac N-5 respectively). Make a 1:10 dilutions for each fraction by taking 100 μL and diluting it with 900 μL OB. Make 1:2000 dilutions for each fraction by taking 75μL from the 1:10 dilution and fill up to 15 mL with OB. Make 1:10,000 dilutions for each fraction by taking 1 mL from the 1:2000 dilution and fill up to 5 mL with OB.

To test which fraction and dilution is most appropriate for the calcein assay, run a test sample. To two rows of 96-well plate add 150 μL outside buffer. To one of the rows containing outside buffer, add an 10 μL of 5% Triton. Add 50μL of each liposome fraction-dilution combination to two wells: one to a well with Triton and another to a well without Triton. Measure the calcein fluorescence for each well using a plate reader. The appropriate fraction-dilution combination should have a 4x increase in fluorescence reading between the well without Triton and the well with Triton.

After selecting the proper fraction-dilution combination, add 100 μL OB to each well to be used for the kinetic experiment. Add enough protein for each well to reach a desired concentration (note that the final volume will be 200 μL). Dilute in enough OB to reach 150 μL total volume. On one well add 150 μL OB to serve as the negative control. To another well add 100 μL of OB and 50 μL 5% Triton to serve as the positive control. To each well including controls, add 50 μL of liposome solution. For room temperature kinetic experiment, the plate was left and calcein fluorescence was measured every 2 minutes for 2 hours. For elevated temperature kinetic experiment, plates were wrapped in aluminum foil and incubated at desired temperature, fluorescence was measured every 15 minutes for 2 hours. At the end of the experiment, add 10 μL 5% Triton to get the maximum amount of fluorescence for each well.

5.3.2 Lipid Packing Assay

Dried lipid mixtures containing 0.5 mol% Merocyanine 540 (MC540) were resuspended in SLB buffer to a concentration of 1 mg/mL. LUVs were prepared as in Section 5.3.1. An aliquot containing 0.1 mg of total lipids was then transferred to a glass cuvette and filled to capacity (900 μL).

LUVs were incubated with 20 nM cBid or 50 nM of Bax for 1 h at room temperature. Additionally, LUVs with Bax were incubated at 43°C to activate Bax. MC540 fluorescence was measured in glass cuvettes using a Jasco Spectrofluorometer FP 8300. MC540 was excited at 495 nm and an emission sweep was measured between 540 to 660 nm with a 1-nm bandwidth.

Four to five independent measurements were acquired for all conditions. The emission peak at 585 nm was used to compare the different conditions. These experiments were performed by a master's student Katharina Sporbeck under my supervision.

5.3.3 Preparation of Supported Lipid Bilayers

Dried lipid mixtures were suspended in PBS to a concentration of 10 mg/mL. The suspension was distributed to 10-μL aliquots, which can be stored at -20°C. To one 10-μL aliquot, 140 μL of SLB buffer was added. This was then extruded using 200-nm polycarbonate membrane to form LUVs or bath sonicated for 10 minutes until the suspension becomes clear to produce SUVs.

LUVs were incubated with proteins at desired concentration (50 nM for Bax, and 20 nM for cBid) and temperatures (room temperature or 43°C).

(Proteo-)Liposome solutions were deposited on freshly cleaved mica (or directly to coverslip surface for FCS). Calcium chloride was added to a final concentration of 3 mM and incubated at 37°C for 10 minutes. SLBs were washed with SLB buffer 20x, taking care avoid exposing the surface to air. The SLBs were cooled down to room temperature before microscopy.

5.4 Atomic Force Microscopy

5.4.1 Imaging

SLBs were imaged using a JPK NanoWizard II system (JPK Instruments, Berlin, Germany) mounted on an Axiovert 200 Inverted Microscope (Carl Zeiss). Intermittent contact (IC or tapping) mode images were taken using V-shaped silicon nitride cantilevers with a typical spring constant of 0.08 N/m. Bruker DNP-10 (nominal tip radius 40 nm) was used for routine imaging before force spectroscopy and Bruker SNL-10 (nominal tip radius 2 nm) was used to achieve higher resolution. The cantilever oscillation was tuned to a frequency between 3-10 kHz, and the amplitude was set between 0.2-0.5 V. The amplitude was varied during the experiment to minimize the force of the tip on the bilayer. The scan rate was set to 0.7-1 Hz. The height, deflection and phase-shift signals were collected, simultaneously, in both trace and retrace directions. Bilayer thickness was measured based on the height profiles from the mica (membrane defects) to the membrane bulk.

5.4.2 Force Spectroscopy

The calibration of sensitivity, resonance frequency, and effective spring constant (via the thermal noise method) of the cantilever were performed before each experiment. The total z-piezo displacement was set to 400 nm and the indenting speed was set to 800 nm/s for the approach and 200 nm/s for the retraction. A 5 μm x 5 μm area was selected after imaging. This area was divided in a 16 x 16 grid, and a force curve was acquired for each position (total of 256 curves per area of interest). All experiments were carried out at different positions of the bilayer under the same conditions, so that the effect of the speed of the breakthrough could be neglected. Force curves were processed using the accompanying JPK processing software. We applied a smoothing function, baseline correction and tip-sample separation correction to the force curves to give accurate thickness and force measurements.

5.5 Confocal Microscopy

Samples were imaged using a commercial LSM 710 (Carl Zeiss, Jena, Germany) at 25°C. The excitation light of a helium-neon laser at 633 nm, a DPSS laser at 561 nm or of an argon laser at 488 nm was reflected by a dichroic mirror (MBS 488/561/633) and focused through a Zeiss C-Apochromat 40x, NA = 1.2 water immersion objective onto the sample. The fluorescence emission was collected by the objective and directed by spectral beam guides to photomultiplier tube detectors. Unless specified, the pinhole was set to only let 1 airy unit of emission from the sample to pass through.

5.5.1 Fluorescence Recovery After Photobleaching

Using the set up for confocal microscopy (using only the Argon 488-nm laser), the pinhole was fully opened to collect all the fluorescence emission and compensate for mitochondria movement. The spectral beam guides were set to collect emission from 505-600 nm. For whole cell FRAP, areas of interest were bleached using 100% laser power and intensity was recorded every second. For single mitochondria FRAP, areas of interest were bleached using 75% laser power (Argon, 488 nm) and intensity was recorded every 120 ms for at least 30s. Recovery curves were fitted with a single exponential to acquire half time and mobile fraction.

Diffusion coefficients were calculated according to (Mitra and Lippincott-Schwartz, 2010):

$$D = \frac{r_{bleach}^2}{t_{1/2}} \tag{5.1}$$

where r_{bleach} is the radius of the circular bleach region and $t_{1/2}$ is the fitted half time of the recovery.

5.5.2 Förster Resonance Energy Transfer through Acceptor Photobleaching

For FRET experiments, the microscope set up similar to FRAP was used. Time lapse images were collected every 120 ms, using the Argon 488-nm laser for excitation. The spectral beam guides were set to collect emission from 505-540 nm (GFP Channel) and from 580-650 nm (mCherry Channel). Intensities from 20 frames from each channel for the pre-bleaching step and post-bleaching steps were averaged. The FRET efficiency was calculated based on the donor GFP fluorescence intensity:

$$\%FRET = \frac{(I_{GFP,post-bleach} - I_{BG}) - (I_{GFP,pre-bleach} - I_{BG})}{I_{GFP,post-bleach} - I_{BG}} \tag{5.2}$$

where $\%FRET$ is the FRET efficiency. I are fluorescence intensities of the following: $GFP, pre-bleach$ = GFP channel before bleaching, $GFP, post-bleach$ = GFP channel after bleaching, BG = background.

5.6 Fluorescence Correlation Spectroscopy

FCS experiments were conducted at 25°C using the same microscope setup described above. The photons from the fluorescence emission were directed to avalanche photodiodes of the ConfoCor3 module (Carl Zeiss, Inc.).

5.6.1 Microscope Calibration

The microscope was calibrated before every experiment using dilute solutions of fluorescent dyes: Alexa-488 (D = 435 $\mu m^2/s$) for dyes excited by the 488-nm Argon laser. Rhodamine B (D = 450 $\mu m^2/s$) for dyes excited by the 561-nm DPSS layer, and Alexa 633 (D = 340$\mu m^2/s$) for dyes excited by the 633 HeNe laser. Fluctuation traces were acquired for 30 s. The ConfoCor 3 module was used for online correlation of the fluctuation traces and fitting with a 3D Free diffusion model:

$$G(\tau) = \frac{1}{N}\left(1 + \frac{\tau}{\tau_D}\right)^{-1}\left(1 + \frac{\tau}{\tau_D^2 SP}\right)^{-1/2} \tag{5.3}$$

where G(τ) is the autocorrelation function, N is the number of fluorescent particles in the detection volume, τ is the lag time, SP is the structure parameter (aspect ratio) of the Gaussian detection volume, and τ_D is the diffusion time (i.e., the average time a particle spends in the detection volume).

The siye of the confocal volume characterized by the waist radius of the detection volume, ω_0 and its extention to the optical axis, $\omega_z (= SP * \omega_0)$ are calculated from the literature values of diffusion coeffcient and the fitted values for the diffusion time and the structure parameter using:

$$D = \frac{\omega_0^2}{4\tau_D} \tag{5.4}$$

5.6.2 FCS of Supported Lipid Bilayers

Photon detection was carried out with the avalanche photodiodes of the ConfoCor3 module, which were also used for online correlation of the fluorescence intensity trace. Data analysis was performed with software written in MATLAB (MathWorks). The autocorrelation curves were fitted with a 2D diffusion model with elliptical Gaussian detection (equation 5.5) using a nonlinear least-squares fitting algorithm

$$G(\tau) = \frac{1}{N}\left(1 + \frac{\tau}{\tau_D}\right)^{-1} \tag{5.5}$$

where ω_0 is the waist radius of the focal volume obtained from calibration measurements and τ_D is the diffusion time of the dye derived from autocorrelation curves.

5.7 Scanning Fluorescence Correlation Spectroscopy of Mitochondria of Living Cells

SFCS experiments were conducted at 25°C using the same microscope setup described above. Avalanche photodiodes of the Confocor3 module were used to detect photons, and photon arrival times were recorded using a hardware correlation Flex02-01D (http://correlator.com).

5.7.1 Two Focus Fluorescence Cross Correlation Spectroscopy

For two focus FCCS, the detection volume was repeatedly scanned with two lines perpendicular to the mitochondria. The distance d, was measured by photobleaching on a film of dried fluorophore. Each scan time was 1.89 ms.

5.7.2 Two Color Fluorescence Cross Correlation Spectroscopy

For two color FCCS, the detection volume was repeatedly scanned with a single line perpendicular to the mitochondria with alternating excitation lines (488 and 561 nm). Each scan time was 1.53 ms.

5.7.3 Data Analysis of SFCS

Using software created in MatLab, We binned the photon stream in 2 μs and arranged it as a matrix such that every row corresponded to one line scan. From this, the signal from two foci can be isolated (for two focus FCCS) or the spectral crosstalk and bleed through can be removed (for two color FCCS). We corrected for mitochondria movements by calculating the maximum of a running average over several hundred line scans and shifting it to the same column. We fitted an average over all rows with a Gaussian and we added only the elements of each row between 2.5σ and -2.5σ to construct the intensity trace. Photobleaching was also corrected according to **REF**. The intensity traces were autocorrelated and cross-correlated, and these traces were fitted with different model functions.

5.7.4 Derivation of Dissociation Constant from Two-Color FCS

The dissociation reaction of a complex to two species is given by the chemical reaction:

$$\mathrm{AB} \rightleftharpoons \mathrm{A} + \mathrm{B} \tag{5.6}$$

This equilibrium is described by the dissociation constant (K_d)

$$K_d = \frac{[\mathrm{A}]\,[\mathrm{B}]}{[\mathrm{AB}]} \tag{5.7}$$

In FCS, species A and B are labeled with fluorophores, however, the degree of labelling is always less than 100% (because incomplete reactions) and therefore a labelling correction must be implemented. In cells, fluorescent proteins are often used, and the degree of labelling depends on the maturation efficiency of the fluorescent protein and the amount of endogenous proteins in the cell. It is possible to remove or minimize the levels of endogenous proteins by knocking out our knocking down their expression. In this, the degree of labelling is now only dependent on the maturation efficiency of the fluorescent protein.

In the following example, A is labeled with a red fluorophore (A_R) and B is labeled with a green fluorophore (B_G). Unlabelled species will have a subscript of 0 (A_0 and B_0). Therefore the possible combinations for the complex include a doubly-labeled species ($A_R B_G$), two possible singly-labeled species ($A_0 B_G$ and $A_R B_0$) and a species without any labels ($A_0 B_0$).

To calculate for the K_d, we need to know the total concentration of unbound A ($[A]_t$), unbound B ($[B]_t$) and the complex ($[AB]_t$). These can be expressed as sums of the labeled and unlabelled species:

$$[A]_t = [A_0] + [A_R] \tag{5.8}$$
$$[B]_t = [B_0] + [B_G] \tag{5.9}$$
$$[AB]_t = [A_R B_G] + [A_0 B_G] + [A_R B_0] + [A_0 B_0] \tag{5.10}$$

If the degree of labeling for A is x and that for B is y, the total unbound species ($[A]_t$, and $[B]_t$) can be calculated if we know the concentration of the labeled unbound species ($[A_R]$ and $[B_G]$).

$$[A]_t = \frac{[A_R]}{x} \tag{5.11}$$
$$[B]_t = \frac{[B_G]}{y} \tag{5.12}$$

We can also derive a probability for each of the complex species that we have:

$$[A_R B_G] = (x)(y) * [AB]_t \tag{5.13}$$
$$[A_0 B_G] = (1-x)(y) * [AB]_t \tag{5.14}$$
$$[A_R B_0] = (x)(1-y) * [AB]_t \tag{5.15}$$
$$[A_0 B_0] = (1-x)(1-y) * [AB]_t \tag{5.16}$$

From these probabilities we can derive expressions of each species as a function of the doubly-labeled species.

$A_0 B_G$ expressed as $A_R B_G$:

$$\begin{aligned}
\frac{[A_0B_G]}{[A_RB_G]} &= \frac{(1-x)(y)*[AB]_t}{(x)(y)*[AB]_t} \\
\frac{[A_0B_G]}{[A_RB_G]} &= \frac{(1-x)y}{xy} \\
[A_0B_G] &= \frac{(1-x)y}{xy}[A_RB_G] \qquad (5.17)
\end{aligned}$$

A_RB_0 expressed as A_RB_G:

$$\begin{aligned}\frac{[A_RB_0]}{[A_RB_G]} &= \frac{(x)(1-y)*[AB]_t}{(x)(y)*[AB]_t}\\ \frac{[A_RB_0]}{[A_RB_G]} &= \frac{x(1-y)}{xy}\\ [A_RB_0] &= \frac{x(1-y)}{xy}[A_RB_G]\end{aligned} \tag{5.18}$$

A_0B_0 expressed as A_RB_G:

$$\begin{aligned}\frac{[A_0B_0]}{[A_RB_G]} &= \frac{(1-x)(1-y)*[AB]_t}{(x)(y)*[AB]_t}\\ \frac{[A_0B_0]}{[A_RB_G]} &= \frac{(1-x)(1-y)}{xy}\\ [A_RB_0] &= \frac{(1-x)(1-y}{xy}[A_RB_G]\end{aligned} \tag{5.19}$$

From the autocorrelation curves of FCS measurements, we get the concentration of all the red particles $[R]_t = N_R/V_{eff}$, and all the green particles $[G]_t = N_G/V_{eff}$. This is related to the different species by means:

$$[R]_t = [A_R] + [A_RB_0] + [A_RB_G] \tag{5.20}$$
$$[G]_t = [B_G] + [A_0B_G] + [A_RB_G] \tag{5.21}$$

From the cross correlation curve and subsequent calculation of the % cross correlation (CC), we can derive $[A_RB_G]$.

$$\%CC_R = \frac{G_{RG}(0)}{G_R(0)} = \frac{[A_RB_G]}{[G]_t}, \%CC_R = \frac{G_{RG}(0)}{G_G(0)} = \frac{[A_RB_G]}{[R]_t} \tag{5.22}$$

Once we have $[A_RB_G]$, we can use it to calculate the different parameters needed to calculate K_d.

Using Equations 5.20 and 5.18, we can calculate $[A_R]$.

$$\begin{aligned}[A_R] &= [R]_t - [A_RB_0] - [A_RB_G]\\ [A_R] &= [R]_t - \frac{x(1-y)}{xy}[A_RB_G] - [A_RB_G]\\ [A_R] &= [R]_t - \frac{x(1-y)+xy}{xy}[A_RB_G]\\ [A_R] &= [R]_t - \frac{x-xy+xy}{xy}[A_RB_G]\\ [A_R] &= [R]_t - \frac{x}{xy}[A_RB_G]\end{aligned} \tag{5.23}$$

Using Equations 5.21 and 5.17, we can calculate $[B_G]$.

$$
\begin{aligned}
[B_G] &= [G]_t - [A_0B_G] - [A_RB_G] \\
[B_G] &= [G]_t - \frac{(1-x)(y)}{xy}[A_RB_G] - [A_RB_G] \\
[B_G] &= [G]_t - \frac{(1-x)y + xy}{xy}[A_RB_G] \\
[B_G] &= [G]_t - \frac{y - xy + xy}{xy}[A_RB_G] \\
[B_G] &= [G]_t - \frac{y}{xy}[A_RB_G] \qquad (5.24)
\end{aligned}
$$

Using the result of equation 5.23 into equation 5.11, gives $[A]_t$. Using the result of equation 5.24 into equation 5.12 gives $[B]_t$. Equation 5.13 is used to calculate $[AB]_t$.

5.8 Particle-based Diffusion Simulations

Simulations of mitochondrial diffusion was done using Smoldyn. The mitochondria was modelled as a cylinder capped at the end with hemispheres with a diameter of 500 nm (Figure 5.2A). All surfaces were reflective, and the mitochondria length is 9 μm.

For diffusion inside the mitochondria, particles were randomly generated inside the compartment. For diffusion on the surface of the mitochondria, particles were randomly generated on the surface. Simulations were run with a step time of 1 ms, and a total time of 1500 to 2000 seconds depending on the simulated Diffusion coefficient. The simulated diffusion coefficients range from 0.1 to 10 $\mu m^2/s$, following initial fitting of the experimental data with the 2D Gaussian model.

For diffusion inside the mitochondria with cristae, barriers were placed along the length of the mitochondria(Figure 5.2B). The barrier size is 500 x 500 nm square on the y-z plan (perpendicular to the axis of the mitochondria). The barriers are 150 nm apart and are offset in the z-axis so that they are blocking 80% of the mitochondrial volume(Figure 5.2C-D). For example, at position (0, 0, 0), there is a barrier centered at (0, 0, 50) so that particles can pass through below this barrier. At position (150, 0, 0) and at (-150, 0, 0), there are barriers centered at (150, 0, -50) and (-150, 0, -50), respectively so that particles can pass through above these barrier. Looking from the y axis (x-z plane view), particles should move in a zigzag manner in order to traverse the length of the mitochondria.

The number of particles within a box of dimension 500 nm x 500 nm x 3000 nm which are equivalent to the dimensions of a confocal volume were counted for each time step to generate an intensity trace. The intensity trace was autocorrelated with a multi-tau algorithm in MatLab written by Jonas Ries. The resulting autocorrelation curves were fitted with different diffusion models. Particle count on a second box translated 500 nm in the x-axis was also recorded to simulate two-focus FCS.

Simulation codes are given in the appendix.

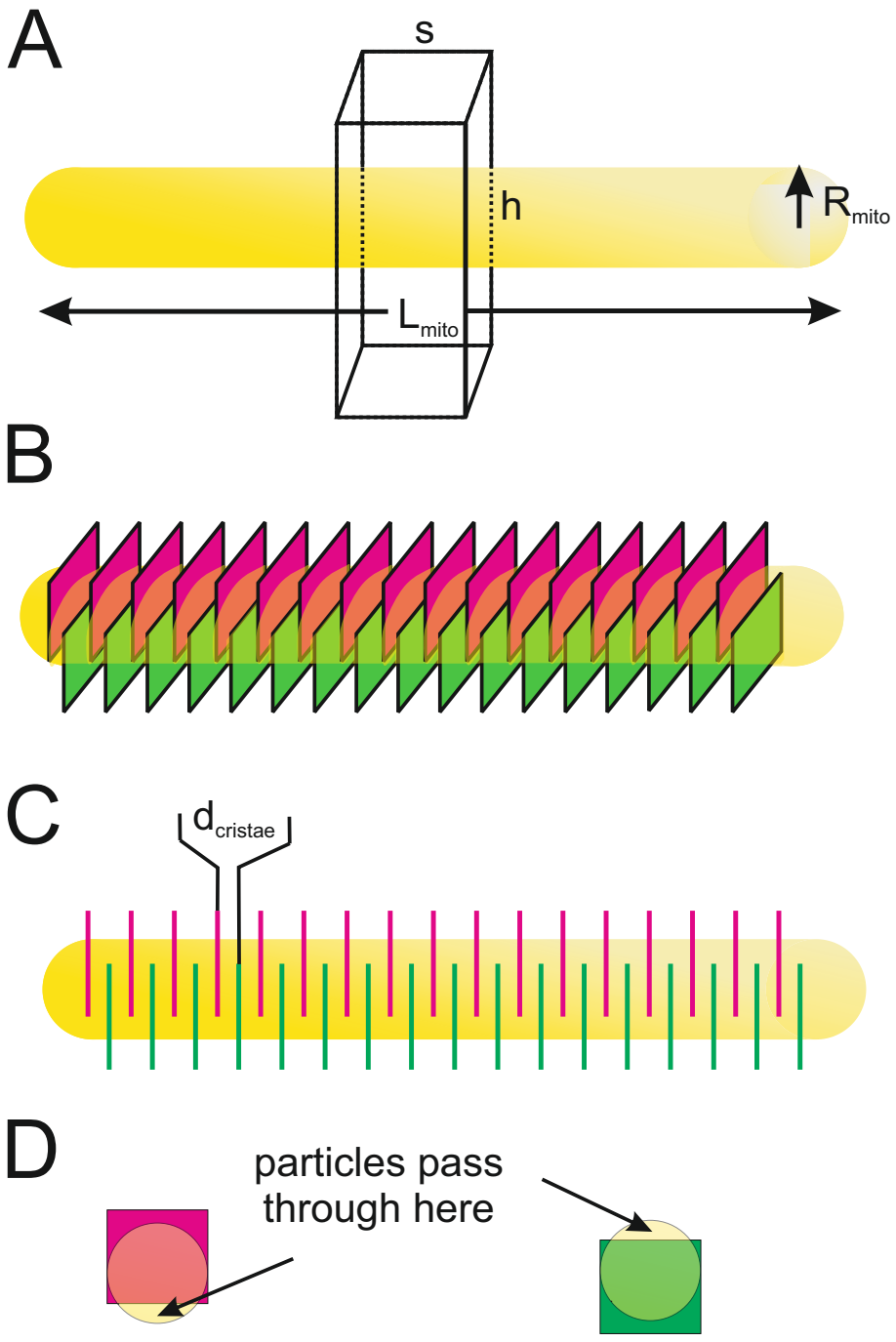

Figure 5.2: Particle-based Simulation of Mitochondrial Diffusion (A) General model of diffusion in a mitochondria made up of a cylinder capped by hemispheres. R_{mito}=250 nm, L_{mito}=9μm, Box dimensions: 500 nm x 500 nm x 3000 nm (s x s x h). Particles were randomly generated on the surface or inside the compartment. (B) To model diffusion with cristae, 500 nm x 500 nm squares where generated perpendicular to the axis of the mitochondria. Half of the squares were offset in the positive z-direction (pink squares) and the negative z-direction (green squares). (C) A slice of the mitochondria showing particles can pass through by a zig-zagging movement. d_{crust}=150 nm. (D) a rotated view of (C) showing a the barriers only partially covering the tube to allow diffusion.

Part III

Results and Discussion

Chapter 6

Characterizing cardiolipin-containing membranes

Cardiolipin plays a key role in the normal functioning of the cell. It is unique among other lipids because of its four acyl chains. In this thesis, I used CL-containing membranes that mimic the amount found in mitochondria of living cells (5-20%), as CL has been proposed to be an an important lipid in Bcl-2 protein interactions (Lutter et al., 2000, Kim et al., 2004, Lucken-Ardjomande et al., 2008, Bleicken et al., 2013b). However, as not much is known about the role of CL on the lipid bilayer organization, I decided to characterize CL-containing membranes before increasing the complexity of the system by adding Bcl-2 proteins. This part was published in 2013 (Unsay et al., 2013).

6.1 Formation of cardiolipin-containing membranes requires calcium

Most protocols for the formation of supported bilayers by vesicle rupture requires Ca^{2+} (Raviakine and Brisson, 2000). However, CL forms non-lamellar phases in the presence of divalent cations (like Mg^{2+}, Ca^{2+}) (Rand and Sengupta, 1972, Ortiz et al., 1999). Mixing CL with other lipids may prevent this to some extent (Macdonald and Seelig, 1987). As a means to deter the formation of these non-lamellar phases, I prepared bilayers composed of EPC and varying molar ratio of CL (0%, 5%, 10%, 20%) with or without calcium. The compositions estimate the range of values of cardiolipin found in mitochondria. In parallel experiments, my collaborator Dr. Katia Cosentino did experiments on a more complicated lipid mixture mimicking the outer mitochondrial membrane composition (MitoMix).

In the absence of calcium, 0%CL-EPC and 5%CL-EPC showed continuous lipid phase in confocal microscopy (Figure 6.1 A-B). Vesicles composed of 10%CL and 20%CL did not rupture and only deposited on top of the mica. In contrast, all compositions formed a continuous phase on top of mica support in the presence of calcium (Figure 6.1 D-F). To check whether the bilayers are fluid, a small portion of the bilayer was bleached and the fluorescence recovery was measured. Only bilayers formed in the presence of calcium showed fluid lipid phase (Figure 6.1 G-H).

Richter and Brisson (2005) showed that negatively charged lipids do not form continuous bilayers on mica in the absence of calcium due to their inability to form stable interactions with the support. Calcium also induces fusion of CL-containing vesicles (Wilschut et al., 1982), which is important in SLM preparation (Cremer and Boxer, 1999, Richter and Brisson, 2005, Richter et al., 2006). This indicates the importance of electrostatic interactions in the adsorption and consequential rupture of CL-containing vesicles in forming stable, continuous bilayers.

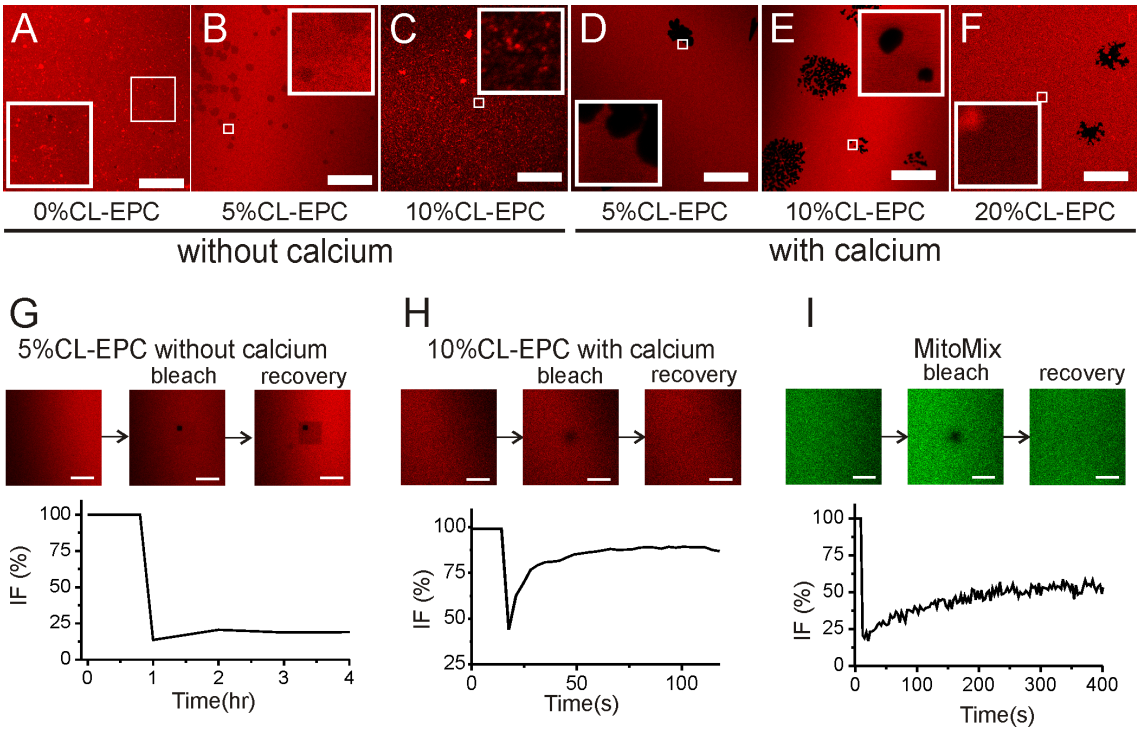

Figure 6.1: Confocal Microscopy of supported lipid membranes. Bilayers prepared without calcium (A–C). (A) Fluid bilayer formed by EPC (inset: 50 x 50 μm^2 close-up image of the indicated white square on the original image; some bright spots may be seen, and these are simply unfused vesicles adsorbed on the surface of the membrane). (B) 5% CL-EPC prepared without calcium produced a continuous phase (inset: 10 x 10 μm^2 close-up image of the indicated white square). 10% CL-EPC (C) and 20% CL-EPC (results not shown) vesicles adsorbed only to the mica surface without undergoing rupture and bilayer formation (inset: 10 x 10 μm^2 close up). (D–F) Bilayers prepared with calcium showed fluid bilayers (insets: 10 x 10 μm^2 close-up image; dark regions are membrane defects). (G–I) Photobleaching experiments show that bilayers prepared in the presence of calcium, but not in the absence, are fluid. (G) CL-EPC bilayers prepared without calcium did not recover fluorescence after photobleaching, (H) whereas they did with calcium. (I) MitoMix also formed continuous fluid bilayers in the presence of calcium. Scale bars represent 50 μm in A–F and 100 μm in G–I. (reprinted with permission from Joseph D. Unsay, Katia Cosentino, Yamunadevi Subburaj, Ana J. García-Sáez, "Cardiolipin effects on Membrane Structure and Dynamics", *Langmuir* (2013) 29, 15878-15887. Copyright 2013 American Chemical Society.)

6.2 Cardiolipin changes the fluidity of supported membranes

Fluorescence Correlation Spectroscopy (FCS) was used to characterize the CL effects on membrane fluidity. FCS probes the diffusion of a fluorescent molecule in and out of the confocal volume. By characterizing the diffusion of the lipidic dye, DiD, in the membrane I was able to measure the fluidity of the different bilayer compositions. CL-EPC bilayers were more fluid compared to pure EPC bilayers (Figure 6.2). The diffusion coefficient of DiD in pure EPC bilayers is $4 \pm 1\ \mu m^2/s$. In the presence of cardiolipin, this increased to $7 \pm 2\ \mu m^2/s$ in 10%CL-EPC, but no further changes were observed for 20%CL-EPC ($6 \pm 2\ \mu m^2/s$). The same effects could be seen in membranes with MitoMix composition.

Here, I showed that CL increases bilayer fluidity compared to that of pure EPC bilayers which is in contrast to previous studies (Yamauchi et al., 1981, Pöyry et al., 2009). Three reasons may explain the increased fluidity: (1) higher unsaturation introduced by the presence of CL (EPC has more than 50% unsaturated fatty acids, where as CL has 95% unsaturated fatty acid based on product specifications from Avanti Polar Lipids, Inc.), which would make the bilayer more fluid (Sarcina et al., 2003, Niemelä et al., 2006); (2) it

could also be due to concentration-dependent and lipid-specific interactions between CL and EPC; or (3) the effect of calcium ions on the lipid packing and structure.

Nichols-Smith et al. (2004) showed that CL and PC interact strongly as monolayers and condense in the presence of a physiological salt sub phase, implying that the addition of CL may hinder the lateral diffusion of the lipid particles due to head group interactions. These interactions are concentration-dependent: there are stable and strong interactions for 5% CL-PC monolayers, but for 10% and 20% CL-PC, these interactions become weaker and less stable. In contrast, Khalifat et al. (2011) showed that interactions of the CL headgroups do not necessarily affect the fluidity of the hydrophobic core. Taken together, the competition of attractive headgroup interactions versus increased hydrophobic core fluidity could explain why there was no dramatic changes in the fluidity but rather slight increase from 5% to 10% CL-EPC and consequent plateau from 10% to 20% CL-EPC.

Another reason attributes diffusion to area per lipid molecule. A study by Javanainen et al. (2013) showed that lipids in systems with lower area per lipid molecule diffuse more slowly than lipids in a system with a higher lipid area per molecule. In the previously mentioned study by Nichols-Smith et al., they showed that the excess area for 5%CL-PC system was higher than that for 10% and 20 CL-PC system. The latter two had comparable excess area. As the excess area of the monolayer is inversely related to the area per lipid molecule, this translates to a lower area per lipid molecule for 5%CL-PC compared to 10% and 20% CL-EPC. This coincides with the slower diffusion in 5%CL-PC.

Lastly, interactions between CL and calcium lead to changes in lipid packing and structure. This could have consequences in increasing isotropic and flip-flop motion of lipids (Gerritsen et al., 1980), and decreasing the barrier properties of CL-PC vesicles (Mandersloot et al., 1981). These changes may also increase the lateral diffusion of lipidic dyes in the membrane.

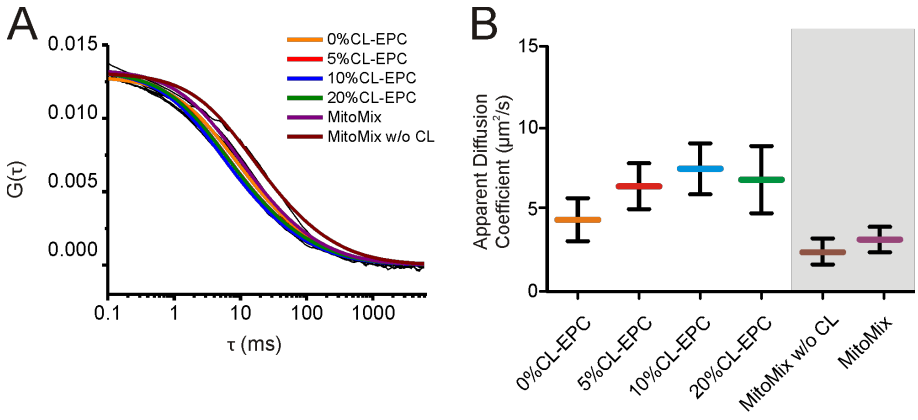

Figure 6.2: Cardiolipin increases membrane fluidity.(A) Representative autocorrelation curves (fitted with a 2D diffusion model with elliptical gaussian detection) obtained for the different lipid compositions under study. (B) Apparent diffusion coefficient calculated for the corresponding membranes. The horizontal bars show the average values, and the errors correspond to the standard deviation. We have measured 75-80 FCS curves for the CL-EPC mixtures and 40 curves for the MitoMix membranes. A pairwise t test showed a significant difference under all conditions except those between the pairs: 10%/20% and 5%/20% CL-EPC. (reprinted with permission from Joseph D. Unsay, Katia Cosentino, Yamunadevi Subburaj, Ana J. García-Sáez, "Cardiolipin effects on Membrane Structure and Dynamics", *Langmuir* (2013) 29, 15878-15887. Copyright 2013 American Chemical Society.)

6.3 Cardiolipin forms flat but thicker supported bilayers

I then characterized the topology and mechanical properties of the cardiolipin-containing membranes using AFM Imaging and force microscopy. AFM acquires images with a res-

Table 6.1: Table of AFM Results for Cardiolipin-containing Supported Bilayers

System	Force Spectroscopy[a,b]			AFM Imaging[b]	
	Type of Peak	Breakthrough Force (nN)	Bilayer Thickness (nm)[c]		Roughness (nm)
0%CL-EPC	A	5.4 ± 0.4	2.5 ± 0.3	2.9 ± 0.3	0.28 ± 0.04
5%CL-EPC	A	1.4 ± 0.8[d]	3.1 ± 0.6	3.2 ± 0.2	0.23 ± 0.05
		6.8 ± 0.3[d]			
	B	0.9 ± 0.1	5 ± 1[e]	4.9 ± 0.3[f]	
	C	3 ± 6[d]			
		7 ± 1[d]			
10%CL-EPC	A	1.0 ± 0.7	5 ± 2	6.0 ± 0.3	0.37 ± 0.06
	B	1.5 ± 0.1[d]	6 ± 2		
		3.5 ± 0.9[d]			
	C	8.8 ± 0.8			
20%CL-EPC	A	1.1 ± 0.6	5.8 ± 0.6	5.1 ± 0.9	0.33 ± 0.05
	A	4.7 ± 1.6	7.0 ± 1.1		
	A	7.6 ± 1.3			
MitoMix	A	4.2 ± 0.6[d]	3.6 ± 0.1	4.5 ± 1.4	0.22 ± 0.07
		7.4 ± 0.3[d]			
	B	4.3 ± 0.4	4.7 ± 0.8		
	C	5.1 ± 0.4			

[a] Histograms from force and height distributions were fitted with a Gaussian function to elucidate the peak values.
[b] Errors are given as the standard deviation of the distribution
[c] Bilayer thickness was measured using two methods: height profiles from the AFM Images and Force Spectroscopy. For AFM images, thickness was measured from mica (bottom of membrane defect) to the top of the membrane. For Force Spectroscopy, see Figure 6.5A.
[d] Two populations of breakthrough force resulted from the fitting of the force distribution.
[e] For force curves with two peaks, the thickness from peak B and peak C were added.
[f] Thickness of flower-like domains were measured from the mica.
(reprinted with permission from Joseph D. Unsay, Katia Cosentino, Yamunadevi Subburaj, Ana J. García-Sáez,"Cardiolipin effects on Membrane Structure and Dynamics", *Langmuir* (2013) 29, 15878-15887. Copyright 2013 American Chemical Society.)

olution of a few nanometers by scanning a sharp probe over the surface of a sample. Furthermore, surface features are also analyzed with a vertical resolution of about 0.5 nm, as such AFM gives a 3D view of the sample inaccessible to conventional microscopy techniques.

Aside from 5%CL-EPC, all other compositions showed flat lipid bilayers. Interestingly in the case of 5%CL-EPC, I occasionally (about 33% of the time) observed the presence of domain-like structures at the edge of membrane defects. These structures are higher than the surrounding membrane by 1.7 ± 0.2 nm. I then looked at the dynamics of these structures and saw that they grow over time until a certain size or until they fuse and cover the whole bilayer. This suggests that the 5% CL-EPC bilayers are initially similar to pure EPC bilayers and evolve with time toward membrane organizations similar to those observed for higher CL concentrations.

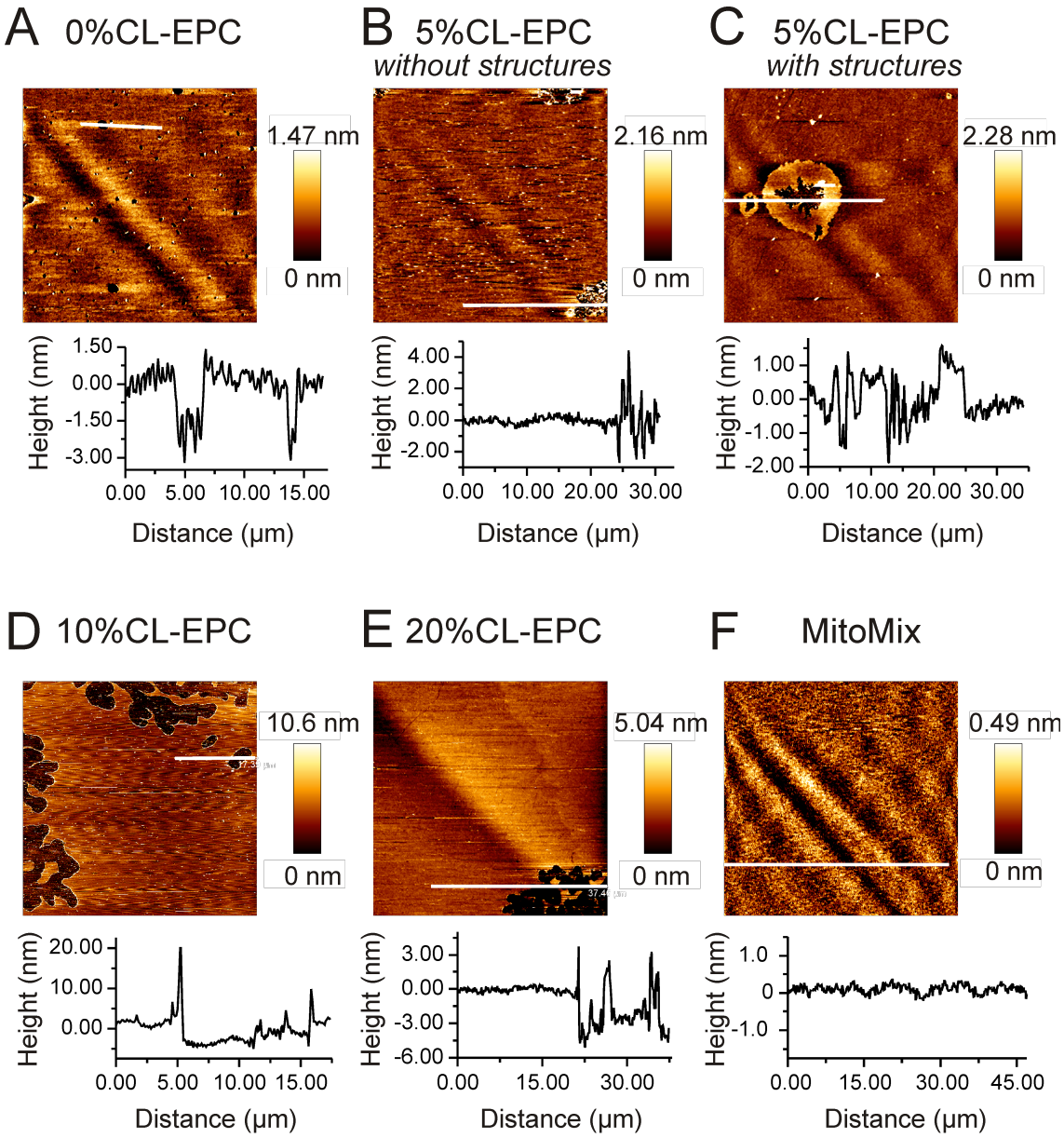

Figure 6.3: AFM imaging of cardiolipin-containing supported bilayers. (A) Pure EPC. (B) 5% CL-EPC without structures at the edge of the defect. (C) 5% CL-EPC with structures at the edge of the defect. (D) 10% CL-EPC. (E) 20% CL-EPC. (F) MitoMix. The height profiles below each image correspond to the white line in the image. All images are 50 μm on each side. The diagonal lines and other patterns (that look like interference patterns) that appear in all images are artifacts of the AFM, which we cannot remove during image processing.(reprinted with permission from Joseph D. Unsay, Katia Cosentino, Yamunadevi Subburaj, Ana J. García-Sáez, "Cardiolipin effects on Membrane Structure and Dynamics", *Langmuir* (2013) 29, 15878-15887. Copyright 2013 American Chemical Society.)

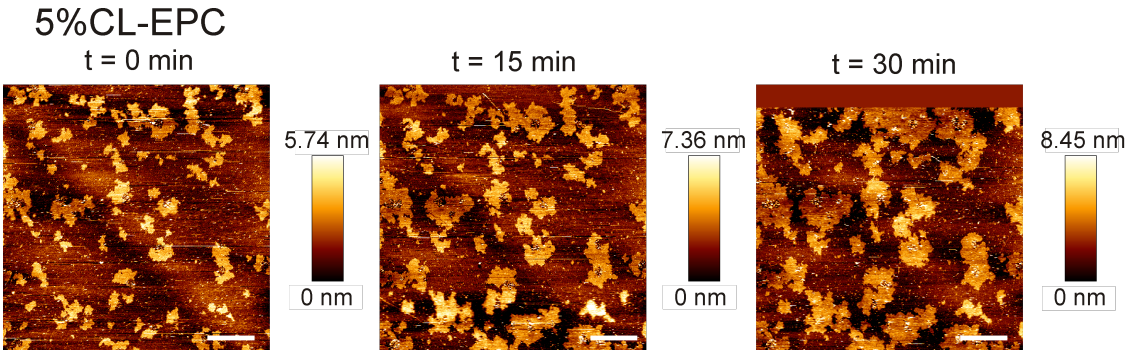

Figure 6.4: Growth of structures in 5%CL-EPC over time. AFM image of the same area in a 5%CL-EPC bilayer shows growth of structures at the edge of the defects over time. Scale = 20 μm. (reprinted with permission from Joseph D. Unsay, Katia Cosentino, Yamunadevi Subburaj, Ana J. García-Sáez,"Cardiolipin effects on Membrane Structure and Dynamics", *Langmuir* (2013) 29, 15878-15887. Copyright 2013 American Chemical Society.)

6.4 Cardiolipin affects the mechanical properties of supported bilayer

In addition to high resolution imaging, AFM can also be used to probe the mechanical properties of the bilayer in Force Spectroscopy mode. In this mode, the AFM tip approaches the bilayer surface in order to obtain force-distance curves. After contact, the tip continues to press on the sample and the force increases up to a certain value where we see a jump in the force from a high value to a lower value (Figure 3.13 and 6.5A). This is interpreted as the force needed to break the membrane. As one of the axis measures the movement of the cantilever the distance measured between the initial high force value and the resulting low force value represents the thickness of the bilayer. Continuing to press on the sample (solid support) only increases the force.

Using force spectroscopy mode on CL-containing bilayers resulted in curves with either a single or double breakthrough events (Figure 6.5A and B). In pure EPC membranes, only a single breakthrough event is present. From here on, I refer to the peak on the curves with single event as Peak A. On the force curves with double breakthrough events, the first or peak with lower force value is Peak B, and the second or peak with higher force value is Peak C.

I first consider the behavior of Peak A. Pure EPC showed a single population at 5.4 $\pm$ 0.4 nN. CL decreased the breakthrough force in a concentration-dependent fashion. 5% CL-EPC clearly showed two distributions, one population is still close to the values of pure EPC bilayers (6.8 $\pm$ 0.3 nN) and one is lower at 1.4 $\pm$ 0.8 nN. Increasing concentrations of CL, showed only one population (1.0 $\pm$ 0.7 nN and 1.1 $\pm$ 0.6 nN for 10% and 20% CL-EPC, respectively).

Double piercing events in force experiments were controversial and not fully explained so far (Canale et al., 2010, Alessandrini et al., 2012). The two peaks may be due to three things: (1) accumulated lipid material on the tip that breaks during the force spectroscopy experiment; (2) a bilayer with uncoupled leaflets, where the probe pierces through each leaflet one by one, or; (3) they may reflect a special organization of the membrane, such as the presence of double bilayers or even nonlamellar structures. Indeed, these two peaks were only present with CL.

The breakthrough force distributions were wider in Peak B and Peak C than in Peak A. Peak B generally follows the distribution of Peak A for the different CL-containing bilyers, but peak C is higher and closer to the distribution of pure EPC. The higher values for peak C may indicate coupling of the membrane to the support, which can increase its

breakthrough force.

To verify the hypothesis that the double peaks reflect a different membrane organization, I plotted the thickness of the different membranes. The thickness of the bilayer estimated from single piercing events increased with CL content from 2.5 ± 0.3 nm for pure EPC up to 5.8 ± 0.6 nm for 20% CL-EPC. This is approximately the same value that we obtained from the sum of the thickness of Peak B and Peak C (7.0 ± 1.1 nm for 20% CL-EPC) and roughly corresponds to double the thickness of a lipid bilayer in the liquid disordered state.

Similar to CL-EPC, bilayers with MitoMix composition showed single and double piercing events. Interestingly, the force distribution of MitoMix is similar to 5% CL-EPC in that there are two populations although of very different values. The thickness values were also higher, but not double the value of the pure EPC bilayers.

6.5 Cardiolipin increases the propensity of membranes to form non-lamellar structures

In AFM imaging, I showed that all of the bilayers were flat and homogeneous except for 5% CL-EPC, which presented membrane defects surrounded by higher structures that grew in time. Interestingly, the sum of the thickness of these higher structures with the normal thickness of the bulk of the membrane is similar to the thickness values found for 10% and 20% CL-EPC. This suggests that the 5% CL-EPC membranes are initially similar to pure EPC membranes and evolve with time toward membrane organization similar to those with higher CL concentrations.

I thought in the beginning that these could be thermotropic phases (solid gel and liquid lamellar). However, the transition temperature of the main lipid component for EPC and CL suggests otherwise. The transition temperature for 1-palmitoyl-2-oleoyl-sn-glycero-3-phosphatidylcholine is -20°C, CL from bovine heart is 19°C and 40%CL-EPC is 4°C (Domènech et al., 2006). It was reported that interaction with a solid support can change the thermotropic transition temperature (Seeger et al., 2009), but this only happens when the bilayers are prepared below the transition temperatures. It is clear that that these structures are not in the gel phase. Cooling hysteresis may also play a role in the presence of these higher structures as bilayers are prepared at 37°C and imaged at room temperature (Lewis et al., 2007). Kinetically trapped phases may persist depending on the cooling rate of the sample.

On the basis of these evidences, I hypothesize that these higher structures could be double apposed bilayers or even nonlamellar structures (Figure 6.6). It is important to note that the formation of double bilayers also implies the presence of highly curved membrane regions, which may contain nonlamellar organization of the lipids in the contact zones between both bilayers. For 5% CL-EPC, cardiolipin may induce the formation of these structures at the edge of the defects because of the local lipid packing defects induced by the presence of the hole in the membrane. These nonlamellar structures may represent a more stable organization of lipids because they grow with time until the formation of a flat topography. By increasing the CL concentration, these structures a were preferred as right from the beginning and I didn't see an evolution with time.

So far, there have not been any reported double bilayer formations for CL-EPC bilayers in this range of concentrations. Even contrary to this, the dilution of CL with PC decreased its propensity to form nonlamellar (inverted hexagonal) structures even in the presence of calcium (Macdonald and Seelig, 1987). However, the presence of two peaks in the force curves support my hypothesis. In addition, CL can exploit its interaction with calcium to stabilize these apposed bilayers, via formation of inverse micelles. Alternatively, the two CL phosphatidyl moieties could also span the two bilayers to stabilize it. Furthermore,

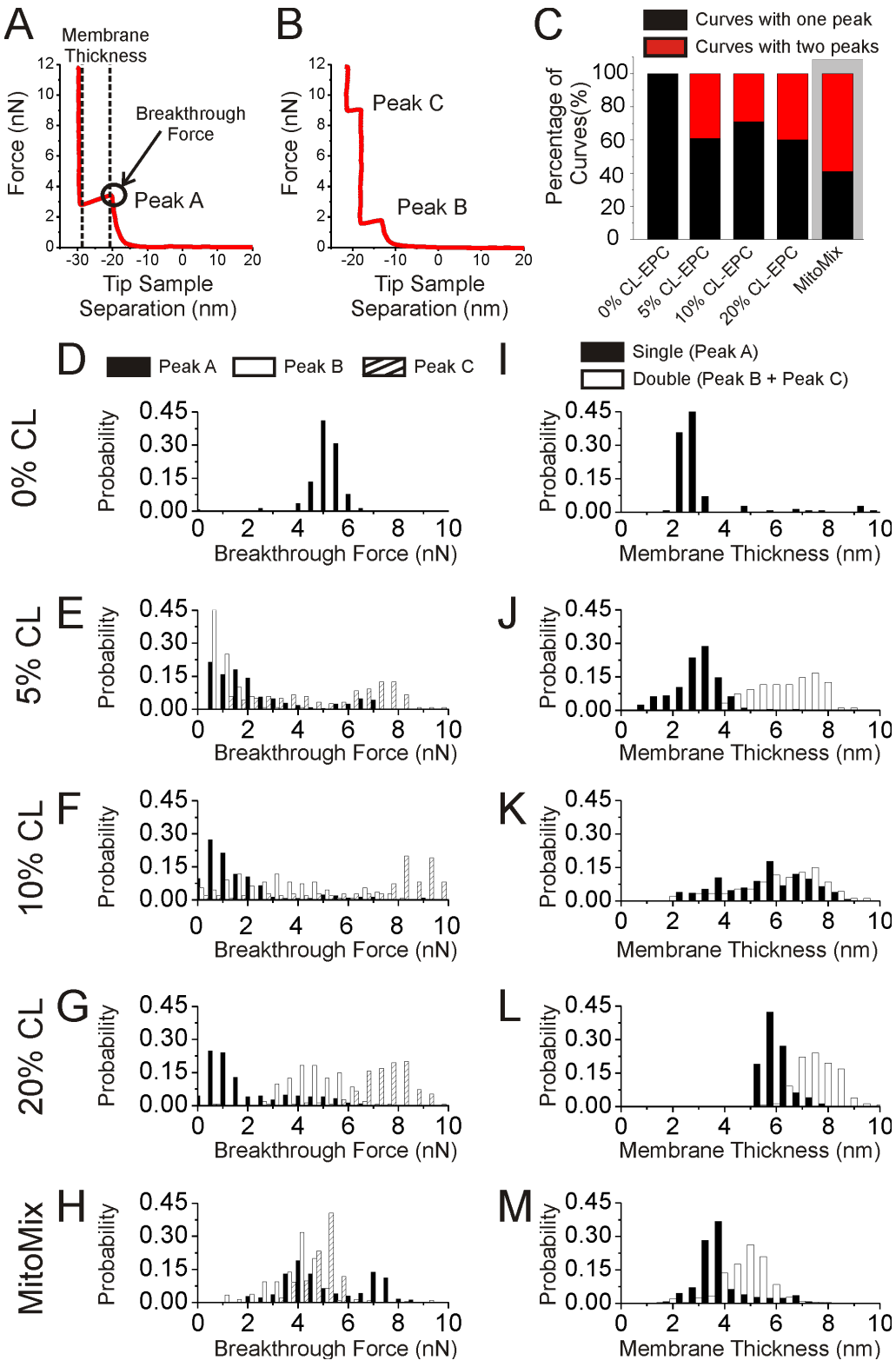

Figure 6.5: Force spectroscopy of cardiolipin-containing supported bilayers. (A) Curves with single piercing events, Peak A. (B) Curves with double piercing events, Peak B and Peak C. (C) Percentage of curves with single (black) and double (red) piercing events for the different membrane compositions. Breakthrough force and thickness distribution of different membranes: (D, I) Pure EPC, (E, J) 5%CL-EPC, (F, K) 10%CL-EPC, (G, L) 20% CL-EPC and (H, M) MitoMix. (reprinted with permission from Joseph D. Unsay, Katia Cosentino, Yamunadevi Subburaj, Ana J. García-Sáez, "Cardiolipin effects on Membrane Structure and Dynamics", *Langmuir* (2013) 29, 15878-15887. Copyright 2013 American Chemical Society.)

mica, the solid support, may induce inter leaflet flip-flop with anionic lipids (Richter et al., 2006) introducing a higher CL content in the leaflet interacting with the support. This creates a higher CL concentration enough to induce hexagonal phases which PC suppresses in fully mixed systems. Perhaps all of these are even present in the bilayers. Although I could not distinguish between these hypotheses, the results indicate that CL promotes the formation of lipid arrangements beyond the canonical lipid bilayer.

Even in more complex mixtures like MitoMix, this tendency to form nonlamellar structures is present. While one would expect MitoMix to behave similarly to 5% CL-EPC, it in fact does not. The presence of other lipids could be the reason. MitoMix has several negatively charged lipids like PI and PS (both 10 mol %). Furthermore, another lipid PE, which is prone to form nonlamellar phases, is present in high amounts (27 mol %). PE and CL were shown to induce domains at the temperatures below the main phase-transition point of the system (Domènech et al., 2007c).

Studies on the lipid propensity to form lamellar/nonlamellar strucutres show that negatively charged lipids and unsaturated acyl chains favor the formation of hexagonal HII phases in the presence of positive charges (Sankaram et al., 1989, Lewis and McElhaney, 2009). Hexagonal phases have thickness values in the range of 4 to 5 nm (Marrink and Mark, 2004, Alessandrini and Muscatello, 2009). In this context, the findings for MitoMix may suggest preferential formation of hexagonal phases over other structures.

Formation of nonlamellar phases may have implications in lipid packing. In a recent study following the publication of the original paper, Zeczycki et al. (2014) showed that CL may have different effects for different lipid compositions. In some cases where the lipid is loosely packed, CL condenses the lipids, whereas it may decrease in an opposite case. For example, in a composition similar to MitoMix (PC/PE/PS/PI/CL), lipid packing was decreased.

This propensity of CL-containing membranes have biological implications as CL-deficient mitochondria show different morphologies lacking cristae-like structures (Mileykovskaya and Dowhan, 2009). They may also stabilize highly-curved structures usually found in mitochondrial contact sites (Harner et al., 2011, Jakobs and Wurm, 2014). Indeed, single vesicle studies also show that CL is key to the formation of membrane invaginations under acidic pH conditions (Khalifat et al., 2011).

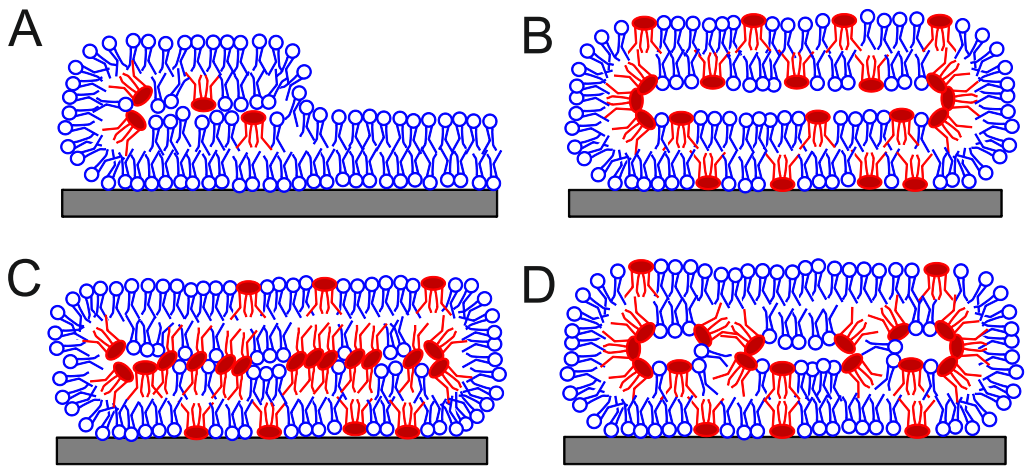

Figure 6.6: Models proposed for CL-EPC membrane polymorphisms. (A) 5% CL-EPC system with higher structures at the edge, induced and stabilized by CL. (B) 20% CL-EPC as a double bilayer with a water layer in between. (C) 20% CL-EPC as a double bilayer with interacting layers induced by CL, which can span both bilayers. (D) 20% CL-EPC containing non-lamellar structures. (reprinted with permission from Joseph D. Unsay, Katia Cosentino, Yamunadevi Subburaj, Ana J. García-Sáez,"Cardiolipin effects on Membrane Structure and Dynamics", *Langmuir* (2013) 29, 15878-15887. Copyright 2013 American Chemical Society.)

Chapter 7

Membrane effects of Bax and cBid

The embedded together model described in Chapter 1 argues for an active role of the MOM in the interactions between Bcl-2 protein which is supported by several studies (Lutter et al., 2000, Kuwana et al., 2002, Terrones et al., 2004, Bleicken et al., 2013a,b, Shamas-Din et al., 2015, Lucken-Ardjomande et al., 2008). However, the effects of Bcl-2 protein on membrane properties are not well studied. Bid (and its active forms, cleaved Bid or cBid and truncated Bid or tBid) is the most commonly studied member of the Bcl-2 family in membrane remodelling. Previous studies show that tBid preferentially binds to membranes containing CL, a lipid found only in mitochondria and chloroplasts of eukaryotic cells (Lutter et al., 2000, Shamas-Din et al., 2015). Interaction of tBid with CL is specific, cannot be blocked by the anti-apoptotic protein Bcl-xL (Kim et al., 2004), and does not require the BH3-domain. This is supported by structural studies on membrane insertion of tBid, suggesting that the protein adopts multiple membrane-associated or membrane-inserted conformations, while the BH3-domain is free to interact with other Bcl-2 proteins (Shamas-Din et al., 2013a, Shivakumar et al., 2014). However, more recently, it has been shown that CL is expendable in tBid?s recruitment to the mitochondria and that the protein MTCH2 may interact with tBid and recruit it to the mitochondria in the absence of CL (Raemy et al., 2016). Once inserted, tBid can induce the formation of nonlamellar phases in the presence of calcium as well as membrane permeabilization in vesicles containing lipids with negative intrinsic curvature (Epand et al., 2002a).

Although Bax pore forming activity has been well characterized, the effect of pore formation on the membrane physical properties are poorly described. Bax forms pores of different sizes depending on its concentration in the membrane (Bleicken et al., 2013a, Saito et al., 2000, Gillies et al., 2015) . Recent structural evidences show that Bax does not necessarily need to line the whole pore for stabilizing it (Grosse et al., 2016, Salvador-Gallego et al., 2016, Xu et al., 2013) in support of the toroidal model proposed for Bax pores (Cosentino et al., 2016, Qian et al., 2008). Using Bcl-2 peptides able to mimic the activity of the full-length proteins (García-Sáez et al., 2004, 2005), we previously showed that Bax-α5 stabilizes the line tension both at lipid phase boundaries and at membrane pore edges (García-Sáez et al., 2007a). This effect has also been well-characterized for other antimicrobial peptides, like melittin, that exert a similar pore-forming activity (Sengupta et al., 2008). There is also evidence that Bax has a thinning effect on liposomes (Satsuma et al., 2012) , similar to those reported for pneumolysin (Gilbert et al., 1999) and antimicrobial peptides (Longo et al., 1998, Huang, 2006, Lee et al., 2008). However, whether this is a general mechanism of this type of proteins and how the interplay between cBid and Bax modify other properties of the lipid membrane to mediate MOM permeabilization remains unclear.

In this chapter, I studied the independent effects of Bax and cBid on supported membranes with MOM-like lipid compositions using the force spectroscopy mode of AFM.

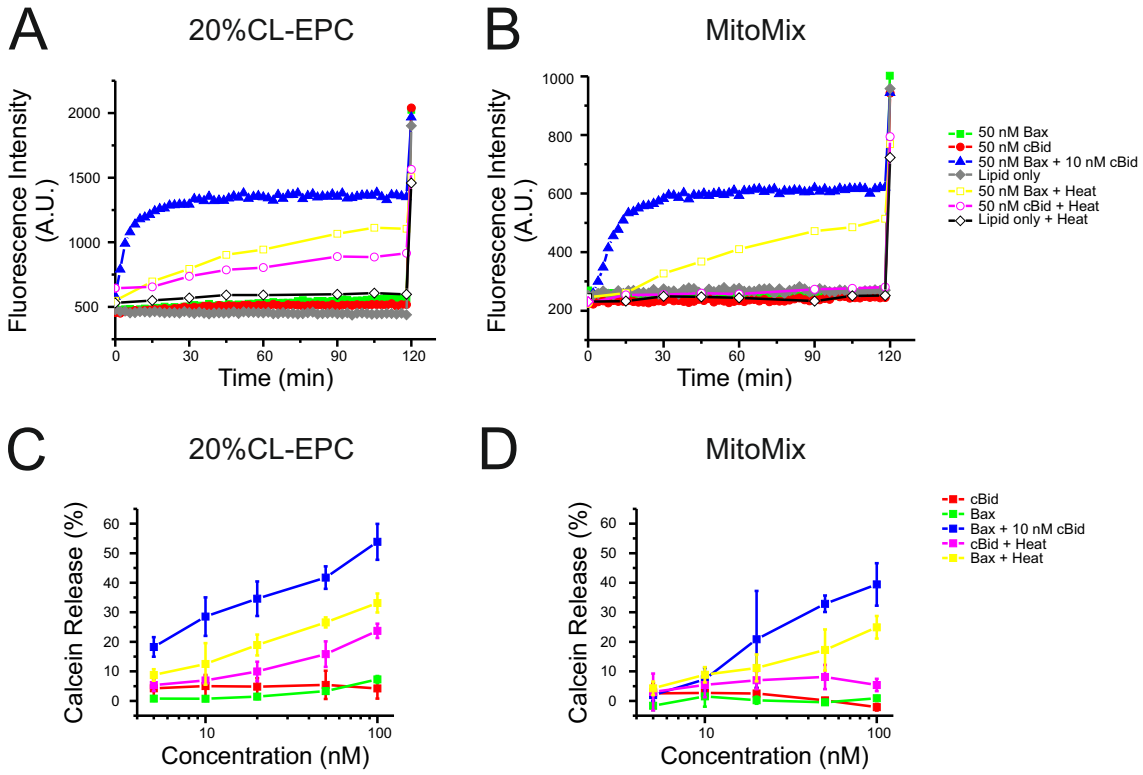

Figure 7.1: Calcein Release Assay. (A-B) Representative raw data of calcein release for 20%CL-EPC(A) and MitoMix (B). (C-D) Summary of calcein release at 60 min vs. concentration of protein for 20%CL-EPC (C) and MitoMix (D). Graph legends are given in the figure.

Here, I chose the composition with a 20% CL-EPC composition due to their flat topology as reported in the previous section. This high amount of CL is also important for cBid binding (Kim et al., 2004). The same experiments were repeated in parallel in MitoMix composition by Dr. Katia Cosentino. Due to the findings in the previous chapter that the supported lipid bilayers seem to form non-lamellar structures, it is not appropriate to still call them bilayers, as such, in this chapter, I instead refer to them as supported lipid structures (SLS).

7.1 Heat-activated Bax permeabilizes large unilamellar vesicles

To characterize the membrane effects of individual players of the Bcl-2 family, I implemented a protocol to activate Bax *in vitro* independently of cBid or any other BH3-only protein or peptide (Pagliari et al., 2005). In a previous study, Hermann et al (2014) characterized different ways of activating Bax in order to permeabilize 20% CL-EPC giant unilamellar vesicles while keeping them intact, such as mild heat treatment, addition of detergents and acidic pH.

To test the activity of cBid and activated Bax in my system, I performed experiments of calcein release from Large Unilamellar Vesicles (LUV). Both 20%CL-EPC and MitoMix LUVs were permeabilized in the presence of heat-activated Bax and cBid-activated Bax, (thus confirming the activity of cBid as well). In contrast, LUVs incubated with only Bax or only cBid at room temperature did not show significant permeabilization (Figure 7.1).

I also checked the concentration dependence to ascertain that the permeabilization is indeed due to the pore activity of the protein. Figure 7.1C and D shows these graphs for both lipid mixtures. Note that even at high concentrations, Bax alone and cBid alone did

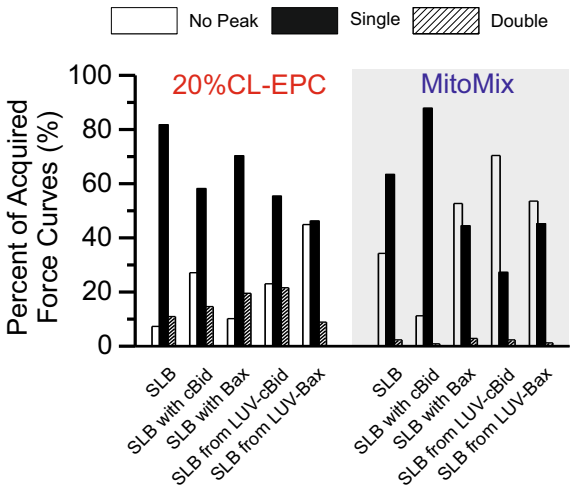

Figure 7.2: Occurence of Different Types of Force Curves.

not show significant permeabilization for both lipid mixtures.

It is interesting to note that in 20%CL-EPC LUVs, heating the liposomes in the presence of cBid also permeabilized the membrane to a certain extent (Figure 7.1C). This is not observed in MitoMix LUVs. It has been shown that under the right conditions (presence of cardiolipin and calcium ions), tBid has some pore-forming properties *in vitro* (Epand et al., 2002a). In my case, the increased temperature and the presence of higher concentrations of CL (compared to MitoMix) and cBid, may have triggered permeabilization of calcein in 20%CL-EPC liposomes. It is not clear whether it is due to the propensity of CL to form non-lamellar phases, as MitoMix also contains an increased amount of PE (27.2mol%), another lipid that promotes formation of hexagonal phases. However, the presence of other lipids may have hindered this tendency (Macdonald and Seelig, 1987). It seems that this is specific to CL's lipid structure and shape as Cho et al (2011) saw this permeabilizing effect of tBid only in CL and PS containing vesicles but not PA, PI, PG, or PIP2. In the case of MitoMix, CL and PS only comprise 4.4% and 10 mol% of the total lipids in MitoMix, which may not be enough to promote the permeabilization. It is also hard to predict whether the presence of CL has physiological implication in Bcl-2 protein activity in cells, as recently, Raemy et al. (2016) showed that in HCT116 cells, CL and a protein, MTCH2, can have redundant functions in the recruitment of tBid.

7.2 cBid lowers the breakthrough force of membranes

To investigate the effects of cBid and Bax on lipid membranes, I used force spectroscopy (FS). The information that can be deduced from FS was discussed in Chapters 3 and 6. Figure 7.2 shows the fraction of force curves with no breakthrough event, single breakthrough events and double breakthrough events. The fraction of double breakthrough events was relatively constant but low for both 20% CL-EPC and MitoMix. Furthermore, there was an increasing fraction of force curves that did not have peaks (especially in MitoMix). There are three possibilities why this is not detected. Firstly, the peaks may be below the detection limit of the AFM. Secondly, the peaks may be above our endpoint force measurement (12 nN). Since the general trend is a lowering of the breakthrough force (shown late), this makes the latter less likely. Lastly, the curves may not have a defined peak, but rather shoulders, which cannot be analyzed by the detection program (Cosentino et al, submitted, Unsay et al.2015)

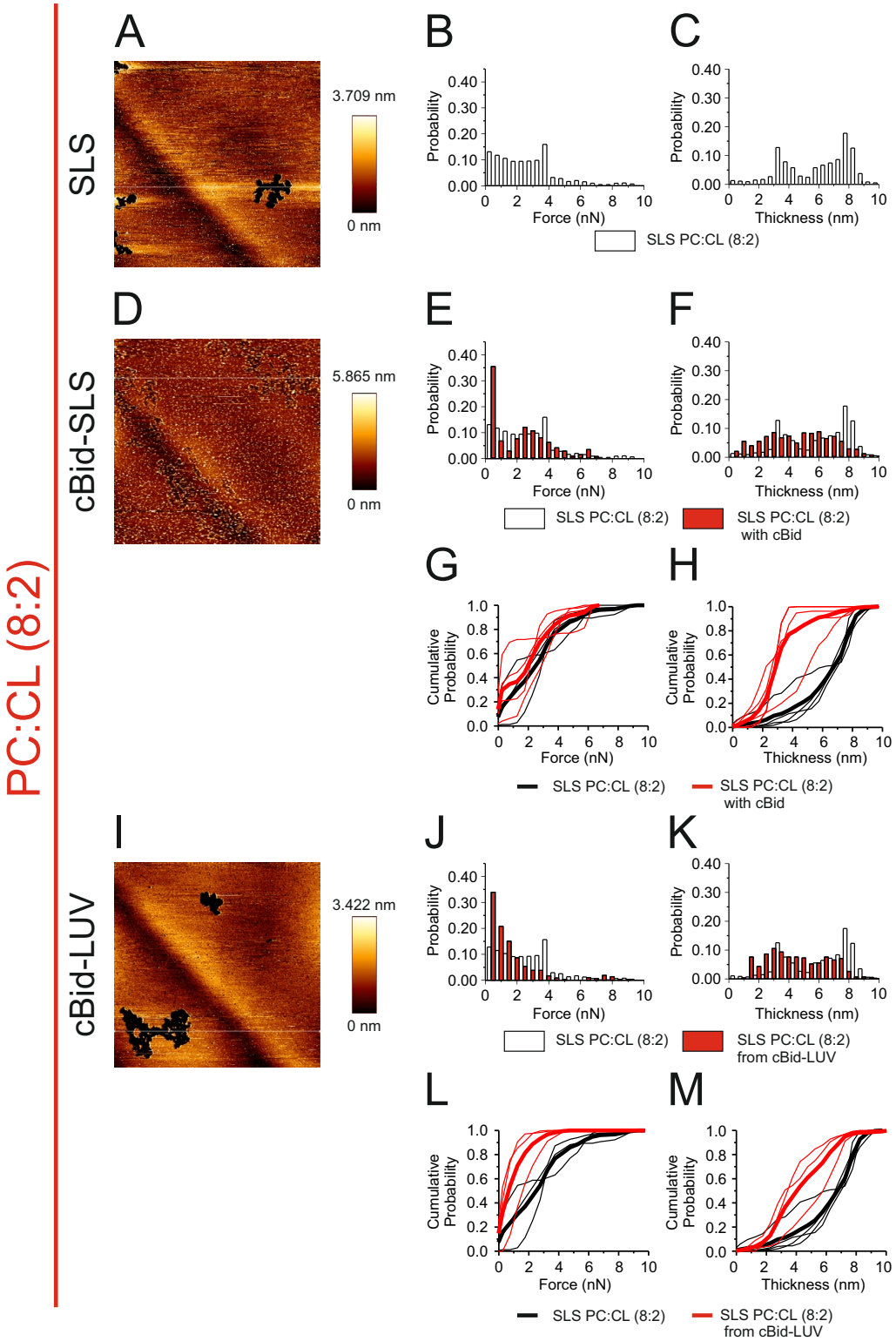
PC:CL (8:2)
SLS
cBid-SLS
cBid-LUV
A
B
C
D
E
F
G
H
I
J
K
L
M
3.709 nm
0 nm
5.865 nm
0 nm
3.422 nm
0 nm
Probability
Force (nN)
Thickness (nm)
Cumulative Probability
SLS PC:CL (8:2)
SLS PC:CL (8:2) with cBid
SLS PC:CL (8:2) from cBid-LUV

Figure 7.3 (previous page): Membrane effects of cBid on 20%CL-EPC Membranes. (A-C) AFM images and force spectroscopy distributions for breakthrough force and thickness of pure 20%CL-EPC SLSs. (D-F) Effect of cBid on pre-formed SLSs and comparison of force and thickness values before (white bars) and after the addition of the protein (red bars). (G-H) Cumulative distribution plots of SLS (black) and cBid-SLS (red) showing differences in force (G) and thickness (H). Each plot represents a single repetition. Thick lines represent average cumulative distributions for all the repetitions for SLS and cBid-SLS samples. (I-K) Effects of cBid in LUVs and comparison of force and thickness values before (white bars) and after the addition of the protein (red bars). cBid-LUVs were used to prepare the SLSs. (L-M) Cumulative distribution plots of SLS (black) and cBid-LUV (red) showing differences in force (L) and thickness (M). Each plot represents a single repetition. Thick lines represent average cumulative distributions for all the repetitions for SLS and cBid-LUV samples. Pictures scale is 50 μm. Diagonal lines are artifacts of the reflection of the laser at the back AFM cantilever and cannot be removed by image processing. These are only evident in large scan areas such as the ones provided here and they do not affect the force spectroscopy measurements. Histograms are normalized for better comparison (the number of points varied between 500 and 1500).

I first tested the influence of cBid on pre-formed SLSs (cBid-SLSs). Before addition of the protein, the bilayers looked flat (roughness of 0.4 nm and 0.2 nm for 20% CL-EPC and MitoMix, respectively) and homogeneous (Figure 7.3A and 7.4A). The breakthrough force values were widely distributed around 2-3 nN for both lipid compositions (2 ± 2 nN for 20% CL-EPC and 2.8 ± 0.3 nN for MitoMix), but MitoMix also presented a second population at 6.8 ± 0.4 nN in agreement with previous data (Figure 7.3B, 7.4B and Table 7.1). After addition of 20 nM cBid, I could clearly observe the presence of the protein on the surface of the membrane, with structures that ranged from 2 to 10 nm high (Figure 7.3D and 7.4D). In addition, I observed a decrease of the breakthrough force values to 0.7 ± 0.2 nN in half of the breakthrough events in the 20% CL-EPC system (the other half maintained the original breakthrough force at 3 ± 1 nN) (Figure 7.3E and Table 7.1), while in the MitoMix SLSs the two breakthrough force populations disappeared to give a single one at 3.8 ± 0.4 nN (Figure 7.4E). This suggests a reorganization of the lipids in the presence of cBid.

This effect was even more enhanced in SLSs formed from LUVs pre-incubated with cBid (cBid-LUVs) (Figure 7.3I and 7.4I) as shown in the cumulative distribution plots (compare Figure 7.3G with 7.3L and Fig. 7.4G with 7.4L). In this case, the breakthrough force values dropped down to 1 ± 1 nN for 20% CL-EPC and 1.6 ± 0.6 nN for MitoMix (Figure 7.3J, 7.4J and Table 7.1). This difference between cBid-SLS and cBid-LUV could be due to the different sample preparation methods. In pre-formed SLSs incubated with cBid, protein insertion may be hindered by non-specific interactions with the solid mica support. If cBid is incubated in LUVs before the formation of SLS, the protein may be able to insert with more freedom before interacting with the mica.

Another possibility is that the surface concentration in the cBid-SLS is different than in cBid-LUVs. Theoretical calculations of protein-to-lipid ratios (P/L ratio) indicate that P/L ratio is higher in cBid-SLS than in cBid-LUV. To check this, my colleague, Katia Cosentino, employed total internal reflection fluorescence (TIRF) microscopy and used Alexa 488-labeled proteins under the same conditions as the AFM experiments 7.5. We saw that the particle density between cBid-SLS and cBid-LUV is the same, indicating that while the theoretical P/L ratio is different, the total amount of protein inserting into the membrane is similar for both systems and excess protein in the cBid-SLS system may have been removed during washing steps.

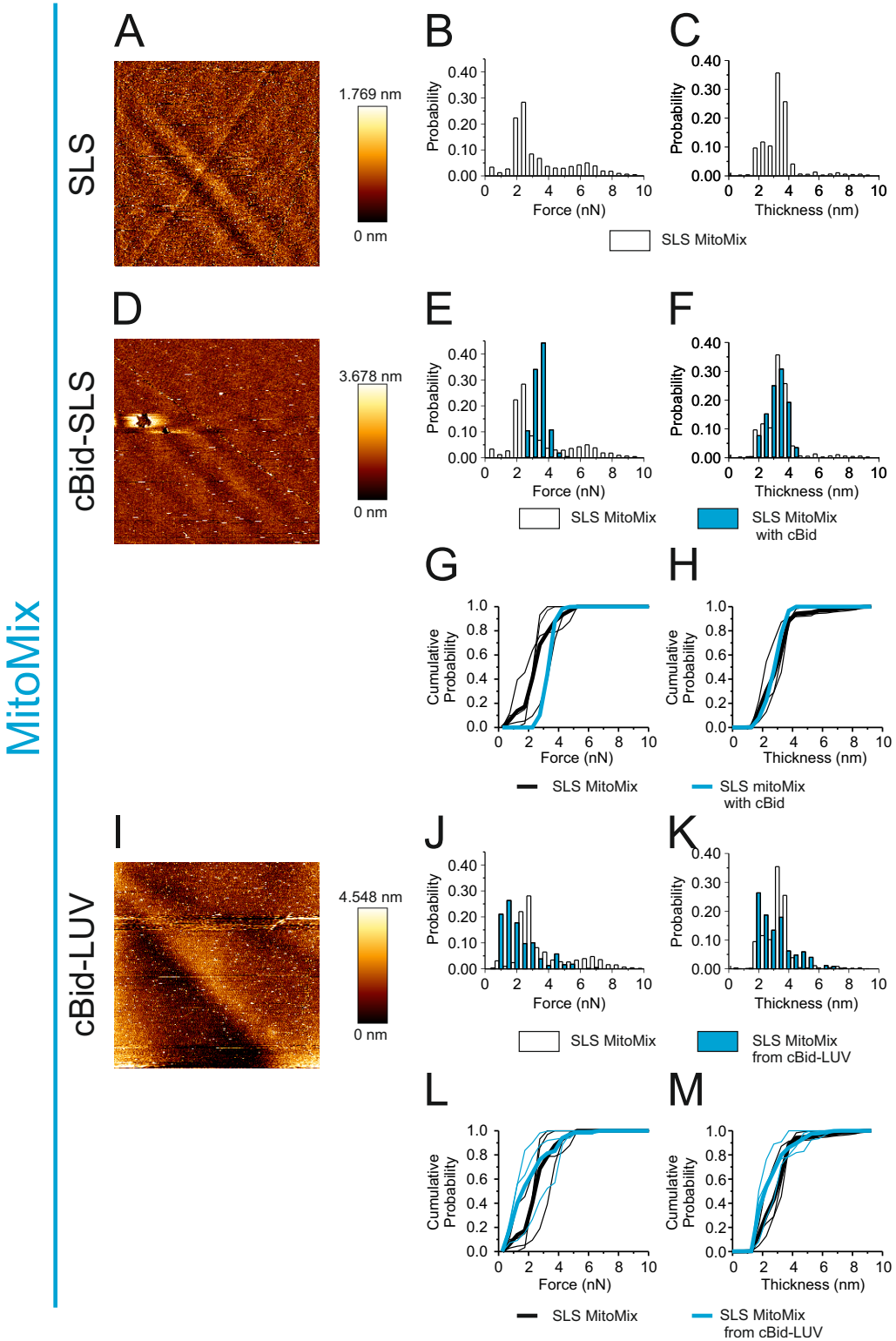
MitoMix
SLS
cBid-SLS
cBid-LUV
A
B
C
D
E
F
G
H
I
J
K
L
M
1.769 nm
0 nm
3.678 nm
0 nm
4.548 nm
0 nm
Probability
Force (nN)
Thickness (nm)
Cumulative Probability
SLS MitoMix
SLS MitoMix with cBid
SLS mitoMix with cBid
SLS MitoMix from cBid-LUV

Figure 7.4 (previous page): Membrane effects of cBid on MitoMix Membranes. (A-C) AFM images and force spectroscopy distributions for breakthrough force and thickness of MitoMix SLSs. (D-F) Effect of cBid on pre-formed SLSs and comparison of force and thickness values before (white bars) and after the addition of the protein (blue bars). (G-H) Cumulative distribution plots of SLS (black) and cBid-SLS (blue) showing differences in force (G) and thickness (H). Each plot represents a single repetition. Thick lines represent average cumulative distributions for all the repetitions for SLS and cBid-SLS samples. (I-K) Effects of cBid in LUVs and comparison of force and thickness values before (white bars) and after the addition of the protein (blue bars). cBid-LUVs were used to prepare the SLSs. (L-M) Cumulative distribution plots of SLS (black) and cBid-LUV (blue) showing differences in force (L) and thickness (M). Each plot represents a single repetition. Thick lines represent average cumulative distributions for all the repetitions for SLS and cBid-LUV samples. Pictures scale is 50 m. Diagonal lines are artifacts of the reflection of the laser at the back AFM cantilever and cannot be removed by image processing. These are only evident in large scan areas such as the ones provided here and they do not affect the force spectroscopy measurements. Histograms are normalized for better comparison (the number of points varied between 600 and 2000).

Table 7.1: Table of Force Spectroscopy Results for Bax and cBid Effects on Membranes [a]

System	20%CL-EPC		20%CL-EPC	
	Breakthrough Force (nN)	Membrane Thickness (nm)	Breakthrough Force (nN)	Membrane Thickness (nm)
SLS	2 ± 2	3.5 ± 0.6 (34%) 7.6 ± 0.8 (66%)	2.8 ± 0.3 (58%) 6.8 ± 0.4 (42%)	3.4 ± 0.4[d]
cBid-SLS[b]	0.7 ± 0.2 (43%) 3 ± 1 (57%)	3 ± 1 (47%) 6 ± 1 (53%)	3.8 ± 0.4	3.3 ± 0.7
Bax-SLS[b]	4 ± 2	4 ± 3 (42%) 8 ± 0.5 (58%)	3.2 ± 0.6 (53%) 6.2 ± 0.4 (47%)	3.1 ± 1.1
cBid-LUV[c]	1 ± 1	3 ± 2 (72%) 7 ± 1 (29%)	1.6 ± 0.6	2.7 ± 0.8
Bax-LUV[c]	0.6 ± 0.2 (80%) 7 ± 2 (20%)	3 ± 1	2.3 ± 1.1	3.4 ± 1.1[d]

[a]The distribution histograms were fitted with a Gaussian and the resulting peaks are reported as the mean value. Errors are expressed as the standard deviation of the Gaussian fitting. The area under the curve corresponds to the % of the population for distributions displaying multiple populations. Each sample was compared to the control by plotting the empirical cumulative distribution functions.
[b]Proteins were added directly to SLSs and analyzed.
[c]Proteins were incubated in LUVs and the resulting proteo-LUVs were used to make the SLSs, which were then analyzed.

7.3 cBid induces a rearrangement of the lipids in SLSs

In the absence of proteins, membrane thickness measured from the breakthrough forces presented two populations for the 20% CL-EPC mixture: a major one (66%) at 7.6 ± 0.8 nm and a smaller one (34%) at 3.5 ± 0.6 nm (Figure 7.3C). This difference in bilayer thickness is not evident from the AFM images. It could be that the underlying structures are below the lateral resolution limit of the AFM tip (<20 nm).

I also cannot discard the possibility that in some regions, the AFM tip could deform the membrane before rupture. To check this possibility, I separated the force curves with

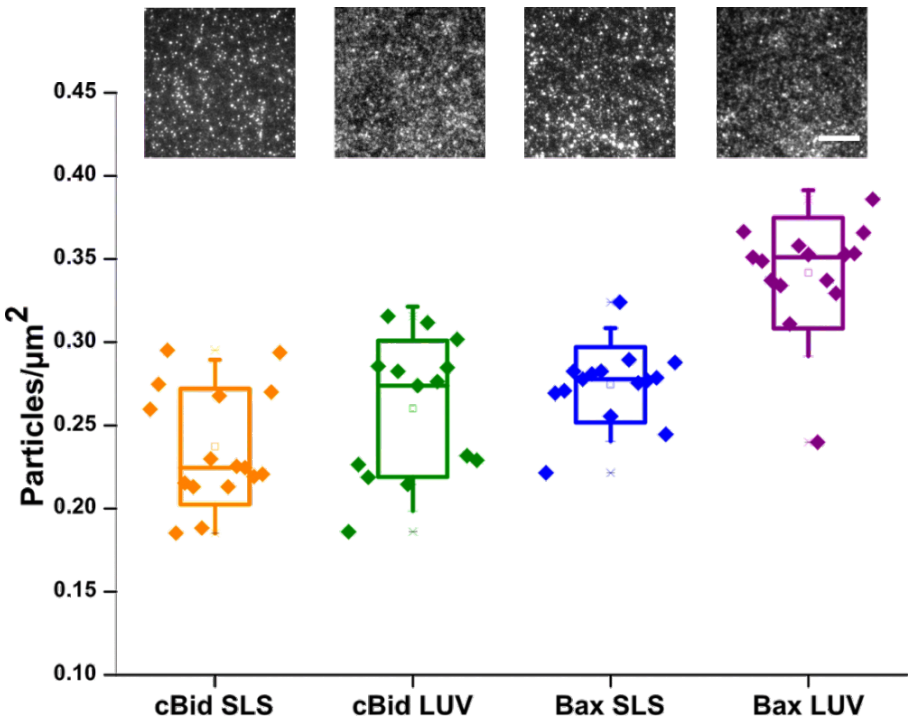

Figure 7.5: Protein concentration on the lipid surface. Fluorescently-labeled variants of 20 nM Bax or cBid were directly added to the SLS or preincubated in LUVs from which SLSs were formed. The samples were imaged by TIRF microscopy. Representative images for each experiment are reported. The number of particles were measured by a home-built software. Particle detection was performed applying the same threshold to all the samples. Data are from 3 different repetitions. Scale bar is 10 μm.

single breakthrough events having more than 4 nm thickness ("thick" section) and those below 4 nm thickness ("thin" section). I then created an average force curve from all the gathered force curves similar to Alessandrini et al. (2012) and fitted a model from Das et al. (2010):

$$F = \frac{\pi \kappa_A R_{tip}}{4} \left(\frac{2x}{d_{membrane} - x} \right)^2 \tag{7.1}$$

where κ_A is the area stretching modulus or the force needed to deform the membrane at a certain direction, R_{tip} is the radius of the AFM tip, x is the tip-sample separation and d is the membrane thickness.

Figure 7.6A shows the fitting of the averaged curves. Because the curve had shoulders prior to breakthrough, Das et al (2010) suggests to fit the curves in the areas between the shoulder. In my case, these were (i) the area in the contact region (the tip sample separation where the AFM tip is starting to push on the membrane), and (ii) the area just prior to breakthrough.

Alessandrini et al (2012) reported an area stretching modules for POPE membranes of 0.07-0.16 N/m. Nichols-Smith et al (2004) obtained 0.149 and 0.115 N/m for 5% and 9% CL-PC, respectively, using micropipette aspiration, indicating that CL lowers the area stretching modulus. Additional CL may lower this further. While I obtain much lower values, I see a relative difference between two types of force curves. Alessandrini et al (2012) suggested that looking at the slope of the line prior to the breakthrough event should already give an idea of the relative area stretching modulus between the two instances. A higher slope indicates a higher area stretching modulus. Figure 7.6B shows such a linear fitting, and indeed, the slope of the thin section is lower than that of the

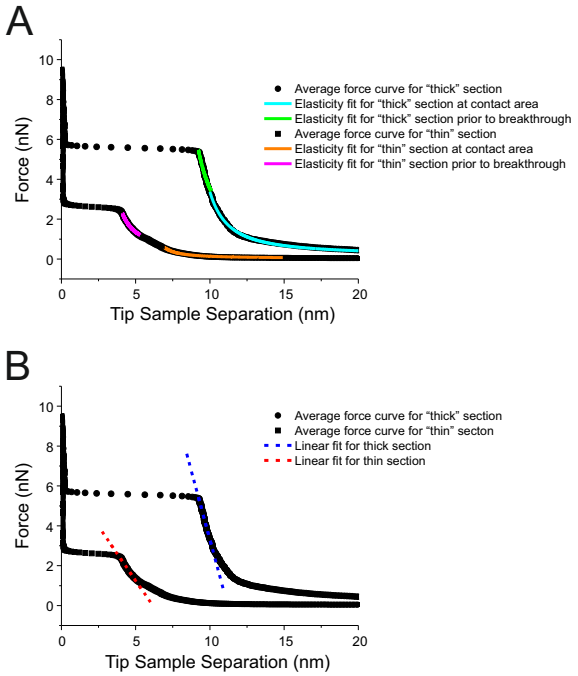

Figure 7.6: Elasticity fitting for force curves. (A) Force curves with thickness greater than 4 nm ("thick section", black circle) fitted with equation 7.1 in the contact area (cyan) and prior to breakthrough (green). Force curves with thickness less than 4 nm ("thin section", black squares) fitted with equation **??**eq:Elasticity in the contact area (orange) and prior to breakthrough (magenta). (B) same averaged curves in (A) but fitted with a line prior to breakthrough.

thick section.

Decrease in area stretching modulus indicate that a lower stress is required to achieve a given change in membrane area and suggest a weakening of the cohesive strength of the membrane. In the case for 20%CL-EPC, it seems to suggest that while I do not see topographical differences with AFM imaging, there are areas in the bilayer which are more prone to deformation.

In contrast, breakthrough events for MitoMix SLSs yielded only one thickness population centered at 3.4 ± 0.4 nm (Figure 7.3C and Table 7.1). This might reflect the different concentrations of CL, a non-lamellar lipid, present in the two samples. We have previously reported this effect in SLSs with increasing amounts of CL, which could be due to the formation of non-lamellar structures induced during the SLS formation process by calcium (Unsay et al., 2013).

When cBid was added to 20%CL-EPC SLSs, I still detected two populations of thickness values (3 ± 1 and 6 ± 1 nm), but this time having similar proportions (47% and 53%, respectively compared to 34% and 66%, respectively in SLSs without cBid) and broader distributions (Figure 7.3F, 7.3H and Table 7.1). The lower population (3 ± 2 nm) became even predominant (72%) when cBid was pre-incubated in LUVs before formation of the SLSs (Figure 7.3K, 7.3M and Table 7.1). When cBid was added to MitoMix SLSs, or pre-incubated with MitoMix LUVs before formation of SLSs, the respective populations were all centered at around a value of 3 nm (3.3 ± 0.7 nm for cBid-SLS and 2.7 ± 0.8 in cBid-LUV) (Figure 7.4F, H, K, M, and Table 7.1).

Taken together, these data indicate that cBid decreases the fraction of lipid bilayer with ∼7 nm thickness, which might be associated with reorganization of non-lamellar structures typical of CL-enriched membranes into a more deformable bilayer conformation, characterized by a thickness of 3 nm. It is important to note that, in contrast to Bax, these membrane alterations are not related with pore formation as cBid does not permeabilize

membranes at our given conditions. These observations may have implications for the role of cBid in the remodelling of the mitochondrial membrane during apoptosis.

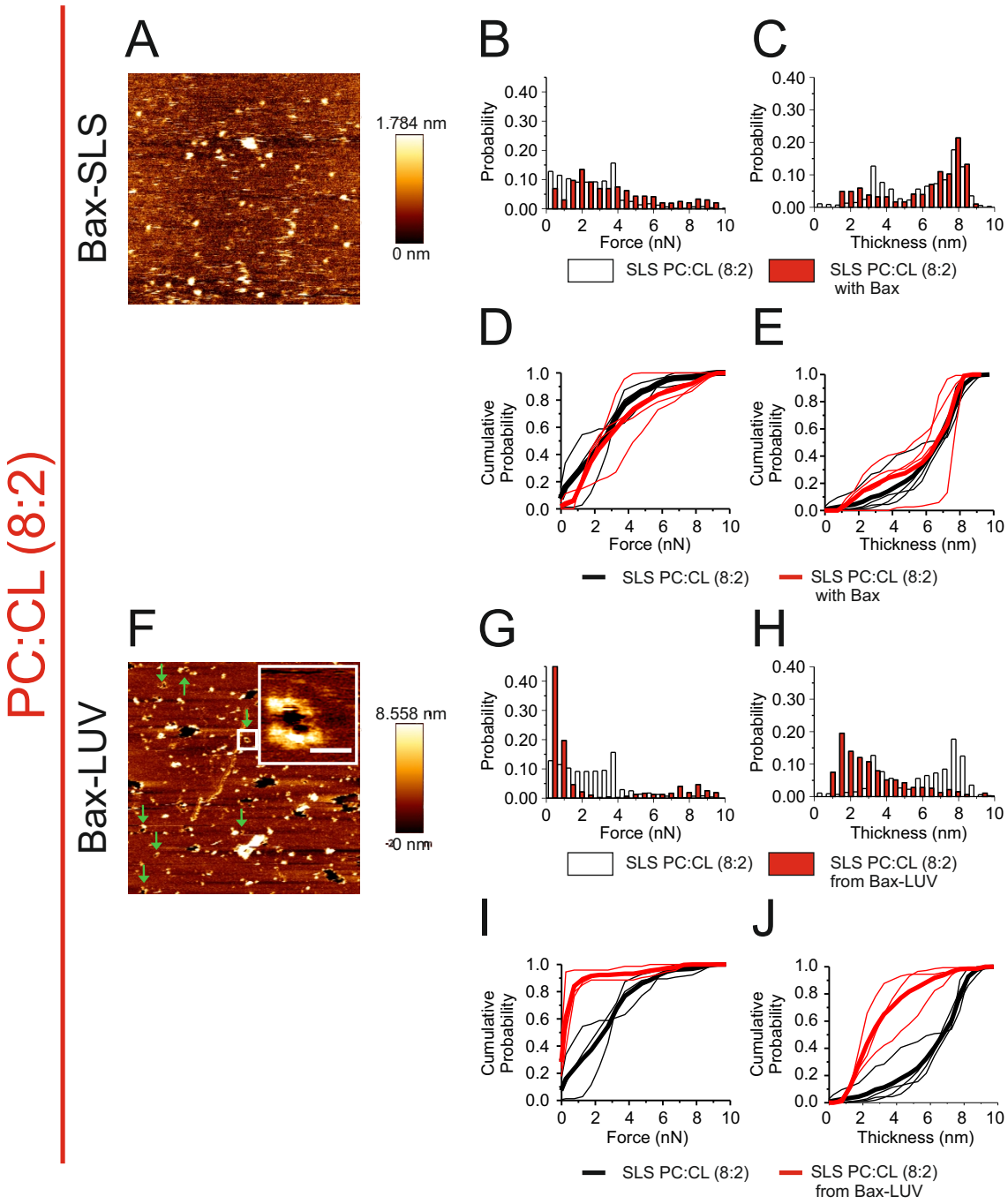

Figure 7.7 (previous page): Membrane effects of Bax on 20%CL-EPC Membranes.(A) AFM image for 20%CL-EPC SLSs with heat-activated Bax. (B-C) Effect of Bax on pre-formed SLSs and comparison of force and thickness values before (white bars) and after the addition of the protein (red bars). (D-E) Cumulative distribution plots of SLS (black) and Bax-SLS (red) showing differences in force (D) and thickness (E). Each plot represents a single repetition. Thick lines represent average cumulative distributions for all the repetitions for SLS and Bax-SLS samples. (F-H) Effects of heat-activated Bax incubated with LUVs. Bax-LUVs were used to prepare the SLSs. (F) Image of a SLS containing Bax pores (green arrows) together with membrane defects. The inset is a zoom-in of a representative pore (scale bar is 100nm). (G-H) Comparison of force and thickness values before (white bars) and after the addition of the protein (red bars). (I-J) Cumulative distribution plots of SLS (black) and Bax-LUV (red) showing differences in force (I) and thickness (J). Each plot represents a single repetition. Thick lines represent average cumulative distributions for all the repetitions for SLS and Bax-SLS samples. Pictures scale is 5 μm. Histograms are normalized for better comparison (the number of points varied between 500 and 1500).

7.4 Oligomeric, but not monomeric Bax changes properties supported lipid structures

Most *in vitro* research with Bax so far has been based on the activation of the protein with cBid or BH3 peptides. As a result, most knowledge about how this protein affects membranes cannot be fully separated from cBid. In order to dissect the effect of Bax on lipid bilayers independently of cBid, I exclusively activated Bax by heating at 43 °C. Interestingly, when I added heat-activated Bax to SLSs (Bax-SLS), I observed only a slight increase and broader distribution of the force values: 4 ± 2 nN in 20% CL-EPC (Figure 7.7A-B and D) and 3.2 ± 0.6 nN in MitoMix, with the latter having a second population at 6.2 ± 0.4 nN (and 7.8A-B and D). Subburaj et al (2015) have recently shown that under these conditions, Bax stays in the membrane in a monomeric, non-diffusive form. I checked if these changes are due to the heating of the SLSs during Bax activation, but this is not the case (Figure 7.9). In this scenario, the small changes observed were likely due to the insertion of monomeric Bax, which does not significantly affect the membrane's physical properties.

To investigate if the oligomeric state of Bax plays a role on its effects on membrane organization, I prepared the SLSs from liposomes incubated with heat activated Bax. Under these conditions, Bax is able to self-associate in the free-standing membranes of the liposomes and is later present in the SLS as a mixture of oligomeric species based on dimer units (Subburaj et al., 2015). Bax is able to induce pore formation of different size in model membranes. (Saito et al., 2000, Epand et al., 2002b, Bleicken et al., 2013a, Salvador-Gallego et al., 2016). Figures 7.7F and 7.8F clearly show the presence of membrane defects and pores on SLSs from liposomes previously incubated with heat activated Bax (Bax-LUV), for both studied lipid compositions. Interestingly, pore formation correlates with a drastic decrease of the breakthrough force to 0.6 ± 0.2 nN in 20%CL-EPC (Figure 7.7G, 7.7I and Table 7.1), which is less apparent in MitoMix, with an average value of 2.3 ± 1.1nN (Figure 7.8G, 7.8I and Table 7.1).

To exclude that the different behavior in the Bax-SLS and Bax-LUV systems was due to differences in P/L ratio, we measured particle density by TIRF microscopy (Figure 7.5). Although particle densities in Bax-SLS and Bax-LUV samples are statistically different ($p < 0.05$), the measured lipid/particle (L/Pa) ratio values are quite similar, being $4.898x10^6$ and $5.741x10^6$ for Bax-SLS and Bax-LUV, respectively. Therefore, particle concentration at the surface cannot account for the different behavior we observed, but rather this is due to the different nature of Bax, monomeric versus oligomeric. Solely Bax insertion in the membrane is not sufficient and needs to be accompanied by oligomerization in order

to modify the mechanical properties of the membrane. This also strengthens a correlation between the alteration of the mechanical properties and membrane permeabilization induced by Bax oligomers.

For the same reason, the insertion of monomeric Bax in SLSs did not result in any change in thickness (Figure 7.7C, 7.7E and Table 7.1). However, when I allowed Bax to oligomerize in LUVs, Bax restricted the thickness to that of a single bilayer (3-4 nm, Unsay et al. (2013)) in the 20% CL-EPC system (Figure 7.7H, 7.7J and Table 7.1). No changes in the membrane thickness were observed in the MitoMix system for both Bax-SLS and Bax-LUV (Figure 7.8C, E, H, J and Table 7.1).

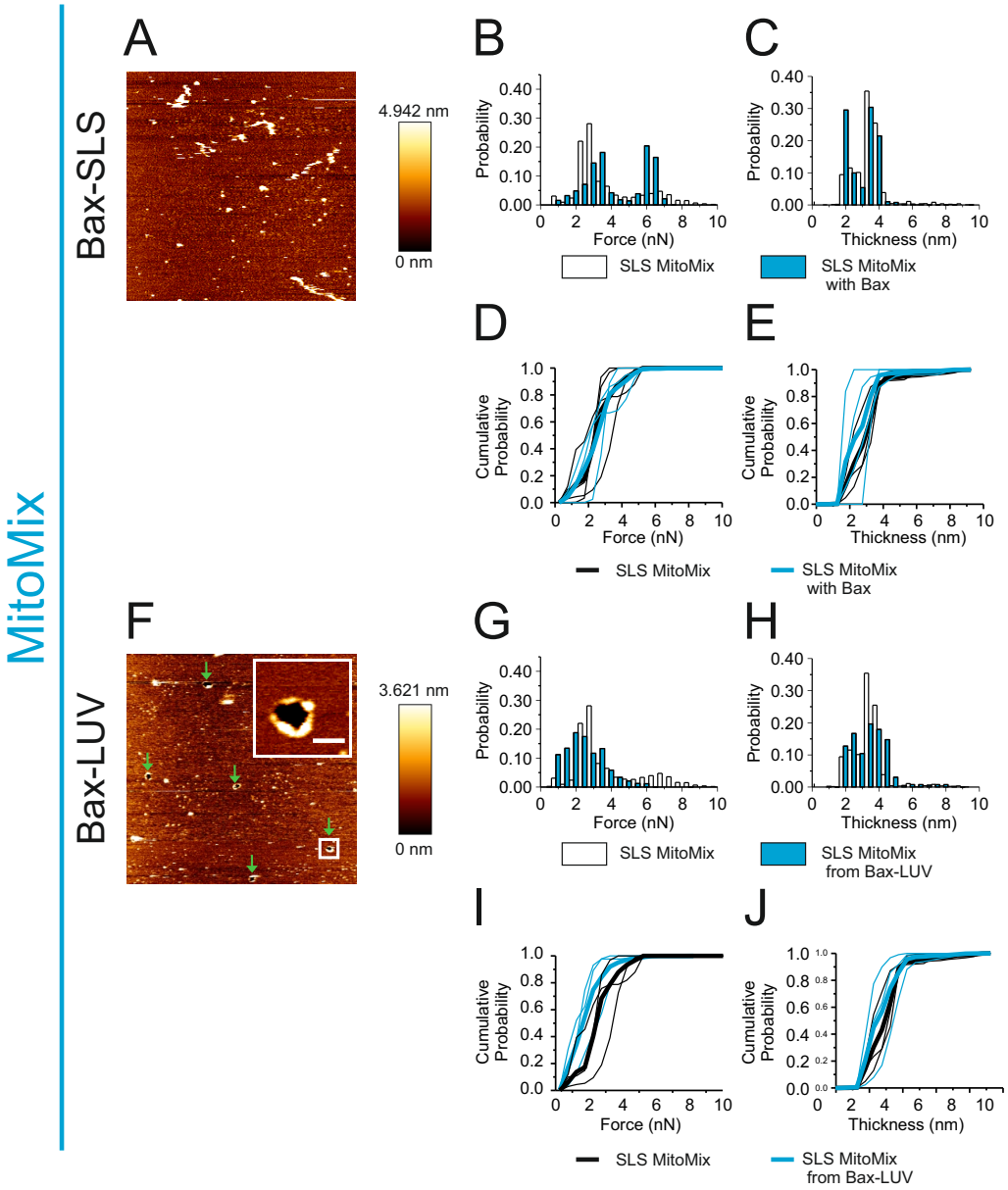

Figure 7.8 (previous page): Membrane effects of Bax on MitoMix Membranes.(A) AFM image for MitoMix SLSs with heat-activated Bax. (B-C) Effect of Bax on pre-formed SLSs and comparison of force and thickness values before (white bars) and after the addition of the protein (blue bars). (D-E) Cumulative distribution plots of SLS (black) and Bax-SLS (blue) showing differences in force (D) and thickness (E). Each plot represents a single repetition. Thick lines represent average cumulative distributions for all the repetitions for SLS and Bax-SLS samples. (F-H) Effects of heat-activated Bax incubated with LUVs. Bax-LUVs were used to prepare the SLSs. (F) Image of a SLS containing Bax pores (green arrows). The inset is a zoom-in of a representative pore in the figure (scale bar is 100 nm). (G-H) Force and thickness values are compared before (white bars) and after the addition of the protein (blue bars). (I-J) Cumulative distribution plots of SLS (black) and Bax-LUV (blue) showing differences in force (I) and thickness (J). Each plot represents a single repetition. Thick lines represent average cumulative distributions for all the repetitions for SLS and Bax-SLS samples. Pictures scale is 5 μm. Histograms are normalized for better comparison (the number of points varied between 600 and 2000).

7.5 Commentary on double breakthrough events

Double breakthrough events during force spectroscopy measurements of supported bilayers present challenges in data analysis and interpretation. Because of their numbers, I decided to not include these double breakthrough events in my analysis on the membrane effects of cBid and Bax. I do, however, acknowledge that they also require further discussion. As such, this section provides a detailed examination of these events in the context of cardiolipin-containing SLSs, cBid and Bax. For clarity, the peaks of single breakthrough events are denoted as Peak A. The first peak in the force curves with double breakthrough events is denoted as Peak B and the second peak is denoted as peak C as shown on Figure 7.10A.

Multiple breakthrough events imply the piercing of multiple uncoupled thin materials after another. In supported lipid structures, this could mean three things: (i) that there is a double bilayer, one on top of another or other non-lamellar structures, (ii) there is uncoupling of the two leaflets of the bilayer so that I pierce one after another, or (iii) there is dirt (including protein or lipidic material) on top of a single bilayer or accumulated on the tip (Canale et al., 2010, Alessandrini et al., 2012, Unsay et al., 2013).

Alessandrini et al (2012) characterized the breakthrough in POPE (and POPG in supplemental material) bilayers under different temperatures, loading rate and cantilever stiffness. They studied bilayers with coupled and uncoupled leaflet, the latter producing two breakthrough events. In this paper, they showed that peaks of the force distribution of the first and second breakthrough events would differ depending on how strongly coupled the two leaflets are.

Furthermore, accumulation of dirt may be assessed based on the how double peaks distribute on an image. The AFM acquires the force curves in a serpentine manner and if dirt has indeed accumulated on the tip, then the double breakthrough events would accumulate on the image in a non-random fashion following the manner of acquisition. Figure 7.11 shows a force map of two representative 20%CL-EPC SLSs indicating that dirt did not accumulate.

Lastly, as I assume an overall non-lamellar structure and not merely one bilayer on top of another, there is possibility that this is more complicated than our simplistic models. Clearly, it is hard to distinguish between these possibilities via AFM and further analysis of the supported membrane by structural techniques (like neutron scattering) may be necessary.

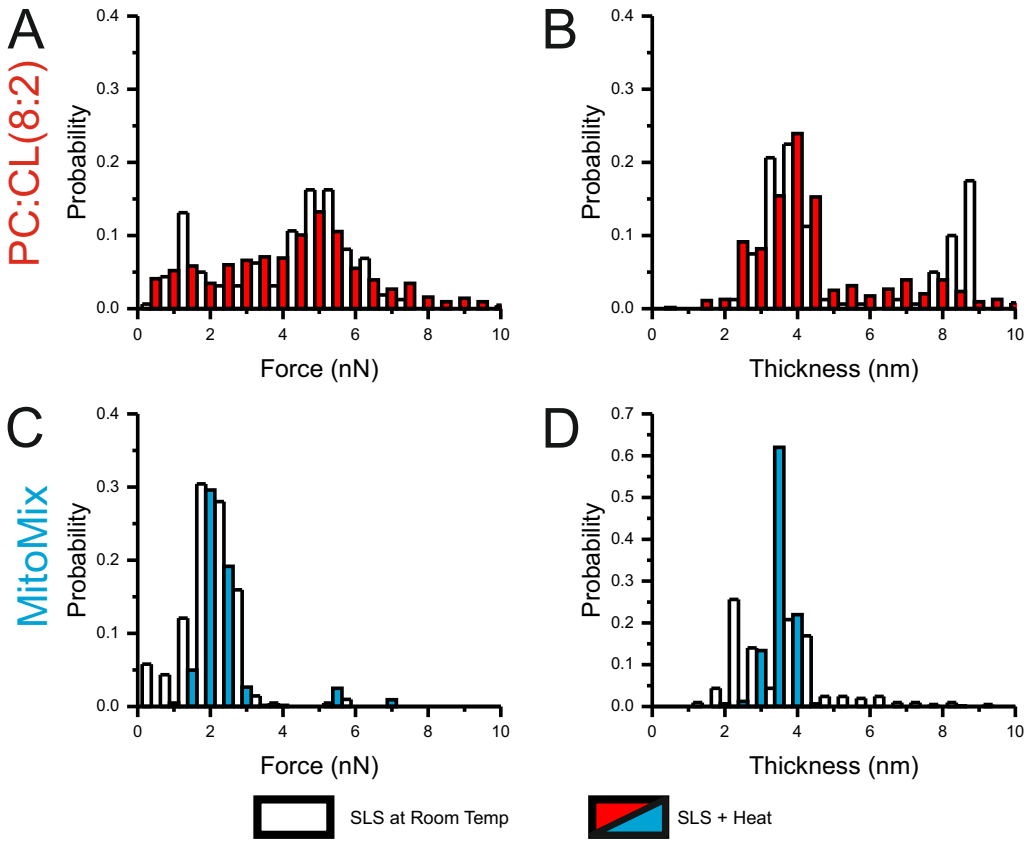

Figure 7.9: Effect of heat activation on the physical properties of SLSs. (A) Force and (B) thickness distribution for 20%CL-EPC before heating (white bars) and after heating (red bars). (C) Force and (D) thickness distribution for MitoMix before heating (white bars) and after heating (blue bars). .

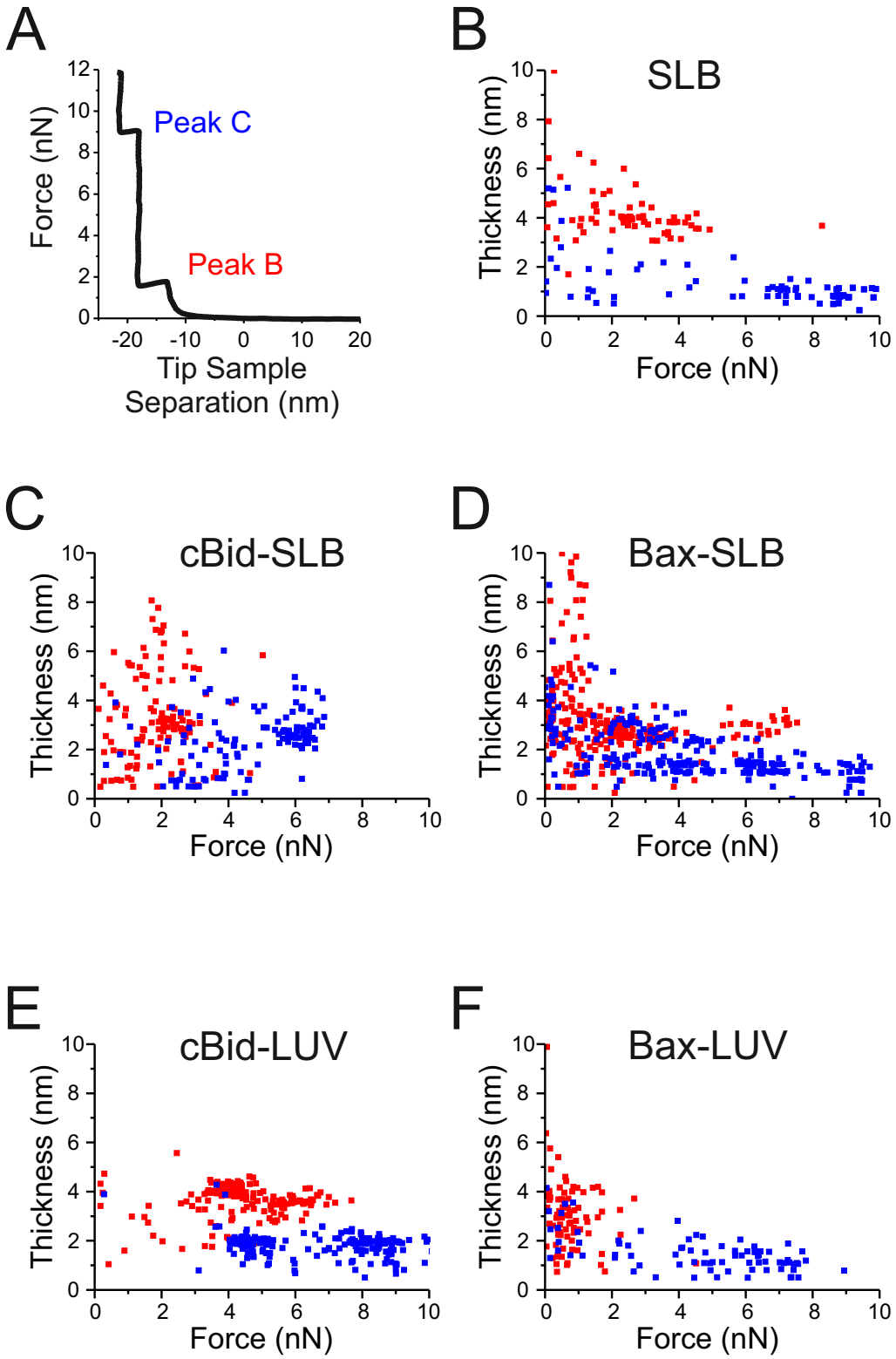

Figure 7.10: Double Breakthrough Events from 20%CL-EPC membranes.(A) A representative force curve showing double breakthrough events. (B-F) Thickness vs. Breakthrough Force scatter plots for different samples: (B) SLS only, (C) cBid-SLS, (D) Bax-SLS, (E) cBid-LUV, and (F) Bax-LUV. Peak B is given as red squares and Peak C as blue squares.

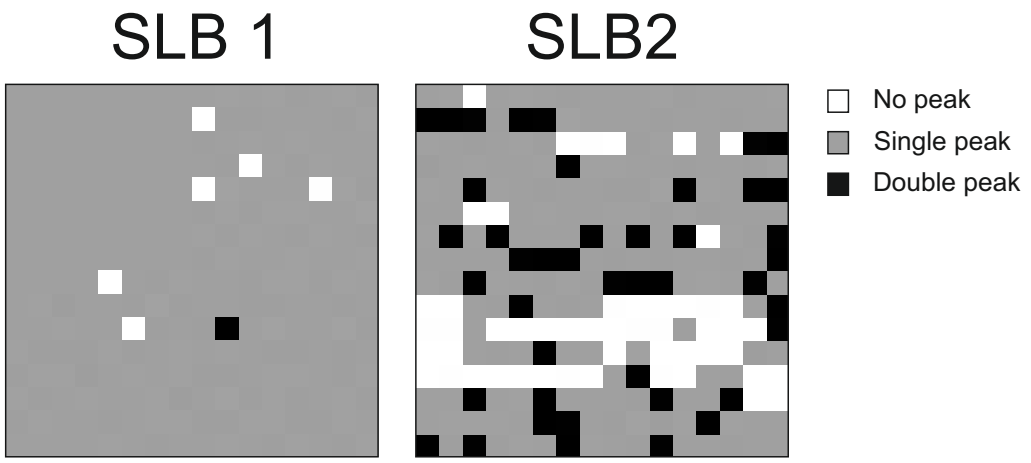

Figure 7.11: Distribution of Breakthrough Events in Force Maps of 20%CL-EPC membranes. Two representative force maps are shown for comparison. The double breakthrough events appear randomly across the force maps.

7.6 Lipid packing does not change in the presence of Bax or cBid

While both cBid and oligomeric Bax lower breakthrough force and change membrane thickness, only oligomeric Bax creates pores in the membrane. From the calcein permeabilization assay shown in Figure 7.1, cBid alone does not open up pores in the membrane systems used for AFM experiments. In a previous study we have shown that Bcl-xL is able to induce pore formation in vesicles in the presence of cBid, but these pores are not stable and eventually close up (Bleicken et al., 2013b). This indicates that even if a pore is opened by other means, cBid is not able to stabilize pores. In this scenario, I hypothesize that the reduction in breakthrough force by cBid is caused by changes in the lipid packing, resulting in a reduction of the attraction forces between the membrane components. This, in turn, would reduce the energy of membrane rearrangement and eventual rupture instead of actually stabilizing the edge of a hole in the membrane.

To test this hypothesis, I measured how cBid and Bax individually affect relative lipid packing in LUVs using the fluorescence marker MC540. The fluorescence emission of MC540 increases in more hydrophobic environments, thus the relative intensity of MC540 is indicative of lipid packing: loosely packed bilayers have higher MC540 fluorescence and tightly packed membranes have lower MC540 fluorescence (Stillwell et al., 1993, Williamson et al., 1983).

It has been previously shown that aside from lipid packing, the fluorescence intensity of MC540 is sensitive to temperature changes (Langner and Hui, 1993). This is not related to partitioning of the fluorophore between the lipid membrane and the aqueous environment, but rather to a change in the quantum yield of MC540. I then measured the MC540 fluorescence intensity as a function of temperature in pure EPC, 20%CL-EPC, and MitoMix (Figure 7.12A-C, black data points). After that, I normalized the intensity to measurements of MC540 in ethanol, which Langner and Hui (1993) claimed to mimic the polarity that MC540 experiences while in the membrane (Figure S2A-C, red data points). I see that while the ratio slightly increases then decreases with increasing temperature, these changes are not significant. Based on these experiments, I indeed showed that the change in the fluorescence intensity of MC540 is not due to changes in lipid phases, but simply due to its sensitivity to temperature.

With then tested the effect of our proteins on liposomes containing MC540. I incubated the liposomes with different concentrations of proteins and normalized to lipid only

samples. In the case of heat-activated Bax, I also subjected the liposomes without proteins to heat treatment, and normalized the Bax-containing samples to this.

I show that for our controls BSA (non-inserting) and Melittin (inserting), the MC540 did not show any significant changes for 20%CL-EPC and MitoMix compositions (Figure 7.12D and G, respectively). This is a bit surprising as melittin is an amphiphatic pore-forming peptide that has an affinity to negatively charged membranes (Dathe and Wieprecht, 1999, Takahashi et al., 2013). This could indicate that the insertion of peptides or protein may not be enough to induce any changes in the fluorescence intensity of MC540. On the other hand, the liposome may compensate for the insertion of melittin by changing its surface area/size.

I also tested the effect of cleaved (cBid) and uncleaved Bid, and also saw no significant differences across different concentrations (Figure 7.12E and H). This indicates that while cBid binds to the membrane (Bleicken et al., 2013b, Epand et al., 2002a), this binding is not enough to change the fluorescence intensity of MC540. Similar to melittin, it could be that the liposome may be compensating for the insertion of cBid by changing its surface area/size. Both melittin and cBid have been shown to increase the local curvature of membranes (in a mechanism that releases small vesicles from larger ones) (Takahashi et al., 2013, Bleicken et al., 2016). This should imply a decrease in packing of the membrane as smaller vesicles are highly curved and are also less packed. On the other hand, the curved regions may be too few compared to the rest of the membrane that its effects is challenging to detect it experimentally. This shows that MC540 may not be the best probe to characterize this magnitude of lipid packing changes.

Finally, I looked at Bax only, cBid-activated Bax (Bax + cBid) and heat-activated Bax (Bax + Heat). As with cBid, no significant difference can be measured between different conditions with respect to the liposome only sample in both lipid mixtures. Again, it is still possible that there are packing effects, but MC540 is not an appropriate method to detect it.

7.7 Proapoptotic Bid and Bax exhibit distinct membrane remodelling activities

In this work, I studied the effect of Bax and its activator cBid on SLSs mimicking the mitochondrial lipid composition by force spectroscopy. In order to discriminate the role of each individual player, I have studied their effect independently of each other. In one case I have used cBid, which is the active, cleaved form of Bid, comprised by two fragments p7 and p15. Upon binding to membranes, cBid loses the p7 fragment and retains essentially tBid (p15) in the membrane (Bleicken et al., 2012). tBid activates pro-apoptotic Bcl-2 members, Bax and Bak, resulting in their oligomerization and permeabilization of the MOM.

Here, I have analyzed the effect of cBid added to pre-formed supported lipid structures (cBid-SLSs) and to liposomes from which supported lipid structures were formed (cBid-LUVs). I observed a reduction of the breakthrough force in both cases, although to different extent. It has been suggested that tBid binds and embeds in the membrane with different conformations (Shamas-Din et al., 2013a). In this process it exposes its BH3 domain that can in turn bind to other Bcl-2 family members and possibly recruit them to the membrane (García-Sáez et al., 2009, Yao et al., 2009, Bleicken et al., 2013b). Shivakumar et al. (2014) also report different degrees of tBid insertion in the membrane, as fast diffusing, slow diffusing and immobile tBid molecules. This suggests that the detected membrane remodelling could be promoted by the initial steps of binding/insertion of cBid, which are similar in the two systems. It could also be a difference in the protein-to-lipid ratio (P/L) between the cBid-SLS and cBid-LUV, but we saw that in practice, the

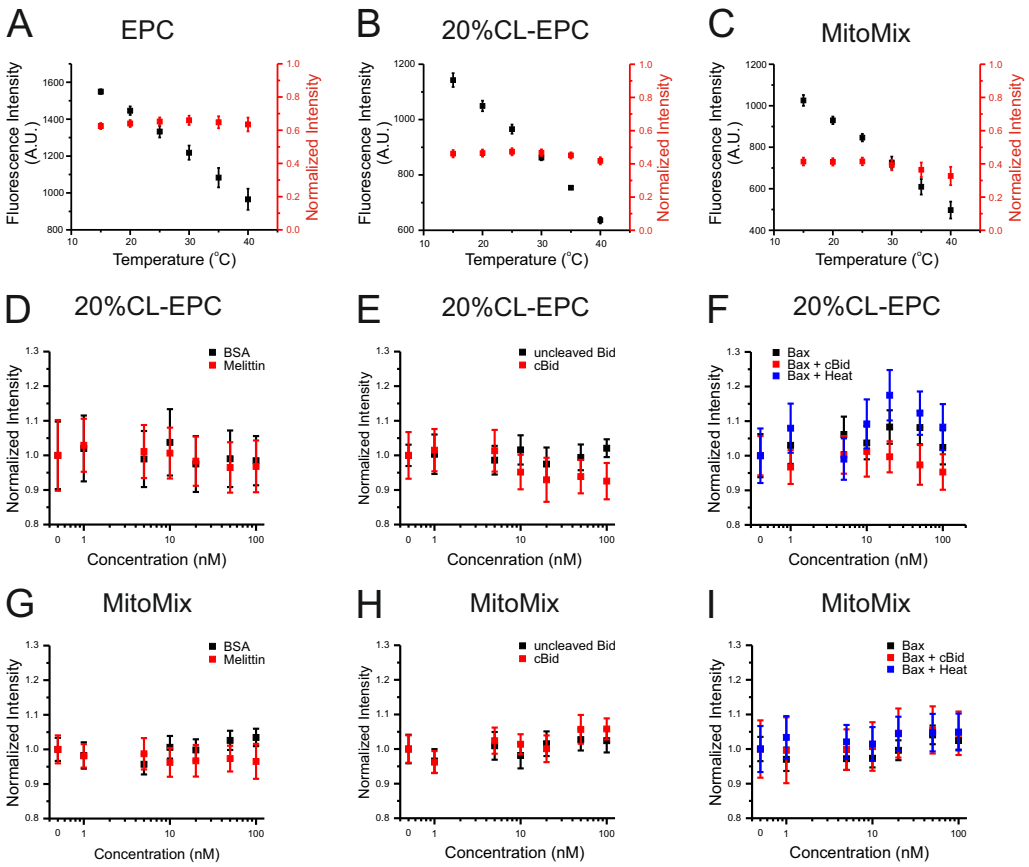

Figure 7.12: Lipid Packing Assay.(A-C) Effect of temperature on the fluorescence intensity of MC540 (black data) in different lipid mixtures: (A) Egg PC, (B) 20%CL-EPC, and (C) MitoMix. Fluorescence intensity is then normalized to a solution of MC540 in ethanol at the given temperature (red data). (D-I) Protein effects on the fluorescence intensity of MC540 in 20%CL-EPC (D-F) and MitoMix (G-I): BSA and melittin (D and G), cBid and uncleaved Bid (E and H), Bax, cBid-activated Bax and heat-activated Bax (F and I)

particle density in the membranes are similar. Thus, the difference in the breakthrough force between both systems suggests that interaction with the solid support upon initial membrane binding likely hinders the overall effect of cBid.

The presence of cBid also altered the distribution of thickness values of 20% CL-EPC membranes in favor of a single thickness centered at 3 nm (typical of a single bilayer Unsay et al. (2013)) instead of the one at 7 nm (Table 7.1). While the asymmetric insertion of antimicrobial peptides (Lee et al., 2004) or proteins (Satsuma et al., 2012) to a bilayer has been shown to induce membrane thinning, I cannot be certain if this is also the case for supported membranes – especially those with propensity to form non-lamellar structures. Thus, this shift to lower thickness values can also be interpreted as a reorganization of the non-lamellar structures by cBid. In agreement with this, the thickness values of MitoMix samples are not changed by cBid, placing to the same value of 3 nm.

It has been proposed that tBid helps the reorganization of CL in the membrane, which could alter the local membrane curvature (Kim et al., 2004, Epand et al., 2002a, Bleicken et al., 2016). These structures might act as points of entry for Bcl-2 proteins – especially for Bax and Bak – in the mitochondria due to their low breakthrough force. In support of this hypothesis, it has been shown that highly curved structures induced by the mitochondrial fission protein Drp-1 also stimulate Bax oligomerization (Montessuit et al., 2010, Brooks et al., 2011). Furthermore, a recent study showed the localization of Bax on highly-curved regions arising from membrane budding/tethering in giant unilamellar vesicles (Bleicken et al., 2016). Putting these observations from previous studies together with the results, the picture that emerges suggests the role of cBid as promoter of possible rearrangements in the membrane that might prepare the ground for Bax membrane insertion and permeabilization. While this has not been observed in the MitoMix composition, it is also tempting to speculate that this only happens in CL-rich regions of the mitochondria, such as the contact sites between the inner and outer membrane. It has been previously shown that Bid-CL interaction at these contact sites contribute to cristae reorganization and cytochrome c release (Kim et al., 2004)

In contrast to cBid, the behavior of Bax added to pre-formed supported lipid structures (Bax-SLSs) or to liposomes from which supported lipid structures were formed (Bax-LUVs) was very different, indicating that the form in which Bax is inserted in the membrane may play a role on how the membrane structure and physical properties are affected.

Subburaj et al (2015) have previously shown that full-length Bax inserts into SLSs as a monomer. They suggest that Bax spans the membrane and makes non-specific interaction with the support that hinders its oligomerization. In these conditions, the insertion of the monomeric protein induces a slight increase of the breakthrough force, while it does not affect the thickness, indicating that the insertion increases the amount of material in a fixed membrane area and may hinder lateral movement of lipids, and therefore hinder the breakthrough in relation to Huang's Two-State model (Huang, 2000). This model states that a mere insertion of peptides in a lipid membrane, which happens at low P/L ratio, is not enough to form pores. At low P/L ratio, the protein insertion increases the area of the membrane without producing pores. However, in our case, SLSs will not be able to compensate for the insertion by changing the area, resulting in no effect on the breakthrough force. At high P/L ratio, the changes induced by the proteins is also higher to a point that pores can readily form (Huang, 2006). Interestingly, it has been proposed that oligomerization is a necessary step for pore forming peptides (Sengupta et al., 2008) and proteins (Cosentino et al., 2016), and here, Bax is not an exception.

Only when Bax oligomerization was allowed by incubating the protein with LUVs prior to SLS formation, did I observe a decrease in the breakthrough force. Similar to the TIRF experiments with cBid, Bax-SLS and Bax-LUV also showed similar particle densities, indicating that these differences could not be attributed to differences between the

theoretical P/L ratio of these systems. Considering that oligomerized Bax forms stable toroidal pores in membrane (Bleicken et al., 2013a, Salvador-Gallego et al., 2016), it is reasonable to associate this decrease in breakthrough force with a decrease of the line tension to favor membrane permeabilization. However, unlike the findings of Sengupta et al. (2008), Bax dimers have a definite structure (Bleicken et al., 2014), and therefore might not form similar disordered toroidal pores as antimicrobial peptides. Our results pinpoint that the effects of Bax on the membrane depend on its proper inserted conformation and oligomerization.

To better understand the implications of such reduction in the force and its correlation to the effects of Bcl-2 proteins in membranes, I considered at the Continuum Nucleation Model for the rupture of thin films by a sharp probe derived by Butt and Franz (2002). They described the energy of the hole with radius r_{hole} produced by the AFM tip as:

$$E = 2\pi r_{hole}\Gamma + \pi r_{hole}^2(S - \frac{F}{2\pi R_{tip}}) \tag{7.2}$$

Where the first term, $2\pi r_{hole}\Gamma$, represents the free energy cost associated with exposing the hydrophobic core to the aqueous environment and Γ is the line tension. The second term, $\pi r_{hole}^2 S$, is the change in interfacial free energy. S is called the "spreading pressure" as it quantifies the tendency of the bilayer to spread into the gaps between the tip and substrate. This term is equivalent but opposite to membrane tension, that is a stress on the membrane that contributes instead to the opening of the pore. The last term characterizes the load F, exerted by an AFM tip with radius R_{tip} on the film. The first two terms are commonly encountered when describing the energetics of statistical lipidic pores and are also applicable to pore-forming proteins (Lee et al., 2004), or vesicle rupture during electroporation (Dimitrov and Jain, 1984, Zhelev and Needham, 1993).

In the context of force spectroscopy experiments on supported bilayers, the pore opening is driven by the load of the AFM tip and the pore closing is driven by two factors: line tension and spreading pressure. In Butt and Franz's model, they showed that a lower mean breakthrough force is associated with a low spreading pressure and/or low line tension (Butt and Franz, 2002, García-Sáez et al., 2007a, Chiantia et al., 2006).

One question that comes to mind in my system is the possibility of having non-lamellar phases. In a sense, is the continuum nucleation model still applicable in this case?

In the presence of other molecules aside from lipids, the driving force of pore stabilization is based on the ability of specific molecules, in this case proteins (can also be called line actants), to balance the pore closing tendency (due to the energetic cost of exposing hydrophobic chains to aqueous environment). The existence of stable non-lamellar (whether be it hexagonal or cubic, among others) phases may hinder spreading once an AFM tip has punctured the membrane, if the attractive forces between the lipids is greater than its interaction with the solid support and surrounding medium. On the other hand, a collapse of these phases, in the case where the interaction between the lipids is weaker than the interaction between lipid and support and/or medium, may result in an easier spreading after puncture. As another example, if the membrane adopts a "double bilayer" structure, it would expose a higher area of hydrophobic molecules compared to single bilayers during breakthrough, and would probably then require more stabilizing effect from the line actant. All these effects could still be accounted for by the two parameters: line tension and spreading pressure.

Fitting the force histograms with the continuum nucleation model (Butt and Franz, 2002), I obtained a decrease of the line tension in the presence of Bax of 43% for Mito-Mix and 87% for CL-EPC SLSs from Bax-LUV. These values are greater than the one reported for Bax peptides on DOPC membranes (30%) (García-Sáez et al., 2007a). In contrast to the peptides, the full-length protein exhibits higher levels of regulation (from

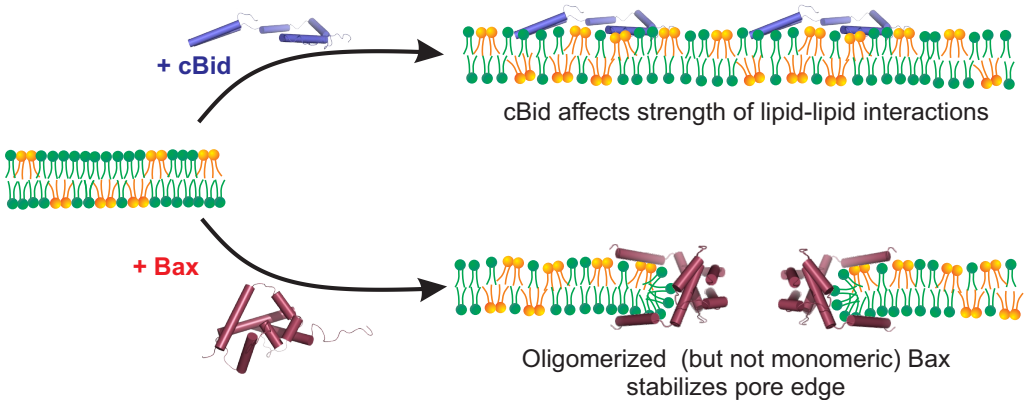

Figure 7.13: Distinct membrane remodelling properties of Bax and cBid.cBid induces changes in CL-containing membranes by lowering the strength of lipid-lipid interactions. Monomeric Bax does not change the membrane properties, but oligomeric Bax lowers the line tension at the edge of a pore. Here, oligomeric Bax is represented by the "clamp model" according to Bleicken et al 2014

insertion to oligomerization). Bax contains two helices involved in pore formation and it also oligomerizes in the membrane, which would locally increase the concentration of line-actant components and explain the larger reduction in line tension at the pore edge. In agreement with this, previous studies showed that the size of Bax pores could be increased by increasing its membrane density (Bleicken et al., 2013a, Saito et al., 2000). Simulation studies on pore-forming peptides suggests that oligomerization/aggregation is a necessary step to introduce toroidal pores (Sengupta et al., 2008). This also makes the case of cBid's inability to form pores in physiological conditions.

Furthermore, cardiolipin could play a role and enhance this effect, which could explain the higher change of line tension in 20% CL-EPC compared to MitoMix.

Interestingly, the data on membrane thickness suggests that in the presence of cBid or Bax the membrane mostly adopts a thickness similar to that of a single bilayer despite our previous findings that high CL content can induce the formation non-lamellar structures during SLS formation (Unsay et al., 2013). In the context of cBid-LUV and Bax-LUV, it could also be possible that the insertion of the protein affects the way the proteo-LUVs are adsorbing, fusing and spreading on the surface of the solid support, and therefore affect the apparent membrane thickness.

In summary, here I showed that cBid and Bax are capable of individually reorganizing the membrane by modifying its mechanical properties and thickness. In contrast to cBid, oligomerization and associated pore formation are required for Bax-mediated alterations of the membrane organization. This might be related with the role of cBid in preparing the membrane for Bax insertion. Altogether, our results show that cBid and Bax exert distinct effects on the lipid structure and physical properties of the membrane.

Chapter 8

Hunting for pores: Structure of Bax in the membrane

While Bax permeabilization of the membrane is well established in the field of apoptosis, the structure of the Bax pore remains elusive. Though high-resolution images of Bax pores on membranes are available (Epand et al., 2002b), the study used preformed Bax oligomers stabilized by detergents and calcium ions, which may alter both the 3D structure of Bax and the membrane as discussed before. These Bax oligomers were inserted in pre-formed bilayers using high amounts of calcium and shown to form 100-nm pores in the membrane with proteins purportedly fully lining the edge of the pore.

Another study examining nanodisc-embedded Bax molecules using cryogenic electron microscopy showed that nanodisc-embedded Bax monomers where able to formxs 3.5-nm pores, large enough to permit passage of small molecules, such as cytochrome c (Xu et al., 2013). While the study presupposes that the size of the nanodisc and nanodisc:Bax ratio should allow only one Bax molecule per nanodisc, this was not directly confirmed due to the resolution limit of cryo-EM and the iterative 3D reconstruction method used. More recently, our group used electroparamagnetic resonance to reconstruct Bax dimer structures in the membrane using double electron-electron resonance, which measures the distance between two unpaired electrons from spin labels at different positions of the molecule (Bleicken et al., 2014). This new structure coincided well with the structure by Czabotar et al. (2013) showing the dimerization domain of active Bax (consisting of α2-4 and a part of α5). Furthermore, by labeling the supposedly transmembrane helices (α5, α6 and α9), our structure suggested that α5 and α6 may interact superficially in the context of a membrane pore, prompting us to favor the clamp model over the previous umbrella model. Therefore, we cannot exclude that the pores from the nanodisc observed by Xu et al. (2013) may be stabilized by a dimer rather than a monomer. Regardless, these structural studies provide strong evidence that Bax, either as a monomer or dimer, can form pores without necessarily having to line the full edge of the pore.

In the previous chapter, I used AFM to strengthen the arguments for this clamp model by showing that LUVs incubated with activated Bax adopt a membrane thickness of around 3-4 nm in contrast to thicker membranes for the case of 20%CL-EPC. To further understand the Bax structures in membranes, I used AFM to achieve high-resolution imaging capabilities inaccessible to conventional light microscopy techniques.

Heat-activated Bax was used to survey the different structures formed by Bax in the membrane. Similar to previous studies, I used 20% CL-EPC membranes. Parallel experiments were performed by Dr. Katia Cosentino using MitoMix. Bax oligomers in membranes were formed by incubating Bax with LUVs at 43°C. The resulting proteo-LUVs were used to make supported bilayers as described in the previous section.

This study was part of a greater effort to study Bax structures in mitochondria of live

cells using super resolution imaging, performed by Raquel Salvador-Gallego.

8.1 Oligomerized Bax forms different structures in model membranes

The AFM images of the membrane with and without protein (Figure8.1A and B, respectively) show great differences in topology. Most of these structures were aggregates and beyond the resolution limit of the AFM tip used. These aggregates may be as small as 20-30 nm in diameter. More importantly, non-random structures were seen in the AFM images (in both CL-EPC and MitoMix membranes). Among these non-random structures were lines, arcs and rings.

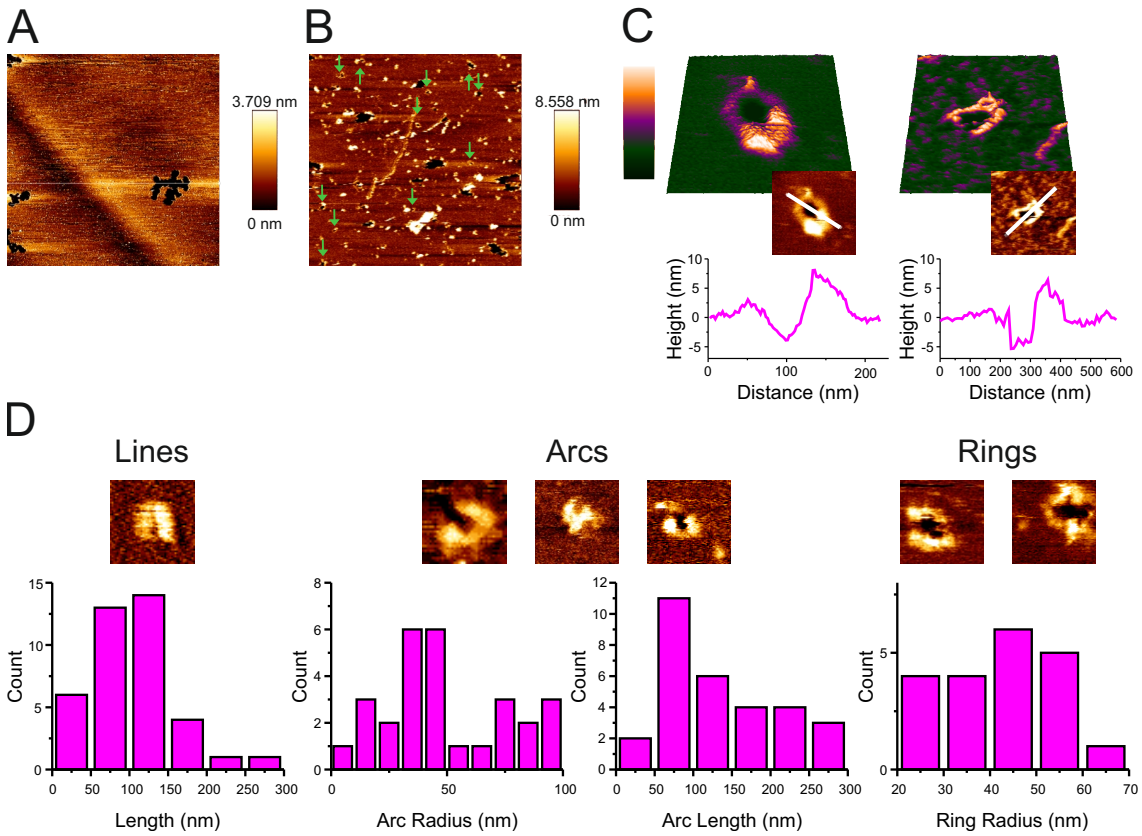

Figure 8.1: Full rings and arc-shaped Bax assemblies are associated with membrane pores in AFM.(A) AFM image of a control SLS prepared from 20%CL-EPC LUVs. The bilayer appears flat without aggregates or defects. Image is 50 x 50 μm. (B) AFM image of an SLS prepared from 20%CL-EPC LUVs pre-incubated with heat-activated Bax. Green arrowheads indicate the presence of membrane pores, which are heterogeneous in size and shape. The pore edges show protrusions corresponding to Bax clusters. Image size is 5 x 5 μm. (C) 3D AFM topography of a Bax ring (left) and left (right). Both images reveal a circular dark hole spanning the lipid membrane (green). Bax molecules around the pore rim (magenta and white) protrude 5-10 nm above the membrane plane, as confirmed by the height profiles below each image (corresponding to the white line in the 2D image insets). The topography of the arc structure revealed a pore only partially surrounded by Bax molecules, while lipids alone formed the remainder of the pore rim. Images are shown in a 35° tilted representation. (D) Quantitative analysis of the distinct structures found in activated Bax on SLSs. The total number of structures is shown in all measurements.

Interestingly, partially lined (arcs) and fully lined (rings) pores with higher structures were visible in the membranes (Figure 8.1C). Unlike structures visible around the defects of 5% CL-EPC, these structures varied in height along the edge of the pore. While the

composition of these structures at the edge could not be determined by AFM, they are likely due to the presence of the protein. However, I cannot exclude the additional presence of lipids.

The dimensions of the non-random structures are shown in Figure 8.1D. The length of the arcs was around 130 ± 70 nm, but the radius of curvature is 60 ± 50 nm. Importantly, I was able to visualize membrane pores associated with defined structures in samples containing Bax (Fig 8.1B and C). These pores were heterogeneous in size and shape, but generally round with diameters ranging from around 25 - 130 nm. They appeared as steep depressions of 3.85 ± 0.47 nm in the flat surface of the lipid bilayer, correlating with the membrane thickness. The pores were characterized by the presence of higher structures, corresponding to Bax molecules distributed along the pore rim. Of the complete rings that were resolved, 81% contained a pore in the interior. In the case of arc-shaped assemblies, 10% were also associated with membrane pores, where Bax molecules covered only a fraction of the pore rim and the rest corresponded to naked lipid bilayer. These results provide a functional link between the structures identified by super resolution microscopy and AFM.

8.2 Bax rings and arcs: evidence for proteolipidic pores

Pore formation of Bax remains the most accepted model of MOMP, mostly based on structural resemblance of Bcl-2 family members to bacterial pore forming proteins (Suzuki et al., 2000) and in vitro experiments using artificial membrane systems (Antonsson et al., 2000, Basañez et al., 2002, Kuwana et al., 2002, Lovell et al., 2008). Until the advent of super resolution microscopy, our ability to see small structures in cells was limited by the resolution limit of light (Hell and Wichman, 1994, Betzig et al., 2006). Taking advantage of two super resolution techniques, single molecule localization microscopy (SMLM) and stimulated emission depletion (STED), our group and another group independently studied Bax structures in mitochondria of apoptotic cells (Salvador-Gallego et al., 2016, Grosse et al., 2016).

My colleague, Raquel Salvador Gallego and her collaborators found similar structures in mitochondria of apoptotic cells and model membranes (Figure 8.2). The quantification of the sizes from SMLM was also in good agreement with AFM showing that Bax activity and structure in vivo is similar to that in model membranes. Furthermore, they showed that these structures were significantly less abundant in Bax mutants that fail to oligomerize. While I cannot discount the possibility of having smaller structures (resolution limit is around 20 nm for SMLM and 20-45 nm for AFM), these techniques suggest that these structures are heterogeneous in size. This is consistent with previous studies that Bax pores can range from 3.5 to several hundreds of nanometers (Antonsson et al., 2000, Epand et al., 2002b, Kuwana et al., 2002, Annis et al., 2005, Dewson et al., 2008, Bleicken et al., 2013a, Czabotar et al., 2013). Such heterogeneity is in contrast with results obtained from other pore-forming proteins (Sonnen et al., 2014, Metkar et al., 2015).

SMLM and AFM also demonstrate that lipids directly participate in the pore architectures formed by Bax and that the protein molecules do not necessarily have to cover the full rim of the pore. These findings argue in favor of a model in which Bax assembles into a flexible toroidal pore structure able to change in size depending on Bax density in the membrane (Bleicken et al., 2013a). This would explain the different sizes of pores and oligomers without discarding that additional proteins like Bak or other unknown factors, not detected in this study, could also be forming part of the pore structure. Incomplete coverage has been observed in some pore-forming proteins (Sonnen et al., 2014, Metkar et al., 2015) and as previously mentioned, has been suggested to be in nanodiscs with active Bax (Xu et al., 2013). On the other hand Grosse et al (2016). provided a 3D-STED

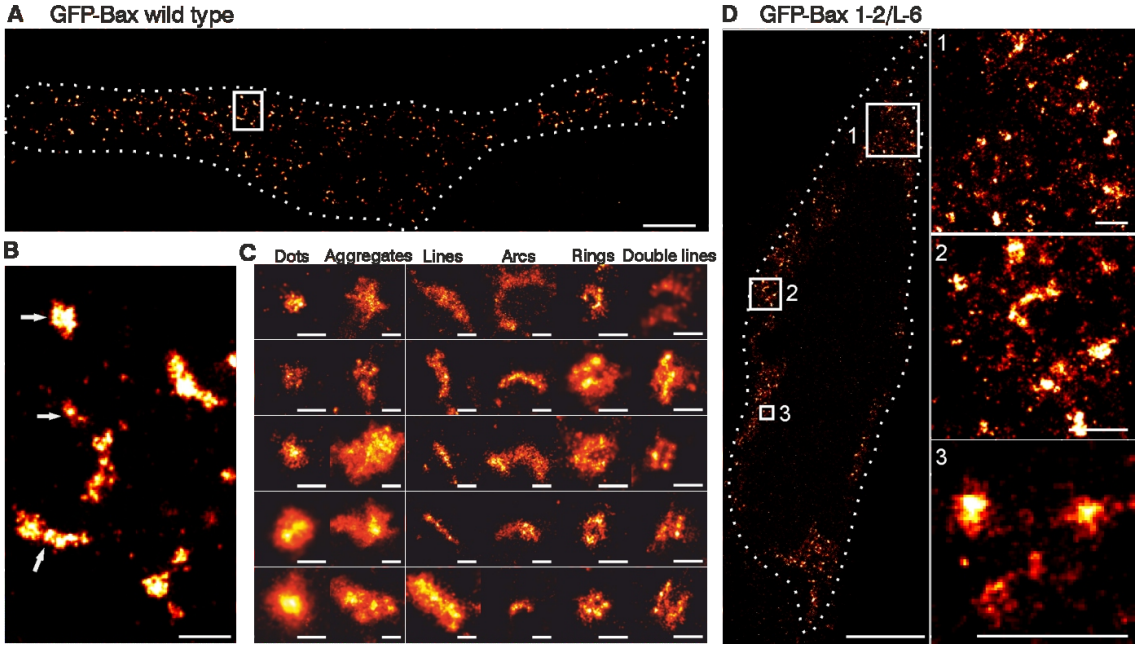

Figure 8.2: Super-resolution of Bax by single-molecule localization microscopy reveals non-random structures in apoptotic mitochondria.(A) Overview of a reconstructured super-resolution image of GFP-Bax wildtype (WT)-overexpressing HeLa cells stained with Alexa Fluor 647-anti-GFP nanobodies. Image was acquired on fixed cells 3 h after apoptosis induction with staurosporine. Dotted line shows the cell shape. Scale bar 5 μm (B) Magnified super-resolution image corresponding to the white rectangle in (A) showing the shapes of GFP-Bax WT structures (white arrow). Scale bar, 500 nm. (C) Gallery of typical GFP-Bax WT structures during apoptosis found in all the analyzed cells. Scale bars, 100 nm. (D) Overview (left) and 3 enlarged insets (right) of HeLa cells overexpressing GFP-Bax 1-2/L-6 mutant (localizes to but does not permeabilize mitochondria) stained with Alexa Fluor 647-anti-GFP nanobodies. Figure shows reconstructed super-resolution images acquired without apoptosis induction. Reproduced with permission from John Wiley and Sons, Inc.

reconstruction of the rings devoid of membrane material in the center, suggesting the formation of pores completely lined with protein. The main difference between the studies of Salvador-Gallego et al. and Grosse et al. (2016) is that in the former, the cells were imaged in early apoptosis, whereas the latter study imaged cells in late apoptosis.

As mentioned in Chapter 7, Bax lowers the line tension at the edge of an open pore, however it does not do this by building a poly-peptide wall that buries the hydrophobic membrane core, but rather, by releasing the curvature stress at the membrane edge (Ros and García-Sáez, 2015).

It also important to consider that structures detected by SMLM could correspond to the same type of supramolecular organization observed from different angles or with different degrees of assembly. On the one hand, observed rings could be those assemblies that are perpendicular to the optical axis while on the other hand, structures could be those that are in a different orientation with respect to the optical axis. Within the cell, the tubules of mitochondrial network could adopt all possible orientation and the authors showed that Bax does not prefer any region of the mitochondria, but rather binds heterogeneously in foci during early apoptosis before mitochondrial fragmentation. As a result, it is unlikely that most Bax rings would be detected.

Taking the AFM results, it could also be argued that these structures could represent different stages in the assembly of nascent evolving Bax pores. This is due to the fact that in AFM the orientation of the membrane is the same. And still, different structures (lines, arcs and rings) can be seen in the membrane. In this scenario, Bax molecules could be hypothesized to first organize into linear and arc-shaped structures and some of them

would evolve into complete rings. It could also be that the lines and arcs are kinetically trapped intermediates of this process.

These observations in the pore-forming process imply a new molecular mechanism of Bax assembly during apoptosis (Figure 8.3). Upon activation, Bax would accumulate in the mitochondria, where it would undergo a conformational change accompanied by extensive membrane insertion (García-Sáez et al., 2004, Annis et al., 2005). Bax molecules would then associate via their dimerzation domain (Dewson et al., 2008, Bleicken et al., 2010, Dewson et al., 2012, Czabotar et al., 2013, Bleicken et al., 2014) and continue to assemble into large oligomers (Subburaj et al., 2015), which might contain Bak or other MOM proteins (Zhou and Chang, 2008). These oligomers would initially organize as linear and arc-shaped structures, some of which would induce the opening of pores responsible for release of apoptotic factors during MOMP (Figure 8.3A). In order to stabilize these pores, Bax oligomers would partially line the pore edge and incorporation of additional Bax molecules would lead to full rings and to growth in pore size (Figure 8.3B).

The results presented here lay the groundwork for understanding Bax assembly and interactions that regulate intrinsic apoptosis. In a commentary by Grant Dewson (2016), he mentions that crucial questions remain including the actual assembly mechanism of these pores. However, he also reiterates that the evidence that such pores actually exist raises confidence that these questions can be answered in the future.

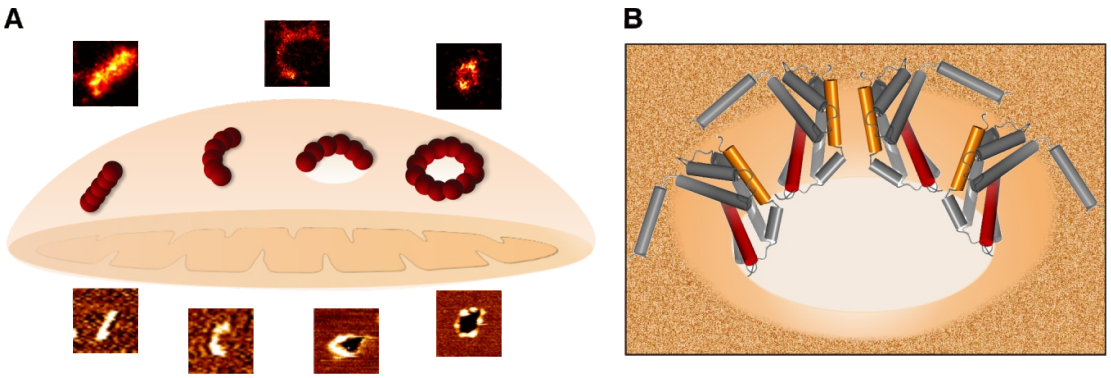

Figure 8.3: Model for the supramolecular organization of Bax at the MOM during apoptosis.(A) Illustration of the the possible roles for the Bax non-random assemblies revealed by SMLM and AFM during apoptosis. Linear and arc clusters not perforating the membrane could correspond to Bax at the initial stages of gathering on healthy mitochondria. They would evolve toward opening of membrane pores, where the protein is partially or fully lining the pore rim. We cannot exclude that a fraction of the linear and arc assemblies correspond to Bax pores overserved from different orientations. Then number of red shperes (Bax dimers) is illustrative and does not necessarily correlate with the actual number present in these structures. (B) The mechanism by which Bax permeabilizes the membrane is mainly by releasing curvature stress at the pore edge. Full as well as partial coverage can reduce line tension and stabilize the open pore state. The illustration shows an incomplete ring assembly of active Bax dimers adopting a clamp-like structure at the pore interface (Bleicken et al, 2014). Reproduced with permission from John Wiley and Sons, Inc.

Chapter 9

Scanning FCS in Mitochondria of Living Cells

Mitochondria are dynamic organelles that are responsible for energy production in most eukaryotes. Mitochondria also play a role in regulation of cell death, lipid synthesis, maintenance of calcium homeostasis and control of reactive oxygen species (McBride et al., 2006). As a result of these functions, mitochondria need to continuously fuse and divide to meet metabolic demands and remove damaged organelles (Wai and Langer, 2016). The spectrum of mitochondrial morphology is characterized between hyperfused tubular networks and fragmented. The dynamic nature of mitochondria is highlighted in morphological changes that they undergo in response to metabolic input.

Characterization of the different proteins involved in mitochondrial processes have already been widely studied (McBride et al., 2006). However, techniques to study function and structure in living cells have only been recently applied. I point in particular to the characterization of interactions between Bcl-2 family of proteins where until recently, most studies were done in vitro (Das et al., 2015, Leber et al., 2007). The challenge of finding appropriate techniques remains.

In this chapter, I developed Scanning FCS to determine dynamics and concentrations of fluorescent proteins in mitochondria of living cells. The two color version of the method serves, for the first time, to quantify protein/protein interactions in the physiological environment of the mitochondria.

9.1 Design of Scanning FCS in mitochondria

Taking inspiration from Scanning FCS in GUVs (Ries and Schwille, 2006), I positioned a tubular mitochondria perpendicular to the scanning path of the confocal microscope (Figure 9.1A). In this way, I made a kymograph/pseudo-image, stacking each line scan next to one another(Figure 9.1B). The dimensions of the kymograph is scan position vs. time (the time resolution is the scanning rate of the confocal volume, and this is also the smallest time lag of the correlation).

From the kymograph, I selected a region that corresponds to one mitochondria(Figure 9.1C). A Gaussian was fitted on the fluorescence intensity signal of each scan and the peak of the Gaussian was used to align the scans. The area under the Gaussian corresponds to the fluorescence signal from the mitochondria and I used this to construct the fluctuation trace for FCS with a time resolution equal to the scan rate (Figure 9.1D and E) using the same protocol as (Unsay and García-Sáez, 2013).

Unlike in *in vitro* model membranes where the lipid bilayer has a fixed thickness, mitochondria may have varying thickness. As such, I reasoned that the size of the detection volume should be adjusted to make sure that we capture the whole mitochondria in just

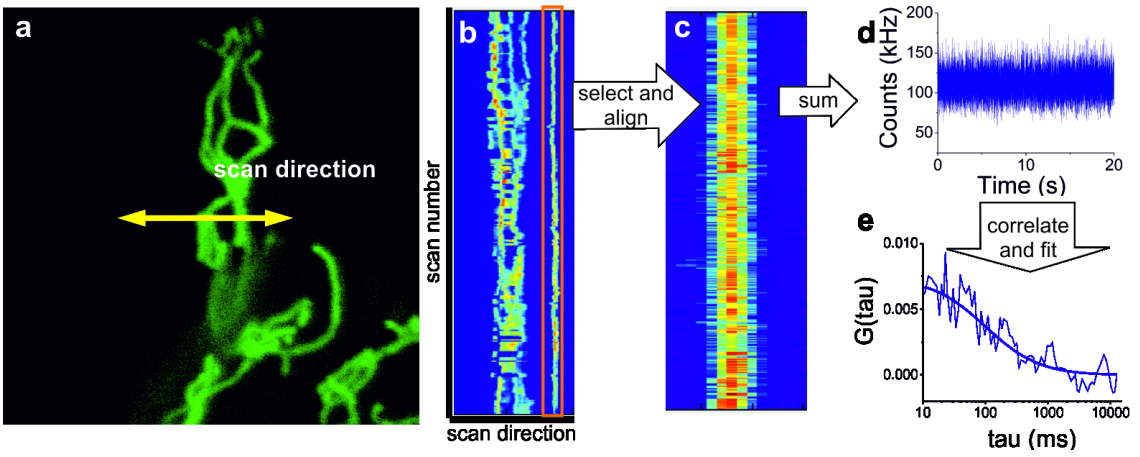

Figure 9.1: Principle of Scanning FCS in Mitochondria. (A) The detection volume is scanned perpendicular to the longitudinal axis of the mitochondria. (B) Each scan is used to construct a pseudo-image, where a specific mitochondria can be selected (orange box). (C) the selected signal is aligned. (D) The signal from each scan is summed up and will correspond to one point in the fluctuation trace. (E) The fluctuation trace is then correlated and fitted with an appropriate diffusion model.

one confocal volume. In this regard, I took confocal images of mitochondria expressing GFP targeted to various compartments of the mitochondria:

- EGFP-TMB-Bcl-xL: EGFP fused to the transmembrane-domain of Bcl-xL, which is targeted to the outer membrane (Kaufmann et al., 2003)
- mitoGFP: GFP fused to the signaling sequence of cytochochrome c oxidase subunit VIII, which is targeted to the inner membrane (Reis et al., 2012)
- SOD2-GFP: GFP fused to the full-length superoxide dismutase 2, which targeted to the matrix (Connor et al., 2007)

I then measured the diameter of mitochondria expressing the different GFP constructs by fitting a Gaussian function to the line profile perpendicular to the mitochondria. The full width at half maximum of the fitting corresponds to the average diameter of the corresponding mitochondrial compartment. Table 9.1 shows the mitochondrial diameters obtained when GFP was over-expressed in these compartments. From calibration measurements, I measured the typical dimension of ω_0 to be 0.23 ± 0.01 μm when the pinhole is opened to collect only 1 airy unit (AU) of the point spread function (PSF) using the 488-nm laser for excitation. When the pinhole is opened at 2 AU, $\omega_0 = 0.38 \pm 0.09 \mu m$.

Table 9.1: Diameter of Mitochondria

Construct	Diameter (μm)
Outer Membrane (EGFP-TMB-Bcl-xL)	0.46 ± 0.10
Inner Membrane (mitoGFP)	0.42 ± 0.13
Matrix (SOD2-GFP)	0.32 ± 0.07

Based on these measurements, a pinhole set at 1AU might be sufficient to capture the whole mitochondria. I also measured SFCS using a pinhole size corresponding to 2AU. However, the measurements in 2AU were very dispersed (data not shown) and were not further considered.

9.2 1D Free Diffusion is an appropriate model to characterize diffusion in mitochondria

In SFCS of GUVs, the model normally used to describe the diffusion of the fluorophores is the two dimensional (2D) Free Diffusion with an elliptical gaussian detection (Ries and Schwille, 2006):

$$G(\tau) = \frac{1}{N}\left(1+\frac{\tau}{\tau_D}\right)^{-1/2}\left(1+\frac{\tau}{\tau_D S^2}\right)^{-1/2} \tag{9.1}$$

This model assumes free diffusion in the optical axis (z-axis), as well as the axis perpendicular to the scanning path on the sample plane (x-axis, assuming the scanning path is the y-axis). In the design of this model, the fluorophore is confined to the plane of the membrane (y = 0), and thus there are no fluctuations in this axis. The alignment of the peaks of the membrane contribution also corrects for the movement of the signal due to membrane undulation, and thus also removes fluctuations in the y-axis.

I used this as a starting point to determine the most appropriate model for mitochondria. This model is not most suited to describe diffusion in the mitochondria because the diffusion in the z-axis is confined to the walls of the mitochondria.

Gennerich and Schild presented a solution to diffusion in small cytosolic compartments (Gennerich and Schild, 2000). My colleague Eduard Hermann adapted their solution to the case of the mitochondria, where the diffusion in the x-axis is free, in the z-axis is confined, and non-existent in the y-axis to give the following equations: .

$$\begin{aligned} G(\tau) &= \frac{1}{N}\left(1+\frac{\tau}{\tau_D}\right)^{-1/2} g_{z*}(\tau) \\ g_{z*}(\tau) &= \begin{cases} 1+\dfrac{Z^4}{45}\left(1-0.1004Z^2+0.00361Z^4\right) exp\left(-\left(\dfrac{\pi}{S\cdot Z}\right)^2\dfrac{\tau}{\tau_D}\right), & Z\in[0,3.1] \\ 1+\left(\dfrac{Z}{\sqrt{\pi}}-1\right) exp\left(-\dfrac{0.83\pi^2}{S\cdot Z}\dfrac{\tau}{\tau_D}\right)\left(1+\dfrac{\tau}{S^2\tau_D}\right)^{-1/2}, & Z\in[3.1,8] \end{cases} \\ &\text{where } Z = \frac{d_{mito}}{\omega_z} \end{aligned} \tag{9.2}$$

where d_{mito} is the diameter of the mitochondria and ω_z is the axial extension of the confocal volume.

However, Gennerich and Schild also presented limitations and simplifications of the model. In one case, they derived the limit of 2D diffusion model $G_{xy}(\tau)$: what should be the ratio (Z) between the diameter of the compartment (d_{mito}) and the axial extension of the diffusion volume (ω_z) so that fluctuations in the z-axis can be neglected. They derived this limit to be $Z < 0.833$. In the case of the mitochondria, the measured diameters are 0.46 ± 0.10 μm, 0.42 ± 0.13 μm, and 0.32 ± 0.07 μm for the outer membrane, inner membrane and matrix, respectively (Table 9.1). I also measured the typical dimensions of the confocal volume of our microscope, and when the pinhole is opened to collect 1 AU of the PSF from the focal point using a 488-nm laser for excitation, the measured axial extension is 1.6 ± 0.2 μm. The ratio is less than the limit 0.833 in all cases. Thus, in SFCS of mitochondria, fluctuations in the z-axis can be neglected and an apparent one dimensional (1D) free diffusion model can be used:

$$G(\tau) = \frac{1}{N}\left(1+\frac{\tau}{\tau_D}\right)^{-1/2} \tag{9.3}$$

Lastly, in the group of Koopman, they characterized mitochondria diffusion using a free 3D diffusion model (Willems et al., 2009, Koopman et al., 2007).

$$G(\tau) = \frac{1}{N}\left(1+\frac{\tau}{\tau_D}\right)^{-1}\left(1+\frac{\tau}{\tau_D S^2}\right)^{-1/2} \tag{9.4}$$

They compared the fitting of their data to the one of Gennerich and Schild, and concluded that the quality of data is the same and that the free 3D diffusion model is more robust. Because of the simplicity of this model, they were also able to fit with multiple components. They showed that the mitochondrial movement contributes to the diffusion of the fluorescent particles. This was evident by a 2nd component slower diffusion time when they fitted their data with multiple components.

In view of these numerous possibilities, I fitted the experimental data from SFCS with these different models: 1D free diffusion ("1D Free", Eq. 9.3), 2D Free with Gaussian Detection ("2D Gauss", Eq. 9.1), 3D free diffusion ("3D Free", Eq. 9.4), and both cases of the 2D confined diffusion from (34) ("2D Conf A" and "2D Conf B" for case 1 ($Z \in [0, 3.1]$) and case 2 ($Z \in [3.1, 8]$) of Eq. 9.2, respectively).

Figure 9.2 shows autocorrelation curves from different compartments fitted with different models. 3D Free deviated most from the other models in diffusion time (Figure 9.2C). Both confined diffusion model gave higher variations in the number of particles, N, and tend to estimate it higher than the simpler models (9.2D). In these models, $G(0) \neq \frac{1}{N}$. 1D Free, 2D Gauss and 2D Conf A gave similar values for τ_D. 1D Free and 2D Gauss gave similar values for N. The model for the confined diffusion is also not very robust as a measurement of the mitochondrial diameter is always necessary to fit this model.

To further check and eliminate possible candidate models, I fitted simulated autocorrelation curves using the different models. I used smoldyn, a particle-based simulator, to generate fluctuation traces, then, I autocorrelated these traces using a multi-tau algorithm code written by Jonas Ries, and finally fitted the autocorrelation curves with the different models.

To simulate the mitochondria accurately, I ran two versions: the first one is 2D diffusion on the surface of a cylindrical tube (with hemisphere ends to close the tube) to simulate diffusion in the outer membrane; the second one is 3D diffusion inside the same cylindrical tube to simulate the diffusion in the matrix. The diffusion on the inner membrane is quite complex as it may approximate the diffusion on the surface of a tube (similar to the outer membrane), however, the presence of cristae invaginations may also give an apparent 3D diffusion if the proteins can diffuse into the invaginations. In a third set of simulations, I then included barriers to simulate the presence of cristae encountered by a particle diffusing inside the tube. The dimensions of the cristae are based on the mitochondrial architecture simulated by Dieteren et al (2011).

Figure 9.3A and B show a sample fitting of the three models with the simulated curves with residuals. The diffusion coefficients were calculated from the fitting using τ_D and the relationship:

$$D = \frac{\omega_0^2}{4\tau_D} \tag{9.5}$$

The waist radius (250 nm) was based on a fixed simulation parameter. Figure 9.3 C shows the comparison of the simulated diffusion coefficients ($D_{simulated}$) and diffusion coefficient calculated from the fitting ($D_{fitting}$). 1D Free diffusion showed the most accurate $D_{fitting}$ compared to the other models (10-20% error), except when I modeled the diffusion inside the mitochondria with cristae barriers (giving 40-50% error). Meanwhile, 3D Free diffusion gave the largest error (∼90%). On the other hand, 2D Gauss model tends to

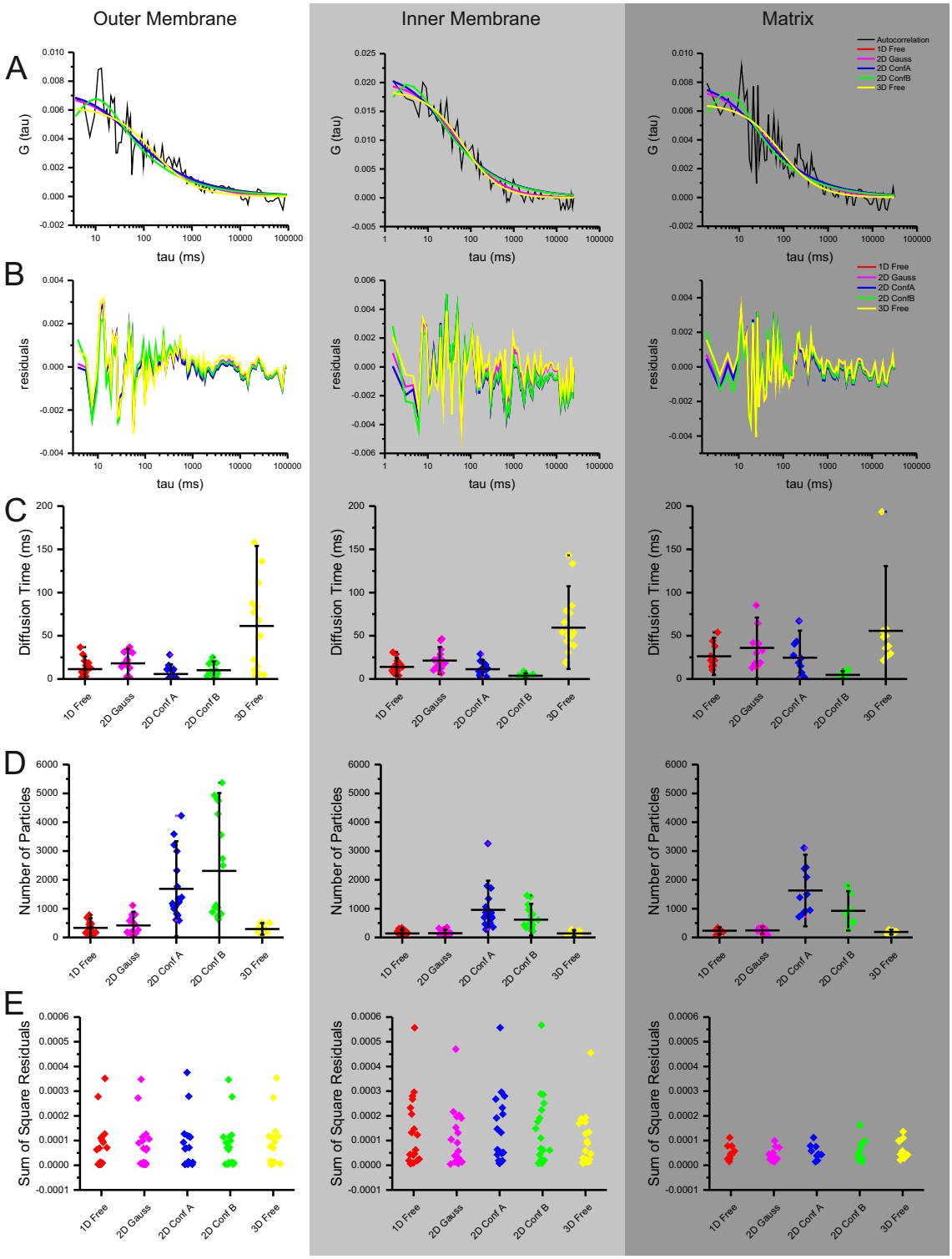

Figure 9.2: Fitting Experimental Curves with Different Diffusion Models. (A) Autocorrelation curves (black) were fitted with different models: 1D Free diffusion (1D, red), 2D free diffusion with elliptical Gaussian detection (2D Gauss, magenta), 2D Confined diffusion case 1 from Eq. ??eq:2DConf (2D Conf A, blue), 2D confined diffusion from Eq. ??eq:2DConf (2D Conf B, green) and 3D free diffusion (3D, yellow). (B) Residuals of the the fitting. Comparison of derived parameters: (C) Diffusion time, (D) Number of Particles, and (E) Sum of Square Residuals.

have a lower sum of square residuals compared to the other models. However, the relative error from of $D_{fitting}$ from $D_{simulated}$ is approximately 20-30%.

From the fluctuation traces, I also calculated the average number of particles in the detection volume, and compare this with the fitted N. Figure 9.3 D shows that 2D Conf A model is over-estimating the number of particles, and the N from 1D and 2D free diffusion estimate the number of particles accurately.

Based on this, I hypothesize that 1D Free and 2D Gauss are equally good models to characterize diffusion in different mitochondrial compartments. I then used Bayesian Interaction Criterion (BIC) to determine the better model. BIC is a criterion for model selection among a finite set of models (Schwarz, 1978, Wit et al., 2012). In fitting different models, it is possible to increase likelihood or goodness of fit by adding more parameters, but this leads to overfitting. BIC resolves this by introducing a penalty for the number of parameters in the model. The formula for BIC based on the sum of square residuals is given:

$$BIC = n \ln\left(\frac{SSR}{n}\right) + k \ln(n) \tag{9.6}$$

Where n is the number of points being fitted by the model and k is the number of free fitting parameters. 1D Free diffusion model gave the overall lower BICs, compared to other models. The lowest difference is between 1D Free and 2D Gauss resulting in BIC = 2-4 depending on the compartment. This shows that 1D Free diffusion is a better model to fit the data.

Based on these observations, I decided to use the 1D free diffusion model in further fitting of the FCS data in mitochondria.

9.3 Probing Dynamics in Different Compartments of Mitochondria

FCS measurements require the calibration of the confocal volume to provide accurate measurements of the diffusion coefficient. However, differences in the environment between the calibration and the biological sample often lead to distortion of the confocal volume (Enderlein et al., 2004, 2005), resulting into erroneous quantification of the diffusion coefficient. One technique to compensate for this distortion is two-focus FCS (Dertinger et al., 2007).

In two-focus FCS, two detection volumes are displaced by a known distance and the fluorescent particles diffuse through them. The correlation of the signal from one focus to the other focus produces a temporal correlation between the two distinct positions. This allows us to calculate for the time it takes for the particle to traverse the space between the two foci. As the two foci are in the same sample environment, the shape and size of the two foci should be the same. We can then uncouple the diffusion coefficient from the shape parameters (Eq. 9.5), and fit them independently with the models. Essentially, measurements become calibration free.

In this section, I compared the use of one-focus and two-focus FCS in different mitochondrial compartments. I also compared these measurements to fluorescence recovery after photobleaching (FRAP) experiments, which was a technique of choice in most applications so far for dynamic characterization in living cells, and provide evidence that FCS can more accurately determine diffusion coefficients. Furthermore, the mathematical fitting provides the number of particles in the detection volume, which allows for the accurate calculation of the concentration of labeled proteins in the mitochondria of living cells.

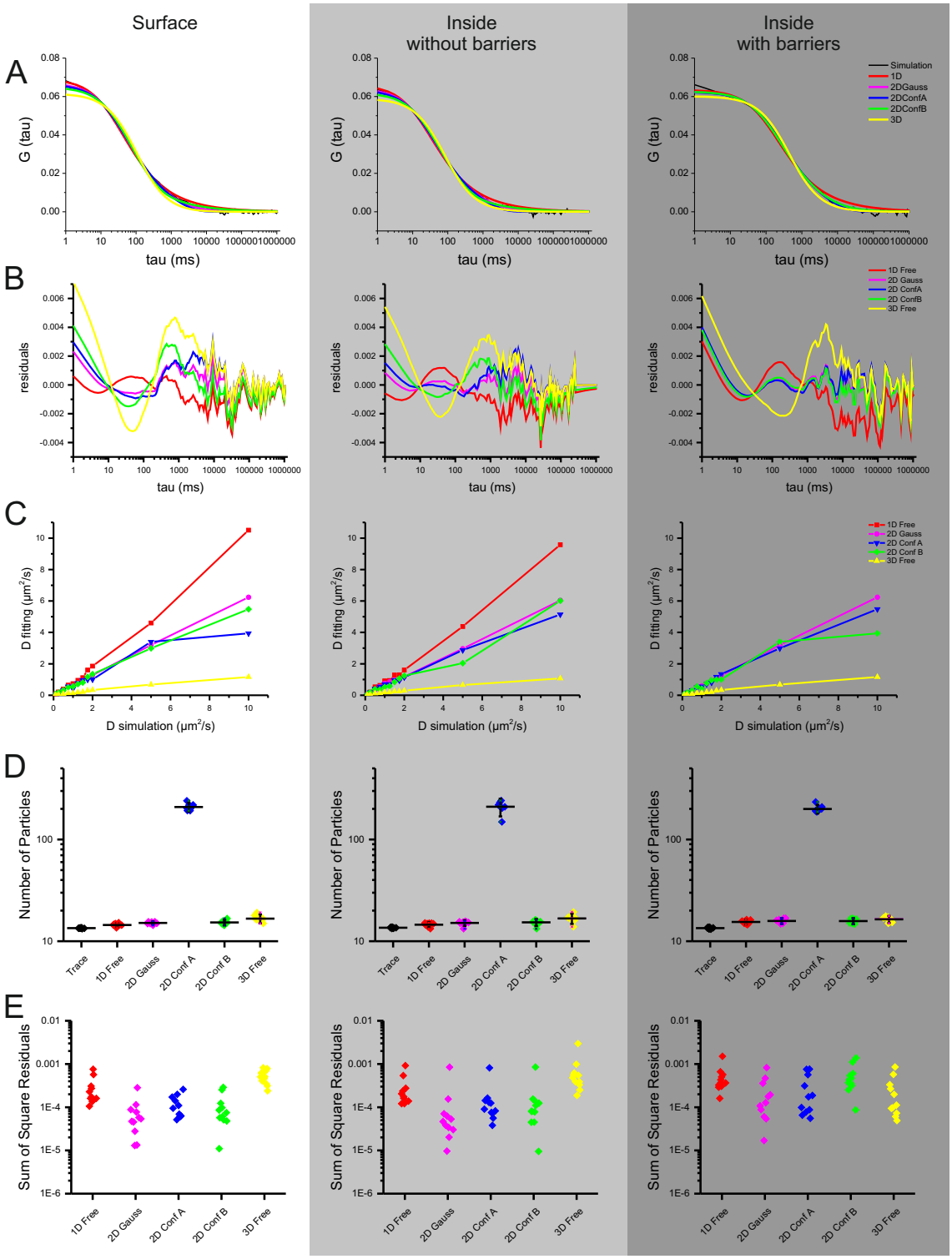

Figure 9.3: Fitting Simulated Curves with Different Diffusion Models. (A) Autocorrelation curves (black) were fitted with different models: 1D Free diffusion (1D, red), 2D free diffusion with elliptical Gaussian detection (2D Gauss, magenta), 2D Confined diffusion from case 1 of Eq. 9.2 (2D Conf A, blue), 2D confined diffusion from case 2 of Eq. 9.2 (2D Conf B, green) and 3D free diffusion (3D, yellow). (B) Residuals of the the fitting. Comparison of derived parameters: (C) Diffusion coefficient (calculated from Eq. 9.5 using acquired diffusion time and simulation parameter ω_0=0.25 μm) compared with theoretical diffusion coefficients, (D) Number of Particles compared to a calculated average particle number from the traces, and (E) Sum of Square Residuals.

9.3.1 Two-focus SFCS in mitochondria accurately determines diffusion coefficient

In one-focus SFCS, one scans a line perpendicular to the mitochondria and fits the resulting autocorrelation curve with the 1D Free diffusion model (Eq. 9.3) to acquire the diffusion time of GFP. A calibration measurement can be used to to convert diffusion time to diffusion coefficient using Eq. 9.5. In two-focus SFCS, one scans two parallel lines perpendicular to the mitochondria with a known distance. The distance was experimentally determined by measuring the distance between two lines obtained by bleaching of dried fluorescent dye samples resulting from repeatedly scanning the two parallel lines ($d = 0.56\mu m$). The resulting auto- and cross-correlation curves were fitted globally using the following equation:

$$G_{12}(\tau) = G_1(\tau) * exp\left[-\frac{d^2}{4D\tau + \omega_0^2}\right] \tag{9.7}$$

with the 1D Free Diffusion model describing the diffusion component of the model ($G_1(\tau)$, Eq. 9.3). Figure 9.4A and B show representative auto- and cross-correlation curves for one- and two-focus SFCS, respectively.

As a comparison, I also measured FRAP on single mitochondria for each compartment. Figure 9.4 C shows the individual recovery curves (blue) for the different compartments, as well as the average curve (black) with the standard deviation (orange area). The curves were fitted with a single exponential and the half time ($t_{1/2}$) of recovery was acquired. I then used the following equation to calculate for the diffusion coefficient (Mitra and Lippincott-Schwartz, 2010, Goodwin and Kenworthy, 2005):

$$D = \frac{r_{bleached}^2}{4t_{1/2}} \tag{9.8}$$

Where $r_{bleached}$is the radius of the bleached circular region.

Figure 9.4 D and Table 9.2 show the comparison of the calculated diffusion coefficients. The variation of the calculated diffusion coefficient is high in one-focus SFCS compared to two-focus SFCS in all compartments. The two-focus SFCS measurements also agree with the FRAP measurements better than the one-focus measurements, except for measurements in the outer membrane. However, the two-focus and FRAP measurements are significantly different in all cases ($p < 0.05$).

Table 9.2: Diffusion Coefficients in Mitochondria of Living Cells

Technique	Diffusion Coefficient ($\mu m^2/s$)		
	Outer Membrane	Inner Membrane	Matrix
One-Focus FCS	1.6 ± 1.7	1.4 ± 1.2	1.0 ± 1.2
Two-Focus FCS	0.4 ± 0.3	0.4 ± 0.2	0.5 ± 0.4
FRAP	0.07± 0.06	0.3 ± 0.2	0.2 ± 0.2

FRAP and FCS are complementary techniques to measure particle mobility in cells. One main difference is the time resolution, with FCS being more applicable to faster dynamics. FRAP is also able to give information about the fraction of immobile molecules. Both techniques rely on analytical models to describe the diffusion (and other processes like binding) and calculate for accurate diffusion coefficients. In most cases, FRAP and FCS measurements have shown some discrepancies (Calizo and Suzanne, 2013, Mueller et al., 2008) and some groups have tried to cross-validate the two techniques to derive the source of these discrepancies (Stasevich et al., 2010). Among others, one main source is the lack of analytical models to describe accurately the processes happening during

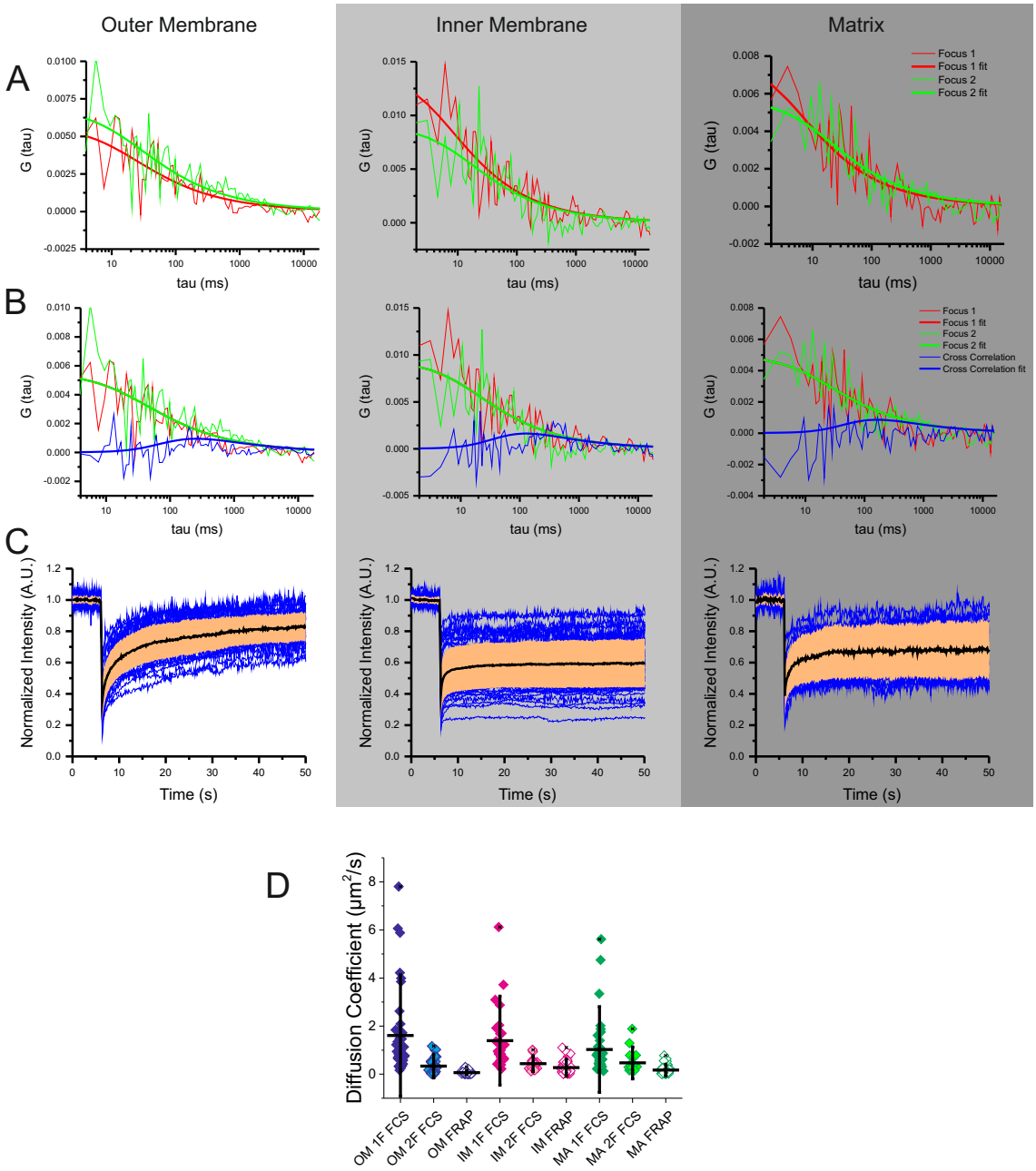

Figure 9.4: Accurate Determination of Diffusion Coefficients in Mitochondria of Living Cells using Two-Focus SFCS. (A) Autocorrelation curves for two foci from different compartments fitted independently with the 1D Free Diffusion model. (B) Same data in (A) including the cross correlation between the two foci fitted globally with two-focus model (Eq. 9.7). (C) Single mitochondria fluorescence recovery after photobleaching (FRAP) experiments. Blue curves are individual FRAP traces, black curves shows the average recovery curve with orange area as the standard deviation of the measurements. (D) Comparison of diffusion coefficients obtained from one-, two-focus FCS, and FRAP.

recovery of fluorescence intensity in FRAP experiments (Mueller et al., 2008). FRAP measurements in mitochondria have been done before and the calculation of diffusion coefficient was done via assumption of simple geometries (Mitra and Lippincott-Schwartz, 2010) or through complicated numerical analysis (Partikian et al., 1998). In Partikian et al. (1998), the calculated diffusion coefficient for the matrix of the mitochondria is 20 $\mu m^2/s$. This is similar to the calculated diffusion coefficient from FCS as reported by Willems et al. (2009) and Koopman et al.(2007), but very different to this study's results.

This value is an order of magnitude different from both of FRAP and SFCS measurements in the matrix. Upon careful inspection of the papers, it showed that the mitoGFP (Partikian et al., 1998) and mitoEYFP (Koopman et al., 2007, Willems et al., 2009) used by the authors contained the same sequence as the mitoGFP in this study, used target GFP to the inner membrane. All databases (UniProt, Entrez) point to the localization of this protein into the inner membrane and not the matrix. Nevertheless they measured a diffusion coefficient much higher than those measured for SOD2-GFP ($0.5 \pm 0.4\ \mu m^2/s$) or mitoGFP ($0.4 \pm 0.2\ \mu m^2/s$).

In order to figure out this discrepancy, I checked some of the control measurements in the papers as this faster diffusion maybe due to diffusion of GFP in the cytosol. Indeed, the authors showed that the signal in the extracellular matrix and the nucleus was uncorrelated, and therefore no autofluorescing molecules were detected. However, a control where FCS was measured in the cytosol was not included. I then measured point FCS in the cytosol of HeLa cells over-expressing mitoGFP and GFP (not targeted to any compartment, from pEGFP-N1 empty vector). The diffusion coefficient of non-targetted GFP in the cytosol is $23 \pm 5\ \mu m^2/s$ ($n_{samples} = 13$) and that for mitoGFP is $18 \pm 4\ \mu m^2/s$ ($n_{samples} = 21$). The average number of particles for mitoGFP in the cytosol is 185 ± 128 and that for mitochondria is 1000 ± 800, indicating that there's a 5x to 10x more mitoGFP particles in the mitochondria than in the cytosol and that I cannot discount that the authors could also possibly be measuring some diffusion in the cytosol.

As a further comparison, I checked for diffusion coefficients calculated using super resolution tracking of mitochondrial proteins (Appelhans et al., 2012). Appelhans et al. determined a major population diffusion coefficient of $0.14 \pm 0.01\ \mu m^2/s$ in the outer membrane using Tom20-Halo/TMR (they also showed a second population with anomalous confined diffusion, which they described as immobile, with diffusion coefficient less than $0.005\ \mu m^2/s$). The authors attributed these different populations to the possibility of Tom20 to form complexes with larger translocases. They also measured diffusion of hFis1, a protein adaptor of mitochondrial fission protein Drp1, and is not part of a larger complex. In this case, they measured a diffusion coefficient of $0.410\ \mu m^2/s$. As the outer membrane probe in the SFCS study only contains a mitochondrial anchoring sequence of Bcl-xL, it should, in theory, not oligomerize. This agrees well with the diffusion coefficient measured for hFis1. However, unlike the data on hFis1, I could also show from FRAP experiments that there's an immobile fraction of the outer membrane construct (30%). This could be due to the limited reservoir of fluorescent molecules in the mitochondria and that the translocation from cytosol to mitochondria is not fast enough to be measured at the time of the experiment.

Appelhans et al. also tracked complex II (Succinate Dehydrogenase) and complex V (ATP Synthase) in the inner membrane of the mitochondria. For complex V measurements, they showed two populations of diffusion behavior. One population was freely diffusing while the other population was diffusing in a restricted manner. However, all of these tracks were diffusing orthogonal to the longitudinal axis of the mitochondria. For complex II, tracks were either unrestricted and moves through the whole mitochondria, or also trapped orthogonal to the longitudinal axis of the mitochondria. The authors rationalize this by differentiating the inner membrane of the mitochondria into different regions. One region is the inner boundary membrane, which is the membrane parallel to the outer membrane, where proteins could move freely. The second region is attributed to the cristae of the mitochondria, which are invaginations in the inner membrane. The authors hypothesized that the confinement of the molecules diffusing orthogonal to the longitudinal axis of the mitochondria are those molecules residing in the cristae membranes, while those that are freely diffusing are in the inner boundary membrane and this presupposes the presence of a diffusion barrier in the cristae junctions. The diffusion

coefficient measured in the inner boundary membrane is 0.161 $\mu m^2/s$ and 0.003 $\mu m^2/s$ for the cristae membrane. Our measurements using mitoGFP agree with the results with the inner boundary membrane indicating that the mitoGFP we are measuring in FCS corresponds to a population that resides in this region. However, from FRAP experiments, I was able to measure that the mobile fraction was only 30% in the inner mitochondria, indicating perhaps that the molecules whose diffusion coefficient I was measuring are only those in the inner boundary membrane and not those trapped in the cristae membrane.

In summary, Two-Focus FCS measurements of fluorescent probes in mitochondrial compartments agree with the different methods of FRAP and super resolution single particle tracking. Both FCS and super resolution tracking are able to more accurately quantify diffusion coefficients compared to FRAP, and this makes them a technique of choice. Unfortunately, super resolution single particle tracking is not as robust compared to both FRAP and FCS and requires special dyes and special instrumentation that may present a different set of challenges. On the other hand, FRAP still finds its use in relatively slow processes, where FCS measuring times may become impractical. However, unless a theoretical model to characterize diffusion in mitochondria can be derived, FCS remains far superior in measuring the diffusion coefficient.

9.3.2 Quantifying Concentration in Mitochondria of Living Cells

Another information that one can get from FCS is the number of particles in the focal volume and this allows for to accurate determination of protein concentration in living cells.

The two standard methods used for measuring proteins in cells is western blot (in cases when an antibody is present for the protein of interest) or flow cytometry (which requires fluorescent tagging of the protein of interest, either by making fusion constructs and subsequent over expression or through immunolabeling). While flow cytometry gives information on the single cell level, there is no direct way of calculating number of particles from fluorescence intensity. Calibration beads are often used to standardize measurements in flow cytometry and this uses the parameter "molecules of equivalent soluble fluorophores" (MESF) parameter (Schwartz et al., 2002, Wang et al., 2002, Gaigalas et al., 2005). However, these MESF cannot be taken as an accurate molecular equivalent in cells as the molecular extinction coefficient in buffer is different in cells, and therefore intensity cannot be directly correlated to number of molecules.

On the other hand, Western blot has been routinely used to quantify proteins of interest from cells. Sample loss is the main draw back of western blot, as this method requires multiple steps to process the cellular material. Thus, the results obtained from western blot provide a lower bound estimate of the number of particles in the cells. Semi-quantitative western blots use loading controls to normalize between samples and see relative levels of proteins between samples (Colella et al., 2012). For truly quantitative western blots, purified proteins are used to construct a calibration curve within the same gel of the samples. The signal response from the calibration should behave in a describable manner (linear, exponential or sigmoidal) so that the signal response from the samples can be correlated to concentration. In this regard, both chemiluminescence or fluorescence detection methods have been previously used for quantitative western blots (Lindner et al., 2012, Zellner et al., 2008). However, obtaining purified proteins to serve as a calibration standard is a limiting factor in many occasions.

As a result, FCS is of a particular interest to quantify proteins at the single cell level. Quantification of fluorophores has been done before in the cytosol and the nucleus (Weidemann et al., 2003), but not in mitochondria.Figure 9.5A shows a western blot sample against GFP on wild type HeLa cells and HeLa cells stably expressing mitoGFP. A loading control using anti-GAPDH was also used. Calibration samples using purified

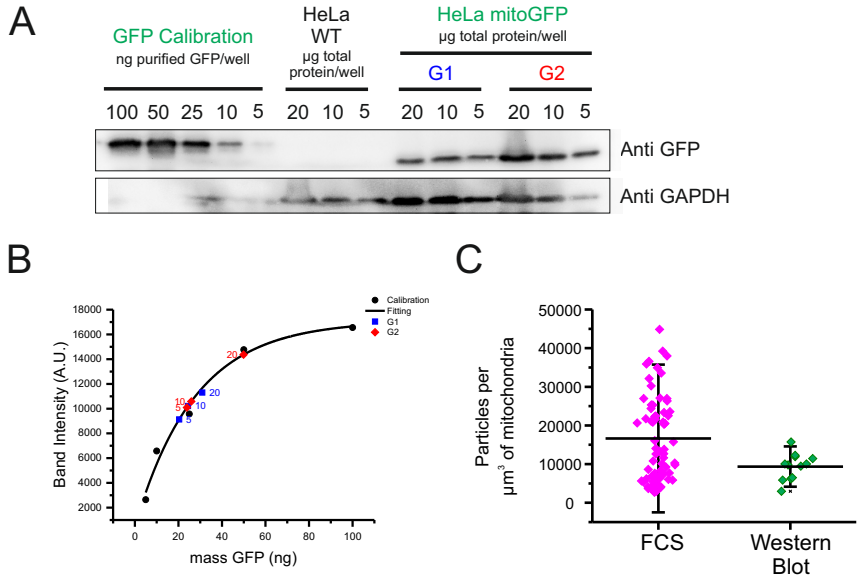

Figure 9.5: Quantifying Concentration in Mitochondria of Living Cells. (A) Western Blot of wild type (WT) Hela cells and HeLa cells stably-expressing mitoGFP, together with a GFP calibration. GFP calibration are from commercially-available purified GFP (BioVision, Inc.). This contains two 6xHis tags on the N- and C-terminal, and therefore migrates differently from mitoGFP on the gel. Anti-GAPDH was used as a loading control. (B) Signal from Western Blot were processed by ImageJ and a calibration curve was constructed by fitting the points to an exponential curve. The graph also shows the derived signal from the samples. Labels indicate the total protein loaded per well (μg) for each data point. (C) Comparison of particles per μm^3 of mitochondria derived from FCS and western blot.

GFP with 6xHisTag on both N- and C-terminal is also shown (The tags change the way the purified GFP migrates, and shows a higher MW compared to mitoGFP). Figure 9.5B shows the calibration curve used for this particular blot fitted with an exponential and the intensities derived from two samples (G1 and G2). Figure 9.5C shows the comparison of number of particles per μm^3 of mitochondria acquired from FCS and from Western Blot, showing indeed that the Western Blot underestimates the number of particles compared to FCS. On the other hand, there is a higher variance in the concentration values, possibly catching unequal levels of expression between cells in the population.

9.4 Characterizing Interactions in Mitochondria of Living Cells

Aside from diffusion, FCS can also measure interactions, specifically, with the two-color version of the method. In two-color FCS, fluorescence fluctuations from differently labeled species are collected from two spectrally distinct channels and the signal of one channel is correlated with the signal of the other channel. A positive cross correlation amplitude indicates that a fraction of the molecules are co-dffusing. In cases where two species of interest are labeled using two different fluorescent dyes, then a positive cross correlation between the spectral channels of the two dyes indicates an interaction between the two species. The amplitude of the cross correlation curve is directly proportional to the fraction of molecules diffusion together as a single particle.

Two color SFCS was previously used in giant unilamellar vesicles (García-Sáez et al., 2009) and the plasma membrane of living cells (Ries et al., 2009b) to measure interactions of proteins. In the same manner, I used two color SFCS to measure interactions of different proteins in the mitochondria of living cells. This includes interaction between Bcl-2 family members, and also between other proteins in the mitochondria. Among others, I also chose

to work with proteins from the tricarboxylic acid cycle as some interactions are already well-known in these systems. Specifically, I worked with Isocitrate dehydrogenase and succinyl dehydrogenase. Unfortunately, some of these constructs, when over-expressed, killed the cells and were not considered further.

9.4.1 Interaction of tBid and Bcl-xL

In previous studies, García-Sáez et al. (2009), measured the interactions of tBid and Bcl-xL in solution and in GUVs. They showed that there is minimal interaction in solution with a dissociation constant (K_d) of 200 nM (120 molecules per μm^3). In membranes, the K_d could not be calculated because of the constant cross correlation over different concentrations measured (around 45%, which is the maximum possible taking into account the degree of labelling of the proteins used). The authors estimated the K_d to be lower than 10 molecules per μm^2.

I then used SFCS in mitochondria to validate their findings in living cells. I over expressed Bcl-xL-mCherry and tBid-GFP in HeLa Cells. Unlike the *in vitro studies* that used spectrally separate organic fluorescent dyes, working with these fluorescent proteins presents the challenge of cross talk (cross excitation of one fluorophore by the other laser, resonance energy transfer, and crossover of signal from one fluorophore to another detector). Cross talk leads to false cross correlation, and must therefore be taken into consideration or eliminated.To minimize the cross talk between the two spectral channels, I used pulsed interleaved excitation FCS (PIE FCS) (Muller et al., 2005).

In the mitochondria of HeLa cells, tBid exhibited a high cross correlation with Bcl-xL (42 $\pm$18%), indicating strong interaction. However, I could not calculate a direct dissociation constant because endogenous Bid and Bcl-xL are present in HeLa cells, and therefore an accurate determination of how many of these proteins are labeled could not be achieved.

Together with my lab colleague, Fabronia Murad, we generated Bcl-xL/Bid double KO (DKO) MEFs from the Bid KO MEFs using the CRISPR/Cas9 system. I then expressed tBid-GFP and Bcl-xL-mCherry in these DKO MEFs and measured FCS both in the cytosol and the mitochondria. As a negative control, I measured the interaction of mitoGFP with Bcl-xL-mCherry.

Figure 9.6 shows the FCS curves for measurements in these DKO MEFs both in the cytosol (A-B) and the mitochondria (D-E). Measurements in the cytosol were fitted with 3D anomalous diffusion model as in Weidemann et al. (2003). From the autocorrelation curves, one can immediately notice that the amplitude in the mitochondria was smaller compared to that of the cytosol, indicating the preference of these proteins to translocate to the mitochondria.

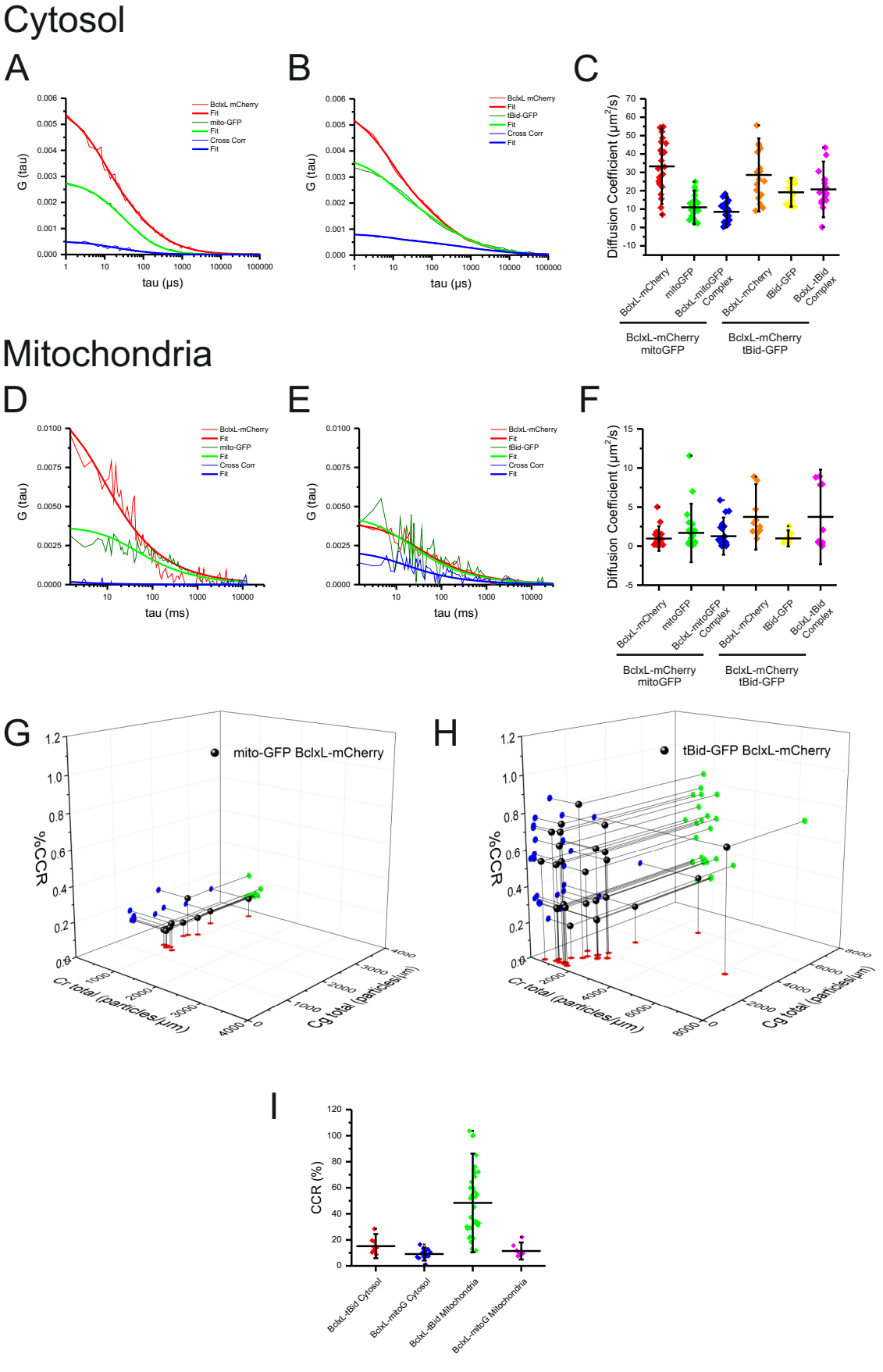
Cytosol
A
B
C
G (tau)
tau (µs)
BclxL mCherry
Fit
mito-GFP
tBid-GFP
Cross Corr
Diffusion Coefficient (µm²/s)
BclxL-mCherry
mitoGFP
BclxL-mitoGFP Complex
tBid-GFP
BclxL-tBid Complex
BclxL-mCherry mitoGFP
BclxL-mCherry tBid-GFP
Mitochondria
D
E
F
tau (ms)
G
H
mito-GFP BclxL-mCherry
tBid-GFP BclxL-mCherry
%CCR
Cr total (particles/µm)
Cg total (particles/µm)
I
CCR (%)
BclxL-tBid Cytosol
BclxL-mitoG Cytosol
BclxL-tBid Mitochondria
BclxL-mitoG Mitochondria

Figure 9.6 (previous page): Interaction of tBid and Bcl-xL in Mitochondria of Bid/Bcl-xL Double Knockout Mouse Embryonic Fibroblasts (A-C) Point FCS in the cytosol. (A) Autocorrelation (green and red) and Cross correlation (blue) curves between mito-GFP and Bcl-xL-mCherry (negative control). (B) Autocorrelation (green and red) and Cross correlation (blue) curves between tBid-GFP and Bcl-xL-mCherry. (C) Diffusion coefficients of the different species in the cytosol. (D-F) Scanning FCS in the mitochondria. (D) Autocorrelation (green and red) and Cross correlation (blue) curves between mito-GFP and Bcl-xL-mCherry (negative control). (E) Autocorrelation (green and red) and Cross correlation (blue) curves between tBid-GFP and Bcl-xL-mCherry. (F) Diffusion coefficients of the different species in the cytosol. (G-H) Percent cross correlation (%CC) with respect to calculated concentrations of each species. (G) Negative control and (H) tBid/Bcl-xL. (I) Summary of %CC measured in the cytosol and mitochondria.

Figure 9.6 C and F shows the diffusion coefficients derived from the two-color FCS measurements. One main limitation of our microscopy system is that we cannot implement two-focus with PIE-FCS. As such, all reported diffusion coefficients with PIE-FCS were from one-focus measurements. The diffusion coefficients measured in the cytosol were typical diffusion coefficients from literature. In the mitochondria, the diffusion coefficients were similar to diffusion in the outer membrane from the previous sections. Similar to the result of Garcia-Saez et al (2009), I did not see differences in the diffusion coefficient in membranes despite having formed complexes.

Figure 9.6 G and H shows the percent cross correlation (%CC) of the different samples in the mitochondria of DKO cells, while Figure 9.6 I shows the summary of all the %CC in both mitochondria and cytosol. Notice that the %CC of tBid/Bcl-xL in the cytosol is not significantly different from mitoGFP/Bcl-xL, indicating very weak to almost no interaction in the cytosol. On the other hand, the interaction in mitochondria is stronger, similar to that measured in HeLa cells.

As these are DKO MEFs, the degree of labeling depends on the maturation efficiency of the fluorescent proteins (90%, Ulbrich and Isacoff (2007), Anderluh et al. (2014)), and I can therefore compute for the K_d. Details on the computation and labelling correction are given in the methods section (Section 5.7.4). For tBid and Bcl-xL, the reaction is as follows:

$$\begin{aligned} \text{Bcl-xL/tBid} &\rightleftharpoons \text{Bcl-xL} + \text{tBid} \\ K_d &= \frac{[\text{Bcl-xL}]\,[\text{tBid}]}{[\text{Bcl-xL/tBid}]} \end{aligned} \tag{9.9}$$

where Bcl-xL/tBid represents the complex, and Bcl-xL and tBid are unbound molecules. Square brackets denote concentration. Figure 9.7A shows the calculated K_d for tBid/Bcl-xL complex in cytosol and the mitochondria. On the average, we calculated a K_d of 300 $\pm$ 300 nM in mitochondria and 150 $\pm$ 73 nM in the cytosol.

Note that the variation in the calculated K_d is quite large. This can in part be due to cell-to-cell variability. It should be mentioned that I measured cells with elongated mitochondria (healthy cells). In these cells, we expect that apoptosis has not yet occurred, and while it is tempting to speculate that Bcl-xL is able to strongly interact with tBid in these cells (as evidenced by the cell's health), it could also be that other Bcl-2 members are sequestering tBid or Bcl-xL from each other. This results in a higher K_d.

One way to eliminate the high variability is to construct a histogram (Figure 9.7B) and take the peak as the most probable K_d. In this way, the K_d range having the largest population is given more attention. If I do this, I see that the peak is 44 ± 78 nM, indicating that most of the interaction is quite strong compared to the cytosol ($K_d = 170 \pm 110$ nM).

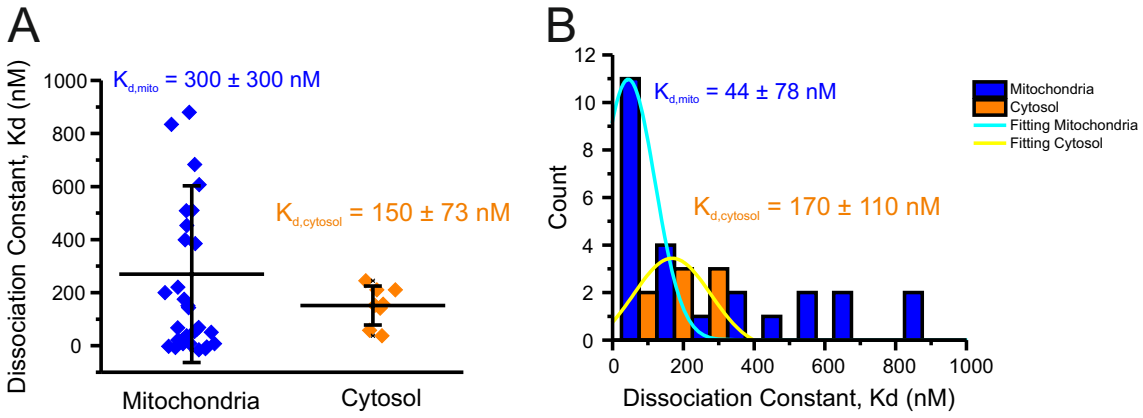

Figure 9.7: Dissociation Constant (K_d) of tBid/Bcl-xL complex. (A) Comparison of K_ds between tBid-GFP/Bcl-xL-mCherry complex in the mitochondria and cytosol. Values are the average of all the measurements and the error is given as the standard deviation. (B) Histograms of the K_d and corresponding Gaussian fitting, the value is the peak K_d value from the Gaussian curve and the errors are given as the standard deviation of the Gaussian curve.

Another group previously measured interactions of anti-apoptotic Bcl-2 proteins (Bcl-xL and Bcl-2) with BH3-only proteins (Bid, Bim and Bad) (Liu et al., 2012) using Fluorescence Lifetime Imaging (FLIM)/FRET. However, one of FLIM/FRET's limitation is its inability to make an absolute quantification of the K_d because of the dependence of the calculations on fluorescence intensity and not particle numbers. The authors did show some relative comparisons, however. For example, addition of inhibitor drugs like ABT-737 and ABT-263 can lower the FLIM/FRET efficiency, and therefore the strength of the interactions between anti-apoptotic members and Bid or Bad.

In summary, this is the first time, to the best of our knowledge, that dissociation constants have been measured in mitochondria of living cells. In the context of apoptosis, there is a need to move out from looking at pairs of proteins as an isolated system, but also to contemplate parallel interactions with other family members. This makes the calculation of K_d in cells not only particularly challenging, but would also require restraint on speculating biological regulatory roles. Nevertheless, this is a first step towards the direction of quantifying the Bcl-2 interactome.

9.4.2 Interactions of the subunits of Succinate Dehydrogenase Complex

To show, as proof of principle, that this technique is widely applicable to other biological systems, I measured the interactions between the subunits (A, B, C and D) of Succinate Dehydrogenase (SDH) Complex (Otherwise known as respiratory Complex II). SDHA is a peripheral membrane protein that is anchored by SDHB to a membrane-inserted heterodimer of SDHC and SDHD (Oyedotun and Lemire, 2004, Sun et al., 2005).

Functionally, SDHA is a flavoprotein that catalyzes the oxidation of succinate to fumarate through its covalently-attached flavin adenine nucleotide (FAD). During this reaction, FAD is reduced to FADH_2, which then supplies SDHB with high-energy electrons. SDHB contains Fe-S clusters, which transport the electrons to the membrane-anchor SDHC-SDHD sub complex. This sub complex contains a ubiquinone-binding site and during the process, dumps the high energy electrons to a bound ubiquinone. The reduced ubiquinone is then used further down the electron transport chain to produce the proton gradient across the mitochondrial inner membrane. As such, the SDH complex is the only complex that is both involved in the tricarboxylic acid cycle and the electron transport chain.

I then measured the interaction of several subunits of SDH. Specifically, I measured the

interaction of SDHA with itself using two-color PIE-SFCS. I also measured the interaction of SDHC with SDHD. Similar to the previous section, the main drawback of using PIE is that we have not implemented two-focus measurements with it, which makes diffusion coefficient measurements less accurate.

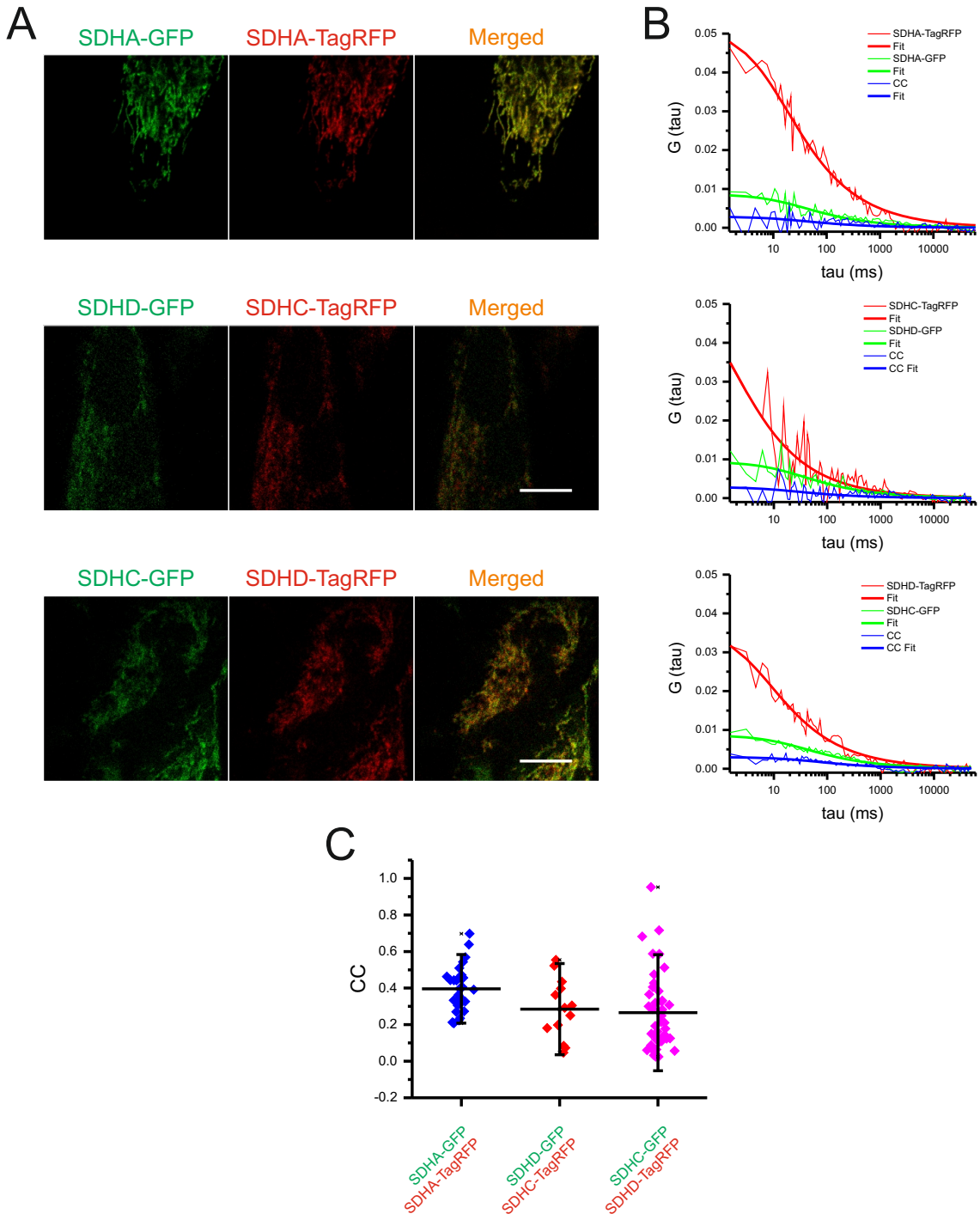

Figure 9.8: Interactions between the subunits of Succinyl Dehydrogenase. (A) Confocal microscopy images of the different SDH subunit combinations. (B) Sample auto- and cross-correlation curves for each condition tested. (C) comparison of %CC between the different SDH subunits.

Figure 9.8 A and B shows the representative confocal microscopy images and FCS curves of the interactions of these subunits in HeLa cells. Figure 9.8B shows the self-interaction of SDHA (SDHA-GFP and SDHA-TagRFP). and interaction of SDHC with SDHD. I also checked whether the differences in the tag will affect the interaction. Thus,

I compared the %CC when SDHC-GFP interacts with SDHD-TagRFP or if the labels were reversed. Figure 9.8C shows a summary of the %CC of these different pairs. SDHA-SDHA interacts more strongly than SDHC-SDHD ($p < 0.05$), which is quite surprising. Furthermore, changing the tags did not show a significant difference in the %CC.

It has been previously reported that SDH complexes form trimers in *E. coli* (Yankovskaya et al., 2003). And while the 3D crystal structure suggests a possible interaction interface in the membrane anchored subunits (Yankovskaya et al., 2003 and PDB structure 1NEK), I saw a weaker interactions between SDHC and SDHD. These results suggest that the interactions may be weak and they are prone to disassembly and/or exchange. However, this is not a very feasible given that the tight binding between subunits and between complexes is required to prevent leakage of reactive oxygen species, which may form during electron transport (Yankovskaya et al., 2003).

On the other hand, it could also be because they interact so strongly that they don't exchange subunits anymore. The low %CC could be due to the fluorescent variants strongly interacting with endogenous partners.

Another possibility is that the GFP and TagRFP tags could interfere with the complex formation. The latter possibility is supported by the increased interaction when SDHA was the only protein labeled. SDHA-SDHA interaction measurements showed a significantly higher %CC at 40% CC. The 3D crystal structure of SDH trimers show that there is no direct contact between SDHA of different units of complex II, suggesting that there should be enough space to fit a 30-kDa GFP or TagRFP protein.

Furthermore, it has been shown that mitochondrial respiratory complexes are organized into supramolecular assemblies (Bianchi et al., 2004). However, high-resolution structures of these complexes only contain complex I, III, IV, and excludes SDH (Schäfear et al., 2007). Recently, Sousa et al. (2011) showed that SDH can form supramolecular complexes in *E. coli* with other respiratory chain proteins. Here, they tested the oxidoreductase activity of different sucrose gradient fractions of digitonin-solubilized *E. coli* membranes and found out that the succinate dehydrogenase activity coincided with some NADH oxidoreductase activity. They also saw activity in lower molecular weight fractions, which suggests that SDH is present both in supramolecular assemblies or by itself. Considering that FCS is only able to characterize the mobile particles, it is not clear whether the interactions I measuried indicate SDH as being part of a supramolecular assembly.

Considering that in the super resolution tracking experiments by Appelhans et al. (2012), the authors showed that SDH exists either in the inner boundary membrane or in the cristae membrane. Those in the cristae membrane could be the fraction of SDH complexes present with other respiratory chain proteins. Whereas those in the inner boundary membrane could be SDH complexes which are not part of supramolecular assemblies. To verify this, further experiments including two-color tracking or two-color FCS with other respiratory proteins would be required.

Overall, the results with the SDH complex exemplifies both the power and limitations of two-color FCS: It can be used to characterize interactions in living cells, but care must be taken to ensure that fluorescent tagging does not affect the system's behaviour.

9.5 Outlook and Future Directions

In summary, this work on mitochondrial SFCS provides new tool to study protein dynamics and interactions in mitochondria of living cells. While SFCS has definite limitations, it proved to be better than FRAP in determining the diffusion coefficient of proteins in the mitochondria.

Furthermore, I have shown the potential of SFCS in mitochondria to be used as a tool to measure interactions in living systems. With the right biological controls, its ability

to directly calculate K_d makes it an attractive biophysics tool to characterize interaction networks that regulate cellular processes. Of course, as one of the many tools, using it in conjunction with other single molecule techniques like particle tracking, FLIM/FRET or even dynamic super resolution microscopy would pave the way to a better understanding of biological processes in living system.

Publications

Accepted Articles

- Bax assembly into rings and arcs in apoptotic mitochondria is linked to membrane pores. Salvador-Gallego R, Mund M, Cosentino K, Schneider J, Unsay JD, Schraermeyer U, Engelhardt J, Ries J, and García Sáez, AJ. *EMBO J.* 2016; 35(4), pp 389-401**(with cover art)**

- A Single Herpesvirus Protein Can Mediate Vesicle Formation in the Nuclear Envelope. Lorenz M, Vollmer B, Unsay JD, Klupp BG, García-Sáez AJ, Mettenleiter TC, Antonin W. *J. Biol. Chem.* 2015, doi: 10.1074/jbc.M114.627521

- Cardiolipin Effects On Membrane Structure and Dynamics. Unsay JD, Cosentino K, Subburaj Y, García-Sáez AJ. *Langmuir.* 2013; 29 (51), pp 15878-15887 **(with cover art)**

Book Chapters, Reviews, and Protocols

- Atomic Force Microscopy Imaging and Force Spectroscopy of Supported Lipid Bilayers. Unsay JD, Cosentino K, García-Sáez AJ. *J. Vis. Exp.* 2015; 101, e52867, doi:10.3791/52867

- Microscopy of Model Membranes: Understanding how Bcl-2 proteins mediate apoptosis. Das KK, Unsay JD, and García Sáez, AJ. In A. Iglič and CV. Kulkarni(Eds.) *Advanced Planar Lipid Bilayers and Liposomes.* 2015; Vol. 21

- Scanning Fluorescence Correlation Spectroscopy in Model Membrane Systems. Unsay JD, and García Sáez, AJ. In J. Herrmann and D. Rapaport (Eds.) "Membrane Biogenesis: Methods and Protocols", *Methods in Molecular Biology*, 2013; Vol. 1033, pp. 185-205 Humana Press, New-York.

Submitted/Under Review

- Proapoptotic cBid and Bax exhibit distinct membrane remodelling activities: An AFM Study. Unsay JD, Cosentino K, Sporbeck K, García-Sáez AJ (Under Review, BBA - Biomembranes)

- Force mapping study of equinatoxin II effect in membranes presenting phase domains. Cosentino K, Hermann E, Ros U, Unsay JD, García-Sáez AJ (Under Review, Biophysical Journal)

In Preparation

- Scanning Fluorescence Correlation Spectroscopy for Mitochondria of Living Cells. Unsay JD, Murad F, García-Sáez AJ (In Preparation)

Bibliography

J. M. Adams and S. Cory. The bcl-2 protein family: Arbiters of cell survival. *Science*, 281:1322–1326, 1998.

L. Aguilar, G. Ortega-Pierres, B. Campos, R. Fonseca, M. Ibáñez, C. Wong, N. Farfan, J. M. Naciff, M. A. Kaetzel, J. R. Dedman, and I. Baeza. Phospholipid membranes form specific nonbilayer molecular arrangements that are antigenic. *Journal of Biological Chemistry*, 274:25193–25196, 1999.

L. Albertazzi, D. Arosio, L. Marchetti, F. Ricci, and F. Beltram. Quantitative fret analysis with the e^0gfp-mcherry fluorescent protein pair. *Photochemistry and Photobiology*, 85: 287–297, 2008.

A. Alessandrini and U. Muscatello. Afm and ftir spectroscopy investigation of the inverted hexagonal phase of cardiolipin. *J Phys Chem B*, 113(11):3437–44, 2009.

A. Alessandrini, H. M. Seeger, T. Caramaschi, and P. Facci. Dynamic force spectroscopy on supported lipid bilayers: Effect of temperature and sample preparation. *Biophysical Journal*, 103(1):38–47, 2012.

A. Anderluh, E. Klotzsch, A. W. A. F. Reismann, M. Brameshuber, O. Kudlacek, A. H. Newman, H. Sitte, and G. J. Schütz. Single molecule analysis reveals coexistence of stable serotonin transporter monomers and oligomers in the live cell plasma membrane. *Journal of Biological Chemistry*, 289:4387–4394, 2014.

M. G. Annis, E. L. Soucie, P. J. Dlugosz, J. A. Cruz-Aguado, L. Z. Penn, B. Leber, and D. W. Andrews. Bax forms multispanning monomers that oligomerize to permeabilize membranes during apoptosis. *EMBO Journal*, 24:2096–2103, 2005.

B. Antonsson, S. Montessuit, S. Lauper, R. Eskes, and J.-C. Martinou. Bax oligomerization is required for channel-forming activity in liposomes and to trigger cytochrome c release from mitochondria. *Biochem J*, 345:271–278, 2000.

T. Appelhans, C. P. Richter, V. Wilkens, S. T. Hess, J. Piehler, and K. B. Busch. Nanoscale organization of mitochondrial microcompartments revealed by combining tracking and localization microscopy. *Nano Lett*, 12(2):610–6, 2012.

D. Ardail, J.-P. Privat, M. Egret-Charlier, C. Levrat, F. Lerme, and P. Louisot. Mitochondrial contact sites lipid composition and dynamics. *Journal of Biological Chemistry*, 265:18797–18802, 1990.

S. Arnold and B. Kadenbach. Cell respiration is controlled by atp, an allosteric inhibitor of cytochrome-c oxidase. *European Journal of Biochemistry*, 249:350–354, 1997.

H. Ashida, H. Mimuro, M. Ogawa, T. Kobayashi, T. Sanada, M. Kim, and C. Sasakawa. Cell death and infection: a double-edged sword for host and pathogen survival. *J Cell Biol*, 195(6):931–42, 2011.

E. U. Azeloglu and K. D. Costa. Atomic force microscopy in mechanobiology: measuring microelastic heterogeneity of living cells. *Methods Mol Biol*, 736:303–29, 2011.

G. Bar, R. Brandsch, and M.-H. Whangbo. Effect of viscoelastic properties of polymers on phase shift in tapping mode atomic force microscopy. *Langmuir*, 14:7343–7347, 1998.

R. Barattin and N. Voyer. Chemical modifications of atomic force microscopy tips. *Methods Mol Biol*, 736:457–83, 2011.

S. Basak and A. Raman. Dynamics of tapping mode atomic force microscopy in liquids: Theory and experiments. *Applied Physics Letters*, 91(6):064107, 2007.

G. Basañez, J. C. Sharpe, J. Galanis, T. B. Brandt, J. M. Hardwick, and J. Zimmerberg. Bax-type apoptotic proteins porate pure lipid bilayers through a mechanism sensitive to intrinsic monolayer curvature. *J Biol Chem*, 277(51):49360–5, 2002.

E. Basso, L. Fante, J. Fowlkes, V. Petronilli, M. A. Forte, and P. Bernardi. Properties of the permeability transition pore in mitochondria devoid of cyclophilin d. *J Biol Chem*, 280(19):18558–61, 2005.

P. A. Beales, C. L. Bergstrom, N. Geerts, J. T. Groves, and T. K. Vanderlick. Single vesicle observations of the cardiolipincytochrome c interaction: Induction of membrane morphology changes. *Langmuir*, 27(10):6107–6115, 2011.

M. Benoit and C. Selhuber-Unkel. Measuring cell adhesion forces: theory and principles. *Methods Mol Biol*, 736:355–77, 2011.

E. Betzig, G. H. Patterson, R. Sougrat, O. W. Lindwasser, S. Olenych, J. S. Bonifacino, M. W. Davidson, J. Lippincott-Schwartz, and H. F. Hess. Imaging intracellular fluorescent proteins at nanometer resolution. *Science*, 313(5793):1642–5, 2006.

C. Bianchi, M. L. Genova, G. P. Castelli, and G. Lenaz. The mitochondrial respiratory chain is partially organized in a supercomplex assembly. *Journal of Biological Chemistry*, 279:36562–36569, 2004.

G. Binnig and H. Rohrer. Scanning tunneling microscopy. *Surface Science*, 126:236–244, 1983.

G. Binnig, H. Rohrer, C. Gerber, and E. Weibel. Surface studies by scanning tunneling microscopy. *Physical Review Letters*, 49(1):57–61, 1982.

G. Binnig, C. F. Quate, and C. Gerber. Atomic force microscope. *Physical Review Letters*, 56(9):930–933, 1986.

C. D. Blanchette, A. Loui, and T. V. Ratto. *Tip Functionalization: Applications to Chemical Force Spectroscopy*. Springer Science+Business Media, LLC, New York, NY, USA, 2008.

S. Bleicken, M. Classen, P. V. Padmavathi, T. Ishikawa, K. Zeth, H. J. Steinhoff, and E. Bordignon. Molecular details of bax activation, oligomerization, and membrane insertion. *J Biol Chem*, 285(9):6636–47, 2010.

S. Bleicken, A. J. García-Sáez, E. Conte, and E. Bordignon. Dynamic interaction of cbid with detergents, liposomes and mitochondria. *PLoS ONE*, 7(4):e35910, 2012.

S. Bleicken, O. Landeta, A. Landajuela, G. Basañez, and A. J. García-Sáez. Proapoptotic bax and bak proteins form stable protein-permeable pores of tunable size. *Journal of Biological Chemistry*, 288(46):33241–33252, 2013a.

S. Bleicken, C. Wagner, and A. J. García-Sáez. Mechanistic differences in the membrane activity of bax and bcl-xl correlate with their opposing roles in apoptosis. *Biophysical Journal*, 104(2):421–431, 2013b.

S. Bleicken, G. Jeschke, C. Stegmueller, R. Salvador-Gallego, A. J. García-Sáez, and E. Bordignon. Structural model of active bax at the membrane. *Molecular Cell*, 2014.

S. Bleicken, G. Hofhaus, B. n. Ugarte-Uribe, R. Schröder, and A. J. García-Sáez. cbid, bax and bcl-xl exhibit opposite membrane remodelling activities. *Cell Death and Disease*, 7:e2121, 2016.

A. Boisen, O. Hansen, and S. Bouwstra. Afm probes with directly fabricated tips. *Journal of Micromechanics and Microengineering*, 6:58–62, 1996.

C. Brooks, S.-G. Cho, C.-Y. Wang, T. Yang, and Z. Dong. Fragmented mitochondria are sensitized to bax insertion and activation during apoptosis. *American Journal of Physiology Cell Physiology*, 300:C447–C455, 2011.

N. A. Burnham, X. Chen, C. S. Hodges, G. A. Matei, E. J. Thoreson, C. J. Roberts, M. C. Davies, and S. J. B. Tendler. Comparison of calibration methods for atomic-force microscopy. *Nanotechnology*, 14:1–6, 2002.

H.-J. Butt and V. Franz. Rupture of molecular thin films observed in atomic force microscopy i. theory. *Physical Review E*, 66:031601, 2002.

H.-J. Butt and M. Jaschke. Calculation of thermal noise in atomic force microscopy. *Nanotechnology*, 6:1–7, 1995.

H.-J. Butt, P. Siedle, K. Seifert, K. Fendler, T. Seeger, E. Bamberg, and A. L. Weisenhorn. Scan speed limit in atomic force microscopy. *journal of Microscopy*, 169:75–84, 1993.

R. C. Calizo and S. Suzanne. Discrepancy between fluorescence correlation spectroscopy and fluorescence recovery after photobleaching diffusion measurements on g-protein-coupled receptors. *Anal Biochem*, 440:40–48, 2013.

C. Canale, M. Jacono, A. Diaspro, and S. Dante. Force spectroscopy as a tool to investigate the properties of supported lipid membranes. *Microscopy Research and Technique*, 73 (10):965–972, 2010.

C. Canale, B. Torre, D. Ricci, and P. C. Braga. Recognizing and avoiding artifacts in atomic force microscopy imaging. *Methods Mol Biol*, 736:31–43, 2011.

E. T. Castellana and P. S. Cremer. Solid supported lipid bilayers: From biophysical studies to sensor design. *Surface Science Reports*, 61(10):429–444, 2006.

G. M. Cereghetti, A. Stangherlin, O. Martins de Brito, C. R. Chang, C. Blackstone, P. Bernardi, and L. Scorrano. Dephosphorylation by calcineurin regulates translocation of drp1 to mitochondria. *Proc Natl Acad Sci U S A*, 105(41):15803–8, 2008.

A. Chacinska, C. M. Koehler, D. Milenkovic, T. Lithgow, and N. Pfanner. Importing mitochondrial proteins: machineries and mechanisms. *Cell*, 138(4):628–44, 2009.

H. Chen and D. C. Chan. Physiological functions of mitochondrial fusion. *Ann N Y Acad Sci*, 1201:21–5, 2010.

S. Chiantia, J. Ries, N. Kahya, and P. Schwille. Combined afm and two-focus sfcs study of raft-exhibiting model membranes. *ChemPhysChem*, 7(11):2409–2418, 2006.

S. Chiantia, N. Kahya, and P. Schwille. Raft domain reorganization driven by short- and long-chain ceramide: a combined afm and fcs study. *Langmuir*, 23:7659–7665, 2007.

J. E. Chipuk and D. R. Green. How do bcl-2 proteins induce mitochondrial outer membrane permeabilization. *Trends in Cell Biology*, 18:157–164, 2008.

J. E. Chipuk, G. P. McStay, A. Bharti, T. Kuwana, C. J. Clarke, L. J. Siskind, L. M. Obeid, and D. R. Green. Sphingolipid metabolism cooperates with bak and bax to promote the mitochondrial pathway of apoptosis. *Cell*, 148(5):988–1000, 2012.

E. Y. Cho, C.-H. Yun, and T. Ahn. Effects of phospholipids on the functional regulation of tbid in membranes. *Molecular and Cellular Biochemistry*, 363(1-2):395–408, 2011.

A. D. Colella, N. Chegenii, M. N. Tea, I. L. Gibbons, K. A. Williams, and T. A. Chataway. Comparison of stain-free gels with traditional immunoblot loading control methodology. *Analytical Biocehmistry*, 430:108–110, 2012.

K. M. Connor, N. Hempel, K. K. Nelson, G. Dabiri, A. Gamarra, J. Belarmino, L. Van De Water, B. M. Mian, and J. A. Melendez. Manganese superoxide dismutase enhances the invasive and migratory activity of tumor cells. *Cancer Res*, 67(21):10260–7, 2007.

S. M. Cook, K. M. Lang, K. M. Chynoweth, M. Wigton, R. W. Simmonds, and T. E. Schäffer. Practical implementation of dynamic methods for measuring atomic force microscope cantilever spring constants. *Nanotechnology*, 17(9):2135–2145, 2006.

S. Cory, D. C. S. Huang, and J. M. Adams. The bcl-2 family: roles in cell survival and oncogenes. *Oncogene*, 22:8590–8607, 2003.

K. Cosentino and A. J. García-Sáez. Mitochondrial alterations in apoptosis. *Chem Phys Lipids*, 181:62–75, 2014.

K. Cosentino, U. Ros, and A. J. García-Sáez. Assembling the puzzle: Oligomerization of alpha-pore forming proteins in membranes. *Biochimica et Biophysica Acta*, 1858: 457–466, 2016.

P. S. Cremer and S. G. Boxer. Formation and spreading of lipid bilayers on planar glass supports. *Journal of Physical Chemistry B*, 103:2554–2559, 1999.

C. T. Culbertson, S. C. Jacobson, and J. M. Ramsey. Diffusion coefficient measurements in microfluidic devices. *Talanta*, 56:265–272, 2002.

P. E. Czabotar, D. Westphal, G. Dawson, S. Ma, C. Hockings, W. D. Fairlie, E. F. Lee, S. Yao, A. Y. Robin, B. J. Smith, D. C. S. Huang, R. M. Kluck, J. M. Adams, and P. M. Colman. Bax crystal structures reveal how bh3 domains activate bax and nucleate its oligomerization to induce apoptosis. *Cell*, 152:519–531, 2013.

P. E. Czabotar, G. Lessene, A. Strasser, and J. M. Adams. Control of apoptosis by the bcl-2 protein family: implications for physiology and therapy. *Nature Reviews Molecular Cell Biology*, 15:49–63, 2014.

C. Das, K. H. Sheikh, P. D. Olmsted, and S. D. Connell. Nanoscale mechanical probing of supported lipid bilayers with atomic force microscopy. *Phys Rev E Stat Nonlin Soft Matter Phys*, 82(4 Pt 1):041920, 2010.

K. K. Das, J. D. Unsay, and A. J. García-Sáez. *Microscopy of Model Membranes: Understanding How Bcl-2 Proteins Mediate Apoptosis*, volume 21, pages 63–97. Academic Press, 2015.

M. Dathe and T. Wieprecht. Structural features of helical antimicrobial peptides- their potential to modulate activity on model membranes and biological cells. *Biochimica et Biophysica Acta*, 1462:71–87, 1999.

G. Daum and J. E. Vance. Import of lipids into mitochondria. *Prog Lipid Res*, 36:103–130, 1997.

B. De Kruijff, A. J. Verkleij, J. Leunissen-Bijvelt, C. J. A. Van Echteld, J. Hille, and H. Rijnbout. Further aspects of the ca2+-dependent polymorphism of bovine heart cardiolipin. *Biochimica et Biophysica Acta*, 693:1–12, 1982.

C. Delettre, G. Lenaers, J.-M. Griffoin, N. Gigarel, C. Lorenzo, P. Belenguer, L. Pelloquin, J. Grosgeorge, C. Turc-Carel, E. Perret, C. Astarie-Dequeker, L. Lasquellec, B. Arnaud, B. Ducommun, J. Kaplan, and C. P. Hamel. Nuclear gene opa1, encoding a mitochondrial dynamin-related protein, is mutated in dominant optic atrophy. *Nature Genetics*, 26:207–210, 2000.

T. Dertinger, V. Pacheco, I. von der Hocht, R. Hartmann, I. Gregor, and J. Enderlein. Two-focus fluorescence correlation spectroscopy: A new tool for accurate and absolute diffusion measurements. *ChemPhysChem*, 8(3):433–443, 2007.

T. Dertinger, A. Loman, B. Ewers, C. B. Müller, B. Krämer, and J. Enderlein. The optics and performance of dual-focus fluorescence correlation spectroscopy. *Optics Express*, 16 (19):14353–14368, 2008.

S. Desagher, A. Osen-Sand, A. Nichols, R. Eskes, S. Montessuit, S. Lauper, K. Maundrell, B. Antonsson, and J.-C. Martinou. Bid-induced conformational change of bax is responsible for mitochondrial cytochrome c release during apoptosis. *Journal of Cell Biology*, 144:891–901, 1999.

P. Desjardins and S. Ledoux. The role of apoptosis in neurodegenerative diseases. *Metabolic Brain Disease*, 13:79–96, 1998.

G. Dewson. Doughnuts, daisy chains and crescent moons: the quest for the elusive apoptotic pore. *EMBO J*, 35(4):371–3, 2016.

G. Dewson, T. Kratina, H. W. Sim, H. Puthalakath, J. M. Adams, P. M. Colman, and R. M. Kluck. To trigger apoptosis, bak exposes its bh3 domain and homodimerizes via bh3:groove interactions. *Molecular Cell*, 30(3):369–380, 2008.

G. Dewson, S. Ma, P. Frederick, C. Hockings, I. Tan, T. Kratina, and R. M. Kluck. Bax dimerizes via a symmetric bh3:groove interface during apoptosis. *Cell Death Differ*, 19 (4):661–70, 2012.

C. E. J. Dieteren, S. C. A. M. Gielen, L. G. J. Nijtmans, J. A. M. Smeitink, H. G. Swarts, R. Brock, P. H. G. M. Willems, and W. J. H. Koopman. Solute diffusion is hindered in the mitochondrial matrix. *Proceedings of the National Academy of Sciences*, 108: 8657–8662, 2011.

M. A. Digman, C. M. Brown, P. Sengupta, P. W. Wiseman, A. R. Horwitz, and E. Gratton. Measuring fast dynamics in solutions and cells with a laser scanning microscope. *Biophysical Journal*, 89(2):1317–1327, 2005.

D. S. Dimitrov and R. K. Jain. Membrane stability. *Biochim Biophys Acta*, 779:437–468, 1984.

Ò. Domènech, F. Sanz, M. T. Montero, and J. Hernández-Borrell. Thermodynamic and structural study of the main phospholipid components comprising the mitochondrial inner membrane. *Biochimica et Biophysica Acta (BBA) - Biomembranes*, 1758(2):213–221, 2006.

Ò. Domènech, A. Morros, M. E. Cabañas, M. T. Montero, and J. Hernández-Borrell. Thermal response of domains in cardiolipin content bilayers. *Ultramicroscopy*, 107(10-11):943–947, 2007a.

Ò. Domènech, A. Morros, M. E. Cabañas, M. Teresa Montero, and J. Hernández-Borrell. Supported planar bilayers from hexagonal phases. *Biochimica et Biophysica Acta (BBA) - Biomembranes*, 1768(1):100–106, 2007b.

Ò. Domènech, L. Redondo, L. Picas, A. Morros, M. T. Montero, and J. Hernández-Borrell. Atomic force microscopy characterization of supported planar bilayers that mimic the mitochondrial inner membrane. *J Mol Recognit*, 20(6):546–53, 2007c.

A. L. Edinger and C. B. Thompson. Death by design: apoptosis, necrosis and autophagy. *Current Opinion in Cell Biology*, 16(6):663–669, 2004.

C. Eggeling, C. Ringemann, R. Medda, G. Schwarzmann, K. Sandhoff, S. Polyakova, V. N. Belov, B. Hein, C. von Middendorff, A. Schonle, and S. W. Hell. Direct observation of the nanoscale dynamics of membrane lipids in a living cell. *Nature*, 457(7233):1159–62, 2009.

J. Enderlein, I. Gregor, D. Patra, and J. Fitter. Arts and artefacts of fluorescence correlation spectroscopy. *Current Pharmaceutical Biotechnology*, 5:155–161, 2004.

J. Enderlein, I. Gregor, D. Patra, T. Dertinger, and U. B. Kaupp. Performance of fluorescence correlation spectroscopy for measuring diffusion and concentration. *ChemPhysChem*, 6(11):2324–2336, 2005.

R. F. Epand, J.-C. Martinou, M. Fornallaz-Mulhauser, D. W. Hughes, and R. M. Epand. The apoptotic protein tbid promotes leakage by altering membrane curvature. *Journal of Biological Chemistry*, 277(36):32632–9, 2002a.

R. F. Epand, J.-C. Martinou, S. Montessuit, R. M. Epand, and C. M. Yip. Direct evidence of membrane pore formation by the apoptotic protein bax. *Biochemical and Biophysical Research Communications*, 298:744–749, 2002b.

G. Feldmann, D. Haouzi, A. Moreau, A.-M. Durand-Schneider, A. Bringuier, A. Berson, A. Mansouri, D. Fau, and D. Pessayre. Opening of the mitochondrial permeability transition pore causes matrix expansion and outer membrane rupture in fas-mediated hepatic apoptosis in mice. *Hepatology*, 13:674–683, 2000.

K. Fernald and M. Kurokawa. Evading apoptosis in cancer. *Trends Cell Biol*, 23(12): 620–33, 2013.

P. L. T. M. Frederix, P. D. Bosshart, and A. Engel. Atomic force microscopy of biological membranes. *Biophysical Journal*, 96(2):329–338, 2009.

C. Frezza, S. Cipolat, O. Martins de Brito, M. Micaroni, G. V. Beznoussenko, T. Rudka, D. Bartoli, R. S. Polishuck, N. N. Danial, B. De Strooper, and L. Scorrano. Opa1 controls apoptotic cristae remodeling independently from mitochondrial fusion. *Cell*, 126(1):177–89, 2006.

J. R. Friedman, L. L. Lackner, M. West, J. R. DiBendetto, J. Nunnari, and G. K. Voeltz. Er tubules mark sites of mitochondrial division. *Science*, 334:358–362, 2011.

A. M. Fuentes-González, A. Contreras-Paredes, J. Manzo-Merino, and M. Lizano. The modulation of apoptosis by oncogenic viruses. *Virology Journal*, 10:182, 2013.

G. Fuertes, D. Gimenez, S. Esteban-Martin, A. J. García-Sáez, O. Sanchez, and J. Salgado. *Role of membrane lipids for the activity of pore forming peptides and proteins*, pages 31–55. Advances in Experimental Medicine and Biology. Springer New York, 2010/08/07 edition, 2010.

A. Gaigalas, L. Wang, A. Schartz, G. E. Marti, and R. F. Vogt. Quantitating fluorescence intensity from fluorophore: Assignment of mesf values. *Journal of Research of the National Institute of Standards and Technology*, 110:339–353, 2005.

R. Garcia and A. San Paulo. Amplitude curves and operating regimes in dynamic force microscopy. *Ultramicroscopy*, 82:79–83, 2000.

S. Garcia-Manyes, G. Oncins, and F. Sanz. Effect of temperature on the nanomechanics of lipid bilayers studied by force spectroscopy. *Biophysical Journal*, 89(6):4261–4274, 2005.

A. J. García-Sáez, I. Mingarro, E. Perez-Paya, and J. Salgado. Membrane-insertion fragments of bcl-xl, bax, and bid. *Biochemistry*, 43(34):10930–43, 2004.

A. J. García-Sáez, M. Coraiola, M. Dalla Serra, I. Mingarro, G. Menestrina, and J. Salgado. Peptides derived from apoptotic bax and bid reproduce the poration activity of the parent full-length proteins. *Biophysical Journal*, 88(6):3976–3990, 2005.

A. J. García-Sáez, M. Coraiola, M. D. Serra, I. Mingarro, P. Muller, and J. Salgado. Peptides corresponding to helices 5 and 6 of bax can independently form large lipid pores. *FEBS J*, 273(5):971–81, 2006.

A. J. García-Sáez, S. Chiantia, J. Salgado, and P. Schwille. Pore formation by a bax-derived peptide: Effect on the line tension of the membrane probed by afm. *Biophysical Journal*, 93(1):103–112, 2007a.

A. J. García-Sáez, S. Chiantia, and P. Schwille. Effect of line tension on the lateral organization of lipid membranes. *J Biol Chem*, 282(46):33537–44, 2007b.

A. J. García-Sáez, J. Ries, M. Orzaez, E. Perez-Paya, and P. Schwille. Membrane promotes tbid interaction with bcl(xl). *Nat Struct Mol Biol*, 16(11):1178–85, 2009.

E. Gavathiotis, D. E. Reyna, M. L. Davis, G. H. Bird, and L. D. Walensky. Bh3-triggered structural reorganization drives the activation of proapoptotic bax. *Mol Cell*, 40(3): 481–92, 2010.

A. Gennerich and D. Schild. Fluorescence correlation spectroscopy in small cytosolic compartments depends critically on the diffusion model used. *Biophysical Journal*, 79: 3294–3306, 2000.

W. J. Gerritsen, B. De Kruijff, A. J. Verkleij, J. De Gier, and L. L. M. van Deenen. Ca2+-induced isotropic motion and phosphatidylcholine flip-flop in phosphatidylcholine-cardiolipin bilayers. *Biochimica et Biophysica Acta*, 598:554–560, 1980.

R. J. C. Gilbert, R. K. Heenan, P. A. Timmins, N. A. Gingles, T. J. Mitchell, A. J. Rowe, J. Rossjohn, M. W. Parker, P. W. Andrew, and O. Byron. Studies on the structure and mechanism of a bacterial protein toxin by analytical ultracentrifugation and small-angle neutron scattering. *J Mol Biol*, 293:1145–1160, 1999.

L. A. Gillies, H. Du, B. Peters, C. M. Knudson, D. D. Newmeyer, and T. Kuwana. Visual and functional demonstration of growing bax-induced pores in mitochondrial outer membranes. *Mol Biol Cell*, 26:339–349, 2015.

J. S. Goodwin and A. K. Kenworthy. Photobleaching approaches to investigate diffusional mobility and trafficking of ras in living cells. *Methods*, 37:154–164, 2005.

M. T. Grijalba, A. E. Vercesi, and S. Schreier. Ca2+-induced increased lipid packing and domain formation in submitochondrial particles. a possible early step in the mechanism of ca2+-stimulated generation of reactive oxygen species by the respiratory chain. *Biochemistry*, 38(40):13279–13287, 1999.

A. Gross, J. M. McDonnell, and S. J. Korsmeyer. Bcl-2 family members and the mitochondria in apoptosis. *Genes & Development*, 13:1899–1911, 1999.

L. Grosse, C. A. Wurm, C. Bruser, D. Neumann, D. C. Jans, and S. Jakobs. Bax assembles into large ring-like structures remodeling the mitochondrial outer membrane in apoptosis. *EMBO J*, 35(4):402–13, 2016.

X. Han, J. Yang, K. Yang, Z. Zhao, D. R. Abendschein, and R. W. Gross. Alterations in myocardial cardiolipin content and composition occur at the very earliest stages of diabetes: A shotgun lipidomics study. *Biochemistry*, 46:6417–6428, 2007.

P. K. Hansma, J. P. Cleveland, M. Radmacher, D. A. Walters, P. E. Hillner, M. Bezanilla, M. Fritz, D. Vie, H. G. Hansma, C. B. Prater, J. Massie, L. Fukunaga, J. Gurley, and V. Elings. Tapping mode atomic force microscopy in liquids. *Applied Physics Letters*, 64(13):1738, 1994.

Z. Hao and T. W. Mak. Type i and type ii pathways of fas-mediated apoptosis are differentially controlled by xiap. *J Mol Cell Biol*, 2(2):63–4, 2010.

M. Harner, C. Korner, D. Walther, D. Mokranjac, J. Kaesmacher, U. Welsch, J. Griffith, M. Mann, F. Reggiori, and W. Neupert. The mitochondrial contact site complex, a determinant of mitochondrial architecture. *EMBO J*, 30(21):4356–70, 2011.

E. Haustein and P. Schwille. Fluorescence correlation spectroscopy: Novel variations of an established technique. *Annual Review of Biophysics and Biomolecular Structure*, 36 (1):151–169, 2007.

F. Heigwer, G. Kerr, and M. Boutros. E-crisp: fast crispr target site identification. *Nature Methods*, 11:122–123, 2014.

S. W. Hell and J. Wichman. Breaking the diffraction resolution limit by stimulated emission: stimulated-emission-depletion fluorescence microscopy. *Optics Letters*, 19(11): 780–782, 1994.

E. Hermann, S. Bleicken, Y. Subburaj, and A. J. García-Sáez. Automated analysis of giant unilamellar vesicles using circular hough transformation. *Bioinformatics*, 30(12): 1747–54, 2014.

F. L. Hoch. Cardiolipins and mitochondrial proton-selective leakage. *Journal of Bioenergetics and Biomembranes*, 30:511–532, 1998.

S. E. Horvath and G. Daum. Lipids of mitochondria. *Prog Lipid Res*, 52(4):590–614, 2013.

H. Huang. Molecular mechanism of antimicrobial peptides: the origin of cooperativity. *Biochimica et Biophysica Acta*, 1758:1292–1302, 2006.

H. W. Huang. Action of antimicrobial peptides: two-state model. *Biochemistry*, 39: 8347–8352, 2000.

J. Humpolíčková, E. Gielen, A. Benda, V. Fagulova, J. Vercammen, M. vandeVen, M. Hof, M. Ameloot, and Y. Engelborghs. Probing diffusion laws within cellular membranes by z-scan fluorescence correlation spectroscopy. *Biophysical Journal*, 91(3):L23–L25, 2006.

A. Ikai. Nanobiomechanics of proteins and biomembrane. *Philosophical Transactions of the Royal Society B: Biological Sciences*, 363(1500):2163–2171, 2008.

S. Jakobs and C. A. Wurm. Super-resolution microscopy of mitochondria. *Curr Opin Chem Biol*, 20:9–15, 2014.

M. Javanainen, H. Hammaren, L. Monticelli, J.-H. Jeon, M. S. Miettinen, H. Martinez-Seara, R. Metzler, and I. Vattulainen. Anomalous and normal diffusion of proteins and lipids in crowded lipid membranes. *Faraday Discussions*, 161:397, 2013.

P. J. Jost, S. Grabow, D. Gray, M. D. McKenzie, U. Nachbur, D. C. S. Huang, P. Bouillet, H. E. Thomas, C. Borner, J. Silke, A. Strasser, and T. Kaufmann. Xiap discriminates between type i and type ii fas-induced apoptosis. *Nature*, 460(7258):1035–9, 2009.

N. Kahya. Probing lipid mobility of raft-exhibiting model membranes by fluorescence correlation spectroscopy. *Journal of Biological Chemistry*, 278(30):28109–28115, 2003.

N. Kahya and P. Schwille. Fluorescence correlation studies of lipid domains in model membranes. *Mol Membr Biol*, 23(1):29–39, 2006.

P. Kapusta. Absolute diffusion coefficients, 2010.

M. Karbowski, Y. J. Lee, B. Gaume, S. Y. Jeong, S. Frank, A. Nechushtan, A. Santel, M. Fuller, C. L. Smith, and R. J. Youle. Spatial and temporal association of bax with mitochondrial fission sites, drp1, and mfn2 during apoptosis. *J Cell Biol*, 159(6):931–8, 2002.

M. Karbowski, K. L. Norris, M. M. Cleland, S. Y. Jeong, and R. J. Youle. Role of bax and bak in mitochondrial morphogenesis. *Nature*, 443(7112):658–62, 2006.

L. Kastrup, H. Blom, C. Eggeling, and S. W. Hell. Fluorescence fluctuation spectroscopy in subdiffraction focal volumes. *Phys Rev Lett*, 94(17):178104, 2005.

T. Kaufmann, S. Schlipf, J. Sanz, K. Neubert, R. Stein, and C. Borner. Characterization of the signal that directs bcl-xl, but not bcl-2, to the mitochondrial outer membrane. *The Journal of Cell Biology*, 160(1):53–64, 2003.

J. F. R. Kerr, A. H. Wyllie, and A. Currie. Apoptosis: a basic biological phenomenon with wide-ranging implications in tissue kinetics. *British Journal of Cancer*, 26:239–257, 1972.

N. Khalifat, J.-B. Fournier, M. I. Angelova, and N. Puff. Lipid packing variations induced by ph in cardiolipin-containing bilayers: The driving force for the cristae-like shape instability. *Biochimica et Biophysica Acta (BBA) - Biomembranes*, 1808(11):2724–2733, 2011.

H. Kim, H.-C. Tu, D. Ren, O. Takeuchi, J. R. Jeffers, G. P. Zambetti, J. J. Hsieh, and E. H. Cheng. Stepwise activation of bax and bak by tbid, bim, and puma initiates mitochondrial apoptosis. *Mol Cell*, 36(3):487–99, 2009.

S. A. Kim, K. G. Heinze, and P. Schwille. Fluorescence correlation spectroscopy in living cells. *Nature Methods*, 4(11):963–973, 2007.

T. H. Kim, Y. Zhao, W. X. Ding, J. N. Shin, X. He, Y. W. Seo, J. Chen, H. Rabinowich, A. A. Amoscato, and X. M. Yin. Bid-cardiolipin interaction at mitochondrial contact site contributes to mitochondrial cristae reorganization and cytochrome c release. *Mol Biol Cell*, 15(7):3061–72, 2004.

T. Kohl and P. Schwille. *Fluorescence Correlation Spectroscopy with Autofluorescent Proteins*, volume 95 of *Advances in Biochemical Engineering*, pages 107–142. Springer-Verlag Berlin Heidelberg, Germany, 2005.

S. Koirala, Q. Guo, R. Kalia, H. Bui, D. M. Eckert, A. Frost, and J. M. Shaw. Interchangeable adaptors regulate mitochondrial dynamin assembly for membrane scission. *Proceedings of the National Academy of Sciences*, 110:E1342–E1351, 2013.

W. J. H. Koopman, M. A. Hink, S. Verkaart, H. J. Visch, J. A. Smeitink, and P. H. Willems. Partial complex i inhibition decreases mitochondrial motility and increases matrix protein diffusion as revealed by fluorescence correlation spectroscopy. *Biochim Biophys Acta*, 1767(7):940–7, 2007.

D. Koppel. Statistical accuracy in fluorescence correlation spectroscopy. *Physical Review A*, 10(6):1938–1945, 1974.

J. W. Krieger, A. P. Singh, N. Bag, C. S. Garbe, T. E. Saunders, J. Langowski, and T. Wohland. Imaging fluorescence (cross-) correlation spectroscopy in live cells and organisms. *Nat Protoc*, 10(12):1948–74, 2015.

T. Kuwana, M. R. Mackey, G. Perkins, M. H. Ellisman, M. Latterich, R. Schneiter, D. R. Green, and D. D. Newmeyer. Bid, bax and lipids cooperate to form supramolecular openings in the outer mitochondrial membrane. *Cell*, 111:331–342, 2002.

J. R. Lakowicz. *Principles of Fluorescence Spectroscopy*. Springer Science+Business Media, LLC, NY, USA, third edition, 2006.

M. Langner and S. W. Hui. Merocyanine interaction with phosphatidylcholine bilayers. *Biochimica et Biophysica Acta*, 1149:175–179, 1993.

B. Leber, J. L. Lin, and D. W. Andrews. Embedded together: The life and death consequences of interaction of the bcl-2 family with membranes. *Apoptosis*, 12(5):897–911, 2007.

B. Leber, F. Geng, J. Kale, and D. W. Andrews. Drugs targeting bcl-2 family members as an emerging strategy in cancer. *Expert Reviews in Molecular Medicine*, 12, 2010.

M.-T. Lee, F.-Y. Chen, and H. W. Huang. Energetics of pore formation induced by membrane active peptides. *Biochemistry*, 43:3590–3599, 2004.

M. T. Lee, W. C. Hung, F. Y. Chen, and H. W. Huang. Mechanism and kinetics of pore formation in membranes by water-soluble amphipathic peptides. *Proceedings of the National Academy of Sciences*, 105:5087–5092, 2008.

F. Legros, A. Lombes, P. Frachon, and M. Rojo. Mitochondrial fusion in human cells is efficient, requires the inner membrane potential, and is mediated by mitofusins. *Mol Biol Cell*, 13(12):4343–54, 2002.

R. N. A. H. Lewis and R. N. McElhaney. The physicochemical properties of cardiolipin bilayers and cardiolipin-containing lipid membranes. *Biochimica et Biophysica Acta (BBA) - Biomembranes*, 1788(10):2069–2079, 2009.

R. N. A. H. Lewis, D. Zweytick, G. Pabst, K. Lohner, and R. N. McElhaney. Calorimetric, x-ray diffraction, and spectroscopic studies of the thermotropic phase behavior and organization of tetramyristoyl cardiolipin membranes. *Biophysical Journal*, 92(9):3166–3177, 2007.

A. M. Lieto, R. C. Cush, and N. L. Thompson. Ligand-receptor kinetics measured by total internal reflection with fluorescence correlation spectroscopy. *Biophysical Journal*, 85:3294–3302, 2003.

E. M. Lifshitz and L. Pitaevskii. *Statistical Physics*, volume 9 of *Course of Theoretical Physics*. Pergamon Press, Oxford, UK, 1980.

A. U. Lindner, C. G. Colcannon, G. J. Boukes, M. D. Cannon, F. Llambi, D. Ryan, K. Boland, J. Kehoe, D. A. McNamara, F. Murray, E. W. Kay, S. Hector, D. R. Green, H. J. Huber, and J. H. M. Prehn. Systems analysis of bcl2 protein family interactions establishes a model to predict responses to chemotherapy. *Cancer Research*, 73:519–528, 2012.

Q. Liu, B. Leber, and D. W. Andrews. Interactions of pro-apoptotic bh3 proteins with anti-apoptotic bcl-2 family proteins measured in live mcf-7 cells using flim fret. *Cell Cycle*, 11(19):3536–42, 2012.

F. Llambi, T. Moldoveanu, S. W. Tait, L. Bouchier-Hayes, J. Temirov, L. L. McCormick, C. P. Dillon, and D. R. Green. A unified model mammalian bcl-2 protein family interactions at the mitochondria. *Molecular Cell*, 44:517–531, 2011.

M. L. Longo, A. J. Waring, L. M. Gordon, and D. A. Hammer. Area expansion and permeation of phospholipid bilayers by influenza fusion peptide and melittin. *Langmuir*, 14:2385–2395, 1998.

J. F. Lovell, L. P. Billen, A. Shamas-Din, C. Fradin, B. Leber, and D. W. Andrews. Membrane binding by tbid initiates an ordered series of events culminating in membrane permeabilization by bax. *Cell*, 135(6):1074–1084, 2008.

S. W. Lowe and A. W. Lin. Apoptosis in cancer.pdf. *Carcinogenesis*, 21:485–495, 2000.

S. Lucken-Ardjomande, S. Montessuit, and J.-C. Martinou. Contributions to bax insertion and oligomerization of lipids of the mitochondrial outer membrane. *Cell Death Differ*, 15(5):929–37, 2008.

M. Lutter, M. Fang, X. Luo, M. Nishijima, X.-s. Xie, and X. Wang. Cardiolipin provides specificity for targeting tbid to mitochondria. *Nature Cell Biology*, 2:754–756, 2000.

J. D. Ly, D. R. Grubb, and A. Lawen. The mitochondrial membrane potential in apoptosis: an update. *Apoptosis*, 8:115–128, 2003.

P. M. Macdonald and J. Seelig. Calcium binding to mixed cardiolipin-phosphatidylcholine bilayers as studied by deuterium nuclear magnetic resonance. *Biochemistry*, 26:6292–6298, 1987.

C. I. Maeder, M. A. Hink, A. Kinkhabwala, R. Mayr, P. I. H. Bastiaens, and M. Knop. Spatial regulation of fus3 map kinase activity through a reaction-diffusion mechanism in yeast pheromone signalling. *Nature Cell Biology*, 9(11):1319–1326, 2007.

D. Magde, E. Elson, and W. Webb. Thermodynamic fluctuations in a reacting system—measurement by fluorescence correlation spectroscopy. *Physical Review Letters*, 29(11): 705–708, 1972.

S. N. Magonov, V. Elings, and M.-H. Whangbo. Phase imaging and stiffness in tapping-mode atomic force microscopy. *Surface Science*, 375:L385–L391, 1997.

J. G. Mandersloot, W. J. Gerritsen, J. Leunissen-Bijvelt, C. J. A. Van Echteld, P. C. Noordam, and J. De Gier. Ca2+-induced changes in the barrier properties of cardiolipin/phosphatidylcholine bilayers. *Biochimica et Biophysica Acta*, 640:106–113, 1981.

S. J. Marrink and A. E. Mark. Molecular view of hexagonal phase formation in phospholipid membranes. *Biophys J*, 87(6):3894–900, 2004.

J.-C. Martinou and R. J. Youle. Mitochondria in apoptosis: Bcl-2 family members and mitochondrial dynamics. *Developmental Cell*, 21:92–101, 2011.

M. P. Mattson. Apoptosis in neurodegenerative disorders. *Nature Reviews Molecular Cell Biology*, 1:120–129, 2000.

N. Mau, A. V. Kajava, C. Bonfils, J.-C. Martinou, and M. C. Harricane. Interactions of bax and tbid with lipid monolayers. *Journal of Membrane Biology*, 207(1):1–9, 2005.

H. M. McBride, M. Neuspiel, and S. Wasiak. Mitochondria: More than just a powerhouse. *Current Biology*, 16:R551–R560, 2006.

M. E. McCurrach, T. M. F. Connor, C. M. Knudson, S. J. Korsmeyer, and S. W. Lowe. Bax-deficiency promotes drug resistance and oncogenic transformation by attenuating p53-dependent apoptosis. *Proceedings of the National Academy of Sciences*, 94:2345–2349, 1997.

L. Meng, T. Huang, X. Wang, S. Chen, Z. Yang, and B. Ren. Gold-coated afm tips for tip-enhanced raman spectroscopy: theoretical calculation and experimental demonstration. *Opt Express*, 23(11):13804–13, 2015.

U. Mennicke and T. Salditt. Preparation of solid-supported lipid bilayers by spin-coating. *Langmuir*, 18:8172–8177, 2002.

U. Meseth, T. Wohland, R. Rigler, and H. Vogel. Resolution of fluorescence correlation measurements. *Biophysical Journal*, 76:1619–1631, 1999.

S. S. Metkar, M. Marchioretto, V. Antonini, L. Lunelli, B. Wang, R. J. Gilbert, G. Anderluh, R. Roth, M. Pooga, J. Pardo, J. E. Heuser, M. D. Serra, and C. J. Froelich. Perforin oligomers form arcs in cellular membranes: a locus for intracellular delivery of granzymes. *Cell Death Differ*, 22(1):74–85, 2015.

G. Meyer and N. M. Amer. Novel optical approach to atomic force microscopy. *Applied Physics Letters*, 53(12):1045, 1988.

E. Mileykovskaya and W. Dowhan. Cardiolipin membrane domains in prokaryotes and eukaryotes. *Biochimica et Biophysica Acta (BBA) - Biomembranes*, 1788(10):2084–2091, 2009.

K. Mitra and J. Lippincott-Schwartz. Analysis of mitochondrial dynamics and functions using imaging approaches. *Curr Protoc Cell Biol*, Chapter 4:Unit 4 25 1–21, 2010.

S. Montessuit, S. P. Somasekharan, O. Terrones, S. Lucken-Ardjomande, S. Herzig, R. Schwarzenbacher, D. J. Manstein, E. Bossy-Wetzel, G. Basañez, P. Meda, and J.-C. Martinou. Membrane remodeling induced by the dynamin-related protein drp1 stimulates bax oligomerization. *Cell*, 142:889–901, 2010.

V. J. Morris, A. R. Kirby, and A. P. Gunning. *Atomic Force Microscopy for Biologists*. Imperial College Press, London, U.K., 2nd edition, 2010.

F. Mueller, P. Wach, and J. G. McNally. Evidence for a common mode of transcription factor interaction with chromatin as revealed by improved quantitative fluorescence recovery after photobleaching. *Biophysical Journal*, 94:3323–3339, 2008.

B. K. Muller, E. Zaychikov, C. Brauchle, and D. C. Lamb. Pulsed interleaved excitation. *Biophys J*, 89(5):3508–22, 2005.

D. J. Muller. Afm: A nanotool in membrane biology. *Biochemistry*, 47:7986–7998, 2008.

S. Nichols-Smith, S.-Y. Teh, and T. L. Kuhl. Thermodynamic and mechanical properties of model mitochondrial membranes. *Biochimica et Biophysica Acta (BBA) - Biomembranes*, 1663(1-2):82–88, 2004.

P. S. Niemelä, M. T. Hyvönen, and I. Vattulainen. Influence of chain length and unsaturation on sphingomyelin bilayers. *Biophysical Journal*, 90(3):851–863, 2006.

Y. Ohsugi, K. Saito, M. Tamura, and M. Kinjo. Lateral mobility of membrane-binding proteins in living cells measured by total internal reflection fluorescence correlation spectroscopy. *Biophys J*, 91(9):3456–64, 2006.

A. Ortiz, J. A. Killian, A. J. Verkleij, and J. Wilschut. Membrane fusion and the lamellar-to-inverted-hexagonal phase transition in cardiolipin vesicle systems induced by divalent cations. *Biophysical Journal*, 77:2003–2014, 1999.

K. S. Oyedotun and B. D. Lemire. The quarternary structure of *Saccharomyces creviceiae* succinate dehydrogenase. *Journal of Biological Chemistry*, 279:9424–9431, 2004.

N. Ozoren and W. S. El-Deiry. Defining characteristics of types i and ii apoptotic cells in response to trail. *Neoplasia*, 4(6):551–7, 2002.

L. J. Pagliari, T. Kuwana, C. Bonzon, D. D. Newmeyer, S. Tu, H. M. Beere, and D. R. Green. The multi domain proapoptotic molecules bax and bak are directly activated by heat. *Proceedings of the National Academy of Sciences*, 102:17975–17980, 2005.

C. S. Palmer, L. D. Osellame, D. Stojanovski, and M. T. Ryan. The regulation of mitochondrial morphology: intricate mechanisms and dynamic machinery. *Cell Signal*, 23 (10):1534–45, 2011.

A. Partikian, B. Ölveczky, R. Swaminathan, A. Li, and A. Verkman. Rapid diffusion of green fluorescent protein in the mitochondrial matrix. *J Cell Biol*, 140:821–829, 1998.

Z. Petrášek and P. Schwille. Precise measurement of diffusion coefficients using scanning fluorescence correlation spectroscopy. *Biophysical Journal*, 94(4):1437–1448, 2008.

E. P. Petrov and P. Schwille. *State of the Art and Novel Trends in Fluorescence Correlation Spectroscopy*, volume 6 of *Springer Series on Fluorescence*, pages 145–197. Springer-Verlag Berlin Heidelberg, 2008.

M. Picard, K. White, and D. M. Turnbull. Mitochondrial morphology, topology, and membrane interactions in skeletal muscle: a quantitative three-dimensional electron microscopy study. *J Appl Physiol (1985)*, 114(2):161–71, 2013.

G. L. Powell and D. Marsh. Polymorphic phase behavior of cardiolipin derivatives studied by 31p nmr and x-ray diffraction. *Biochemistry*, 24:2902–2908, 1985.

S. Pöyry, T. Róg, M. Karttunen, and I. Vattulainen. Mitochondrial membranes with mono- and divalent salt- changes induced by salt ions on structure and dynamics. *Journal of Physical Chemistry B*, 113:15513–15521, 2009.

M. Przybylo, J. Sykora, J. Humpolíčková, A. Benda, A. Zan, and M. Hof. Lipid diffusion in gian unilamellar vesicles is more than 2 times faster than in supported phospholipid bilayers under identical conditions. *Langmuir*, 22:9096–9099, 2006.

S. Qian, W. Wang, L. Yang, and H. W. Huang. Structure of transmembrane pore induced by bax-derived peptide: evidence for lipidic pores. *Proc Natl Acad Sci U S A*, 105(45): 17379–83, 2008.

E. Raemy and J.-C. Martinou. Involvement of cardiolipin in tbid-induced activation of bax during apoptosis. *Chem Phys Lipids*, 179:70–4, 2014.

E. Raemy, S. Montessuit, S. Pierredon, A. H. van Kampen, F. M. Vaz, and J. C. Martinou. Cardiolipin or mtch2 can serve as tbid receptors during apoptosis. *Cell Death and Differentiation*, 23:1165–1174, 2016.

F. A. Ran, P. D. Hsu, J. Wright, V. Agartala, D. A. Scott, and F. Zhang. Genome engineering using the crispr-cas9 system. *Nature Protocols*, 8:2281–2308, 2013.

R. P. Rand and S. Sengupta. Cardiolipin forms hexagonal structures with divalent cations. *Biochimica et Biophysica Acta*, 255:484–492, 1972.

I. Raviakine and A. R. Brisson. Formation of supported phospholipid bilayers from unilamellar vesicles investigated by atomic force microscopy. *Langmuir*, 16:1806–1815, 2000.

L. Redondo-Morata, M. I. Giannotti, and F. Sanz. *Stability of Lipid Bilayers as Model Membranes: Atomic Force Microscopy and Spectroscopy Approach.* Wiley-VCH Verlag GmbH, first edition, 2012.

A. S. Reichert and W. Neupert. Contact sites between the outer and inner membrane of mitochondria - role in protein transport. *Biochimica et Biophysica Acta*, 1592:41–49, 2002.

Y. Reis, M. Bernardo-Faura, D. Richter, T. Wolf, B. Brors, A. Hamacher-Brady, R. Eils, and N. R. Brady. Multi-parametric analysis and modeling of relationships between mitochondrial morphology and apoptosis. *PLoS ONE*, 7:e28694, 2012.

E. A. J. Reits and J. J. Neefjes. From fixed to frap: measuring protein mobility and activity in living cells. *Nature Cell Biology*, 3:E145–E147, 2001.

J. E. Ricci, R. A. Gottlieb, and D. R. Green. Caspase-mediated loss of mitochondrial function and generation of reactive oxygen species during apoptosis. *J Cell Biol*, 160 (1):65–75, 2003.

J. E. Ricci, C. Muñoz-Pinedo, P. Fitzgerald, B. Bailly-Maitre, G. A. Perkins, N. Yadava, I. E. Scheffler, M. H. Ellisman, and D. R. Green. Disruption of mitochondrial function during apoptosis is mediated by caspase cleavage of the p75 subunit of complex i of the electron transport chain. *Cell*, 117(6):773–86, 2004.

R. P. Richter and A. R. Brisson. Following the formation of supported lipid bilayers on mica: A study combining afm, qcm-d, and ellipsometry. *Biophysical Journal*, 88(5): 3422–3433, 2005.

R. P. Richter, R. Bérat, and A. R. Brisson. Formation of solid-supported lipid bilayers. *Langmuir*, 22:3497–3505, 2006.

M. Rief. Reversible unfolding of individual titin immunoglobulin domains by afm. *Science*, 276(5315):1109–1112, 1997.

J. Ries and P. Schwille. Studying slow membrane dynamics with continuous wave scanning fluorescence correlation spectroscopy. *Biophysical Journal*, 91(5):1915–1924, 2006.

J. Ries, E. P. Petrov, and P. Schwille. Total internal reflection fluorescence correlation spectroscopy: Effects of lateral diffusion and surface-generated fluorescence. *Biophysical Journal*, 95(1):390–399, 2008a.

J. Ries, T. Ruckstuhl, D. Verdes, and P. Schwille. Supercritical angle fluorescence correlation spectroscopy. *Biophysical Journal*, 94(1):221–229, 2008b.

J. Ries, S. Chiantia, and P. Schwille. Accurate determination of membrane dynamics with line-scan fcs. *Biophysical Journal*, 96(5):1999–2008, 2009a.

J. Ries, S. R. Yu, M. Burkhardt, M. Brand, and P. Schwille. Modular scanning fcs quantifies receptor-ligand interactions in living multicellular organisms. *Nature Methods*, 6(9):643–645, 2009b.

J. Ries, T. Weidemann, and P. Schwille. *Fluorescence Correlation Spectroscopy*, pages 210–245. Academic Press, 2012.

R. Rigler, Ü. Mets, J. Widengren, and P. Kask. Fluorescence correlation spectroscopy with high count rate and low background: analysis of translational diffusion. *European Biophysics Journal*, 22:169–175, 1993.

U. Ros and A. J. García-Sáez. More than a pore: The interplay of pore-forming proteins and lipid membranes. *J Membr Biol*, 248(3):545–61, 2015.

Q. Ruan, M. A. Cheng, M. Levi, E. Gratton, and W. W. Mantulin. Spatial-temporal studies of membrane dynamics: Scanning fluorescence correlation spectroscopy (sfcs). *Biophysical Journal*, 87(2):1260–1267, 2004.

J. E. Sader. Frequency response of cantilever beams immersed in viscous fluids with applications to the atomic force microscope. *Journal of Applied Physics*, 84(1):64, 1998.

J. E. Sader. Susceptibility of atomic force microscope cantilevers to lateral forces. *Review of Scientific Instruments*, 74(4):2438, 2003.

J. E. Sader and R. C. Sader. Susceptibility of atomic force microscope cantilevers to lateral force: experimental verification. *Applied Physics Letters*, 83:3195–3197, 2003.

J. E. Sader, I. Larson, P. Mulvaney, and L. R. White. Method for the calibration of atomic force microscope cantilevers. *Review of Scientific Instruments*, 66(7):3789, 1995.

J. E. Sader, J. Pacifico, C. P. Green, and P. Mulvaney. General scaling law for stiffness measurement of small bodies with applications to the atomic force microscope. *Journal of Applied Physics*, 97(12):124903, 2005.

S. Saffarian and E. L. Elson. Statistical analysis of fluorescence correlation spectroscopy: The standard deviation and bias. *Biophysical Journal*, 84:2030–2042, 2003.

M. Saito, S. J. Korsmeyer, and P. H. Schlesinger. Bax-dependent transport of cytochrome c reconstituted in pure liposomes. *Nature Cell Biology*, 2:553–555, 2000.

R. Salvador-Gallego, M. Mund, K. Cosentino, J. Schneider, J. D. Unsay, U. Schraermeyer, J. Engelhardt, J. Ries, and A. J. García-Sáez. Bax assembly into rings and arcs in apoptotic mitochondria is linked to membrane pores. *EMBO J*, 35(4):389–401, 2016.

M. B. Sankaram, G. L. Powell, and D. Marsh. Effect of acyl chain composition on salt-induced lamellar to inverted hexagonal phase transitions in cardiolipin. *Biochimica et Biophysica Acta (BBA) - Biomembranes*, 980:389–392, 1989.

J. Sankaran, M. Manna, L. Guo, R. Kraut, and T. Wohland. Diffusion, transport, and cell membrane organization investigated by imaging fluorescence cross-correlation spectroscopy. *Biophys J*, 97(9):2630–9, 2009.

M. Sarcina, N. Murata, M. J. Tobin, and C. W. Mullineaux. Lipid diffusion in the thylakoid membranes of the cyanobacterium synechococcus sp.: effect of fatty acid desaturation. *FEBS Letters*, 553(3):295–298, 2003.

D. Satsuma, N. Kucerka, S. Shivakumar, J. Pencer, C. Griffiths, B. Leber, D. W. Andrews, J. Katsaras, and C. Fradin. Interaction of the full-length bax protein with biomimetic mitochondrial liposomes: A small-angle neutron scattering and fluorescence study. *Biochimica et Biophysica Acta - Biomembranes*, 1818:384–401, 2012.

M. J. Saxton and K. Jacobson. Single particle tracking: Applications to membrane dynamics. *Annual Review of Biophysics and Biomolecular Structure*, 26:373–399, 1997.

E. Schäfear, N. A. Dencher, J. Vonck, and D. N. Parcel. Three-dimensional structure of the respiratory chain supercomplex i1iii2iv1 from bovine heart mitochondria. *Biochemistry*, 46:12579?12585, 2007.

M. Schlame, J. A. Towbin, P. M. Heerdt, R. Jehle, S. DiMauro, and T. J. J. Blanck. Deficiency of tetralinoleoyl-cardiolipin in barth syndrome. *Annals of Neurology*, 51(5): 634–637, 2002.

P. H. Schlesinger, A. Gross, X.-M. Yin, K. Yamamoto, M. Saito, G. Waksman, and S. J. Korsmeyer. Comparison of the ion channel characteristics of proapoptotic bax and antiapoptotic bcl-2. *Proceedings of the National Academy of Sciences*, 94:11357–11362, 1997.

O. Schmidt, N. Pfanner, and C. Meisinger. Mitochondrial protein import: from proteomics to functional mechanisms. *Nat Rev Mol Cell Biol*, 11(9):655–67, 2010.

A. Schwartz, L. Wang, E. Early, A. Gaigalas, Y.-z. Zhang, G. E. Marti, and R. F. Vogt. Quantitating fluorescence intensity from fluorophore: The definition of mesf assignment. *Journal of Research of the National Institute of Standards and Technology*, 107:83–91, 2002.

G. Schwarz. Estimating the dimension of a model. *The Annals of Statistics*, 6:461–464, 1978.

P. Schwille, U. Haupts, S. Maiti, and W. W. Webb. Molecular dynamics in living cells observed by fluorescence correlation spectroscopy with one- and two-photon excitation. *Biophysical Journal*, 77:2251–2265, 1999.

L. Scorrano, M. Ashiya, K. Buttle, S. Weiler, S. A. Oakes, C. A. Mannella, and S. J. Korsmeyer. A distinct pathway remodels mitochondrial cristae and mobilizes cytochrome c during apoptosis. *Developmental Cell*, 2:55–67, 2002.

L. Scorrano, S. A. Oakes, J. T. Opferman, E. H. Cheng, M. D. Sorcinelli, T. Pozzan, and S. J. Korsmeyer. Bax and bak regulation of endoplasmic reticulum ca2+: A control point for apoptosis. *Science*, 300:135–139, 2003.

H. M. Seeger, G. Marino, A. Alessandrini, and P. Facci. Effect of physical parameters on the main phase transition of supported lipid bilayers. *Biophysical Journal*, 97(4): 1067–1076, 2009.

D. Sengupta, H. Leontiadou, A. E. Mark, and S.-J. Marrink. Toroidal pores formed by antimicrobial peptide show significant disorder. *Biochimica et Biophysica Acta (BBA) - Biomembranes*, 1778:2308–2317, 2008.

A. Shamas-Din, S. Binder, W. Zhu, Y. Zaltsman, C. Campbell, A. Gross, B. Leber, D. W. Andrews, and C. Fradin. tbid undergoes multiple conformational changes at the membrane required for bax activation. *Journal of Biological Chemistry*, 288(30): 22111–22127, 2013a.

A. Shamas-Din, J. Kale, B. Leber, and D. W. Andrews. Mechanisms of action of bcl-2 family proteins. *Cold Spring Harb Perspect Biol*, 5(4):a008714, 2013b.

A. Shamas-Din, S. Bindner, X. Chi, B. Leber, D. W. Andrews, and C. Fradin. Distinct lipid effects on tbid and bim activation of membrane permeabilization by pro-apoptotic bax. *Biochem J*, 2015.

S. Shivakumar, M. Kurylowicz, N. Hirmiz, Y. Manan, O. Friaa, A. Shamas-Din, P. Masoudian, B. Leber, D. W. Andrews, and C. Fradin. The proapoptotic protein tbid forms both superficially bound and membrane-inserted oligomers. *Biophys J*, 106(10):2085–95, 2014.

B. D. Slaughter, J. W. Schwartz, and R. Li. Mapping dynamic protein interactions in map kinase signaling using live-cell fluorescence fluctuation spectroscopy and imaging. *Proceedings of the National Academy of Sciences*, 104(51):20320–20325, 2007.

E. Smirnova, L. Griparic, D.-L. Shurland, and A. M. van der Bliek. Dynamin-related protein drp1 is required for mitochondrial division in mammalian cells. *Molecular Biology of the Cell*, 12:2245–2256, 2001.

A. F. Sonnen, J. M. Plitzko, and R. J. Gilbert. Incomplete pneumolysin oligomers form membrane pores. *Open Biol*, 4:140044, 2014.

P. M. F. Sousa, S. T. N. Silva, B. L. Hood, N. Charro, J. a. N. Carita, F. Vaz, D. Penque, T. P. Conrads, and A. M. P. Melo. Supramolecular organizations in the aerobic respiratory chain of *Esoterichia coli*. *Biochemie*, 93:418–425, 2011.

G. C. Sparagna, A. J. Chicco, R. C. Murphy, M. R. Bristow, C. A. Johnson, M. L. Rees, M. L. Maxey, S. A. McCune, and R. L. Moore. Loss of cardiac tetralinoleoyl cardiolipin in human and experimental heart failure. *The Journal of Lipid Research*, 48(7):1559–1570, 2007.

T. J. Stasevich, F. Mueller, A. Michelman-Ribeiro, T. Rosales, J. R. Knutson, and J. G. McNally. Cross-validating frap and fcs to quantify the impact of photobleaching on in vivo binding estimates. *Biophysical Journal*, 99:3093–3101, 2010.

W. Stillwell, S. R. Wassal, A. C. Dumaual, W. D. Ehringer, C. W. Browning, and L. J. Jenski. Use of merocyanine (mc540) in quantifying lipid domains and packing in phospholipid vesicles and tumor cells. *Biochimica et Biophysica Acta (BBA) - Biomembranes*, 1146:136–144, 1993.

S. E. Straus, M. Sneller, M. J. Lenardo, J. M. Puck, and W. Strober. An inherited disorder of lymphocyte apoptosis: The autoimmune lymphoproliferative syndrome. *Annals of Internal Medicine*, 130:591–601, 1999.

Y. Subburaj, K. Cosentino, M. Axmann, E. Pedrueza-Villalmanzo, E. Hermann, S. Bleicken, J. Spatz, and A. J. García-Sáez. Bax monomers form dimer units in the membrane that further self-assemble into multiple oligomeric species. *Nat Commun*, 6:8042, 2015.

D. F. Suen, K. L. Norris, and R. J. Youle. Mitochondrial dynamics and apoptosis. *Genes Dev*, 22(12):1577–90, 2008.

F. Sun, X. Huo, Y. Zhai, A. Wang, J. Xu, D. Su, M. Bartlam, and Z. Rao. Crystal structure of mitochondrial respiratory membrane protein complex ii. *Cell*, 121:1043–1057, 2005.

M. Suzuki, R. J. Youle, and N. Tjandra. Structure of bax: Coregulation of dimer formation and intracellular localization. *Cell*, 103:645–654, 2000.

T. Takahashi, F. Nomura, Y. Yokoyama, Y. Tanaka-Takiguchi, M. Homma, and K. Takiguchi. Multiple membrane interactions and versatile vesicle deformations elicited by melittin. *Toxins*, 5(4):637–664, 2013.

T. Tatsuta, M. Scharwey, and T. Langer. Mitochondrial lipid trafficking. *Trends Cell Biol*, 24(1):44–52, 2014.

M. E. Taylor. Dynamics of piezoelectric tube scanners for scanning probe microscopy. *Review of Scientific Instruments*, 64(1):154, 1993.

R. C. Taylor, S. P. Cullen, and S. J. Martin. Apoptosis: controlled demolition at the cellular level. *Nat Rev Mol Cell Biol*, 9(3):231–41, 2008.

A. Tcherniak, C. Reznik, S. Link, and C. F. Landes. Fluorescence correlation spectroscopy: Criteria for analysis in complex systems. *Analytical Chemistry*, 81(746-754), 2009.

O. Terrones, B. Antonsson, H. Yamaguchi, H.-G. Wang, J. Liu, R. M. Lee, A. Herrmann, and G. Basañez. Lipidic pore formation by the concerted action of proapoptotic bax and tbid. *Journal of Biological Chemistry*, 279:30081–30091, 2004.

E. Thews, M. Gerken, R. Eckert, J. Zapfel, C. Tietz, and J. Wrachtrup. Cross talk free fluorescence cross correlation spectroscopy in live cells. *Biophys J*, 89(3):2069–76, 2005.

C. B. Thompson. Apoptosis in the pathogenesis and treatment of disease. *Science*, 267: 1456–1462, 1995.

N. L. Thompson and D. Axelrod. Immunoglobulin surface-binding kinetics studied by total internal reflection with fluorescence correlation spectroscopy. *Biophysical Journal*, 43:103–114, 1983.

N. L. Thompson, T. P. Burghardt, and D. Axelrod. Measuring surface dynamics of biomolecules by total internal reflection fluorescence with photobleaching receovery or correlation spectroscopy. *Biophysical Journal*, 33:435–454, 1981.

N. Tomsie, B. Babnik, D. Lombardo, B. Mavcic, M. Kanduser, A. Iglic, and V. Kralj-Iglic. Shape and size of giant unilamellar phospholipid vesicles containing cardiolipin. *Journal of Chemical Information and Modeling*, 45:1676–1679, 2005.

B. Torre, C. Canale, D. Ricci, and P. C. Braga. Measurement methods in atomic force microscopy. *Methods Mol Biol*, 736:19–29, 2011a.

B. Torre, D. Ricci, and P. C. Braga. How the atomic force microscope works? *Methods Mol Biol*, 736:3–18, 2011b.

Y. Tsujimoto, L. R. Finger, J. Yunis, P. Nowell, and C. M. Croce. Cloning of the chromosome breakpoint of neoplastic b cells with the t(14;18) chromosome translocation. *Science*, 226(1097-1099), 1984.

B. Ugarte-Uribe and A. J. García-Sáez. Membranes in motion: mitochondrial dynamics and their role in apoptosis. *Biol Chem*, 395(3):297–311, 2014.

B. Ugarte-Uribe, H. M. Muller, M. Otsuki, W. Nickel, and A. J. García-Sáez. Dynamin-related protein 1 (drp1) promotes structural intermediates of membrane division. *J Biol Chem*, 289(44):30645–56, 2014.

M. H. Ulbrich and E. Y. Isacoff. Subunit counting in membrane-bound proteins. *Nature Methods*, 4:319–321, 2007.

J. Unsay, K. Cosentino, Y. Subburaj, and A. J. García-Sáez. Cardiolipin effects on membrane structure and dynamics. *Langmuir*, 29:15878–15887, 2013.

J. Unsay, K. Cosentino, and A. J. García-Sáez. Atomic force microscopy imaging and force spectroscopy of supported lipid bilayers. *J Vis Exp*, 101:e52867, 2015.

J. D. Unsay and A. J. García-Sáez. Scanning fluorescence correlation spectroscopy in model membrane systems. *Methods Mol Biol*, 1033:185–205, 2013.

W. J. Vail and J. G. Stollery. Phase changes of cardiolipin vesicles mediated by divalent cations. *Biochimica et Biophysica Acta*, 551:74–84, 1979.

T. Wai and T. Langer. Mitochondrial dynamics and metabolic regulation. *Trends in Endocrinology & Metabolism*, 27:105–117, 2016.

L. Wang, A. Gaigalas, F. Abbasi, G. E. Marti, R. F. Vogt, and A. Schwartz. Quantitating fluorescence intensity from fluorophore: Practical use of mesf values. *Journal of Research of the National Institute of Standards and Technology*, 107:339–353, 2002.

X. Wang. The expanding role of mitochondria in apoptosis. *Genes & Development*, 15: 2922–2933, 2001.

M. Wasilewski and L. Scorrano. The changing shape of mitochondrial apoptosis. *Trends Endocrinol Metab*, 20(6):287–94, 2009.

M. C. Wei, T. Lindsten, V. K. Mootha, S. Weiler, A. Gross, M. Ashiya, C. B. Thompson, and S. J. Korsmeyer. tbid, a membrane-targeted death ligand, oligomerizes bak to release cytochrome c. *Genes & Development*, 14:2060–2071, 2000.

T. Weidemann, M. Wachsmuth, T. A. Knoch, G. Müller, W. Waldeck, and J. Langowski. Counting nucleosomes in living cells with a combination of fluorescence correlation spectroscopy and confocal imaging. *Journal of Molecular Biology*, 334(2):229–240, 2003.

P. H. G. M. Willems, H. G. Swarts, M. A. Hink, and W. J. H. Koopman. *The Use of Fluorescence Correlation Spectroscopy to Probe Mitochondrial Mobility and Intramatrix Protein Diffusion*, volume 456, pages 287–302. Academic Press, 2009.

P. Williamson, K. Mattocks, and R. A. Schlegel. Merocyanine 540, a fluorescent probe sensitive to lipid packing. *Biochim Biophys Acta*, 732:387–393, 1983.

S. N. Willis, L. Chen, G. Dawson, A. Wei, E. Naik, J. I. Fletcher, J. M. Adams, and D. C. S. Huang. Proapoptotic bak is sequestered by mcl-1 and bcl-xl, but not bcl-2, until displaced by bh3-only proteins. *Genes & Development*, 19:1294–1305, 2005.

S. N. Willis, J. I. Fletcher, T. Kaufmann, M. F. van Delft, l. Chen, P. E. Czabotar, H. Ierino, E. F. Lee, W. D. Fairlie, P. Bouillet, A. Strasser, R. M. Kluck, J. M. Adams, and D. C. S. Huang. Apoptosis initiated when bh3 ligands engage multiple bcl-2 homologs, not bax or bak. *Science*, 315:856–859, 2007.

J. Wilschut, M. Holsappel, and R. Jansen. Ca 2+-induced fusion of cardiolipin/phosphatidylcholine vesicles monitored by mixing of aqueous contents. *Biochimica et Biophysica Acta*, 690:297–301, 1982.

E. Wit, E. van den Heuvel, and J.-W. Romejin. 'all models are wrong...': an introduction to model uncertainty. *Statistica Neerlandica*, 66:217–236, 2012.

T. Wohland, X. Shi, J. Sankaran, and E. H. K. Stelzer. Single plane illumination fluorescence correlation spectroscopy (spim-fcs) probes inhomogeneous three-dimensional environments. *Optics Express*, 18:10627–10641, 2010.

A. Wyllie, C. Bellamy, V. Bubb, A. Clarke, S. Corbet, L. Curtis, D. Harrison, M. Hooper, N. Toft, S. Webb, and C. Bird. Apoptosis and carcinogenesis. *British Journal of Cancer*, 80:34–37, 1999.

X. P. Xu, D. Zhai, E. Kim, M. Swift, J. C. Reed, N. Volkmann, and D. Hanein. Three-dimensional structure of bax-mediated pores in membrane bilayers. *Cell Death Dis*, 4: e683, 2013.

T. Yamauchi, K. Ohki, H. Maruyama, and Y. Nozawa. Thermal adaptation of tetrahymena membranes with special reference to mitochondria: Role of cardiolipin in fluidity of mitochondrial membranes. *Biochimica et Biophysica Acta*, 649:385–392, 1981.

V. Yankovskaya, R. Horsefield, S. Törnroth, C. Luna-Chavez, H. Miyoshi, C. Leger, B. Byrne, G. Cecchini, and S. Iwata. Architecture of succinate dehydrogenase and reactive oxygen species generation. *Science*, 299:700–704, 2003.

Y. Yao, A. A. Bobkov, L. A. Plesniak, and F. M. Marassi. Mapping the interaction of pro-apoptotic tbid with pro-survival bcl-xl. *Biochemistry*, 48:8704–8711, 2009.

H. Yuan, A. A. Gerencser, G. Liot, S. A. Lipton, M. H. Ellisman, G. A. Perkins, and E. Bossy-Wetzel. Mitochondrial fission is an upstream and required event for bax foci formation in response to nitric oxide in cortical neurons. *Cell Death Differ*, 14(3):462–71, 2007.

T. N. Zeczycki, J. Whelan, W. T. Hayden, D. A. Brown, and S. R. Shaikh. Increasing levels of cardiolipin differentially influence packing of phospholipids found in the mitochondrial inner membrane. *Biochem Biophys Res Commun*, 450(1):366–71, 2014.

M. Zellner, R. Babeluk, M. Diestinger, P. Pirchegger, S. Skeledzic, and R. Oehler. Fluorescence-based western blotting for quantitation of protein biomarkers in clinical samples. *Electrophoresis*, 29:3621–3627, 2008.

J. Zhang, P. Chen, B. Yuan, W. Ji, Z. Cheng, and X. Qiu. Real-space identification of intermolecular bonding with atomic force microscopy. *Science*, 342(6158):611–4, 2013.

D. V. Zhelev and D. Needham. Tension-stabilized pores in giant vesicles: determination of pore size and pore line tension. *Biochim Biophys Acta*, 1147(1):89–104, 1993.

L. Zhou and D. C. Chang. Dynamics and structure of the bax-bak complex responsible for releasing mitochondrial proteins during apoptosis. *J Cell Sci*, 121(Pt 13):2186–96, 2008.